CZECH TECHNICAL UNIVERSITY IN PRAGUE
FACULTY OF ELECTRICAL ENGINEERING
DEPARTMENT OF ELECTROMAGNETIC FIELD

HABILITATION THESIS

Resonant Ring Metamaterials

Lukas Jelinek

Prague, April 2014

Preface

This habilitation thesis is meant as a brief abstract covering a particular part of the habilitant's career. It is an attempt to compile the author's works on resonant ring systems, together with relevant work by other authors, and to form a self-consistent and readable text. The habilitant's works are highlighted by an asterisk symbol in the citation brackets, i.e. [X*] indicates work done by the habilitant. Other publications by the habilitant on other topics are included in the habilitation application, but are strictly omitted from this abstract. The author's work on resonant rings has also been covered to a similar extent in a review paper [1*, see Appendix 1].

It is important to stress that this thesis is not a review, and the list of references therefore does not provide complete coverage of the topics presented here. Only those references are cited here which are strictly necessary for setting the general context and for understanding the work that has been done.

Acknowledgements

The work presented in this thesis has been done in close collaboration with Ricardo Marques, Manuel Freire, Francisco Mesa and Raul Berral from the University of Seville, with Juan Baena, currently from the National University of Bogota, with Mikhail Lapine, currently from the University of Sydney, with Jan Machac and Jan Zehentner from the Czech Technical University in Prague and with Mario Silveirinha from the University of Coimbra. I would like to thank all of them for beautiful discussions which have usually resulted in interesting results and publications and have always led to a deeper understanding of electromagnetism and to a lot of fun.

Contents

Chapter 1

Introduction

A general and brief definition of a metamaterial that covers all its variants and its whole scope would be almost impossible. However, a metamaterial is most commonly understood as an artificial medium with macroscopic electromagnetic characteristics (permittivity, permeability, conductivity), i.e. constitutive parameters, that are not attainable in natural materials. Particular examples of great importance are materials with negative values of their constitutive parameters. These materials have attracted a lot of attention among physicists and electrotechnical engineers. From a general perspective, however, a metamaterial should be seen as a material with effective parameters that can be set to almost any value at almost any frequency.

Metaterials have brought important new concepts into classical electromagnetism. Firstly, they have shown that electrodynamics of complex media (particularly with negative material parameters) is far from being satisfactorily explored. Secondly, they have led to proposals for interesting new devices.

One of these was the perfect lens [2], which consists of an isotropic slab of thickness d_lens with material constants ε_in and μ_in surrounded by another isotropic material with parameters ε_out and μ_out. If the materials are chosen [2] in such a way that $\varepsilon_\text{out} = -\varepsilon_\text{in}$ and $\mu_\text{out} = -\mu_\text{in}$, the slab behaves as a perfect lens that transfers all plane waves, including all evanescent harmonics, from the source plane at a distance d_source in front of the lens, to the image plane, which is situated at a distance d_image behind the lens, provided that the distances are chosen such that $k_z^\text{out} d_\text{source} + k_z^\text{out} d_\text{image} = k_z^\text{in} d_\text{lens}$, where k_z is a wavenumber component perpendicular to the slab.

A second interesting device is an electromagnetic cloak [3–5], which consists of a shell of complex material that makes the inner part of the shell completely invisible to electromagnetic radiation. The basic idea behind the cloak is to deform the coordinates so that a given region is completely excluded and to transform this deformation into a flat space filled with an inhomogeneously distributed complex medium. This idea is in fact not completely novel, as it is well known in general relativity [6] that within classical electromagnetism a given gravitational field can always be negated by a properly distributed complex material. The merit of recent works on cloaks thus lie mostly in the awareness of the fact that complex materials of this kind are now available thanks to the development of metamaterials. Currently, the idea of an electromagnetic cloak is becoming a particular case of the broader topic of transformation optics [7] which is extensively developed further.

In brief, metamaterials are nowadays an indivisible part of the classical electromagnetic field theory. Its fundamental theory and its detailed history can be found in several eminent textbooks, see for example [8–10].
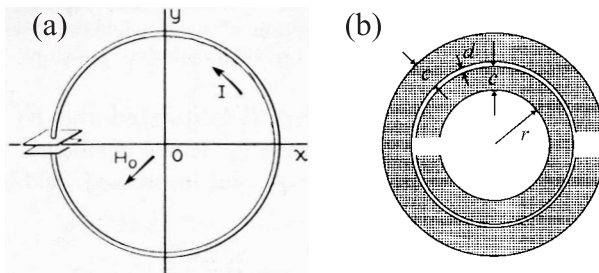

Fig. 1.1: (a) A capacitively loaded metallic ring as depicted in [11], (b) A Split Ring Resonator as depicted in [12].

1.1 Metamaterials Made of Resonant Rings

An important category of metamaterials are artificial materials offering diamagnetic permeability $\mu_r < 1$ (artificial diamagnetics). The idea of creating artificial diamagnetics is in fact more than a century old. It goes back to the work of Weber [13], who realized that a closed metallic loop exhibits diamagnetic properties. However, the magnitude of the magnetic polarizability of a simple closed loop is very limited, due to its unavoidable self-inductance. In order to overcome this difficulty, Schelkunoff and Friis [11] proposed to add a lumped capacitor into the loop (see Fig. 1.1a), creating a resonant system in which the diamagnetic properties are greatly enhanced in the vicinity of the resonance frequency. This preliminary design was improved by Hardy and Whitehead [14] using a distributed capacitance, and was later made popular by Pendry [12] in planar technology (see Fig. 1.1b). From that point, artificial diamagnetics made of resonant rings became one of the core topics in metamaterials and various designs were systematically studied [9]. Resonant rings are the topic that permeates this thesis.

Chapter 2

A Planar Ring Resonator

This chapter will review some basic properties and designs of planar resonant rings and will deal solely with isolated rings placed in a vacuum. It should also be noted that the word "planar" will be used in a loose sense in this section. Any design with one dimension that is much smaller than the other two dimensions will be called planar.

2.1 Polarizability of a Capacitivelly Loaded Ring

Before presenting practical designs, it is instructive to review the simplest case of a capacitivelly loaded ring (CLR), originally proposed in [11]. For this purpose imagine the ring (see Fig. 2.1a) is excited by a time-varying, but almost uniform, electric or magnetic field. The ring is assumed to be significantly smaller than the operation wavelength ($kr \ll 1$), which is a necessary condition for being a component of homogenizable material, and its polarization can be well described by the induced electric dipole moment $\mathbf{p}$ and the magnetic dipole moment $\mathbf{m}$. Following the standard notation [15], these dipole moments are connected to exciting fields via the polarizability tensors as

$$
\begin{aligned}
\mathbf{p} &= \left[\alpha_{ij}^{\text{ee}}\right] \cdot \mathbf{E} + \left[\alpha_{ij}^{\text{em}}\right] \cdot \mathbf{B} \\
\mathbf{m} &= \left[\alpha_{ij}^{\text{me}}\right] \cdot \mathbf{E} + \left[\alpha_{ij}^{\text{mm}}\right] \cdot \mathbf{B},
\end{aligned}
\tag{2.1}
$$

where within the defined coordinate system

$$
\begin{aligned}
\left[\alpha_{ij}^{\text{ee}}\right] &\approx \begin{bmatrix} \alpha_{xx}^{\text{ee}} & 0 & 0 \\ 0 & \alpha_{yy}^{\text{ee}} & 0 \\ 0 & 0 & 0 \end{bmatrix} & \left[\alpha_{ij}^{\text{mm}}\right] &\approx \begin{bmatrix} 0 & 0 & 0 \\ 0 & 0 & 0 \\ 0 & 0 & \alpha_{zz}^{\text{mm}} \end{bmatrix} \\
\left[\alpha_{ij}^{\text{em}}\right] &\approx \begin{bmatrix} 0 & 0 & 0 \\ 0 & 0 & \alpha_{yz}^{\text{em}} \\ 0 & 0 & 0 \end{bmatrix} & \left[\alpha_{ij}^{\text{me}}\right] &\approx \begin{bmatrix} 0 & 0 & 0 \\ 0 & 0 & 0 \\ 0 & -\alpha_{yz}^{\text{em}} & 0 \end{bmatrix}
\end{aligned}
\tag{2.2}
$$

and where the reciprocity theorem [16] has been used to equate α_{zy}^{me} and $-\alpha_{yz}^{\text{em}}$. The form of the electric polarisability α_{ij}^{ee} and magnetic polarisability α_{ij}^{mm} is quite intuitive, and the magnetic polarizability can in fact be easily estimated from Faraday's law as

$$
\alpha_{zz}^{\text{mm}} = \frac{-\mathrm{j}\omega \pi^2 r^4}{\mathrm{j}\omega L + \frac{1}{\mathrm{j}\omega C}},
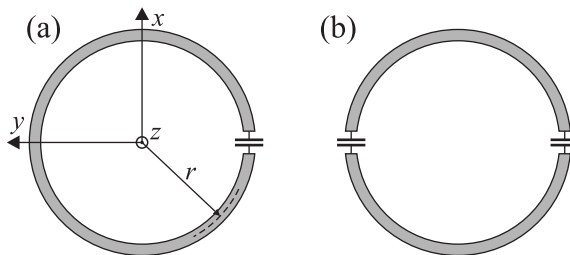\tag{2.3}
$$

Fig. 2.1: A metallic ring loaded by one (a) or two (b) capacitances.
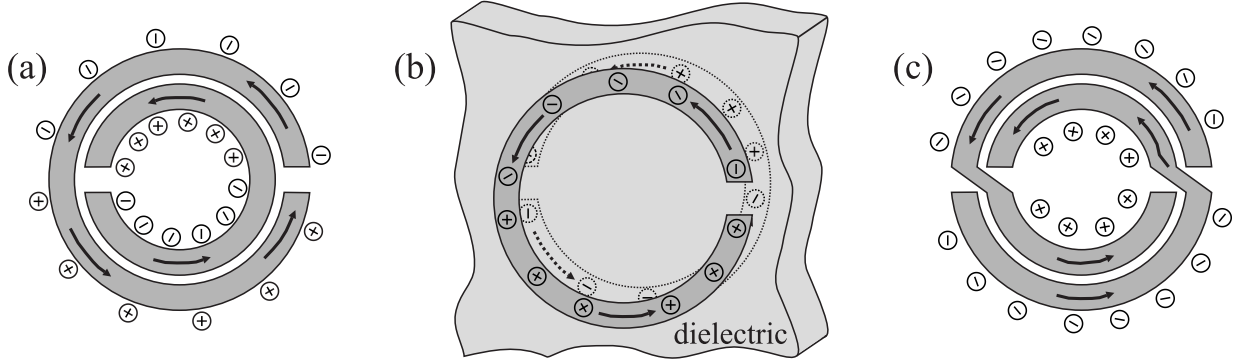
Fig. 2.2: Split Ring Resonator (a) Broadside-Coupled Split Ring Resonator (b) Non-Bianisotropic Split Ring Resonator (c) and the corresponding current and charge densities excited by an axial magnetic field.

where L is the self-inductance of the closed loop and C is the loading capacitance. The form of magnetic polarizability also shows that the ring resonance can be seen as the resonance of a serial resonance circuit in which the inductance is given by the ring, while the majority of the capacitance is concentrated inside the gap. Unlike the electric and magnetic polarisabilities, the presence of magnetoelectric polarizabilities $\alpha_{ij}^{\mathrm{em}}$, $\alpha_{ij}^{\mathrm{me}}$ (or in other words the presence of bianisotropy) is less evident and in fact poses a problem for many applications. Fortunately, there is an easy way to remove them. The method for removing them lies in the geometrical properties of these quantities, which should be more precisely named pseudo-tensors. Having this property in mind, it is straightforward to show that magnetoelectric polarizabilities will identically vanish once the structure exhibits inversion symmetry. This is easily achieved by adding a second capacitor, as shown in (see Fig. 2.1b). The magnetic and electric polarizabilties are practically unaffected by this change, with the only exception that the resonance frequency will be approximately $\sqrt{2}$-times higher, as the capacitances are added in series. It is worth noting that the growing electrical size caused by growing symmetry is a general property of ring resonators, as will be seen also in other designs in the following text.

2.2 Resonant Rings with Distributed Capacitance

The fundamental idea leading to present-day resonant rings is to exchange the lumped gap capacitance for a properly distributed capacitance. A major advantage of this step is that it can be fabricated by printed circuit board methods, and can also be extended to higher frequencies. The basic design following this line is the so-called Split Ring Resonator (SRR) [12,14], depicted in Fig. 2.2a. Its working principle is equivalent to an ordinary CLR, as can be seen from the depicted current and charge distribution excited at resonance by an axial magnetic field. As was shown in [17], the circuit model of the magnetic resonance of SRR also consists of a serial resonant circuit, where the capacitance is a serial connection of the top and bottom halves of the SRR. This paper also contained an ingenious modification of SRR depicted in Fig. 2.2b (commonly abbreviated as BCSRR), which exhibits identical magnetic resonance, but due to its inversion symmetry precludes magnetoelectric coupling. A strictly planar modification of BCSRR was proposed in [18], see Fig. 2.2c, and is commonly abbreviated as NBSRR (Non-Bianisotropic Split Ring Resonator).

It will be shown in the next chapter that topologies with higher symmetry than those of SRR, BCSRR or NBSRR are sometimes desired. The geometries shown in Fig. 2.3 were developed for this purpose [19*, see Appendix 2], [20*, see Appendix 3]. As mentioned in Sec. 2.1, the price to pay for higher symmetries is bigger electrical size.

Apart from purely geometrical changes, there are also important modifications of the resonant rings that bring whole new functionalities. To begin with, it is for example very interesting to ask how an ordinary SRR would perform at optical frequencies, where the magnetic response is practically impossible to find in natural substances. A pioneering work [21] showed that when real metals can no more be considered as perfect conductors at optical frequencies, a novel phenomenon of frequency and amplitude saturation of the magnetic resonance emerges. The reason for this phenomenon is the presence of so-called kinetic inductance [21], which can also be seen as a negative capacitance represented by the negative permittivity of the metal constituting the ring. This kinetic inductance scales differently than the regular inductance, giving rise to the saturation phenomenon. A detailed model of several variants of an optical
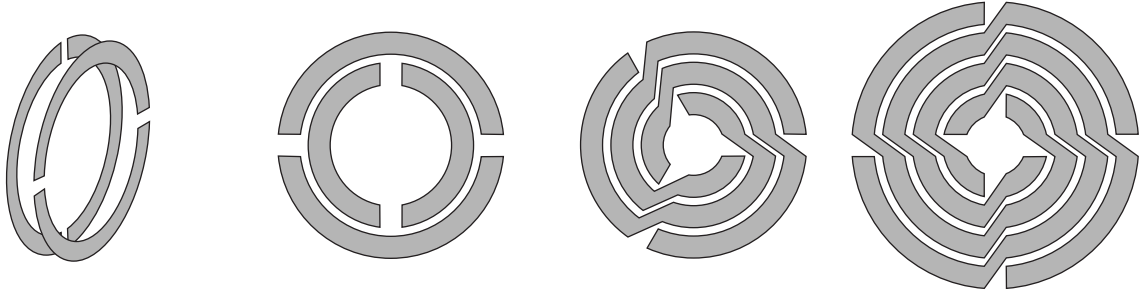
Fig. 2.3: Ring Resonators with various degrees of symmetry.

resonant ring, see Fig. 2.4, was developed in [22*, see Appendix 4] and it was shown that the saturation can (quite counter-intuitively) be postponed by adding additional ring splits. The resonance frequency of
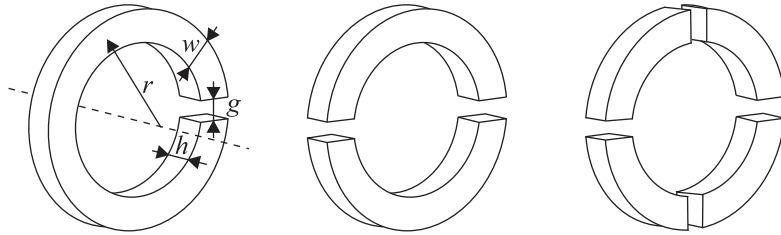

Fig. 2.4: Optical Ring Resonators.

the three designs depicted in Fig. 2.4 is shown in Fig. 2.5. The delayed saturation of the multi-gap rings is evident from the figure. The results unfortunately also suggest that no strong magnetic response can be expected from resonant rings in visible range, which in fact corresponds well with fundamental energetic reasoning [23] concerning the questionable existence of magnetic properties at optical frequencies.
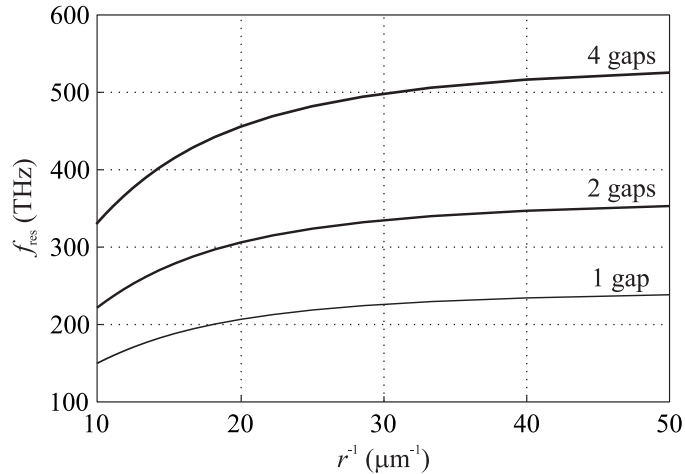

Fig. 2.5: Resonance frequency saturation of the three Optical Ring Resonators from Fig. 2.4 for $w = h = 0.3r$, $g = 0.1r$, $\omega_\mathrm{p} \approx 2.2 \cdot 10^{16}\ s^{-1}$, $f_\mathrm{c} \approx 1.2 \cdot 10^{14}\ s^{-1}$.

Playing with a possible material composing the body of the resonant ring, a very interesting possibility emerges, resulting in so-called Dielectric Ring Resonator [24*, see Appendix 5], which consists of a toroidal ring made of a high permittivity dielectric, see Fig. 2.6. This structure can exhibit exactly the same quasi-static magnetic resonance as metallic resonant rings. The reason for this behavior lies in the equality of the conduction and polarization currents within Ampere's Law, and the necessity to modify the classical definition for the magnetic dipole moment [15] and self-inductance to take into account not only the conduction currents but also the polarization currents [24*, see Appendix 5]. The presence of the capacitance in the gap-less ring may be less intuitive, but careful consideration [24*, see Appendix 5] shows that it is uniformly distributed within the dielectric material of the ring.
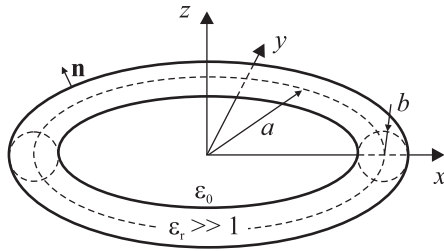
Fig. 2.6: Dielectric Ring Resonator.

Another interesting modification of the regular ring resonator involves exploiting the commonly unwanted magnetoelectric couplings, and leads to the so-called Chiral Split Ring Resonator [25*, see Appendix 6], [26*, see Appendix 7], see Fig. 2.7. A careful look reveals that its structure is a simple
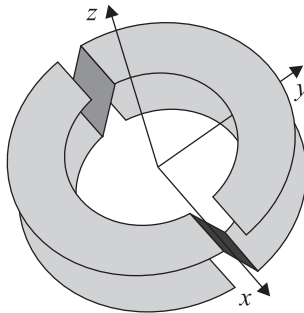

Fig. 2.7: Chiral Split Ring Resonator.

modification of NB-SRR from Fig. 2.2c, and that the current and charge distribution will also necessarily be equal. This results (as expected) in a resonant magnetic polarizability $\alpha_{zz}^{\mathrm{mm}}$. The fundamental difference with respect to NB-SRR however is that the induced charges do not lie in the same plane, and in fact all positive/negative charges lie on the top/bottom, or vice versa. This evidently results in resonant electric dipolar polarizability $\alpha_{zz}^{\mathrm{ee}}$ and magnetoelectric polarizability $\alpha_{zz}^{\mathrm{em}}$ which, curiously, all have the same tensor orientation. Furthermore, it is possible to design the ring in such a way that $c_0^2 \alpha_{zz}^{\mathrm{ee}} = c_0 |\alpha_{zz}^{\mathrm{em}}| = \alpha_{zz}^{\mathrm{mm}}$, which leads to a so-called balanced design [27], [25*, see Appendix 6], [26*, see Appendix 7], which can be used as a basic unit of a bi-isotropic medium transparent for circularly polarized waves, while at the same time exhibiting negative refraction for them [27, 28].

The last presented modification of a resonant ring follows a recent trend in metamaterials to include active elements in order to mitigate the losses and the strong dispersion that are inherent properties of any resonant electrically small system. The simplest idea is to use an active load in the CLR design of Fig. 2.1 instead of just a passive capacitor. One way is to use negative resistance circuits [29*, see Appendix 8], which have a simple hand-made practical design for low RF range as shown in Fig. 2.8. Based on both the measured data and the theoretically predicted data, the magnetic polarizability of such a system shows a positive imaginary part, i.e. a gain, which also brings into play interesting questions on the stability of the active medium [29*, see Appendix 8].
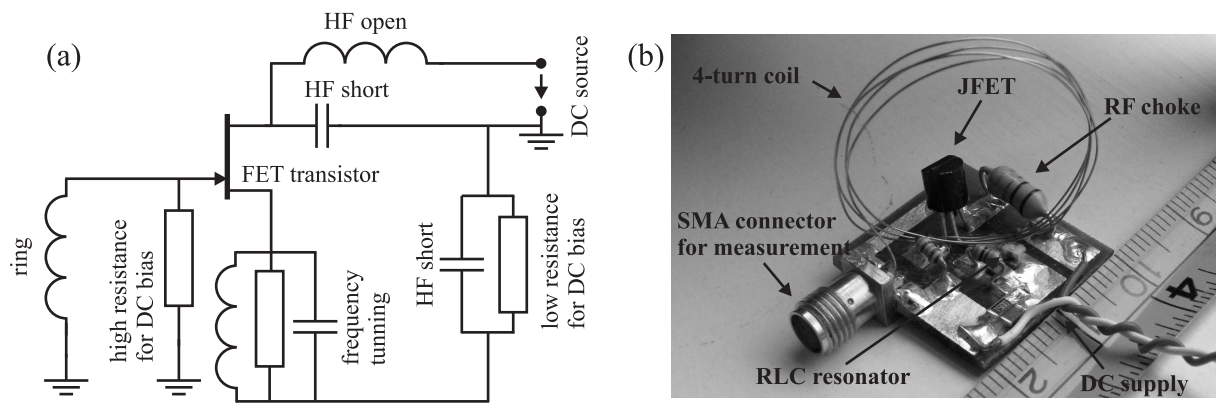
(a)

HF open

HF short

DC source

FET transistor

ring

high resistance for DC bias

frequency tunning

HF short

low resistance for DC bias

(b)

4-turn coil

JFET

RF choke

SMA connector for measurement

RLC resonator

DC supply

Fig. 2.8: (a) Scheme of a ring loaded by a negative resistance transistor circuit (b) and a photograph of a realistic implementation. The ring is actually a four-turn coil made of thin wire.

Chapter 3

Isotropic Ring Resonators

The resonant rings presented in the previous chapter all provide a strongly anisotropic response. This can be useful for certain applications, but isotropic materials are generally of wider use. This is also true for one of the key ideas of metamaterials, the perfect lens [2], which also assumes an isotropic medium.

Before treating the full bulk medium, it is instructive to study stand-alone, but isotropic resonators. The first step in this direction was already taken in [12], where the cubic arrangement depicted in Fig. 3.1a was proposed. However, this proposal is incorrect [20*, see Appendix 3], and does not in fact exhibit
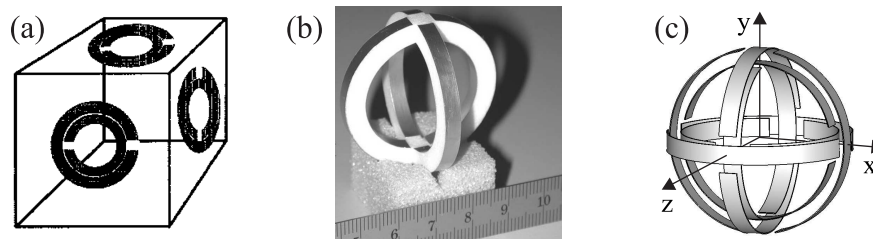

Fig. 3.1: (a) A cubic resonator made of SRRs, as depicted in [12] (c) A 2D isotropic spherical resonator, as depicted in [30] (c) A 3D isotropic spherical resonator, as depicted in [19*, see Appendix 2].

isotropic behavior. The first correct design, though only 2D isotropic, was proposed four years later, in [30], see Fig. 3.1b, but the true isotropic resonator was not proposed until 2006 [19*, see Appendix 2], see Fig. 3.1c. The key point of the design is the use of point groups of symmetry to establish the minimum symmetry requirements on a single ring resonator to be useful for a 3D isotropic design. Through this method it was shown [20*, see Appendix 3] that an ordinary SRR [12] does not exhibit enough symmetry and some more symmetrical designs have to be used, see Sec. 2.2.

The design shown in Fig. 3.1c is theoretically very appealing, and is even superior in several parameters to its successors. Its major drawback, however, is its fabrication complexity, which makes mass-production practically impossible (it should be pointed out that practical metamaterial devices would easily contain thousands of resonators of this kind). In order to remove this drawback, the point groups of symmetry has been used for the original proposal [12], with the aim to set symmetry requirements on the rings that are used. It was shown [20*, see Appendix 3] that only designs following the geometries depicted in Fig. 3.2 are possible candidates for isotropic resonators. Consulting these requirements with the
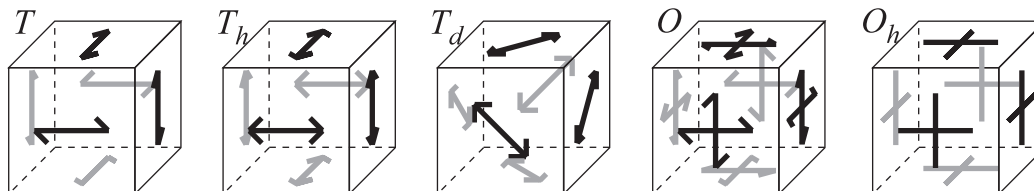

Fig. 3.2: Schematic representation of isotropic cubic resonators with the designation of the corresponding point groups of symmetry, following the Schöenflies notation.

planar rings presented in Sec. 2.2, the resonators shown in the inset of Fig. 3.3c,d were developed and extensively analyzed [20*, see Appendix 3] both theoretically and experimentally. For an experimental

characterization, the resonators were introduced in the center of a mono-mode rectangular waveguide (see Fig. 3.3a) and the transmittance was measured. The resonance of the cube then corresponds to a transmission dip, which should be independent from the rotation of the cube for isotropic designs. The results for the cubic resonator from [12] and two novel designs proposed in [20*, see Appendix 3] are shown in Fig. 3.3b,c,d. The isotropy of the novel resonators is evident from the invariance of the resonant dip. It is also apparent that the cube made of original SRRs [12] is anisotropic. The resonance is not invariant, and, in addition, there are resonances that were not present in stand-alone planar resonators (these resonance can even be of electric type [20*, see Appendix 3]). In order to explain these results, a detailed analytical model was developed in [20*, see Appendix 3] that predicts even the finest details observed in the experiment.
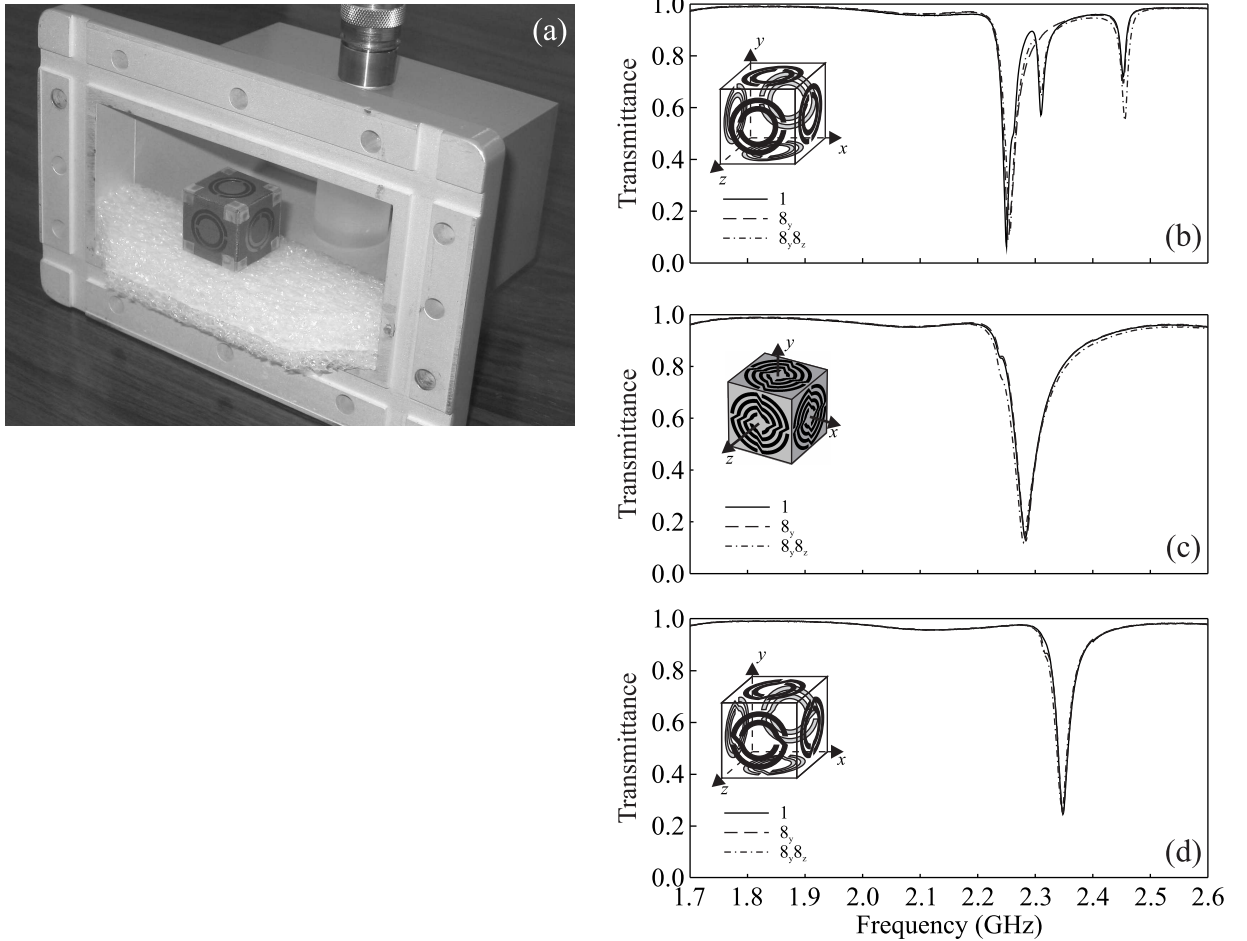

Fig. 3.3: (a) Waveguide-coaxial transition used for measurements with the inserted cubic resonator (b,c,d) Results of the transmittance measurement for three cubic resonators.

The symmetry pattern depicted in Fig. 3.2 is of general validity, and is not restricted to purely magnetic resonators. In fact, as will be shown in the following sections, it has also been successfully used for chiral resonators [25*, see Appendix 6], [26*, see Appendix 7] (see Fig. 3.4a) and for a combination of dielectric resonators with a so-called dielectric wire medium [24*, see Appendix 5] (see Fig. 3.4b).
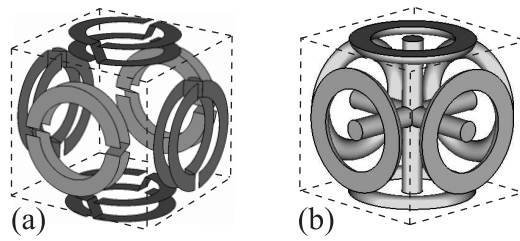
Fig. 3.4: (a) A cubic resonator made of chiral resonant rings (b) A cubic unit cell made of dielectric resonators and a mesh of dielectric wires.

Chapter 4

An Artificial Medium Made of Resonant Rings

4.1 An Unbounded Medium

The previous chapters were devoted to stand-alone resonators. While they are interesting systems on their own, the ultimate goal of metamaterials is to create a medium out of them. This opens whole new degrees of freedom, and metamaterial homogenization has in fact not yet been fully solved, see [31,32] and the references therein. The reason lies in the macroscopic dimensions of the constituting unit cells (e.g. the ring resonators), which can hardly have an electric size as small as that of building blocks of natural media (atoms and molecules), for which the classical homogenization schemes [15,33] were developed. The metamaterials should thus better be denoted as mesoscopic systems with considerably more complex homogenization [31,32]. Fortunately, some of the core ideas of solid state physics (e.g. Lorentz's sphere, Bloch's theorem) are of general validity, and can also be used for metamaterials.

The first serious attempt to homogenize resonant ring metematerials was made as early as in 2002 [34]. The homogenization presented there is purely static and is thus of limited applicability. However, it showed some important routes for future development. For example, it used an approximation of a real resonant ring by an ideal structure-less current loop with certain internal impedance. This approximation by an "extended" magnetic dipole was latter shown [20*, see Appendix 3] to be in fact very precise, and has been used in all the successors of [34]. Two notable examples are [35*, see Appendix 9] and [36*, see Appendix 10], which extended the static homogenization into a fully dynamic homogenization with spatial dispersion effects.
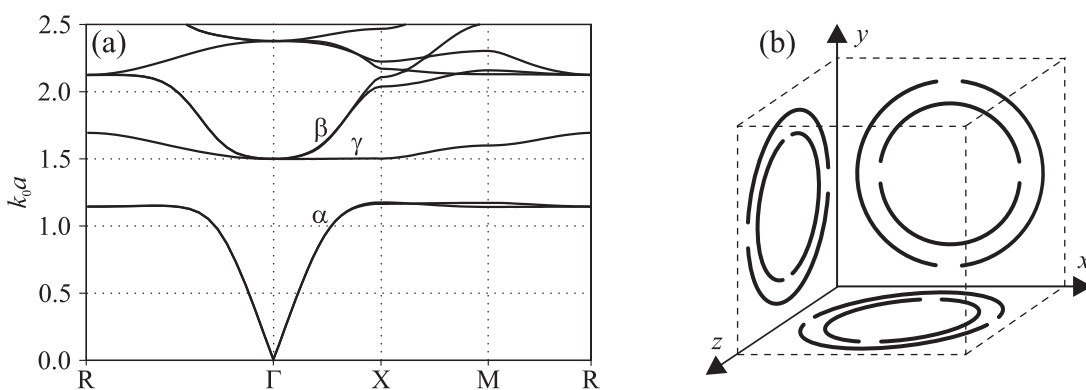

Fig. 4.1: (a) Full wave dispersion diagram of an isotropic material made of double gap SRRs (b) Sketch of the unit cell.

In order to give an idea of what to expect from a resonant ring material, a particular result is shown in Fig. 4.1a, see [35*, see Appendix 9] for more details. The figure shows a dispersion diagram of an isotropic material made of double gap SRRs (see Fig. 4.1b). Notable branches are denoted by α, β, γ. A sketch of an effective permeability corresponding to such a dispersion is shown in Fig. 4.2a. The branch α starts as a light-line along which the resonators exhibit only their static polarizabilites. This light-line starts to bend before the resonance of the rings, preceding a complete band-gap, the most important

region in which the permeability of the system becomes negative [35*, see Appendix 9]. Above the band-gap, two dispersion lines emerge. The β-line is in fact a continuation of α and it begins at the point of zero permeability. The γ-branch does not have any image in the local permeability from Fig. 4.2a, as it belongs to a so-called magneto-inductive wave [37, 38], which is a longitudinal wave that does not couple to the propagative planewave spectrum. This magneto-inductive wave can be considered analogous to plasmons existing in metals at plasma frequency. The isotropy suggested by the symmetry of the unit cell (see Chap. 3) can be checked by plotting the dispersion along different directions, as is done in Fig. 4.2b. The isotropy is clearly visible in the region of allowed homogenization, i.e. not close to the Brillouin boundary.
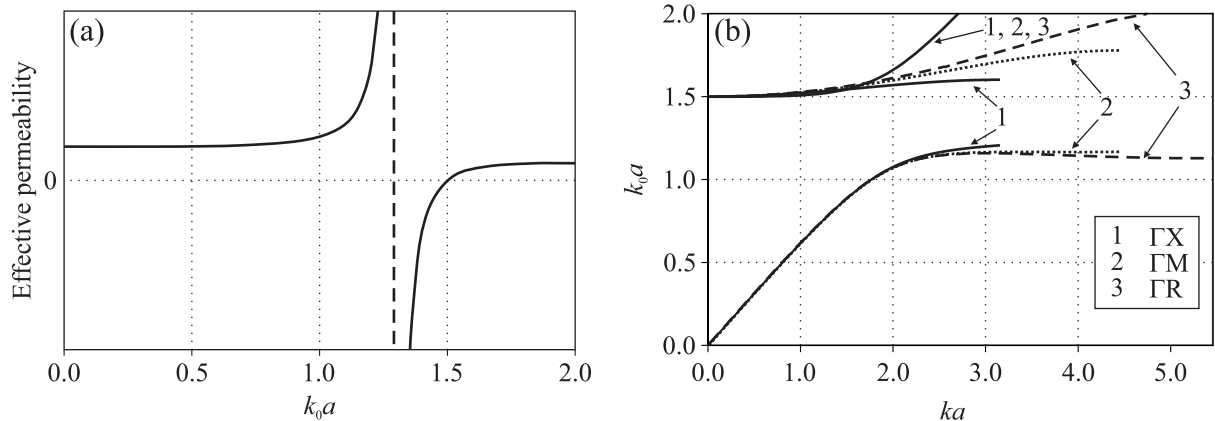

Fig. 4.2: (a) Sketch of the effective permeability corresponding to the dispersion diagram of Fig. 4.1a (b) Dispersion diagrams of the double gap SRR medium along three important directions.

Resonant ring materials can also be combined with other systems to make different functionalities. The most notable of these is the combination of rings with a system offering negative permittivity, in which case one obtains a medium with a negative index of refraction, the key component of a perfect lens [2]. Isotropic negative permittivity is commonly obtained by an orthogonal mesh of connected wires [39, 40]. A particular example of a combined ring-wire system is shown in the inset of Fig. 4.3a, which depicts a unit cell containing dielectric rings and a dielectric wire medium [24*, see Appendix 5]. The corresponding band diagram is shown in Fig. 4.3a, in which the backward-wave band is marked. At this point it is important to mention an interesting feature of dielectric ring resonators, which is the ability to coexist with the true homogeneous negative permittivity medium (ordinary resonant rings cannot do this due to the short-circuiting of their capacitance). A medium of this kind can for example be represented by conductors or semiconductors below their plasma frequency, see [24*, see Appendix 5] for a more extensive discussion. The last representative of a bulk resonant ring medium that will be mentioned here is the balanced chiral composite [25*, see Appendix 6], [26*, see Appendix 7]. Its dispersion diagram and constituting unit cell are depicted in Fig. 4.3b. This is another example of an important class of isotropic media supporting backward waves, in this case working for circularly polarized waves [25*, see Appendix 6], [26*, see Appendix 7].

4.2 Finite Material Samples

The previous section considered unbounded lattices of resonant rings, as is common in classical homogenization schemes. Ultimately, however, all practical metamaterials have to be of finite size. For conventional materials, it is well known [41] that at the boundaries of the material body a transition layer is formed, with properties different from those of the bulk. For large enough samples, this transition layer does not have a significant effect on the overall macroscopic properties. The case of metamaterials is more tricky, since they are constructed with a much smaller number of elements than any macroscopic piece of conventional matter. At the same time, metamaterial elements are usually densely arranged. Finally, metamaterials commonly exhibit negative material parameters which, when combined with sharp edges, may give rise to surface resonances [42].

Possible issues with finite metamaterial samples were addressed in [43*, see Appendix 11], where the surface geometry of a sample was treated. Two possible geometries of a cube made of resonant rings were studied, see Fig. 4.4, and were compared with the cube filled with a homogeneous medium corresponding
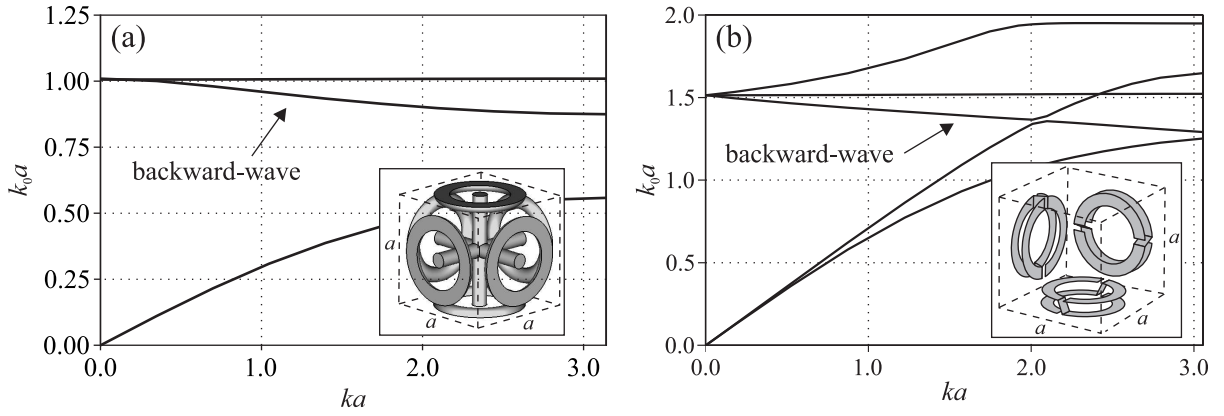
Fig. 4.3: (a) Dispersion diagram of a combined ring-wire system with a unit cell depicted [24*, see Appendix 5] (b) Dispersion diagram of an isotropic balanced chiral medium with a unit cell depicted [25*, see Appendix 6], [26*, see Appendix 7]. Both dispersion diagrams are valid for one of the Cartesian directions.
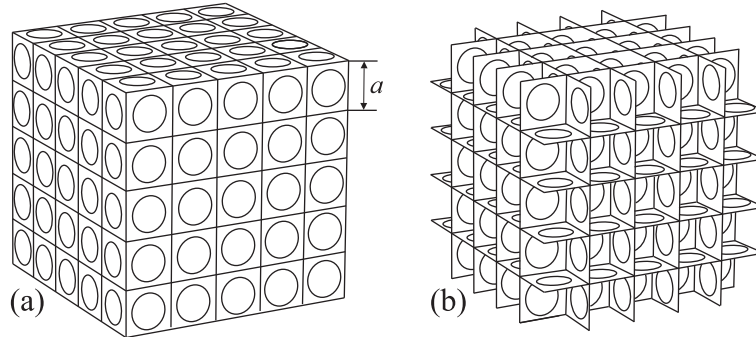
Fig. 4.4: Scheme of a finite cube of resonant ring material with two possible configurations: "flat" (a) and "ragged" (b).

to the homogenized resonant ring metamaterial [35*, see Appendix 9]. The results clearly showed a strong preference for a "ragged" design (Fig. 4.4b) the behavior of which was quite close to that of a homogeneous cube. On the other hand, the "flat" design (Fig. 4.4a) suffered from undesired surface resonances, making this surface treatment inadvisable.

Chapter 5

Systems Made of Resonant Rings

Apart form a purely theoretical contribution to physics, any topic should finally propose some application. The metamaterials are no exception and two selected systems will be presented in this chapter.

5.1 Quasi-Static Magnetic Lenses

A perfect lens [2] is an obvious first choice for an application. Unfortunately, the design of a perfect lens is extremely challenging, as it requires both the permittivity and the permeability to be negative and tuned to particular values. At the same time, the lens should operate within a reasonable bandwidth. These problems in combination virtually put a usable perfect lens into the realm of science fiction. However, there are imaging applications that are not so demanding. There are for example applications that need to perform imaging solely within the near-field of the imaged source, where its electric and magnetic fields are still reasonably decoupled. In such a case it was shown [2] that within the near-field, a magnetic source (TE waves along the optical axis) can be imaged using only negative permeability, while an electric source (TM waves along the optical axis) can be imaged using only negative permittivity. This is a considerable simplification and in fact resonant ring metamaterials presented in this thesis could serve as building blocks for magnetic imaging system of this kind.
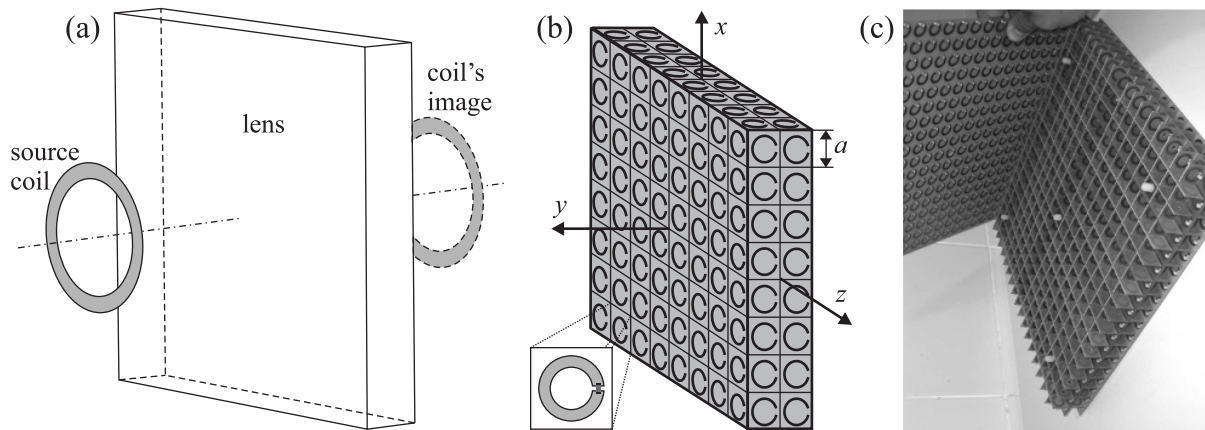

Fig. 5.1: (a) Sketch of a source coil imaging through the magnetic lens (b) Sketch of a realistic magnetic lens made of resonant rings (single split rings loaded by a lumped SMD capacitor are used) (c) Photograph of a fabricated lens.

Near-field magnetic imaging is a key point in image acquisition through nuclear magnetic resonance, which is a technique of eminent importance in medical diagnostics. In this method, the magnetic field generated in spin transitions is usually picked up by simple resonant coils, which are tuned to a specific frequency of the spin transition. In order to mitigate the thermal noise, the tuning is made very selective. This is in fact a very favorable property for resonant and thus narrow-band systems such as resonant ring metamaterials. The major issue in nuclear resonance imaging is the signal-to-noise ratio, the low value of which is mostly given by the very low signal coming from the imaged tissue. The reason for this is twofold. First, the source it-self (a cube of properly magnetized tissue) is very weak. Second, the radiating piece of tissue does not lie on the surface of the body, since it is also necessary to image the

internal part of the body. This means that the source of the radiation is located at some distance from the pick-up coil, and the coil generally losses its sensitivity with growing distance. There is practically no cure for the first these problems. The second problem can however be solved by using an imaging device that will virtually shift the pick-up coil to within the tissue - i.e. using magnetic lens [44], [45*, see Appendix 12].

An ideal lens for magnetic resonance imaging is a slab of isotropic negative permeability $\mu_r = -1$ that exactly copies the magnetic field in the source plane to the image plane. According to perfect lens theory [2] the source plane lies half of the thickness of the lens in front of the lens and the image plane lies half of the thickness of the lens behind the lens, see Fig. 5.1a. A lens of this type has been designed [45*, see Appendix 12] from a two unit cells thick slab of cubic ring resonators, see Fig. 5.1b,c. Although a two unit cell thick slab clearly cannot be considered as made of a homogenous medium, the real life performance of this lens has been very good [45*, see Appendix 12], see Fig. 5.2. In order to understand the lens in greater details, a proper homogenization scheme taking into account its small thickness has been developed [46*, see Appendix 13]. The results surprisingly showed that within the realm of quasi-static TE waves the lens can in fact be approximated by a slab of homogeneous medium, which explained its performance. Subsequently, the lens has been tested in various scenarios [47*, see Appendix 14], both experimentally and theoretically, by means of the detailed discrete model [48*, see Appendix 15]. Usage of the lens in connection with the parallel imaging technique [47*, see Appendix 14] also opened the question of the transversal resolution of the lens. In accordance with the theory, a detailed study [49*, see Appendix 16] did indeed show that the lens resolution can be deeply subwavelength, reaching a size around six unit cells, i.e. around $\lambda/50$, with lambda being the operation wavelength (compare with diffraction limit $\lambda/2$).
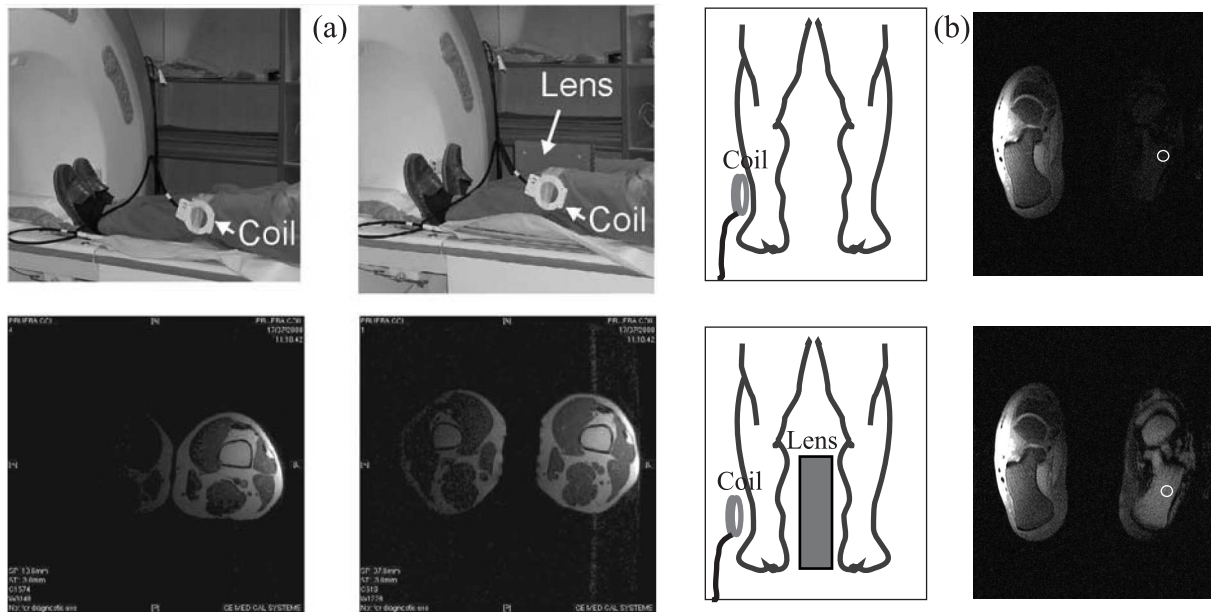

Fig. 5.2: (a) Imaging of knees - a comparison of the same scenario with the lens (right) and without the lens (left), as depicted in [45*, see Appendix 12] (b) Imaging of ankles - a comparison of the same scenario with the lens (bottom) and without the lens (top), as depicted in [47*, see Appendix 14].

5.2 Isotropic Frequency Selective Surface

For propagative waves, a slab of a negative permeability behaves as a reflector. This, in connection with isotropic cubic resonators, see Chap. 3, and their natural frequency selectivity, evoked the idea of creating an angle-independent frequency selective surface [50*, see Appendix 17]. An implementation of a surface of this kind is depicted in Fig. 5.3a. An experimental characterization of this surface did indeed confirm the presumed angle and polarization independence, see Fig. 5.3b, which results from the ability of cubic resonators to excite a magnetic moment that exactly follows the incident field. Outside the resonance band such a surface would be almost transparent, which makes it a possible candidate for multi-reflector antennas. In connection with this kind of application it can be expected that a curved surface would

work as well as the flat surface, since the major response comes from the cubic resonators themselves.
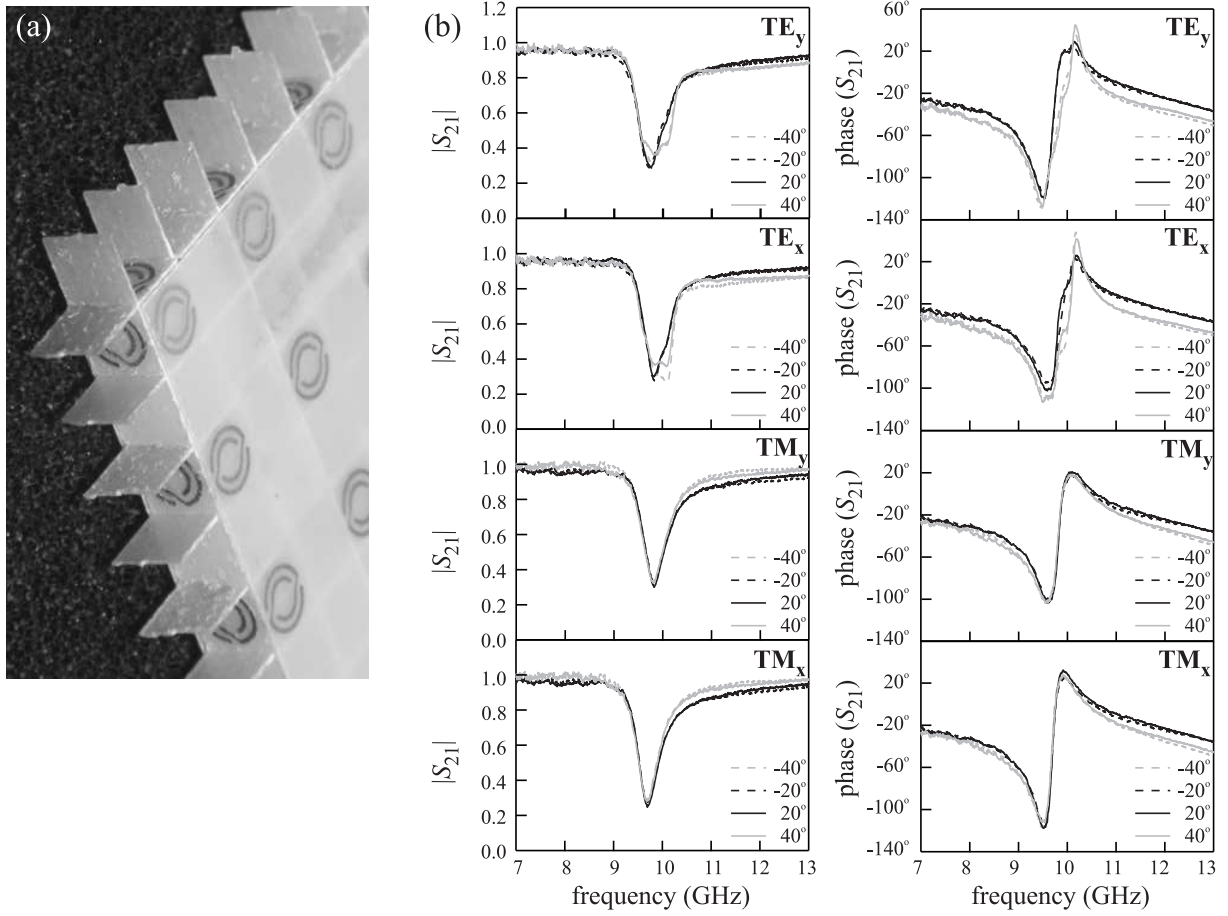

Fig. 5.3: (a) Photograph of a planar frequency selective surface made of isotropic ring resonators (b) Measured transmission coefficient through the surface for several incidence angles and several polarizations.

Chapter 6

Conclusions

The emergence of metamaterials stimulated a wave of interest in classical electromagnetism, even though at that time this area of physics had been considered to be almost exhausted. The major reason was that, in the past, the importance of material properties was often underestimated, or materials were even taken as parasitic components needed only to support metallic structures. Metamaterials have however shown that constitutive parameters are extremely valuable and extremely flexible degree of freedom which can bring whole new functionalities in even the simplest geometries, e.g. a simple slab behaving as a perfect lens [2] or a simple spherical layer behaving as perfect cloak [3–5]. Furthermore, the development of metamaterials brought schemes for the actual design of complex materials, whose properties could, within some fundamental constraints, be designed almost at our will. Finally, metamaterials has shown that classical homogenization concepts developed for natural media are not of general validity, and are not necessarily usable for mesoscopic or strongly dispersive systems.

One of the major branches of metamaterials deals with materials made of resonant rings which aim to manipulate the magnetic properties. This thesis has recapitulated the main lines of research carried out in this area. The presentation started with simple planar resonators, continuing through various modifications of these resonators towards the three-dimensional isotropic systems, including a homogenizable magnetic medium, and ending with selected systems made of this kind of material. As presented here, this topic might seem to be fully solved. However, this is only partly true and there are still some core problems that are waiting to be solved. The most eminent issues for future work are: materials made of randomly-oriented rings (amorphous materials) and materials made of active rings that mitigate the dispersion.

Bibliography

[1] R. Marques, L. Jelinek, M. J. Freire, J. D. Baena, and M. Lapine. Bulk metamaterials made of resonant rings. *P. IEEE*, 99:1660–1668, 2011.

[2] J. B. Pendry. Negative refraction makes a perfect lens. *Phys. Rev. Lett.*, 85:3966–3969, 2000.

[3] U. Leonhardt. Optical conformal mapping. *Science*, 312:1777–1780, 2006.

[4] J. B. Pendry, D. Schurig, and D. R. Smith. Controlling electromagnetic fields. *Science*, 312:1780–1782, 2006.

[5] U. Leonhardt and T. Philbin. General relativity in electrical engineering. *New J. Phys.*, 8:247, 2006.

[6] J. Van Bladel. *Relativity and Engineering*. Springer-Verlag, 1984.

[7] A. E. Dubinov and L. A. Mytareva. Invisible cloaking of material bodies using the wave flow method. *Phys-Usp+*, 53:455–479, 2010.

[8] C. Caloz and T. Itoh. *Electromagnetic Metamaterials: Transmission Line Theory and Microwave Applications*. Wiley-IEEE Press, 2005.

[9] R. Marques, F. Martin, and M. Sorolla. *Metamaterials with Negative Parameters: Theory and Microwave Applications*. John Wiley & Sons, Inc., 2007.

[10] L. Solymar and E. Shamonina. *Waves in Metamaterials*. Oxford University Press, 2009.

[11] S. A. Schelkunoff and H. T. Friis. *Antennas: Theory and Practice*. John Wiley & Sons, Inc., 1952.

[12] J. B. Pendry, A. J. Holden, D. J. Robbins, and W. J. Stewart. Magnetism from conductors and enhanced nonlinear phenomena. *IEEE T Microw. Theory*, 47:2075–2084, 1999.

[13] W. Weber. Ueber den zusammenhang der lehre vom diamagnetismus mit der lehre von dem magnetismus und der elektricität. *Ann. Phys.*, 87:145–189, 1852.

[14] W. N. Hardy and L. A. Whitehead. Split-ring resonator for use in magnetic resonance from 200–2000 mhz. *Rev. Sci. Instrum.*, 52:213–216, 1981.

[15] J. D. Jackson. *Classical Electrodynamics*. John Wiley & Sons, Inc., 3rd edition, 1998.

[16] R. F. Harrington. *Time-Harmonic Electromagnetic Fields*. New York: John Wiley and Sons, Inc., 2001.

[17] R. Marques, F. Medina, and R. Rafii-El-Idrissi. Role of bianisotropy in negative permeability and left-handed metamaterials. *Phys. Rev. B*, 65:144440, 2002.

[18] J. D. Baena, J. Bonache, F. Martin, R. Marques, F. Falcone, T. Lopetegi, M. A. G. Laso, J. Garcia-Garcia, I. Gil, M. F. Portillo, and M. Sorolla. Equivalent-circuit models for split-ring resonatores and complementary split-ring resonators coupled to planar transmission lines. *IEEE T Microw. Theory*, 53:1451–1461, 2005.

[19] J. D. Baena, L. Jelinek, R. Marques, and J. Zehentner. Electrically small isotropic three-dimensional magnetic resonators for metamaterial design. *Appl. Phys. Lett.*, 88:134108, 2006.

[20] J. D. Baena, L. Jelinek, and R. Marques. Towards a systematic design of isotropic bulk magnetic metamaterials using the cubic point groups of symmetry. *Phys. Rev. B*, 76:245115, 2007.

[21] J. Zhou, T. Koschny, M. Kafesaki, E. N. Economou, J. B. Pendry, and C. M. Soukoulis. Saturation of the magnetic response of split ring resonators at optical frequencies. *Phys. Rev. Lett.*, 95:223902, 2005.

[22] V. Delgado, O. Sydoruk, E. Tatartschuk, R. Marques, M. J. Freire, and L. Jelinek. Analytical circuit model for split ring resonators in the far infrared and optical frequency range. *Metamaterials*, 3:57–62, 2009.

[23] L. D. Landau, E. M. Lifshitz, and L. P. Pitaevskii. *Electrodynamics of Continuous Media*. Pergamon Press, 2nd edition, 1984.

[24] L. Jelinek and R. Marques. Artificial magnetism and left-handed media from dielectric rings and rods. *J. Phys.: Condens. Matter*, 22:025902, 2010.

[25] L. Jelinek, R. Marques, F. Mesa, and J. D. Baena. Periodic arrangements of chiral scatterers providing negative refractive index bi-isotropic media. *Phys. Rev. B*, 77:205110, 2008.

[26] R. Marques, L. Jelinek, and F. Mesa. Negative refraction from balanced quasi-planar chiral inclusions. *Micr. and Opt. Techn. Lett.*, 49:2606–2609, 2007.

[27] S. A. Tretyakov, A. Sihvola, and L. Jylh. Backward-wave regime and negative refraction in chiral composites. *Photonics and Nanostruct. Fund. and Appl.*, 3:107–115, 2005.

[28] J. B. Pendry. A chiral route to negative refraction. *Science*, 306:1353–1355, 2004.

[29] L. Jelinek and J. Machac. An FET-based unit cell for an active magnetic metamaterial. *Anten. Wireless Propag. Lett.*, 10:927–930, 2011.

[30] P. Gay-Balmaz and O. J. F. Martin. Efficient isotropic magnetic resonators. *Appl. Phys. Lett.*, 81:939–941, 2002.

[31] C. R. Simovski. Material parameters of metamaterials (a review). *Opt. and Spectrosc+*, 107:726–753, 2011.

[32] C. R. Simovski. On electromagnetic characterization and homogenization of nanostructured metamaterials. *J. Opt.*, 12:013001, 2011.

[33] N. W. Ashcroft and N. D. Mermin. *Solid State Physics*. Cengage Learning, 1976.

[34] M. Gorkunov, M. Lapine, E. Shamonina, and K. H. Ringhofer. Effective magnetic properties of a composite material with circular conductive elements. *Eur. Phys. J. B*, 28:263–269, 2002.

[35] J. D. Baena, L. Jelinek, R. Marques, and M. Silveirinha. Unifed homogenization theory for magnetoinductive and electromagnetic waves in split ring metamaterials. *Phys. Rev. A*, 78:013842, 2008.

[36] M. G. Silveirinha, J. D. Baena, L. Jelinek, and R. Marques. Nonlocal homogenization of an array of cubic particles made of resonant rings. *Metamaterials*, 3:115–128, 2009.

[37] E. Shamonina, V. A. Kalinin, K. H. Ringhofer, and L. Solymar. Magnetoinductive waves in one, two, and three dimensions. *J. Appl. Phys.*, 92:6252–6261, 2002.

[38] R. R. A. Syms, E. Shamonina, V. Kalinin, and L. Solymar. A theory of metamaterials based on periodically loaded transmission lines: interaction between magnetoinductive and electromagnetic waves. *J. App. Phys.*, 97:064909, 2005.

[39] J. B. Pendry, A. J. Holden, W. J. Stewart, and I. Youngs. Extremely low frequency plasmons in metallic mesostructures. *Phys. Rev. Lett.*, 76:4773–4776, 1996.

[40] M. Silveirinha and C. A. Fernandes. Homogenization of 3-d-connected and nonconnected wire metamaterials. *IEEE T Microw. Theory*, 53:1418–1430, 2005.

[41] A. P. Vinogradov, D. P. Makhnovskii, and K. N. Rozanov. Effective boundary layer in composite materials. *J. Communication Technol. Electron.*, 44:317322, 1999.

[42] H. Wallen, H. Kettunen, and A. Sihvola. Surface modes of negative-parameter interfaces and the importance of rounding sharp corners. *Metamaterials*, 2:113–121, 2008.

[43] M. Lapine, L. Jelinek, and R. Marques. Surface mesoscopic effects in finite metamaterials. *Opt. Exp.*, 20:18297, 2012.

[44] M. C. K. Wiltshire, J. B. Pendry, I. R. Young, D. J. Larkman, D. J. Gilderdale, and J. V. Hajnal. Microstructured magnetic materials for rf flux guides in magnetic resonance imaging. *Science*, 291:849–851, 2001.

[45] M. J. Freire, R. Marques, and L. Jelinek. Experimental demonstration of a $\mu = -1$ metamaterial lens for magnetic resonance imaging. *Appl. Phys. Lett.*, 93:231108, 2008.

[46] L. Jelinek, R. Marques, and M. J. Freire. Accurate modeling of split ring metamaterial lenses for magnetic resonance imaging applications. *J. Appl. Phys.*, 105:024907, 2009.

[47] M. J. Freire, L. Jelinek, R. Marques, and M. Lapine. On the applications of $\mu = -1$ metamaterial lenses for magnetic resonance imaging. *Journal of Magnetic Resonance*, 203:81–90, 2010.

[48] M. Lapine, L. Jelinek, R. Marques, and M. J. Freire. Exact modelling method for discrete finite metamaterial lens. *IET Microw. Antenna P.*, 4:1132–1139, 2010.

[49] M. Lapine, L. Jelinek, M. J. Freire, and R. Marques. Realistic metamaterial lenses: Limitations imposed by discrete structure. *Phys. Rev. B*, 82:165124, 2010.

[50] J. D. Baena, L. Jelinek, R. Marques, J. J. Mock, J. Gollub, and D. R. Smith. Isotropic frequency selective surfaces made of cubic resonators. *Appl. Phys. Lett.*, 91:191105, 2007.

Appendixes

The following appendices contain the full texts of the works belonging to the habilitant which are cited in this thesis, i.e. of the works highlighted by an asterisk symbol.

Appendix 1

This appendix contains a full text of Ref. [1]

Bulk Metamaterials Made of Resonant Rings

The realization of 3-D magnetic metamaterials at microwave frequencies is discussed in this paper and an exciting application of such materials is described.

By Ricardo Marqués, Lukas Jelinek, Manuel J. Freire,
Juan Domingo Baena, and Mikhail Lapine

ABSTRACT | In this brief review, we present the fundamentals of bulk resonant ring metamaterial (RRM) theory. Metamaterials made of resonant rings are discussed, and some basic design rules are provided. Homogenization (including spatial dispersion) of 3-D resonant ring latices is reviewed, with emphasis in isotropic designs. Edge effects in finite size metamaterial samples are discussed. Finally, possible applications and future trends are briefly reviewed.

KEYWORDS | Artificial media; homogenization theory; magnetic resonance imaging; magnetic resonators; magneto-inductive waves; metamaterials; spatial dispersion

I. INTRODUCTION

Diamagnetic properties of closed inductive loops were well known in the past (see, for instance, [1]). It was also known that this effect can be enhanced by adding a chip capacitor [2] to the ring. However, it was not until recent years that these effects were systematically studied in order to develop artificial media (or metamaterials) with negative magnetic permeability [3], which may be eventually combined with conducting plates or wires [4] in order to provide a medium with simultaneously negative magnetic permeability and permittivity [5], i.e., the negative refractive index (NRI) medium predicted many years ago [6], [7]. After these seminal works, metamaterial theory became a "hot" scientific topic, with thousands of published scientific papers (for RRM specifically see, for instance, [8], [9], and references therein). Although other alternatives besides resonant rings have been proposed for negative μ metamaterial design, resonant ring technology can be still considered as the "standard" approach to this goal, at least up to optical frequencies, where the combined effects of the kinetic inductance of electrons [10] and high frequency dissipation [11] introduce severe limitations to this approach. In this paper, we will shortly review the fundamentals of resonant ring metamaterial (RRM) theory, with emphasis in isotropic 3-D effective media design. The paper ends with a short discussion on possible applications and future trends for bulk metamaterial technologies.

II. RESONANT RINGS FOR METAMATERIAL DESIGN

A. Resonant Ring Basic Concepts

A closed conducting ring of inductance L and resistance R provides a magnetic moment $\mathbf{m} = -(j\omega\pi^2 r^4/Z)\mathbf{B}_\perp$, where r is the ring radius, $\mathbf{B}_\perp$ is the external magnetic field component perpendicular to the ring, and $Z = j\omega L + R$ is the ring impedance. Since $L \sim \mu_0 r$, this magnetic moment, though opposite to the magnetic field, is not sufficient for providing a negative effective permeability [8]. This effect can be enhanced if the ring impedance $Z = j\omega L + R$ is

R. Marqués, **M. J. Freire**, and **M. Lapine** are with the Departamento de Electronica y Electromagnetismo, Universidad de Sevilla, Sevilla 41001, Spain (e-mail: marques@us.es; freire@us.es; mikhail.lapine@gmail.com).
L. Jelinek is with the Department of Electromagnetic Field, Czech Technical University in Prague, 16627 Prague, Czech Republic (e-mail: l_jelinek@us.es).
J. D. Baena is with the Departamento de Física, Universidad Nacional de Colombia, Bogotá, Colombia (e-mail: jdbaenad@unal.edu.co).

modified by the presence of a series connected capacitance C [2], so that $Z = j\omega L + R + 1/(j\omega C)$ and

$$\mathbf{m} = \alpha(\omega)\mathbf{B}_\perp = \frac{\pi^2 r^4}{L} \frac{\omega^2}{\omega_0^2 - \omega^2 + j\omega R/L}\mathbf{B}_\perp \qquad (1)$$

where $\omega_0 = \sqrt{1/(LC)}$ is the frequency of resonance. Lumped capacitors are available at radio and microwave frequencies. However, attaching a lumped capacitor at microwave frequencies may not be a very practical approach because of some unavoidable parasitic inductance, which cannot be neglected. For this reason, lumped capacitors are rarely used except at radio frequencies. At higher frequencies, it may be advantageous to use conventional printed circuit techniques and substitute the lumped capacitor by a distributed capacitance. This leads to the split ring resonator (SRR), already known and used for some specific applications [12], but first proposed as metamaterial element in [3].

In order to simplify the analysis, avoiding magneto-electric couplings (see below), the geometry proposed in [12] is used in the following. This structure (see Fig. 1) is a broadside-coupled SRR (BC-SRR). As has been shown in [13], near the resonance, the total current (i.e., the sum of the current flowing on both rings) is almost uniform, forming a closed current loop. This current flows from the upper to the lower ring and *vice versa* through the gap between them, as an electric displacement current. Therefore, the total capacitance of the resonator is the series connection of the capacitances through both resonator halves. The resonator inductance can be approximated by the inductance of a single ring (assumed closed) and the magnetic polarizability is still given by (1).

A main advantage of the BC-SRR over the design proposed in [3] is that broadside coupling provides a much higher capacitance than edge coupling, thus allowing for a much smaller electrical size at resonance [13]. The price to pay for this advantage is a more complicated fabrication process, which includes two levels of metalization. Another important advantage (for most applications) of the BC-SRR is the aforementioned absence of magneto-electric coupling. Magneto-electric coupling appears in many SRR designs due to the simultaneous excitation of an electric and a magnetic dipole at resonance. According to reciprocity, the excitation of an electric dipolar moment by an external magnetic field implies the excitation of a magnetic dipolar moment by an external electric field. Therefore, magneto-electric coupling makes the metamaterial bi-anisotropic [14]. Magneto-electric coupling is not present if the SRR is invariant by spatial inversion, as it happens in Fig. 1. In addition to the reported resonant magnetic (or magneto-electric) polarizability, SRRs also show a nonresonant electric polarizability, which can be approximated as the polarizability of a metallic disk of the same radius [15]. Besides the aforementioned edge-coupled and broadside-coupled SRRs, many other SRR designs have been proposed, aimed to specific applications. The interested reader is referred to [8] for a description of some of these proposals. Finally, it may be worth to mention that high permittivity dielectric rings also show a resonant magnetic polarizability similar to (1) [16], due the combined effects of the electric field confinement inside the ring and the internal capacitance, both associated to the high value of the dielectric constant.

Closely related to resonant rings, there are other resonant structures useful for metamaterial design, which deserve some comments. One of them is the "swiss roll," also proposed in [3], which provides a very strong magnetic response at very low frequencies, thus being useful for applications in the megahertz range (see Section IV). Another interesting structure is the complementary SRR (CSRR), proposed in [17]. This resonator is the complementary screen of any planar SRR, whose properties can be related to those of the SRR using Babinet theorem: magnetic and electric polarizabilities are interchanged. However, it must be emphasized that the polarizabilities of the CSRR are only "effective," having opposite sign at both sides of the resonator [17]. This fact makes this element useless for 3-D metamaterial design (although certainly very useful for 2-D metamaterial design).
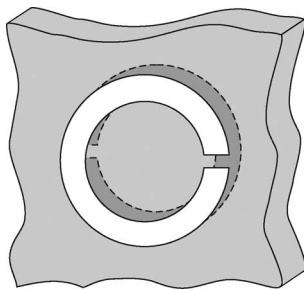
B. SRRs at Optical Frequencies

Upon the success of SRRs at radio and microwave frequencies, such metamaterial elements were studied for operation at terahertz [18] and infrared frequencies [19]. At few terahertz, metals still behave as good conductors. However, at frequencies in the infrared and the visible range, metals are better described as solid plasmas with a complex permittivity approximated by

$$\varepsilon = \varepsilon_0 \left[\varepsilon_i - \frac{\omega_p^2}{\omega(\omega - jf_c)}\right] \qquad (2)$$

where ε_i is the permittivity of the ionic background, ω_p is the angular plasma frequency, and f_c is the frequency of collision of electrons. For metamaterial design, the electrical size of the SRR should be substantially smaller than the wavelength, and the SRR details (for instance, the wire section) even smaller. Therefore, the characteristic lengths of the SRR become of the same order as the mean free path of electrons—which for good conductors is of several tenths of nanometers—and collisions with the SRR boundaries become important [20]. This effect dramatically increases f_c and, therefore, losses, as it has been analyzed in [11] and [21]. Other effects, such as interband electron transitions and surface roughness, also contribute to an increase of metal losses at optical frequencies [11].

Even more important than losses are the effects of the kinetic inductance of electrons L_k [10]. This effect can be also understood as the effect of the negative permittivity of the metal [8], which provides a negative internal capacitance associated with the displacement current inside the metallic ring. This negative internal capacitance is, in fact, equivalent to a positive extra inductance

$$L_k = -\frac{1}{\omega^2 C_{\text{int}}} = -\frac{1}{\omega^2} \frac{2\pi r}{\Re(\varepsilon)S} \approx \frac{2\pi r}{\varepsilon_0 S \omega_p^2} \quad (3)$$

where r is the ring radius and S is the wire section. This additional kinetic inductance must be added to the magnetic inductance L in the expressions for the polarizability of the SRR (1). When the SRR is scaled down in order to achieve resonance at optical frequencies, the kinetic inductance (3) scales as $L_k \sim 1/r$, whereas the magnetic inductance scales as $L \sim r$. Therefore, the kinetic inductance becomes dominant and the frequency of resonance saturates to the constant value $\omega_s = \sqrt{1/L_k C}$ (the capacitance C scales down as $C \sim r$). In addition, the amplitude of the magnetic susceptibility scales as $\chi_m \sim N\alpha$, where $N \sim 1/r^3$ and α is given by (1). Therefore, $\chi_m \sim r/L_k \sim r^2$. That is, the amplitude of the susceptibility decreases dramatically when the SRR is scaled down. Since the magnetic inductance varies as $L \approx \mu_0 r$ with the ring radius r, from (3) follows that the kinetic inductance becomes dominant when the section of the SRR wire becomes of the same order as the plasma wavelength of the metal [8]. For good conductors this effect appears when the wire section approaches to several tens of nanometers. Therefore, both effects analyzed in this section appear simultaneously, making the SRRs useless below these dimensions.

III. THREE-DIMENSIONAL RESONANT RING METAMATERIALS

There is a very high variety of phenomena that may appear in 3-D arrays of resonant rings, even if the analysis is

restricted to homogenizable mixtures. In order not to make the analysis endless, we will restrict ourselves to the important case of isotropic RRM, which has been addressed in [22], [23], and [24] among others. Most of the concepts developed for isotropic designs can be extended to more complex structures, and the reader interested in such composites is referred to the available bibliography [8], [9].

A. Lorentz Homogenization Theory for Cubic Lattices of Resonant Rings

Let us consider an isotropic cubic lattice of electrically small resonant rings, as is sketched in Fig. 2(a). We will consider rings with only magnetic polarizability (1), so that magneto-electric coupling is not considered. We will also neglect the details of the ring design, assuming that the rings can be described by a closed current loop with some internal inductance, capacitance, and resistance (the conditions for the validity of such assumptions have been discussed in [24]). Lorentz homogenization theory of cubic crystals is based on the well-known relation [25] $\mathbf{H}_l = \mathbf{H} + \mathbf{M}/3$ between the local magnetic field $\mathbf{H}_l$, the macroscopic magnetic field $\mathbf{H}$, and the macroscopic magnetization $\mathbf{M}$. This relation is valid for cubic lattices of point magnetic dipoles. However, in cubic lattices of resonant rings of radius r comparable to the lattice constant a, the interaction between the closest rings cannot be approximated as the interaction between two magnetic dipoles. In this case, the local field component normal to the ring $\mathbf{H}_{l,\perp}$ is better approximated by

$$\mathbf{H}_{l,\perp} = \mathbf{H}_\perp + \left\{ \frac{a^3}{\mu_0(\pi r^2)^2}(4M_c + 2M_a) + \frac{1}{3} \right\} \mathbf{M}_\perp \quad (4)$$

where M_c and M_a are the mutual inductances between parallel coplanar and co-axial nearest rings, respectively (couplings between rings placed over perpendicular planes cancel each other). Taking into account the exact mutual
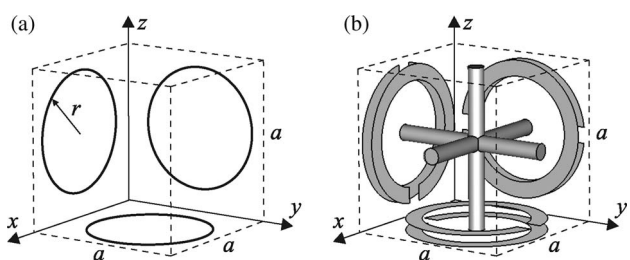

Fig. 2. *(a) The unit cell of an ideal cubic lattice of resonant rings of self-inductance L, self-capacitance C, and resistance R. (b) Unit cell of a NRI medium made by a combination of BC-SRRs and wires.*

inductance between more distant neighbors [26] does not significantly change the result for a cubic lattice. From (4), the magnetic susceptibility of the lattice can be readily found as a function of the ring polarizability α. For α given by (1), this expression is

$$\chi(\omega) = \frac{\omega^2 \mu_0 \alpha_0/(a^3)}{\omega_0^2 - \omega^2[1 + 2M_a/L + 4M_c/L + \mu_0\alpha_0/(3a^3)] + j\omega R/L} \quad (5)$$

where $\alpha_0 = \pi^2 r^4/L$ is the magnitude of the polarizability of an ideal lossless $(R = 0)$ and nonresonant $(\omega_0 = 0)$ ring.

B. Magneto-Inductive Waves in Resonant Ring Metamaterials

In addition to electromagnetic TEM waves with phase constant $k = \omega\sqrt{\mu\epsilon}$, lattices of resonant rings also support magneto-inductive waves [27]. These waves appear at frequencies near the ring resonance and come from the inductive coupling between rings. For a linear chain of rings, with periodicity a, the general dispersion equation for these waves is [27]

$$\frac{\omega_0^2}{\omega^2} = 1 + 2\sum_{n=1}^{\infty} \frac{M_n}{L}\cos(nka) - j\frac{R}{\omega L} \quad (6)$$

where M_n is the mutual inductance between two rings separated by a distance na. In the nearest neighbors approximation, (6) reduces to

$$\frac{\omega_0^2}{\omega^2} = 1 + \frac{M_1}{L}\cos(ka) - j\frac{R}{\omega L}. \quad (7)$$

For an accurate quantitative analysis, (6) must be used, and the summation taken up to the appropriate convergence. However, in order to capture the most salient features of these kind of waves, (7) is sufficient [27]. Therefore, we will use this approximation in our analysis. For a linear chain of co-axial rings, $M_1 \equiv M_a > 0$, and the dispersion relation (7) shows that the magneto-inductive wave is a forward wave. However, for a linear chain of coplanar rings, $M_1 \equiv M_c < 0$, and (7) shows that the magneto-inductive wave is a backward wave. Equation (7) also shows that magneto-inductive waves have a narrow bandwidth $\Delta\omega/\omega_0 \sim M_1/L$ around the frequency of resonance ω_0.

It is also possible to induce magneto-inductive waves in unbounded lattices of resonant rings, the general formula

for these waves being a straightforward generalization of (6) [27]. It is however interesting to explicitly write these expressions for the cubic lattice shown in Fig. 2(a). If we restrict our analysis to waves propagating along a main axis, namely the z-axis of Fig. 2(a), we can distinguish two branches, corresponding to "longitudinal" waves with axial coupling between the rings, and to "transverse" waves with coplanar coupling between rings. For longitudinal waves, we have

$$\frac{\omega_0^2}{\omega^2} = 1 + 2\frac{M_a}{L}\cos(ka) + 4\frac{M_c}{L} - j\frac{R}{\omega L} \quad (8)$$

and for transverse waves

$$\frac{\omega_0^2}{\omega^2} = 1 + 2\frac{M_c}{L}\cos(ka) + 2\frac{M_c}{L} + 2\frac{M_a}{L} - j\frac{R}{\omega L}. \quad (9)$$

From the signs of M_a and M_c it comes out that longitudinal waves are forward and transverse waves are backward.

C. Connection Between Magneto-Inductive Waves and Electromagnetic Waves. Spatial Dispersion

Magneto-inductive and TEM electromagnetic waves are both present in 3-D lattices of resonant rings. Moreover, the interesting region of negative permeability is very close to the frequency of resonance of the rings, where magneto-inductive waves also appear. Therefore, it is crucial to elucidate which are the connections between magneto-inductive and TEM electromagnetic waves. This connection was first investigated in [28] using a transmission line model. Subsequently, it was investigated for a cubic lattice of rings in [29]. In this section, we will mainly follow the analysis reported in [29], which has been adapted to our present purpose. Other approaches to spatial dispersion in metamaterial structures, which provide similar results in many cases, can be found in the literature [30], [31].

Let us consider, for simplicity, a z-polarized magnetic wave propagating along one of the main axis of the structure shown in Fig. 2(a), with propagation constant $\mathbf{k}$, macroscopic magnetic field $H_z = H_{0,z}\exp(-j\mathbf{k}\cdot\mathbf{r})$, and magnetization $M_z = M_{0,z}\exp(-j\mathbf{k}\cdot\mathbf{r})$, associated to a distribution of currents on the rings oriented perpendicular to the z-axis $I_{n_x,n_y,n_z} = I_0\exp(-ja(k_x n_x + k_y n_y + k_z n_z))$. In the nearest neighbors approximation, and for propagation along one of the main axes, couplings between rings located on orthogonal planes cancel. Thus, a straightforward generalization of (4) leads to the

following equation for the current I_0 on the ring at $n_x = n_y = n_z = 0$:

$$
\left(\frac{\omega_0^2}{\omega^2} - 1 + j\frac{R}{\omega L}\right) I_0^z
$$

$$
= \frac{\Phi_{\text{ext}}}{L}
$$

$$
= \frac{\pi r^2 \mu_0}{L} \left\{ H_{0,z} + \frac{a^3}{\mu_0(\pi r^2)^2} \right.
$$

$$
\times \left[2M_c \cos(k_x x) + 2M_c \cos(k_y y) \right.
$$

$$
\left. + 2M_a \cos(k_z z)]M_{0,z} + \frac{1}{3}M_{0,z} \right\}. \quad (10)
$$

The macroscopic wave equation for the magnetization is

$$
(\omega^2 \mu_0 \varepsilon - k^2)\mathbf{H}_0 + (\omega^2 \mu_0 \varepsilon - \mathbf{k}\mathbf{k}\cdot)\mathbf{M}_0 = 0 \quad (11)
$$

where ε is the macroscopic effective dielectric constant of the lattice. By combining (10), (11), and $M_{0,z} = \pi r^2 I_0/a^3$, the wave equation for the currents on the rings is obtained. For waves propagating along the z-axis, we obtain "longitudinal" waves with the dispersion equation

$$
\frac{\omega_0^2}{\omega^2} = 1 + 2\frac{M_a}{L}\cos(k_z a) + 4\frac{M_c}{L} - \frac{2}{3}\frac{\mu_0\alpha_0}{a^3} - j\frac{R}{\omega L} \quad (12)
$$

and for waves propagating along the x-axis (or y-axis), we obtain "transverse" waves with the dispersion equation, shown at the bottom of the page, where $k_m = \omega\sqrt{\varepsilon\mu_0}$. Of course similar results can be obtained for the currents on rings oriented perpendicular to the x- and y-axis of Fig. 2(a). Therefore, both branches of longitudinal and transverse waves coexist along any main axis of the structure.

Equation (12) corresponds to the longitudinal magneto-inductive wave (8) slightly modified by the presence of the volume magnetization. In the long wavelength limit, where $\cos(k_x a) \approx 1$, substitution of (12) into (5) leads to $\chi(\omega) = -1$, i.e., $\mu(\omega) = 0$. Therefore, longitudinal magneto-inductive waves in cubic lattices of resonant rings are the short wavelength continuation of the longitudinal magneto-plasmons that appear in continuous media when $\mu = 0$.

Regarding the long wavelength limit of (13), it corresponds to the transverse electromagnetic waves propagating in a medium of $\mu = \mu_0(1 + \chi_m(\omega))$, with $\chi_m(\omega)$ given by (5). In the short wavelength limit, when $k_x^2 \gg k_m^2$, (13) reduces to

$$
\frac{\omega_0^2}{\omega^2} = 1 + \frac{2M_c}{L}\cos(k_x a) + \frac{2(M_a + M_c)}{L} + \frac{\mu_0\alpha_0}{3a^3} - j\frac{R}{\omega L}. \quad (14)
$$

Equation (14) corresponds to the transverse magneto-inductive waves (9) slightly modified by the effect of the volume magnetization. Therefore, transverse magneto-inductive waves in cubic lattices of resonant rings are the short wavelength continuation of transverse electromagnetic waves. Equation (13) also provides the spatially dispersive magnetic susceptibility $\chi_m(k_x, \omega)$ for transverse plane waves propagating along the x-axis of the lattice (and actually along any other main axis). The general expression for $\overline{\overline{\chi}}_m(\mathbf{k}, \omega)$ for any value of $\mathbf{k}$ becomes much more involved, because the mutual inductances between rings lying on orthogonal planes do not cancel. These expressions can be found in [29], where the reported theory was also checked by careful numerical computations. Finally, it may be worth to mention that, when spatial dispersion is present, the magnetic susceptibility becomes a tensor [29], even if the conditions for an isotropic behavior in the long wavelength limit [24] are fulfilled, thus destroying the isotropic behavior of the metamaterial.

In order to illustrate the typical behavior of TEM electromagnetic and magneto-inductive waves in RRM, the dispersion diagrams for longitudinal (12) and transverse (13) waves along a main axis of Fig. 2(a) are shown in Fig. 3 (solid lines) for some realistic values of the structure parameters. For positive values of the macroscopic permittivity ε, a negative μ forbidden band gap can be clearly appreciated near the resonance $\omega = \omega_0$. As is expected from its magneto-inductive nature, the longitudinal branch presents a flat dispersion curve. The transverse branch behaves as a nondispersive TEM electromagnetic wave at low frequencies, and as a slightly backward magneto-inductive wave when the frequency approaches the forbidden band gap (the reason for which this backward behavior is not clearly seen in the figure is because (14) corresponds to the limit $k_x \to \infty$ and, in practice, k_x reaches the end of the first Brillouin zone long before this limit).

$$
\frac{k_x^2}{k_m^2} - 1 = \chi_m(k_x, \omega) = \frac{\omega^2\mu_0\alpha_0/a^3}{\omega_0^2 - \omega^2[1 + (2M_c/L)\cos(k_x a) + 2(M_a + M_c)/L + \mu_0\alpha_0/(3a^3)] + j\omega R/L} \quad (13)
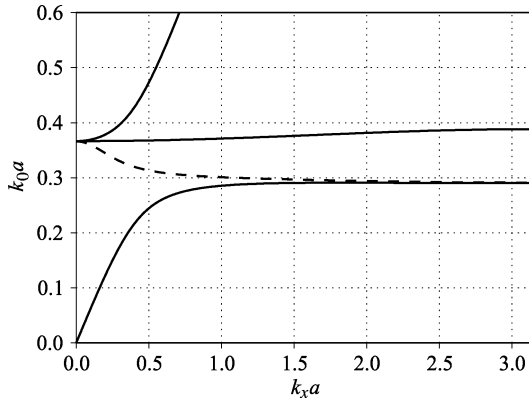$$

Fig. 3. *Dispersion diagrams for longitudinal (12) and transverse (13) waves in the lattice of rings sketched in Fig. 2(a), for two different values of the macoscopic permittivity of the metamaterial. Solid lines: $\varepsilon = 2.5\varepsilon_0$. Dashed lines: $\varepsilon = -\varepsilon_0$ [longitudinal waves (12) are not affected by the macroscopic permittivity]. Structural parameters are $a = \lambda_0/20$, where λ_0 is the wavelength at the frequency of resonance ω_0, $r = 0.45a$, $M_c/L = 0.02$, $M_a/L = -0.015$, $L = 1.1\mu_0 a$, and $R/\omega L \to 0$. The macroscopic permittivity $\varepsilon = 2.5\varepsilon_0$ approximately corresponds to the background static permittivity of the lattice of rings.*

D. Negative Refractive Index Metamaterials

Equation (11) is the wave equation in a medium with $\mathbf{E} = \varepsilon\mathbf{D}$ and magnetization $\mathbf{M}$, regardless of the relation between $\mathbf{H}$ and $\mathbf{M}$. Therefore, ε in (11) is the macroscopic permittivity of the metamaterial, which may be different from the permittivity of the host medium. If this permittivity is negative, then $k_m = \omega\sqrt{\varepsilon\mu_0}$ in (13) becomes imaginary, and a backward passband appears in the regions of negative magnetic permeability. This effect is illustrated in Fig. 3 where the dashed line shows the dispersion equation for transverse waves when $\varepsilon = -\varepsilon_0$. The question arising now is how to make negative the macroscopic permittivity without affecting the permeability of the metamaterial.

The simplest possibility, at least conceptually, is to place the resonant rings in a continuous host medium of negative dielectric permittivity (assuming that such medium is available). This strategy works for rings loaded by a chip capacitor or for dielectric resonant rings [16]. However, for SRRs, the presence of a host medium of negative dielectric permittivity drastically affects the SRR capacitance, making it negative, and therefore equivalent to an inductance. Then, the resonance disappears as well as the negative polarizability. In order to avoid this effect (and also because negative ε media are not easily available at radio frequencies) arrays of metallic wires [4], [5] are commonly used to complement SRR lattices. However, it must be taken into account that not any combination of SRRs and wires provides a left-handed behavior [31], [32]. For this purpose, both sublattices must be combined in such a way that the quasi-static properties (like inductance and/or capacitance) of the elements of each sublattice are not substantially affected by the presence of the comple-

mentary ones. An example of such configurations is shown in Fig. 2(b) [33]. Finally, it may be worth to mention that NRI without wires can be achieved in some specific bi-isotropic SRR cubic lattices [34].

E. Quasi-Static Resonances in Finite Size Resonant Ring Metamaterials

Until now we have focused our analysis on unbounded lattices of resonant rings. However, practical metamaterials must have a finite size, and scattering by the edges may lead to the appearance of eigenmodes that would not be excited in unbounded metamaterials. Actually, even homogeneous finite size negative ε or μ samples present quasi-satic resonances that are excited at the edges and corners of the structure (see [35] and references therein). Moreover, realistic metamaterials are mesoscopic systems, made of a finite number of elements much smaller than the number of atoms in any macroscopic sample. Therefore, it is not clear if the resonances that may appear in finite samples of metamaterials will even correspond to the resonances that may appear in the corresponding homogenized samples of a hypothetical continuous medium with the corresponding effective parameters.

In order to take into account these effects, we have recently developed a code able to solve large (but finite) samples of RRM under arbitrary excitations [36]. This code is based on the computation of the whole impedance matrix for all rings, which is then solved for the specific external excitation [27], [36]. Our preliminary results [37] reveal that indeed extra resonances appear in finite samples of RRM, when they are illuminated by a TEM plane wave. These resonances emerge even when realistic losses are taken into account, and are observed in structures up to at least 10 000 elements. The frequency dispersion of the polarizability of finite samples is qualitatively different from that of samples of continuous media under similar excitation. Therefore, although the homogenization theory of unbounded RRM is now quite well established (at least for the simplest lattices), the behavior of finite samples in the region of negative effective permeability (which is usually the region of interest) is far from being fully understood. Further research is necessary on this topic, of key importance for practical applications [38].

IV. APPLICATIONS AND FUTURE TRENDS

Metamaterial is a relatively new concept, which has provided in the recent years new ideas for the design of old devices such as antennas, frequency selective surfaces, and microwave circuits and filters. Some of these applications of RRM can be seen in [8] and references therein. However, 3-D metamaterial technology itself, that is, the technology for the development of bulk effective artificial media providing new electromagnetic effects, such as super-resolution or cloaking, is still in a very initial stage.
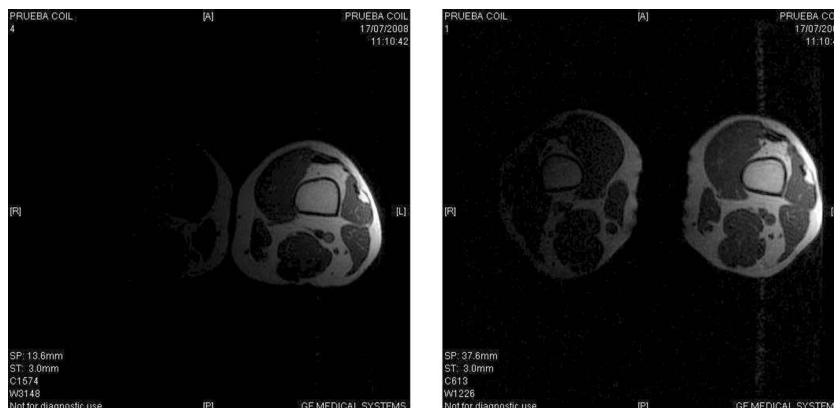
Fig. 4. *MRI images of two human knees obtained without (left) and with (right) the help of a $\mu = -1$ metamaterial lens. The lens is located between both knees (black region the image). Reprinted with permission from [40]. Copyright 2008, American Institute of Physics.*

Therefore, it is not strange if practical applications of bulk metamaterials are still far from being developed. At the present stage of the technology, low-frequency narrow-band applications—for instance, in magnetic resonance medical imaging (MRI) using "swiss rolls" [39], and resonant rings [40]–[43] 3-D metamaterials—seem to be the most promising ones. An example of this kind of applications is shown in Fig. 4, where the enhancement of the image of two human knees obtained using a $\mu = -1$ RRM lens can be seen. Other examples can be seen in [43], where $\mu \to 0$ and $\mu \to \infty$ RRM slabs are used in order to enhance the sensitivity of MRI surface coils.

Applications of bulk RRM in microwave and millimeter wave technology can also be envisaged, with the technological obstacles related to the fabrication process, which may imply the assembling of thousands of micro- or nano-structured elements. Applications at optical frequencies are more challenging, due to the effects analyzed in Section II-B.

From a theoretical point of view, the properties of bulk RRM still present important challenges, mainly with regard to the analysis and characterization of realistic finite samples, which should probably be analyzed using the theoretical tools of the physics of mesoscopic systems. ∎

REFERENCES

[1] W. Weber, "On the relationship of the science of the diamagnetism with the sciences of magnetism and electricity," *Ann. Phys.*, vol. 87, pp. 145–189, 1852.

[2] S. A. Schelkunoff and H. T. Friis, *Antennas Theory and Practice.* New York: Wiley, 1952, p. 584.

[3] J. B. Pendry, A. J. Holden, D. J. Robbins, and W. J. Stewart, "Magnetism from conductors and enhanced nonlinear phenomena," *IEEE Trans. Microw. Theory Tech.*, vol. 47, no. 11, pp. 2075–2084, Nov. 1999.

[4] W. Rotman, "Plasma simulation by artificial dielectrics and parallel-plate media," *IRE Trans. Antennas Propag.*, vol. 10, pp. 82–95, 1962.

[5] D. R. Smith, W. J. Padilla, D. C. Vier, S. C. Nemat-Nasser, and S. Schultz, "Composite medium with simultaneously negative permeability and permittivity," *Phys. Rev. Lett.*, vol. 84, pp. 4184–4187, 2000.

[6] V. E. Pafomov, "Transition radiation and Cerenkov radiation," *Soviet Physics JETP-USSR*, vol. 9, pp. 1321–1324, 1959.

[7] V. G. Veselago, "The electrodynamics of substances with simultaneously negative values of ε and μ," *Sov. Phys. Usp.*, vol. 47, pp. 509–514, 1968.

[8] R. Marqués, F. Martin, and M. Sorolla, *Metamaterials With Negative Parameters: Theory and Microwave Applications.* Hoboken, NJ: Wiley, 2008.

[9] L. Solymar and E. Shamonina, *Waves in Metamaterials.* Oxford, U.K.: Oxford Univ. Press, 2009.

[10] J. Zhou, T. Koschny, M. Kafesaki, E. N. Economou, J. B. Pendry, and C. M. Soukoulis, "Saturation of the magnetic response of split ring resonators at optical frequencies," *Phys. Rev. Lett.*, vol. 95, 223902, 2005.

[11] V. P. Drachev, U. K. Chettiar, A. V. Kildishev, H.-K. Yuan, W. Cai, and V. M. Shalaev, "The Ag dielectric function in plasmonic metamaterials," *Opt. Exp.*, vol. 16, pp. 1186–1195, 2008.

[12] R. D. Black, P. B. Roemer, and O. M. Mueller, "Electronics for a high temperature superconducting receiver system for magnetic resonance microimaging," *IEEE Trans. Biomed. Eng.*, vol. 41, no. 2, pp. 195–197, Feb. 1994.

[13] R. Marqués, F. Mesa, J. Martel, and F. Medina, "Comparative analysis of edge and broad-side coupled split ring resonators for metamaterial design. Theory and experiment," *IEEE Trans. Antennas Propag.*, vol. 51, no. 10, pt. 1, pp. 2572–2581, Oct. 2003.

[14] R. Marqués, F. Medina, and R. Rafii-El-Idrissi, "Role of bi-anisotropy in negative permeability and left handed metamaterials," *Phys. Rev. B*, vol. 65, 144441(1–6), Apr. 2002.

[15] R. E. Collin, *Field Theory of Guided Waves*, 2nd ed. Piscataway, NJ: IEEE Press, 1991, p. 765.

[16] L. Jelinek and R. Marqués, "Artificial magnetism and left-handed media from dielectric rings and rods," *J. Phys., Condens. Matter*, vol. 22, 025902(1–6), Dec. 2009.

[17] F. Falcone, T. Lopetegi, M. A. G. Laso, J. D. Baena, J. Bonache, M. Beruete, R. Marques, F. Martin, and M. Sorolla, "Babinet principle applied to metasurface and metamaterial design," *Phys. Rev. Lett*, vol. 93, 197401(1–4), Nov. 2004.

[18] T. J. Yen, W. J. Padilla, N. Fang, D. C. Vier, D. R. Smith, J. B. Pendry, D. N. Basov, and X. Zhang, "Terahertz magnetic response from artificial materials," *Science*, vol. 303, pp. 1494–1496, 2004.

[19] S. Linden, C. Enkrich, M. Wegener, J. Zhou, T. Koschny, and C. M. Soukoulis, "Magnetic response of metamaterials at 100 terahertz," *Science*, vol. 306, pp. 1351–1353, 2004.

[20] U. Kreibig and M. Vollmer, *Optical Properties of Metal Clusters.* Berlin, Germany: Springer-Verlag, 1995.

[21] V. Delgado, O. Sydoruk, E. Tatartschuk, R. Marqués, M. J. Freire, and L. Jelinek, "Analytical circuit model for split ring resonators in the far infrared and optical frequency range," *Metamaterials*, vol. 3, pp. 57–62, Mar. 2009.

[22] C. R. Simovski and B. Sauviac, "Towards creating isotropic microwave composites with negative refraction," *Radio Sci.*, vol. 39, RS2014, 2004.

[23] T. Koschny, L. Zhang, and C. M. Soukoulis, "Isotropic three-dimensional left-handed metamaterials," *Phys. Rev. B*, vol. 71, 121103, 2005.

[24] J. D. Baena, L. Jelinek, and R. Marqués, "Towards a systematic design of isotropic bulk magnetic metamaterials using the cubic point groups of symmetry," *Phys. Rev. B*, vol. 76, 245115(1–14), Dec. 2007.

[25] J. D. Jackson, *Classical Electrodynamics,* 3rd ed. Hoboken, NJ: Wiley, 1998, pp. 159–162.

[26] M. Gorkunov, M. Lapine, E. Shamonina, and K. H. Ringhofer, "Effective magnetic properties of a composite material with circular conductive elements," *Eur. Phys. J. B*, vol. 28, pp. 263–269, 2002.

[27] E. Shamonina, V. A. Kalinin, K. H. Ringhofer, and L. Solymar, "Magneto-inductive waves in one, two and three dimensions," *J. Appl. Phys.*, vol. 92, pp. 6252–6261, 2002.

[28] R. R. A. Syms, E. Shamonina, V. Kalinin, and L. Solymar, "A theory of metamaterials based on periodically loaded transmission lines: Interaction between magnetoinductive and electromagnetic waves," *J. Appl. Phys.*, vol. 97, 064909, 2005.

[29] J. D. Baena, L. Jelinek, R. Marqués, and M. G. Silveirinha, "Unified homogenization theory for magnetoinductive and electromagnetic waves in split ring metamaterials," *Phys. Rev. A*, vol. 78, 013842(1–5), Jul. 2008.

[30] M. G. Silveirinha, "Generalized Lorentz-Lorenz formulas for microstructured materials," *Phys. Rev. B*, vol. 76, 245117, 2007.

[31] C. Simovski, "Analytical modelling of double-negative composites," *Metamaterials*, vol. 2, pp. 169–185, 2008.

[32] R. Marqués and D. R. Smith, "Comments to electrodynamics of photonic crystals and the problem of left-handed metamaterials," *Phys. Rev. Lett.*, vol. 92, no. 1, p. 059401, Feb. 2004.

[33] L. Jelinek, R. Marqés, F. Mesa, and J. D. Baena, "Isotropic negative refraction index materials by cubic arrangements of SRRs," presented at the 2008 Days on Diffraction, St. Petersburg, Russia, Jun. 2008.

[34] L. Jelinek, R. Marqués, F. Mesa, and J. D. Baena, "Periodic arrangements of chiral scatterers providing negative refractive index bi-isotropic media," *Phys. Rev. B*, vol. 77, 205110(1–6), May 2008.

[35] H. Wallen, H. Kettunen, and A. Sihvola, "Surface modes of negative-parameter interfaces and the importance of rounding sharp corners," *Metamaterials*, vol. 2, pp. 113–121, 2008.

[36] M. Lapine, L. Jelinek, R. Marqués, and M. J. Freire, "Exact modelling method for discrete finite metamaterial lens," *IET Microw. Antennas Propag.*, vol. 4, pp. 1132–1139, Aug. 2010.

[37] R. Marqués, M. Lapine, and L. Jelinek, "Edge effects in finite size resonant ring metamaterials," in *Proc. Metamaterials Int. Conf. Complex Electromagn. Media*

Metamater., Karlsruhe, Germany, 2010, pp. 330–332.

[38] M. Lapine, L. Jelinek, M. J. Freire, and R. Marqués, "Realistic metamaterial lenses: Limitations imposed by discrete structure," *Phys. Rev. B.*, vol. 82, 165124(1–8), Oct. 2010.

[39] M. C. K. Wiltshire, J. B. Pendry, I. R. Young, D. J. Larkman, D. J. Gilderdale, and J. V. Hajnal, "Microstructured Magnetic Materials for RF Flux Guides in Magnetic Resonance Imaging," *Science*, vol. 291, pp. 849–851, Feb. 2001.

[40] M. J. Freire, R. Marqués, and L. Jelinek, "Experimental demonstration of a $\mu = -1$ metamaterial lens for magnetic resonance imaging," *Appl. Phys. Lett.*, vol. 93, 231108(1–3), Dec. 2008.

[41] M. J. Freire, L. Jelinek, R. Marques, and M. Lapine, "On the applications of $\mu_r = -1$ metamaterial lenses for magnetic resonance imaging," *J. Magn. Reson.*, vol. 203, pp. 81–90, Dec. 2009.

[42] J. M. Algaríin, M. J. Freire, M. A. Lopez, M. Lapine, P. M. Jakob, V. C. Behr, and R. Marqués, "Analysis of the resolution of split-ring metamaterial lenses with application in parallel magnetic resonance imaging," *Appl. Phys. Lett.*, vol. 98, 014105(1–3), Jan. 2011.

[43] M. A. Lopez, M. J. Freire, J. M. Algarin, V. C. Behr, P. M. Jakob, and R. Marqués, "Nonlinear split-ring metamaterial slabs for magnetic resonance imaging," *Appl. Phys. Lett.*, vol. 98, 133508(1–3), Apr. 2011.

ABOUT THE AUTHORS

Ricardo Marqués was born in San Fernando (Cádiz), Spain, in 1954. He received the Ph.D. degree from the Universidad de Sevilla, Sevilla, Spain, in 1987.

He is currently Full Professor at the Department of Electrónica y Electromagnetismo, Universidad de Sevilla. Since 1984, he has been with the Microwave Group of this Department, where he developed intensive research on computer-aided design for microwave circuits, wave propagation in ferrites and complex media, and transmission line theory. More recently, his interest focused on the analysis and design of artificial microstructured media with exotic electromagnetic properties (metamaterials) and its applications in optical, microwave, and RF technology, including negative refractive index media and subdiffraction imaging devices. He is the author of about 100 papers in scientific journals of physics and electrical engineering, many contributions to scientific meetings and several books and book chapters. He also was one of the founders and the first coordinator of the Spanish Network on Metamaterials (REME).

Lukas Jelinek was born in Kladno, Czech Republic, in 1980. He received the Ph.D. degree from the Czech Technical University in Prague, Prague, Czech Republic, in 2006.

Currently, he is a Researcher with the Department of Electromagnetic Field, Czech Technical University in Prague. His main fields of interest include wave propagation in complex media, general field theory, and numerical techniques. His recent research interest is focused on metamaterials, specifically on resonant ring systems.

Manuel J. Freire was born in Cádiz, Spain, in 1972. He received the Licenciado and Ph.D. degrees in physics from the University of Sevilla, Sevilla, Spain, in 1995 and 2000, respectively.

From 1995 through 1996, he served in the Royal Naval Observatory of the Spanish Navy in San Fernando, Cádiz. In 1996, he joined the Microwave Group of the Department of Electronics and Electromagnetics, University of Sevilla. In 1998, he was a Visiting Researcher in the Department of Electrical and Computer Engineering, University of Houston, Houston, TX. From 1999 to 2004, he was an Assistant Professor in the Department of Electronics and Electromagnetics, University of Sevilla, where he has been an Associate Professor since 2004. His research interests include leakage in microwave planar circuits, magnetostatic wave propagation in ferrite devices, frequency selective surfaces, and subwavelength imaging with metamaterials for magnetic resonance imaging applications. He is reviewer for the following international journals: *Journal of Applied Physics*, *Applied Physics Letters*, the IEEE Transactions on Microwave Theory and Techniques, *IEE Proceedings Microwaves Antennas and Propagation*, *IEE Proceedings Devices Circuits and Systems*, *Optics Communications*, *Optics Express*, *Metamaterials*, and *Applied Physics A*.

Juan Domingo Baena was born in El Puerto de Santa María, Spain, in August 1976. He received the Licenciado and Ph.D. degrees in physics from the Universidad de Sevilla, Sevilla, Spain, in 2001 and 2006, respectively.

From 2002 to 2007, he was with the Department of Electronics and Electromagnetism, Universidad de Sevilla, where he was involved with the research of metamaterials in the microwave range. Since 2008, he has been an Assistant Professor in the Department of Physics, Universidad Nacional de Colombia, Bogotá, Colombia. His current research interests include theoretical analysis, design, and experimental characterization of complex electromagnetic media and surfaces.

Mikhail Lapine received the Diploma (M.Sc., with honors) in biophysics from Moscow State University, Moscow, Russia, in 1997 and the Ph.D. degree (*summa cum laude*) in physics from Osnabrück University, Osnabrück, Germany, in 2004.

Upon working for a few years in biophysics and biochemistry at Moscow State University (1996–1999), and Osnabrück University (1999–2001), he turned to theoretical electrodynamics with a specific interest to effective medium treatment of metamaterials as well as development of nonlinear, tunable, and reconfigurable metamaterials, and worked on these topics at Osnabrück University (2001–2004; 2008) and Helsinki University of Technology (2005–2007). Since 2008, he has been a Visiting Researcher at the University of Sevilla, Sevilla, Spain and Australian National University, Canberra, Australia. In 2007, he initiated an international journal *Metamaterials* (Elsevier) and since then has acted as the Editor for this journal.

Appendix 2

This appendix contains a full text of Ref. [19]

Electrically small isotropic three-dimensional magnetic resonators for metamaterial design

J. D. Baena
Departamento de Electrónica y Electromagnetismo, Universidad de Sevilla, 41012-Sevilla, Spain

L. Jelinek
Department of Electromagnetic Field, Czech Technical University, Prague, Czech Republic

R. Marqués[a)]
Departamento de Electrónica y Electromagnetismo, Universidad de Sevilla, 41012-Sevilla, Spain

J. Zehentner
Department of Electromagnetic Field, Czech Technical University, Prague, Czech Republic

The problem of the design of artificial magnetic resonators for isotropic metamaterials is addressed. The internal symmetries that ensure an isotropic behavior of such resonators are analyzed and some specific designs based on the proper arrangement of modified split ring resonators are proposed. These proposals are validated by electromagnetic simulations and experiments. The reported results are likely to have applications in the design of devices such as negative refractive index materials, superlenses, and metasurfaces with isotropic response. © *2006 American Institute of Physics*.
[DOI: 10.1063/1.2190442]

After the first practical demonstration of a medium having simultaneously negative permittivity and permeability, also called *left-handed* medium (LHM),[1] a great wave of interest was generated in the scientific community due to the unique physical properties of such LHM.[2,3] Once the feasibility of such media was shown, practical isotropic two-dimensional designs based on well known printed circuit technologies came soon.[4–6] However, the practical implementation of a truly isotropic LHM still remains an open question. Isotropic artificial media with negative permittivity can be made, in principle, by assembling a three-dimensional array of connected wires.[7–9] Proposals for isotropic artificial media having negative permeability include cubic arrays of split ring resonators[10,11] [SRRs; see Fig. 1(a)] and Omega particles,[12] as well as isotropic spherical combinations of SRRs.[13] More recently, a cubic array of modified SRRs and connected wires has been proposed for the implementation of artificial LHM.[14] Regarding cubic arrays of SRRs and Omega particles,[10,12] the couplings between these elements should be investigated before postulating isotropy. Regarding spherical combinations of SRRs, it is well known that they only provide isotropy in two dimensions.[13] Finally, the recently proposed cubic array of modified SRRs and wires[14] clearly provides an isotropic medium, since the unit cell is invariant under all the transformations of the group of symmetry of a cube, i.e., the group generated by the transformations $\{I, -I, C_{4x}, C_{4x}, C_{4x}\}$ (or the O_h group in Schonflies notation). However, the proposed structure is difficult to implement in practice. First of all, very high permittivity dielectrics are involved in its design. Secondly, different from other previously proposed combinations of SRRs and metallic strips,[4] it is made of bulk metallic parts that cannot be manufactured by using standard printed circuit technologies. The aim of this letter is to propose and analyze some practical ways to artificial negative permeability media made

by using modified SRR particles and standard printed circuit technologies (eventually, such structures could be combined with printed strips to produce LHM). First, the minimum group of symmetry providing isotropic behavior will be investigated. Then, it will be shown through experiments that some previous proposals lacking this symmetry do not produce an isotropic response. Finally, some practical proposals possessing such symmetry will be analyzed.

To begin with, let us consider the subgroup of symmetry generated by the two noncommutative products of 90° rotations around two coordinate axes: $\{I, C_{4x} \cdot C_{4y}, C_{4y} \cdot C_{4x}\}$ (i.e., the T group in Schonflies notation). After some cumbersome but straightforward calculations, it is readily shown that any second order tensor invariant by this group of symmetry should be, in fact, a scalar. Nevertheless, this fact does not guarantee that the medium can be characterized by some scalar permittivity ϵ and permeability μ. In fact, magneto-electric couplings (see, for instance, Ref. 15) may cause the medium to be bi-isotropic, or *chiral*.[16] To ensure that the medium is not a chiral medium, it must be invariant by the inversion, $-I$.[17] Thus, to ensure both isotropy and nonchirality, the medium basic units should remain invariant by the symmetry group $\{I, -I, C_{4x} \cdot C_{4y}, C_{4y} \cdot C_{4x}\}$ (or the T_h group in Schonflies notation).

To illustrate the effects of breaking this symmetry, we will consider the basic unit shown in the inset of Fig. 2. It is a cubic array of SRRs, where the SRRs are arranged in such a way that the whole array satisfies inversion symmetry, so
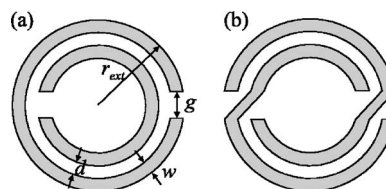

FIG. 1. (a) Split ring resonator (SRR). (b) Nonbianisotropic SRR.
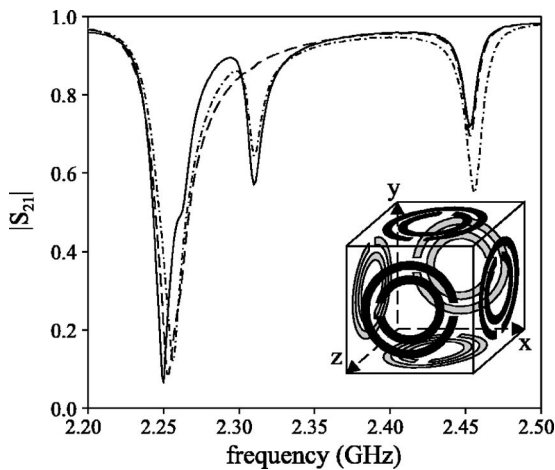
a)Electronic mail: marques@us.es

FIG. 2. Plots of the transmission coefficient ($|S_{21}|$) of a rectangular wave-guide with a cubic array of SRRs (see the inset) placed inside at different orientations. The waveguide is a rectangular $R22$ waveguide, with dimensions of 109×55 mm^2. The dimensions of the SRRs are (see Fig. 1) r_{ext} =7 mm, w=1.25 mm, d=0.5 mm, and g=1 mm. The substrate where the SRRs were printed is ARLONC 250-LX-0193-43-11, with dielectric constant ϵ_r=2.43 and thickness t=0.49 mm. The size of the cube is a =20 mm. Solid line corresponds to the cube oriented with the z axis along the waveguide axis and the y axis along the electric field of the fundamental TE$_{10}$ waveguide mode (the only one excited in the experiment). Dashed and dash-dot lines correspond to rotations C_{8y}, and $C_{8y} \cdot C_{8z}$ of the cube, respectively. Due to the couplings between different SRRs, the original resonance frequency of each single SRR, f=2.321±0.002 GHz, changes and splits into several resonances depending on the orientation.

that chirality is forbidden. It has been shown that if the couplings among the SRRs are neglected, such basic unit has an isotropic response.[11] However, the analyzed basic unit is not invariant by the $\{I, -I, C_{4x} \cdot C_{4y}, C_{4y} \cdot C_{4x}\}$ group of symmetry. In particular, it is not invariant after the transformation $C_{4x} \cdot C_{4y}$, as it can be easily realized by inspection. In fact, it can be also realized by inspection that it is impossible to build up a cubic combination of SRRs invariant by the aforementioned group of symmetry. The basic unit shown in Fig. 2 has been fabricated and placed at different orientations in a rectangular waveguide, in order to measure its response. Before measuring the whole structure, the frequencies of resonance of the different SRRs forming the structure were measured. All of them were found to be inside the interval f =2.321±0.002 GHz. No other resonances appeared in the TE$_{10}$ monomode range of the utilized waveguide, i.e., from 1.7 to 2.6 GHz. As it can be seen in the figure, the analyzed basic unit presents an anisotropic response, which cannot be justified by tolerances in the SRR fabrication process. This experiment shows that couplings between adjacent elements destroy the isotropy when the basic unit do not have the appropriate symmetry, as in this case. Splitting of the original resonance of single SRRs into several resonances is also observed. Similar experimental results were obtained for the cubic array of Omega particles proposed in 12. In that case the response also changes with the orientation, and the resonance is split into four resonances.

In order to overcome the aforementioned difficulties, a modification of the previous structure was analyzed. This modification substitutes the SRRs by the nonbianisotropic SRRs reported in 17, and shown in Fig. 1(b). The resulting structure, which is shown in the inset of Fig. 3, is invariant under the symmetry group $\{I, C_{4x} \cdot C_{4y}, C_{4y} \cdot C_{4x}\}$, without the inversion. The isotropy of the response has been checked by
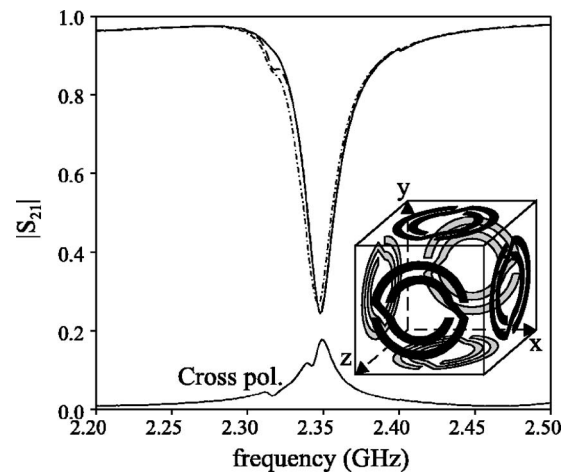

FIG. 3. Plots of the transmission coefficient ($|S_{21}|$) of a rectangular wave-guide with a cubic array of nonbianisotropic SRRs (see the inset) placed inside at different orientations. The waveguide size, the dimensions of the SRR, and the substrate characteristics are as in Fig. 1 (the frequency of resonance of the isolated nonbianisotropic SRRs was found to be in the interval f_0=2.385±0. 002 GHz). The analyzed orientations are the same as in Fig. 1. The transmission coefficient for the cross-polarized wave is also shown.

experiments similar to those reported in Fig. 2. The results are shown in Fig. 3, where an isotropic behavior can be clearly seen. As it was already mentioned, the analyzed structure has no inversion symmetry. Therefore, media made with these basic units may show bi-isotropy. In order to check this possibility the rotation of the plane of polarization of the light by this structure has been investigated experimentally. In the experiment, the structure was placed inside a rectangular waveguide and the cross-polarized transmission coefficient was measured by using appropriate detectors (two orthogonal input and output dipole antennas). The result is also shown Fig. 3, where a chiral behavior (expressed in the rotation of the plane of polarization of the transmitted wave) is clearly observed. Interestingly, it is known that each non-bianisotropic SRR forming the analyzed structure does not show bianisotropy by itself.[17] Therefore, the chirality of the structure comes from the couplings between the SRRs forming the array.

If chirality was not desired, the design must be invariant under the whole group of symmetry $\{I, -I, C_{4x} \cdot C_{4y}, C_{4y} \cdot C_{4x}\}$, including inversion. Two magnetic resonators having this symmetry are shown in Fig. 4. Figure 4(a) shows a spherical arrangement of two-split SRRs, which is a modification of the spherical resonator proposed in Ref. 13. Figure 4(b) shows a cubic array of broadside-coupled double-split SRRs (the design of each SRR is a modification of a previous proposal reported in Ref. 15). This structure has the same symmetries as the resonator shown in Fig. 4(a). In order to illustrate the isotropy of the structure proposed in
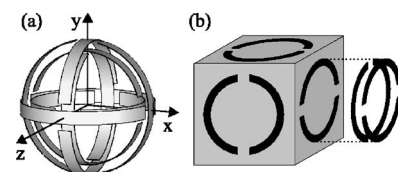

FIG. 4. (a) Spherical isotropic magnetic resonator. (b) Isotropic cubic array of broadside-coupled SRRs possessing the same symmetries as the structure shown in (a).
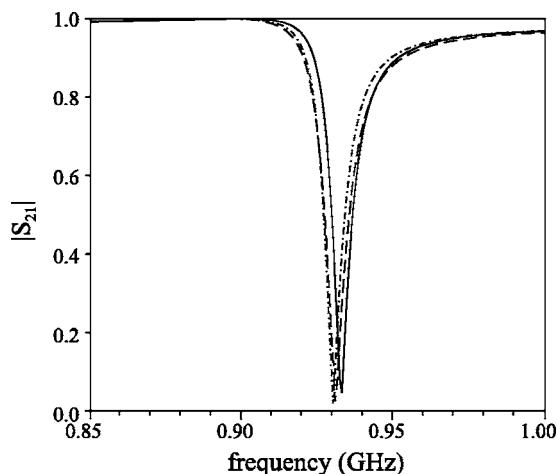
FIG. 5. Plots of the transmission coefficient ($|S_{21}|$) for the spherical resonator shown in Fig. 4(a) placed inside a rectangular waveguide at different orientations. The waveguide is a standard $R9$ waveguide with dimensions of 218×124 mm^2. The dimensions of the resonator are $r_{ext}=20$ mm, $w=4$ mm, $d=3$ mm, and $g=8$ mm. The dielectric filling the space between the broadside-coupled strips has $\epsilon_r=4$. Solid line corresponds to the resonator with the z axis along the waveguide axis and the y axis along the electric field of the fundamental TE$_{10}$ waveguide mode. Dashed and dash-dotted lines correspond to rotations C_{4y}, and $C_{8y} \cdot C_{8x}$ of the resonator, respectively.

Fig. 4(a), its response when it is placed inside a rectangular waveguide has been simulated by using the commercial electromagnetic solver CST MICROWAVE STUDIO. The results of this simulation are shown in Fig. 5. The same transmission coefficient was obtained for all the simulated orientations (the small differences can be attributed to numerical tolerances of the simulation process). Similar results are expected for the structure of Fig. 4(b), since it has the same symmetry as the analyzed spherical resonator.

In summary, the possibility of designing isotropic three-dimensional magnetic resonators by properly arranging modified SRRs has been verified. It has been also verified that the couplings between the different SRRs cannot be ignored in such design. Therefore, the array must show the appropriate structural symmetry in order to achieve an isotropic response. It has been shown that the group of symmetry generated by the transformations $\{I, C_{4x} \cdot C_{4y}, C_{4y} \cdot C_{4x}\}$

(the T group in Schonflies notation) is enough to ensure an isotropic response of the design. However, if a non-bi-isotropic response is desired (for instance, in order to design an effective medium fully characterized by some scalars ϵ and μ), the inversion symmetry must be added to this group (thus forming the T_h group in Schonflies notation). Starting from this analysis, some specific designs of bi-isotropic and non-bi-isotropic resonators have been proposed and tested by experiments and numerical simulations.

[1] D. R. Smith, W. J. Padilla, D. C. Vier, S. C. Nemat-Nasser, and S. Schultz, Phys. Rev. Lett. **84**, 4184 (2000).
[2] V. G. Veselago, Sov. Phys. Usp. **47**, 509 (1968).
[3] J. B. Pendry, Phys. Rev. Lett. **85**, 3966 (2000).
[4] R. A. Shelby, D. R. Smith, S. C. Nemat-Nasser, and S. Schultz, Appl. Phys. Lett. **78**, 489 (2001).
[5] G. V. Eleftheriades, A. K. Iyer, and P. C. Kremer, IEEE Trans. Microwave Theory Tech. **50**, 2702 (2002).
[6] R. Marqués, J. Martel, F. Mesa, and F. Medina, Microwave Opt. Technol. Lett. **36**, 405 (2002).
[7] W. Rotman, IRE Trans. Antennas Propag. **10**, 82 (1962).
[8] J. B. Pendry, A. J. Holden, W. J. Stewart, and I. Youngs, Phys. Rev. Lett. **76**, 4773 (1996).
[9] M. G. Silveirinha and C. A. Fernandes, IEEE Trans. Microwave Theory Tech. **53**, 1418 (2005).
[10] J. B. Pendry, A. J. Holden, D. J. Robbins, and W. J. Stewart, IEEE Trans. Microwave Theory Tech. **47**, 2075 (1999).
[11] C. R. Simovski and B. Sauviac, Radio Sci. **39**, RS2014 (2004).
[12] C. R. Simowski and S. He, Phys. Lett. A **311**, 254 (2003).
[13] P. Gay-Balmaz and O. J. F. Martin, Appl. Phys. Lett. **81**, 939 (2002).
[14] Th. Koschny, L. Zhang, and C. M. Soukoulis, Phys. Rev. B **71**, 121103 (2005).
[15] R. Marqués, F. Medina, and R. Rafii-El-Idrissi, Phys. Rev. B **65**, 144440 (2002).
[16] I. V. Lindell, A. H. Sihvola, S. A. Tretyakov, and A. J. Viitanen, *Electromagnetic Waves in Chiral and Bi-isotropic Media* (Artech House, London, UK, 1994).
[17] J. García-García, F. Martín, J. D. Baena, R. Marqués, and L. Jelinek, J. Appl. Phys. **98**, 033103 (2005).

Appendix 3

This appendix contains a full text of Ref. [20]

Towards a systematic design of isotropic bulk magnetic metamaterials using the cubic point groups of symmetry

J. D. Baena,[*] L. Jelinek,[†] and R. Marqués[‡]

Departamento de Electrónica y Eletromagnetismo, Universidad de Sevilla, Avenida Reina Mercedes s/n, 41012 Sevilla, Spain
(Received 8 May 2007; revised manuscript received 27 September 2007; published 17 December 2007)

In this paper, a systematic approach to the design of bulk isotropic magnetic metamaterials is presented. The roles of the symmetries of both the constitutive element and the lattice are analyzed. For this purpose, it is assumed that the metamaterial is composed of cubic split ring resonators (SRRs) arranged in a cubic lattice. The minimum symmetries needed to ensure an isotropic behavior are analyzed, and some particular configurations are proposed. Besides, an equivalent circuit model is proposed for the considered cubic SRRs. Experiments are carried out in order to validate the proposed theory. We hope that this analysis will pave the way to the design of bulk metamaterials with strong isotropic magnetic response, including negative permeability and left-handed metamaterials.

I. INTRODUCTION

Metamaterials are artificial media exhibiting exotic electromagnetic properties not previously found in nature. Among them, media showing simultaneously negative electric permittivity and magnetic permeability in some frequency range, or "left-handed" metamaterials, are of particular interest. The striking properties of left-handed metamaterials, including backward-wave propagation, negative refraction, and inverse Cerenkov and Doppler effects were first reported by Veselago[1] in 1968. However, the realistic implementations of left-handed metamaterials came several decades later, as a combination of split ring resonators (SRRs) and metallic wires.[2] SRRs are small planar resonators exhibiting a strong magnetic response, which were proposed in 1999 by Pendry *et al.*[3] as suitable "atoms" for the development of negative magnetic permeability metamaterials. One year later, Smith *et al.* demonstrated the possibility of making up a left-handed medium by periodically combining metallic wires—which provide an effective negative permittivity at microwaves[4]—and SRRs.[2] In subsequent works, other SRR designs were proposed,[5–8] in order to reduce electrical size and/or cancel the bianisotropic behavior of the original Pendry's design. However, all the aforementioned implementations of negative permeability and left-handed metamaterials are highly anisotropic—or even bianisotropic[5]—providing only a uniaxial resonant magnetization, while isotropy is needed for many interesting applications of metamaterials, as, for instance, the "perfect lens" proposed by Pendry.[9]

The aforementioned implementations are, in fact, a combination of two separate systems, one providing the negative magnetic permeability (the SRR system) and the other providing the negative electric permittivity (the wire system). How both subsystems can be combined in order to obtain a new system, whose electromagnetic properties were mainly the superposition of the magnetic and the electric properties of each subsystem, is an interesting and controversial issue[10,11] that is, however, beyond the scope of this paper. In what follows, we will assume that it is possible to find some combination of two isotropic subsystems, one made of me-

tallic wires (or other elements providing a negative electric permittivity) and the other made of SRRs, whose superposition gives a left-handed metamaterial, and will focus our attention on the design of isotropic systems of SRRs. Actually, since isotropic media with negative magnetic permeability are not found in nature, an isotropic system of SRRs providing such property in some frequency range will be an interesting metamaterial by itself. These metamaterials could provide the dual of negative electric permittivity media, with similar applications (in imaging,[9] for instance). They would be also of interest for magnetic shielding and other practical applications.

A first attempt to design an isotropic magnetic metamaterial was carried out by Gay-Balmaz and Martin,[12] who designed a spherical magnetic resonator—formed by two SRRs crossed in right angle—which is isotropic in two dimensions. This result was later generalized in Ref. 13, where a fully isotropic spherical magnetic resonator was proposed. However, from a practical standpoint, it is usually easier to work with cubic designs. A first attempt on such direction was made by Simovski and co-workers in Refs. 14–16, where cubic arrangements of planar SRRs and omega particles were proposed [see Figs. 1(a) and 1(b)]. If only the magnetic and/or electric dipole representations of the SRRs and/or omega particles are considered, these arrangements are invariant under cubic symmetries. However, it has been shown[13,17] that this invariance is not enough to guarantee an isotropic behavior since couplings between the planar resonators forming the cubic arrangement can give rise to an anisotropic behavior, even if its dipole representations suggest an isotropic design. The first isotropic metamaterial design fully invariant under the whole group of symmetry of the cube was proposed and simulated in Ref. 18. It is formed by volumetric square SRRs with four gaps, in order to provide 90° rotation symmetries about any of the cube axes. However, this design is unfortunately very difficult to implement in practice because it cannot be manufactured by using standard photoetching techniques, as previous SRR designs,[2,3,5–8,13–17] and the gaps of the SRR have to be filled with a high relative permittivity dielectric (about 100). The idea of using spatial symmetries to design isotropic metama-
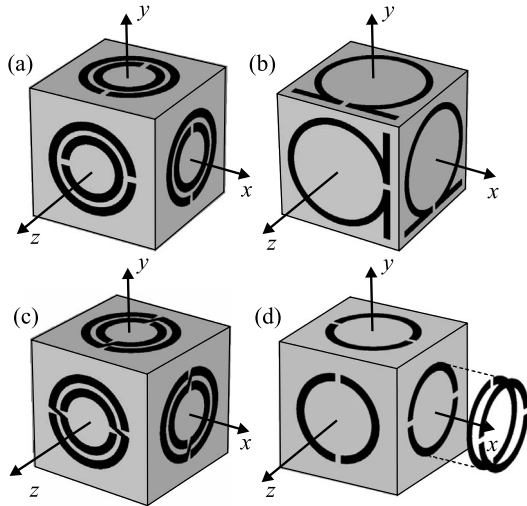
FIG. 1. Cubic constitutive elements for isotropic metamaterial design. Cubes (a) and (b) were studied in Refs. 14–16. Their hidden faces are arranged in such a way that the cube satisfies the central symmetry to avoid magnetoelectric coupling. Cubes (c) and (d) were proposed in Ref. 13 as truly three-dimensional (3D) isotropic cubic resonators.

terials was further developed in Refs. 13, 17, and 19 leading to the structures depicted in Figs. 1(c) and 1(d).

A second group of attempts to design isotropic metamaterials is developed in Ref. 20 and 21. In these works, lattices of dielectric and/or paramagnetic spheres with very high refractive index are proposed. If the refractive index of the spheres is high enough, the internal wavelength becomes small with regard to the macroscopic wavelength, and Mie resonances of the spheres can be used to produce the negative effective permittivity and/or permeability. Since the metamaterial "atoms" are spheres, the isotropy is ensured by simply placing them in a cubic lattice. However, practical difficulties to implement such proposals are not easy to overcome. First of all, lossless media with the very high refractive index needed for the spheres are difficult to obtain. Secondly, the system has a very narrow band.[21]

All the previously reported proposals for isotropic magnetic metamaterial design use a "crystal-like" approach. That is, they are based on the homogenization of a system of magnetic resonators which, according to causality laws, exhibit a strong diamagnetic response above resonance. There is, however, another approach widely used in the microwave community which is based on the transmission line analogy to effective media. Initially proposed for two-dimensional metamaterial design,[22] it was recently generalized to three-dimensional isotropic structures.[23–26] The main advantage of this approach is its broadband operation, since no resonators are necessary for the design. However, it also presents disadvantages with regard to crystal-like approaches. The transmission line approach to metamaterials does not seem to be applicable beyond the microwave range, whereas a significant magnetic response of the SRR has been shown in the terahertz range and beyond.[27,28] In addition, the coupling to free space of the reported transmission line metamaterials seems to be difficult and sometimes needs an additional spe-cific interface (e.g., an antenna array[25]), whereas this coupling is direct in crystal-like metamaterials.

Finally, regarding isotropic left-handed metamaterial design, it should be mentioned that some recent proposals based on random arrangements of chiral particles[29,30] have the advantage of providing simultaneously both electric and magnetic negative polarizabilities. This approach can be straightforwardly extended to the design of SRR magnetic metamaterials, by simply considering random arrangements of such elements. There is, however, a major difficulty with this approach: the constitutive elements in a random composite have to be very small in comparison with the macroscopic wavelength to show a true statistical behavior, but it is not easy to design a SRR much smaller than one-tenth of the wavelength. Due to this fact, periodic arrangements will be considered in what follows.

The main aim of this paper is to present a systematic approach to the design of metamaterial structures based on periodic arrangements of SRRs. The first section is focused on the spatial symmetries which are necessary to ensure an isotropic behavior in the metamaterial. Cubic arrangements of SRRs placed on cubic lattices are considered, and the minimum symmetry requirements for both the individual resonators and the lattices are investigated. The second section is devoted to a deeper analysis of the isotropic cubic SRRs forming the basis of the crystal structure. In the third section, an equivalent circuit model for such cubic SRRs is developed and applied to some specific examples. The fourth section is focused on the experimental verification of the analysis developed in the previous ones. Finally, the main conclusions of the work are presented.

II. ROLE OF CUBIC SYMMETRIES

Let us assume that constitutive elements and the unit cell of the material are much smaller than the operating wavelength. In such a case, the interaction of electromagnetic field with the material is described by means of constitutive relations. Besides, the material is supposed to be linear, so the most general way to express those relations between electromagnetic intensities and electromagnetic flux densities is[31]

$$\mathbf{D} = \boldsymbol{\varepsilon} \cdot \mathbf{E} + \boldsymbol{\xi} \cdot \mathbf{H},$$

$$\mathbf{B} = \boldsymbol{\zeta} \cdot \mathbf{E} + \boldsymbol{\mu} \cdot \mathbf{H}, \tag{1}$$

where $\boldsymbol{\varepsilon}$, $\boldsymbol{\mu}$ are second rank constitutive tensors and $\boldsymbol{\xi}$, $\boldsymbol{\zeta}$ are second rank constitutive pseudotensors. In order to get a macroscopic isotropic behavior, all constitutive tensors and pseudotensors $\boldsymbol{\varepsilon}$, $\boldsymbol{\mu}$, $\boldsymbol{\xi}$, and $\boldsymbol{\zeta}$ must become scalars or pseudoscalars.

Let us now address the problem of forcing the tensors (or pseudotensors) in Eq. (1) to be scalars (or pseudoscalars) for the specific case of a periodic structure. It is well known[32,33] that there are 32 symmetry point groups for periodic crystals which can be classified in 7 crystallographic systems. It is also known that the cubic system is the only one that forces any second rank tensor (or pseudotensor) to be a scalar (or a pseudoscalar).[33] Since any material satisfying the linear constitutive relations [Eq. (1)] and being invariant under the cu-
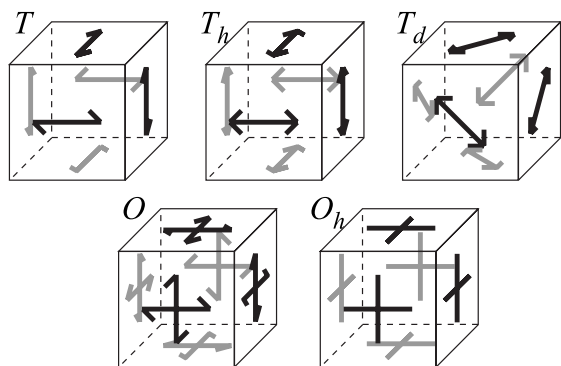
FIG. 2. Objects with the symmetries of the five cubic point groups.

bic symmetries exhibits an isotropic macroscopic behavior, this section will be focused on the analysis of such cubic symmetries. It is clear that any structure invariant under all the symmetry transformations of the cube must be isotropic, as already proposed by Koschny *et al.*[18] Furthermore, the full symmetry group of the cube contains four different subgroups also belonging to the cubic system and, thus, providing an isotropic macroscopic behavior. Since a less symmetric design is subjected to less structural constraints, it may be guessed that using these subgroups—instead of the whole symmetry group of the cube—may have practical advantages. Keeping this in mind, we will first give a short overview on the five cubic point groups. Next, we shall connect these point groups with some real structures made of planar resonators commonly used in metamaterials. This will be done in two parts: the study of the symmetries of the constitutive element, or the *basis*, and the analysis of the suitable periodic arrangements, or the *lattice*. At the end of the section some practical isotropic structures will be specifically analyzed.

A. Cubic point groups

The five cubic point groups are schematically represented in Fig. 2. Following Schöenflies' notation and ordering by degree of symmetry, these groups and their generators are as follows:

(1) $T = \langle \{ \mathbf{1}, \mathbf{4}_x \cdot \mathbf{4}_y, \mathbf{4}_y \cdot \mathbf{4}_x \} \rangle =$ proper rotations of the regular tetrahedron (12 operations);

(2) $T_h = \langle \{ \mathbf{1}, -\mathbf{1}, \mathbf{4}_x \cdot \mathbf{4}_y, \mathbf{4}_y \cdot \mathbf{4}_x \} \rangle = T$ expanded by the inversion (24 operations);

(3) $T_d = \langle \{ \mathbf{1}, -\mathbf{2}_x, \mathbf{4}_x \cdot \mathbf{4}_y, \mathbf{4}_y \cdot \mathbf{4}_x \} \rangle =$ proper and improper rotations of the regular tetrahedron (24 operations);

(4) $O = \langle \{ \mathbf{1}, \mathbf{4}_x, \mathbf{4}_y \} \rangle =$ proper rotations of the cube (24 operations);

(5) $O_h = \langle \{ \mathbf{1}, -\mathbf{1}, \mathbf{4}_x, \mathbf{4}_y \} \rangle =$ full symmetry group of the cube (48 operations).

We have used a widely used notation for symmetry transformations, **1** being the identity operator, $-\mathbf{1}$ the inversion, $\mathbf{n}_p$ an n-fold rotation axis about the p axis, and $-\mathbf{n}_p$ the n-fold axis about the p axis followed by the inversion. For example, the operator $-\mathbf{2}_x$ is the rotation through 180° about the x axis followed by the inversion.

B. Cubic basis

In order to simplify the problem, the symmetries can be separately imposed on the basis and the lattice of the structure. For the sake of simple fabrication, we will assume that the basis is formed by six planar resonators placed over the faces of an inert rigid cube, as in Fig. 1. If the crystal was diluted enough, then the coupling between two neighboring cubes would be much weaker than the coupling between the six SRRs of the same cube and thus each cube could be seen as a single cubic resonator (CR) electromagnetically coupled to others. Such consideration implies that the interaction between the CRs forming the material can be described by dipole-dipole interactions, higher order multipole interactions being negligible. In such approximation, all the CRs are properly described by second rank polarizability tensors connecting the external field, $\mathbf{E}^{ext}$ and $\mathbf{B}^{ext}$, with the dipolar moments, $\mathbf{p}$ and $\mathbf{m}$, induced in the CRs,[31,34]

$$\mathbf{p} = \boldsymbol{\alpha}_{ee} \cdot \mathbf{E}^{ext} + \boldsymbol{\alpha}_{em} \cdot \mathbf{B}^{ext},$$

$$\mathbf{m} = \boldsymbol{\alpha}_{mm} \cdot \mathbf{B}^{ext} - \boldsymbol{\alpha}_{em}^t \cdot \mathbf{E}^{ext}, \quad (2)$$
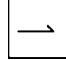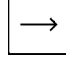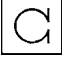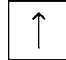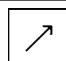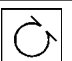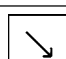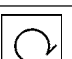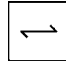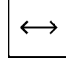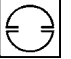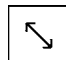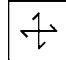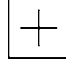
where $\boldsymbol{\alpha}_{ee}$, $\boldsymbol{\alpha}_{mm}$, and $\boldsymbol{\alpha}_{em}$ are the electric, magnetic, and magnetoelectric polarizability tensors, and the superscript t means transpose operation. The constitutive tensors in Eq. (1) can be derived from these polarizabilities and from the lattice structure by applying a homogenization technique.

In what follows, different kinds of CRs will be named by its cubic group symmetry followed by the acronym CR (group-CR). In order to design an isotropic CR, we have to find suitable planar resonators and place them correctly over the cube so as to fulfill the necessary symmetries. Obviously, the planar resonators have to be invariant under certain symmetry transformations of the square. To classify all different possibilities, a list of the symmetry subgroups of the square is shown in Table I, as well as their geometrical representations, and some examples of planar resonators commonly used in metamaterial design and obeying these symmetries. This table also provides a systematic terminology for planar resonators by using the symbol of the symmetry group followed by the term SRR (group-SRR). In what follows, we will use the term SRR in a general sense covering any type of geometry derived from the SRR and the omega particle.

By direct inspection on Fig. 2, it can be seen that any of the five cubic point groups contains three twofold rotation axes (180° rotations) parallel to the edges of the cube. Thus, only resonators belonging to the last five rows of Table I are appropriate for designing isotropic CRs. At this point, it may be worth mentioning that Pendry's SRRs[3] as well as Omega particles[35] are not appropriate for such purpose because they correspond to the C_1-SRR and D_1-SRR topologies. In summary, in order to get an isotropic CR, we have to choose six identical SRRs pertaining to the classes C_2-, D_2-, C_4-, or D_4-SRR and arrange them according to one of the cubic point groups T, T_d, T_h, O, or O_h shown in Fig. 2.

Although all five cubic point groups mentioned above are equally useful to achieve isotropic CRs, a specific choice may strongly affect the properties of an isotropic metamaterial. For instance, using isotropic CRs of low symmetry may

TABLE I. Classification of SRR types based on the symmetry subgroups of the square. The second column shows Schöenflies' notation and the generator of groups. The symbols of transformations are **1** =identity; **4**=90° rotation; **2**=180° rotation; **−4**=−90° rotation; m_x, m_y=line reflections respect to the x and y axes, respectively; $m_{x,y}$, m_{x-y}=line reflections respect to both diagonals of the square. Each group is schematically represented by the objects in the second column which can be replaced by the planar resonators shown in the third column.

SRR types	Symmetry subgroups of the square	Geometrical representation	Examples of resonators
C_1-SRR	$C_1 = \{\mathbf{1}\}$		
D_1-SRR	$D_{1x} = \{\mathbf{1}, \mathbf{m}_x\}$		
	$D_{1y} = \{\mathbf{1}, \mathbf{m}_y\}$		
	$D_{1,x,y} = \{\mathbf{1}, \mathbf{m}_{x,y}\}$		
	$D_{1,x,-y} = \{\mathbf{1}, \mathbf{m}_{x,-y}\}$		
C_2-SRR	$C_2 = \{\mathbf{1}, \mathbf{2}\}$		
D_2-SRR	$D_{2x} = D_{2y} = \{\mathbf{1}, \mathbf{m}_x, \mathbf{m}_y, \mathbf{2}\}$		
	$D_{2xy} = D_{2x\bar{y}} = \{\mathbf{1}, \mathbf{m}_{x,y}, \mathbf{m}_{x,-y}, \mathbf{2}\}$		
C_4-SRR	$C_4 = \{\mathbf{1}, \mathbf{4}, \mathbf{2}, \mathbf{-4}\}$		
D_4-SRR	$D_4 = \{\mathbf{1}, \mathbf{4}, \mathbf{2}, \mathbf{-4}, \mathbf{m}_x, \mathbf{m}_y, \mathbf{m}_{x,y}, \mathbf{m}_{x,-y}\}$		

be quite advantageous since the electrical size of the CRs can be made smaller. This fact can be justified in terms of the LC circuit models for the SRRs[5–8] because the effective capacitances of low symmetry SRRs are usually higher than those of high symmetry SRRs,[8] thus providing a smaller resonance frequency. Following these considerations, the best choice of basis would be a T-CR made of six planar resonators of the C_2-SRR type. A good candidate among all possibilities is the cube shown in Fig. 1(c) made of six nonbianisotropic SRRs (NB-SRRs),[8,36] a configuration already proposed in Refs. 13 and 17. Furthermore, it was shown in Ref. 13 that this configuration shows a bi-isotropic behavior, due to the lack of inversion symmetry of the cubic arrangement. However, sometimes, an effective isotropic medium without bi-anisotropy (ξ, ζ=0) is desired. Since ξ and ζ are pseudotensors, the invariance of the CR under inversion is required in order to avoid such property. In this case, the lowest symmetry group is the T_h group. A CR invariant under the last group of symmetry can be made by using planar resonators of the D_2-SRR type as, for instance, the symmetric SRR[37] or the modified double-slit broadside coupled SSR (BC-SRR) shown in Fig. 1(d).[13] However, as will be shown in the following, such symmetry requirements can be relaxed if the lattice symmetries are properly chosen.

C. Cubic lattices

Above findings give precise instructions for choosing suitable geometries for isotropic metamaterial constitutive elements. The next step is to create an isotropic metamaterial with these elements. The cubic shape of the considered constitutive elements suggests that the best periodical arrangements are the simple cubic (sc), body centered cubic (bcc), and face centered cubic (fcc) lattices shown in Fig. 3. All these lattices obey the full symmetry group of the cube, O_h. Therefore, the whole metamaterial (lattice plus basis) retains the cubic point group symmetries and the macroscopic isotropic behavior.

Although all previously mentioned lattices can provide isotropic metamaterials, it is convenient to look deeply into the possible structures because some particular choices may offer interesting advantages. Regarding Fig. 3, a is the edge size of the CR and b is the edge size of the cubic unit cell. In order to describe CR interactions as dipole-dipole interactions, b must be chosen much larger than a, so that the metamaterial properties can be deduced from Eq. (2) and the appropriate homogenization procedure. However, usually, we are also interested in a high density of dipoles in order to get a strong electromagnetic response. Therefore, b should
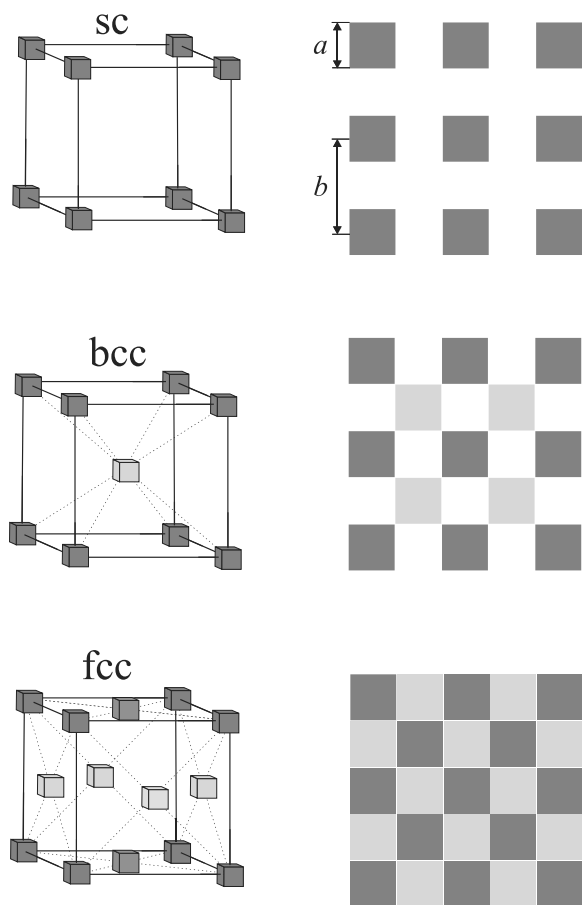
FIG. 3. Cubic Bravais' lattices. Their top views are also depicted for the particular case of $b=2a$. Black and gray small cubes represent cubic resonators on successive planes.

be as small as possible. However, decreasing b may lead to a failure of the aforementioned homogenization procedure. However, in any case, the combination of a basis and a lattice with the appropriate symmetries will provide an isotropic metamaterial, regardless of the homogenization procedure. Finally, there are some practical limitations to the values that a and b can reach as, for instance, the obvious inequality $b \geq a$, derived from the fact that CRs are supposed to be impenetrable.

Additional limitations appear for each specific structure. In the case of a sc lattice with T-, T_d-, or O-CRs, the lack of inversion symmetry implies that opposite sides of a CR are not oriented in the same way. Thus, the constrain $b > a$ is necessary in order to avoid a mutual short circuit between the SRRs of neighboring CRs. To allow the minimum distance $b=a$, the noncentrosymmetric CRs in the sc lattice must be replaced by T_h- or O_h-CRs, so that the SRRs on contacting sides of neighboring CRs exactly overlap. In the case of a bcc lattice, the contact between corners implies that the inequality $b \geq a$ must be fulfilled for any type of CR. Finally, for the fcc lattice, the contact between edges of neighboring CRs establishes the harder condition $b \geq 2a$.

The particular case of an fcc lattice with the minimum cell size, $b=2a$, deserves a specific analysis. When T_h- or O_h-CRs are used as the basis of the fcc lattice, the structure

turns into an sc lattice with the highest possible compactness, i.e., $b=a$, because the *holes* between each eight neighboring CRs have the same shape as the CRs forming the basis. The case of an fcc lattice with a T-, T_d-, or O-CR basis is even more special and interesting because each hole exactly corresponds with the inversion of the CR of the basis. Therefore, although the basis of the structure is not invariant under inversion, the fcc structure is brought into coincidence with itself by inversion centered at the center of a CR, followed by a translation of length a through any of the cube axes. Since the wavelength of the signal illuminating the structure is supposed to be much larger than a, the system can be considered as macroscopically invariant under inversion and, therefore, any bi-isotropic behavior must disappear. Thus, we conclude that a very interesting choice in order to obtain an isotropic metamaterial is the fcc lattice with $b=2a$ and with a basis formed by T-CRs [example in Fig. 1(c)] because of its high compactness, non-bi-isotropic macroscopic behavior, and low degree of symmetry. It is worth recalling here that T-CRs have the lowest symmetry among all the possibilities shown in Fig. 2, which helps to reduce the electrical size of the unit cell, as explained above.

III. RESONANCES AND POLARIZABILITIES OF CUBIC RESONATORS

Until now, only the symmetry of CRs and cubic lattices useful for isotropic periodic metamaterials were analyzed. However, in order to have a complete characterization of the metamaterial, polarizabilities and couplings between individual SRRs must be considered. In dilute crystals, the approach of weak coupling between CRs, but strong coupling between the SRRs of each CR, is valid. Then, the metamaterial characterization involves two separate problems: obtaining the polarizability tensors in Eq. (2) for a single CR and applying the appropriate homogenization procedure to obtain the constitutive parameters for the whole structure. For dense packages, the aforementioned approach is not valid since couplings between SRRs of different CRs can be stronger than SRR couplings inside each individual CR. However, even in these cases, the analysis of the isolated CR resonances and polarizabilities still provides useful information on the behavior of the metamaterial. For instance, it allows to elucidate if the coupling between SRRs in a practical low symmetry CR can be neglected or not. In case they could be neglected, all the analysis in Sec. II B would become irrelevant because the SRRs could be substituted by its equivalent dipoles (as it was assumed in Refs. 14–16), without more considerations on the SRR structure. Therefore, the analysis in this section is necessary in order to justify the practical relevance of the analysis developed in Sec. II. Further, in Sec. IV, an experimental validation of this analysis will be provided.

Let us assume that the CR size is much smaller than the operating wavelength. Thus, an *RLC* circuit model is valid for describing the behavior of single Pendry's SRRs,[3] as well as for any type of modified SRRs[5–8] or omega particles.[38] Furthermore, if the resonators are not too close (so that the interaction energies are small with regard to the self-energy
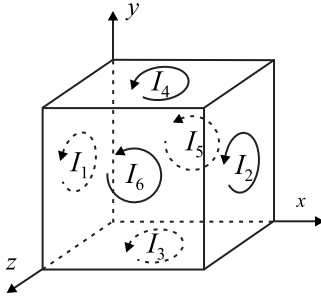
FIG. 4. Definition of the sign of currents in the circuit model for a 3D cubic magnetic resonator.

of each SRR), then the CR can be considered as six *RLC* circuits coupled through mutual impedances. The positive directions of the electric currents on each loop are arbitrarily defined in Fig. 4. The relation between currents and electromotive forces exciting the CR can be written as

$$\mathbf{Z} \cdot \mathbf{I} = \mathbf{F}, \tag{3}$$

where $\mathbf{Z}$ is a 6×6 square impedance matrix, $\mathbf{I}$ is a column matrix whose ith component is the current flowing over the ith SRR, and $\mathbf{F}$ is a column matrix whose ith component is the external electromotive force acting on the ith SRR. The diagonal components of the impedance matrix are the self-impedances of each SRR, i.e., $Z_{ii} = R + j\omega L + 1/(j\omega C)$, with R, L, and C being the resistance, self-inductance, and self-capacitance of a single SRR.[8] The nondiagonal components Z_{ij} are the mutual impedances between the ith and jth SRRs. From the reciprocity theorem,[39] we know that the impedance matrix must be symmetric, i.e., $Z_{ij} = Z_{ji}$. This reduces the number of independent elements of $\mathbf{Z}$ to 21. This number can be further reduced by applying the geometrical symmetries of the CR, as shown in the next paragraph.

The application of any symmetry operation changes the components of $\mathbf{I}$ according to the rule $\mathbf{I}' = \mathbf{S} \cdot \mathbf{I}$, where $\mathbf{S}$ is the corresponding operator of symmetry. It is well known that any symmetry operation $\mathbf{S}$ of the cubic point groups can be expressed as some combination of the three orthogonal four-fold rotations and the inversion, whose matrix representations, in the six-dimensional space defined by $\mathbf{I}$, are

$$\mathbf{4}_x \equiv \begin{bmatrix} \begin{matrix} 1 & 0 \\ 0 & 1 \end{matrix} & 0 & 0 \\ 0 & 0 & \begin{matrix} 0 & -1 \\ -1 & 0 \end{matrix} \\ 0 & \begin{matrix} 1 & 0 \\ 0 & 1 \end{matrix} & 0 \end{bmatrix},$$

$$\mathbf{4}_y \equiv \begin{bmatrix} 0 & 0 & \begin{matrix} 1 & 0 \\ 0 & 1 \end{matrix} \\ 0 & \begin{matrix} 1 & 0 \\ 0 & 1 \end{matrix} & 0 \\ \begin{matrix} 0 & -1 \\ -1 & 0 \end{matrix} & 0 & 0 \end{bmatrix},$$

$$\mathbf{4}_z \equiv \begin{bmatrix} 0 & \begin{matrix} 0 & -1 \\ -1 & 0 \end{matrix} & 0 \\ \begin{matrix} 1 & 0 \\ 0 & 1 \end{matrix} & 0 & 0 \\ 0 & 0 & \begin{matrix} 1 & 0 \\ 0 & 1 \end{matrix} \end{bmatrix},$$

$$-\mathbf{1} \equiv \begin{bmatrix} \begin{matrix} 0 & 1 \\ 1 & 0 \end{matrix} & 0 & 0 \\ 0 & \begin{matrix} 0 & 1 \\ 1 & 0 \end{matrix} & 0 \\ 0 & 0 & \begin{matrix} 0 & 1 \\ 1 & 0 \end{matrix} \end{bmatrix}. \tag{4}$$

They are unitary matrices with the well known property $\mathbf{S}^{-1} = \mathbf{S}^t$. It can be straightforwardly demonstrated that $\mathbf{F}$ follows the same rule of transformation: $\mathbf{F}' = \mathbf{S} \cdot \mathbf{F}$. Therefore, both $\mathbf{I}$ and $\mathbf{F}$ can be considered as vectors. In what follows, $\mathbf{I}$ and $\mathbf{F}$ will be called the "current" and the "excitation" vectors, respectively. Therefore, the impedance matrix $\mathbf{Z}$ is a second rank tensor, following the transformation rule $\mathbf{Z}' = \mathbf{S} \cdot \mathbf{Z} \cdot \mathbf{S}^t$. If the CR remains invariant by the transformation $\mathbf{S}$, then

$$\mathbf{Z} = \mathbf{S} \cdot \mathbf{Z} \cdot \mathbf{S}^t. \tag{5}$$

This equation gives some relations between the components of $\mathbf{Z}$, which can reduce the number of independent components of $\mathbf{Z}$.

Although the current vector $\mathbf{I}$ can be directly solved by multiplying both sides of Eq. (3) by $\mathbf{Z}^{-1}$, in order to identify the different resonances of the CR, it is convenient to expand the solution in terms of the eigenvectors of $\mathbf{Z}$. The eigenvalue problem corresponding to Eq. (3) is

$$\mathbf{Z} \cdot \mathbf{v}_i = z_i \mathbf{v}_i, \tag{6}$$

where z_i are the eigenvalues, $\mathbf{v}_i$ the eigenvectors, and the index $i = 1, \ldots, 6$. The impedance matrix $\mathbf{Z}$ can be expanded in a sum of two terms as

$$Z_{ij} = \left(R + j\omega L + \frac{1}{j\omega C} \right) \delta_{ij} + Z_{ij}(1 - \delta_{ij}), \tag{7}$$

where δ_{ij} is Kronecker's delta. The first term is the self-impedance of a single SRR multiplied by the identity, while the second term is the symmetric matrix of mutual impedances. These mutual impedances are purely imaginary numbers since, in the frame of a quasistatic model, they cannot contain a resistive term. Thus, the second term in Eq. (7) is a purely imaginary symmetrical matrix. Therefore, its eigenvectors can be chosen in such a way that they form a complete and orthogonal basis that diagonalizes this matrix. Furthermore, since the first summand in Eq. (7) is actually a scalar, the eigenvectors of Z_{ij} are actually the same as those of $Z_{ij}(1-\delta_{ij})$. Therefore, the eigenvectors of $\mathbf{Z}$ can be chosen in such a way that they form an orthogonal basis for the considered six-dimensional space. Thus, the current and ex-

citation vectors can be expanded as a summation of such eigenvectors,

$$\mathbf{I} = \sum_i (\mathbf{I} \cdot \mathbf{v}_i)\mathbf{v}_i, \quad \mathbf{F} = \sum_i (\mathbf{F} \cdot \mathbf{v}_i)\mathbf{v}_i. \tag{8}$$

By substituting both expressions into Eq. (3) and applying Eq. (6), we get

$$\mathbf{I} = \sum_i \frac{\mathbf{F} \cdot \mathbf{v}_i}{z_i}\mathbf{v}_i. \tag{9}$$

Therefore, both $\mathbf{F}$ and $\mathbf{I}$ can be expanded in a set of orthogonal modes having mutually proportional excitation and current vectors.

From Eq. (7), we can also obtain information about the structure of the eigenvalues z_i. These eigenvalues must have the form

$$z_i(\omega) = R + j\omega L + \frac{1}{j\omega C} + z_{c,i}(\omega) = j\omega L\left[1 - \frac{\omega_0^2}{\omega^2} + \frac{R}{j\omega L}\right.$$
$$\left. + \frac{z_{c,i}(\omega)}{j\omega L}\right], \tag{10}$$

where ω_0 is the resonance frequency of an isolated SRR ($\omega_0^2 = 1/LC$), and $z_{c,i}(\omega)$ the eigenvalues of the second summand in Eq. (7), which are related to the coupling between SRRs. It can be seen in Eq. (9) that the ith mode resonates when its eigenvalue approaches zero ($z_i \approx 0$). Therefore, the frequency of resonance of the ith mode is given by the relation $z_i(\omega_{0,i}) \approx 0$. If losses and couplings between SRRs are not too strong ($R, z_{c,i} \ll j\omega L$), the frequencies of resonance of the CR can be approximated as

$$\omega_{0,i} \approx \omega_0 - \frac{z_{c,i}(\omega_0)}{2jL}. \tag{11}$$

In what follows, we will apply this equivalent circuit model to the determination of the resonances and polarizabilities of two CRs made from two well known SRRs: Pendry's SRR[3] and NB-SRR.[8]

A. Analysis of an anisotropic cube

Let us now consider the CR shown in Fig. 1(a), made of Pendry's SRRs. In this section, we are going to get some analytical approximation for its resonances and polarizabilities. Note that the cube possesses inversion symmetry and, thus, magnetoelectric coupling is forbidden, so that $\boldsymbol{\alpha}_{em} = 0$ in Eq. (2). It can also be seen by inspection that the considered CR is invariant under the rotation $\mathbf{4}_y \cdot \mathbf{4}_x$. By applying this spatial symmetry, the impedance matrix is reduced to the form

TABLE II. Eigenvalues and a complete set of orthonormal eigenvectors of the impedance matrix [Eq. (12)] corresponding to anisotropic cubic resonators with symmetries $-\mathbf{1}$ and $\mathbf{4}_y \cdot \mathbf{4}_x$, as, for instance, the structures shown in Figs. 1(a) and 1(b).

	Eigenvalues z_i	Eigenvectors $\mathbf{v}_i$
Even modes (magnetic)	$Z_{11} + Z_{12} - Z_{13} - Z_{14}$	$\frac{1}{2}(-1,-1,1,1,0,0)$
		$\frac{1}{2\sqrt{3}}(1,1,1,1,2,2)$
	$Z_{11} + Z_{12} + 2Z_{13} + 2Z_{14}$	$\frac{1}{\sqrt{6}}(-1,-1,-1,-1,1,1)$
Odd modes (electric)	$Z_{11} - Z_{12} - Z_{13} + Z_{14}$	$\frac{1}{2\sqrt{3}}(1,-1,-2,2,1,-1)$
		$\frac{1}{2}(1,-1,0,0,-1,1)$
	$Z_{11} - Z_{12} + 2Z_{13} - 2Z_{14}$	$\frac{1}{\sqrt{6}}(-1,1,-1,1,-1,1)$

$$\mathbf{Z} = \begin{bmatrix} Z_{11} & Z_{12} & Z_{13} & Z_{14} & -Z_{14} & -Z_{13} \\ Z_{12} & Z_{11} & Z_{14} & Z_{13} & -Z_{13} & -Z_{14} \\ Z_{13} & Z_{14} & Z_{11} & Z_{12} & -Z_{14} & -Z_{13} \\ Z_{14} & Z_{13} & Z_{12} & Z_{11} & -Z_{13} & -Z_{14} \\ -Z_{14} & -Z_{13} & -Z_{14} & -Z_{13} & Z_{11} & Z_{12} \\ -Z_{13} & -Z_{14} & -Z_{13} & -Z_{14} & Z_{12} & Z_{11} \end{bmatrix}, \tag{12}$$

where there are only four independent components. The corresponding eigenvalues and its orthonormal eigenvectors are shown in Table II. It is worth noting that the eigenvectors can be classified in even and odd modes: for even (odd) modes, the currents I_{2n-1} and I_{2n} are parallel (antiparallel).

Once the eigenvalue problem is solved, the next step is to write an explicit expression for the excitation vector $\mathbf{F}$ and introduce this expression in Eq. (9), in order to get the currents over the SRRs. To begin with, we will assume that the CR is excited by a homogeneous external magnetic field $\mathbf{B}^{ext} = (B_x^{ext}, B_y^{ext}, B_z^{ext})$, and there is no external electric field. Then, the excitation vector is written as

$$\mathbf{F}_m = -j\omega A(B_x^{ext}, B_x^{ext}, B_y^{ext}, B_y^{ext}, B_z^{ext}, B_z^{ext}), \tag{13}$$

where A is the effective area of the SRR. By introducing Eq. (13) into Eq. (9), the current vector $\mathbf{I}$ is calculated. Finally, the magnetic dipole components of the CR are obtained from $m_x = (I_1 + I_2)A$, $m_y = (I_3 + I_4)A$, and $m_z = (I_5 + I_6)A$. The resulting expression for the magnetic polarizability tensor is
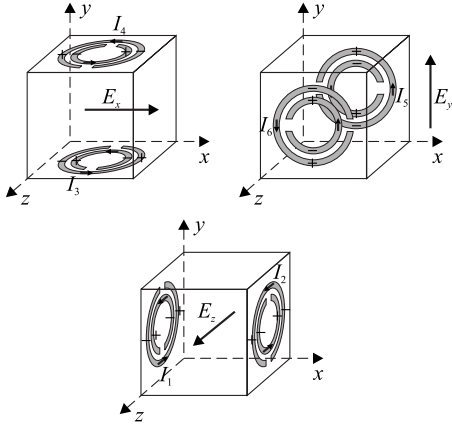
FIG. 5. Electric excitation of the cubic resonator made of Pendry's SRRs.

$$\boldsymbol{\alpha}^{mm} = -j\omega A^2 \frac{2}{3} \left[\frac{1}{Z_{11} + Z_{12} - Z_{13} - Z_{14}} \begin{pmatrix} 2 & -1 & 1 \\ -1 & 2 & 1 \\ 1 & 1 & 2 \end{pmatrix} \right.$$
$$\left. + \frac{1}{Z_{11} + Z_{12} + 2Z_{13} + 2Z_{14}} \begin{pmatrix} 1 & 1 & -1 \\ 1 & 1 & -1 \\ -1 & -1 & 1 \end{pmatrix} \right]. \quad (14)$$

This magnetic polarizability tensor is anisotropic and exhibits two resonances, at those frequencies where $Z_{11} + Z_{12} - Z_{13} - Z_{14} \approx 0$ or $Z_{11} + Z_{12} + 2Z_{13} + 2Z_{14} \approx 0$. Only the even resonances of Table II appear in Eq. (14) because the excitation vector and the odd eigenvectors are orthogonal, i.e., $\mathbf{F}_m \cdot \mathbf{v}_i^{odd} = 0$ in Eq. (9). Just in the limit of no coupling between SRRs ($Z_{ij} = 0$ for $i \neq j$), both resonances converge to the single SRR resonance and $\boldsymbol{\alpha}_{mm}$ becomes a scalar, as mentioned in Refs. 14–16. However, it will be shown in the Sec. IV that this coupling cannot be neglected in most practical configurations.

Apart from the magnetic excitation studied above, it is well known that Pendry's SRR can be excited by an external electric field.[5,6,40] Therefore, an electric response is also expected for this particular CR. The electric excitation of the rings on the cube is sketched in Fig. 5. The external electric field $\mathbf{E}^{ext}$ can excite an SRR only if it has a nonvanishing component contained in the plane of the particle and orthogonal to the imaginary line passing through the slits of the rings.[5,6,40] Therefore, only two SRRs are excited by each Cartesian component of $\mathbf{E}^{ext}$. Thus, for an external and homogeneous electric field of arbitrary direction, the excitation vector has the form

$$\mathbf{F}_e \propto (E_z^{ext}, -E_z^{ext}, -E_x^{ext}, E_x^{ext}, -E_y^{ext}, E_y^{ext}). \quad (15)$$

Taking into account the sign of the charges induced over the rings, it is clear that the electric dipole has to be proportional to

$$\mathbf{p} \propto \begin{pmatrix} I_3 - I_4 \\ I_5 - I_6 \\ I_2 - I_1 \end{pmatrix}. \quad (16)$$

The proportionality constants of Eq. (15) and (16) are given in the Appendix, Eqs. (A2) and (A9). Finally, from Eq. (A9) of the Appendix, we get the following analytical formula for the electric polarizability tensor:

$$\boldsymbol{\alpha}^{ee} = \frac{32d_{eff}^2}{3j\omega\pi^2} \left[\frac{1}{Z_{11} - Z_{12} - Z_{13} + Z_{14}} \begin{pmatrix} -2 & 1 & -1 \\ 1 & -2 & -1 \\ -1 & -1 & -2 \end{pmatrix} \right.$$
$$\left. + \frac{1}{Z_{11} - Z_{12} + 2Z_{13} - 2Z_{14}} \begin{pmatrix} -1 & -1 & 1 \\ -1 & -1 & 1 \\ 1 & 1 & -1 \end{pmatrix} \right], \quad (17)$$

where d_{eff} is an effective distance between the metal strips on each SRR.[5,6] Clearly, this electric polarizability tensor is anisotropic and exhibits two resonances, at those frequencies where $Z_{11} - Z_{12} - Z_{13} + Z_{14} \approx 0$ or $Z_{11} - Z_{12} + 2Z_{13} - 2Z_{14} \approx 0$. Only the odd resonances of Table II appear in Eq. (17) because the excitation vector and the even eigenvectors are orthogonal, i.e., $\mathbf{F}_e \cdot \mathbf{v}_i^{even} = 0$ in Eq. (9).

In summary, it has been shown that the coupling between the faces of the CR made of Pendry's SRRs shown in Fig. 1(a) splits the original resonance of a single SRR in four new resonances. Besides, both magnetic and electric polarizability tensors are anisotropic, as can be seen from Eqs. (14) and (17). Finally, it is worth mentioning that the even modes can also be called magnetic modes because they have a resonant magnetic moment and can be only excited by an external magnetic field but not by an external electric field. Similarly, the odd modes are electric modes because they present a resonant electric dipole, which can be only excited by an external electric field. The reported conclusions are quite relevant for our analysis because they show that a cubic arrangement of Pendry's SRRs will not be only anisotropic but it will also show several different resonances around the isolated SRR resonance, thus destroying any possibility of a single-resonance Lorentzian behavior of the metamaterial.

B. Analysis of an isotropic cube

It was already shown in Sec. II B that, in order to ensure an isotropic behavior, the CR has to be invariant at least under the tetrahedron symmetry group $T = \{\langle \mathbf{1}, \mathbf{4}_x \cdot \mathbf{4}_y, \mathbf{4}_y \cdot \mathbf{4}_x \rangle\}$. The T-CR shown in Fig. 1(c), made of six NB-SRRs,[8,13] is a good example of particle obeying this symmetry. By using the symmetry transformations and the rule [Eq. (5)], its impedance matrix can be significantly reduced to

$$\mathbf{Z} = \begin{bmatrix} Z_{11} & Z_{12} & Z_{13} & -Z_{13} & Z_{13} & -Z_{13} \\ Z_{12} & Z_{11} & -Z_{13} & Z_{13} & -Z_{13} & Z_{13} \\ Z_{13} & -Z_{13} & Z_{11} & Z_{12} & Z_{13} & -Z_{13} \\ -Z_{13} & Z_{13} & Z_{12} & Z_{11} & -Z_{13} & Z_{13} \\ Z_{13} & -Z_{13} & Z_{13} & -Z_{13} & Z_{11} & Z_{12} \\ -Z_{13} & Z_{13} & -Z_{13} & Z_{13} & Z_{12} & Z_{11} \end{bmatrix}, \quad (18)$$

where there are just three independent components. All eigenvalues and a complete set of orthonormal eigenvectors of

TABLE III. Eigenvalues and a complete set of orthonormal eigenvectors of the impedance matrix [Eq. (18)] corresponding to isotropic cubic resonators symmetric under the tetrahedron group $T=\{\langle \mathbf{1}, \mathbf{4}_x \cdot \mathbf{4}_y, \mathbf{4}_y \cdot \mathbf{4}_x \rangle\}$, as, for instance, the structure shown in Fig. 1(c).

	Eigenvalues z_i	Eigenvectors $\mathbf{v}_i$
Even modes	$Z_{11}+Z_{12}$	$\frac{1}{\sqrt{2}}(0,0,1,1,0,0)$
		$\frac{1}{\sqrt{2}}(0,0,0,0,1,1)$
		$\frac{1}{\sqrt{2}}(1,1,0,0,0,0)$
Odd modes	$Z_{11}-Z_{12}-2Z_{13}$	$\frac{1}{2\sqrt{3}}(1,-1,-2,2,1,-1)$
		$\frac{1}{2}(1,-1,0,0,-1,1)$
	$Z_{11}-Z_{12}+4Z_{13}$	$\frac{1}{\sqrt{6}}(-1,1,-1,1,-1,1)$

this matrix are shown in Table III. If we compare Tables III and II, we immediately find some similarities. In both cases, the eigenvectors can be classified into even and odd types, and the eigenvalues in Table III can be obtained from those of Table II by making $Z_{14}=-Z_{13}$. Furthermore, the odd and even subspaces are kept, and only the two subspaces of the even eigenvectors are unified into a single subspace due to the eigenvalue degeneration induced by the additional rotation symmetry $\mathbf{4}_x \cdot \mathbf{4}_y$.

Let us now analyze the resonances and polarizabilities of the T-CR by following the procedure developed in the previous subsection. By considering a homogeneous external magnetic excitation, the corresponding excitation vector [Eq. (13)] can only excite the even modes, thus leading to the isotropic magnetic polarizability tensor

$$\boldsymbol{\alpha}^{mm} = \frac{-2j\omega A^2}{Z_{11}+Z_{12}} \begin{bmatrix} 1 & 0 & 0 \\ 0 & 1 & 0 \\ 0 & 0 & 1 \end{bmatrix}, \quad (19)$$

which, in fact, corresponds to the substitution $Z_{14}=-Z_{13}$ in Eq. (14). The self-impedance in Eq. (19) is given by $Z_{11}=R+j\omega L+(j\omega C)^{-1}$, with R, L, and C being the resistance, self-inductance, and self-capacitance of a single NB-SRR.[8] The mutual impedance in Eq. (19) can be approached as $Z_{12}\approx j\omega M_{12}$, where M_{12} is the mutual inductance between two NB-SRRs placed on opposite sides of the CR. This approximation is reasonable since the electric field is concentrated inside the gap of the NB-SRR, while the magnetic field created by a NB-SRR spreads out in space. Using these relations, the frequency of resonance of the CR can be cal-

culated as $\omega_{res}\approx[C(M_{12}+L)]^{-1/2}$, while the magnetic polarizability tensor takes the form

$$\boldsymbol{\alpha}^{mm} \approx \frac{2\omega^2 C A^2}{1-\omega^2(L+M_{12})C+j\omega RC} \begin{bmatrix} 1 & 0 & 0 \\ 0 & 1 & 0 \\ 0 & 0 & 1 \end{bmatrix}. \quad (20)$$

This formula shows a Lorentzian-like magnetic response, similar to that of the single planar NB-SRR but isotropic in three dimensions.

With regard to the behavior of the considered CR under an external electric excitation, since the NB-SRRs cannot be excited by an external electric field,[8] the present theory predicts the absence of any resonant response to this excitation (of course, the CR will exhibit a nonresonant electric polarizability due to the static electric moments induced on each ring, which is of no interest in the frame of the present discussion). However, experiments reported in Ref. 13 have shown that the considered CR exhibits a weak magnetoelectric coupling at the same resonant frequency, $\omega_{res}=[C(M_{12}+L)]^{-1/2}$, as in Eq. (20). Therefore, this phenomenon does not affect neither the isotropy nor the single-resonance behavior of the considered CR. Since the tetrahedron symmetry group, T, does not include the inversion transformation, this result is not forbidden for T-CRs. Although the origin of this effect will be qualitatively explained below in Sec. IV, it can be advanced that it is basically due to a second order electric interaction between SRRs, which is ignored in the equivalent circuit approximation developed in this section. Actually, the presence of this second order effect near the CR resonance shows how important the analysis of the spatial symmetries is in order to predict the behavior of metamaterial resonators: it seems that any effect not forbidden by symmetry will actually appear in practice, regardless of the equivalent circuit models. It is worth recalling here that this magnetoelectric coupling disappears if the T-CRs are arranged in an fcc lattice with $b=2a$, as explained at the end of Sec. II B.

IV. EXPERIMENTS

For the experimental verification of the theory developed in the previous sections, some anisotropic and isotropic CRs were manufactured. Each CR was inserted into a standard WR430 waveguide, as shown in Fig. 6. The testing procedure starts from the fact that the particle is isotropic if their polarizability tensors are invariant by any rotation. Therefore, all CRs were subjected to several rotations and the transmission coefficient through the waveguide was measured using a network analyzer HP-8510. If the measured CR were isotropic, then the measured transmission coefficient would remain invariant after rotations.

Namely, two anisotropic cubes made of Pendry's SRRs and omega particles and two isotropic cubes made of C_2-SRRs (actually NB-SRRs[8]) and C_4-SRRs (see insets in Fig. 7) were implemented. All SRRs were etched on Arlon 250-LX substrate with dielectric constant $\varepsilon_r=2.43$, loss tangent $\tan\delta<0.002$, and thickness $t=0.49$ mm. In order to check the similarity between the SRRs belonging to the same CR, their resonance frequencies were measured by placing
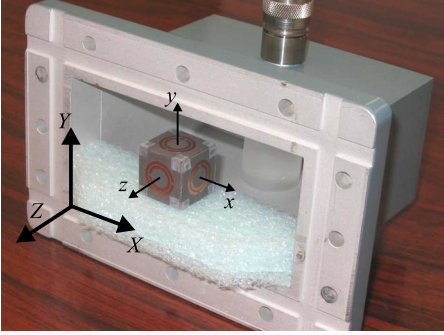
FIG. 6. (Color online) Experimental setup for checking the isotropy of cubic resonators. In the illustration, a cubic resonator made of Pendry's SRR is placed inside a pair of standard waveguide-coaxial transitions WR430 connected to a network analyzer HP-8510-B. The transversal dimensions of the waveguide are 109 $\times$ 55 mm^2 and its frequency range is 1.7–2.6 GHz. The cube is held by a piece of electromagnetically inert foam at an arbitrary orientation.

each one in the E plane of the waveguide, obtaining the following values: $f_0^{Pendry's\ SRR}=(2.321\pm0.002)$ GHz, $f_0^{\Omega}=(2.216\pm0.002)$ GHz, $f_0^{C4-SRR}=(2.399\pm0.001)$ GHz, and $f_0^{NB-SRR}=(2.385\pm0.002)$ GHz. These results show that significant deviations from these values (of more than 0.002 GHz) in the measured resonances of the transmission coefficients for the CRs must be interpreted as a resonance splitting due to SRR couplings, and not due to fabrication imprecision. The SRRs were assembled over a cube of isotropic dielectric (ROHACELL 71 HF, $\varepsilon_r=1.07$, $\tan\delta$ <0.0002) of size $2\times2\times2$ cm^3. More details on the preparation of the experiments are given in Ref. 41.

A. Anisotropic cubes

First, the CRs not satisfying the necessary spatial symmetries for isotropy were tested. Figure 7(a) shows the transmission coefficient through the waveguide loaded with the CR made of Pendry's SRRs. Two observations are apparent: there are three major resonance peaks and none of them stays invariant under rotations of the cube. Therefore, this CR is anisotropic, as theoretically predicted by the symmetry theory in Sec. II B. However, the circuit model developed in Sec. III A predicts the presence of four different resonances, but not three, as can be observed in Fig. 7(a). Although this fourth resonance is not clearly visible in Fig. 7(a), the dip at the lowest frequency is split into two dips for the other different orientation shown in Ref. 42, thus recovering the agreement with the theory. Furthermore, in Ref. 42, the nature of each resonance is identified as electric or magnetic.

The cube composed of omega particles was also experimentally tested. This cube has symmetry properties identical as the cube made of Pendry's SRR, i.e., it is invariant under the inversion and the rotation $\mathbf{4}_y\cdot\mathbf{4}_x$. The transmission coefficient for this measurement is depicted in Fig. 7(b), where similar results as for the SRR cube can be observed. Namely, the original resonance of a single omega particle now appears split in several resonances and the transmission coeffi-
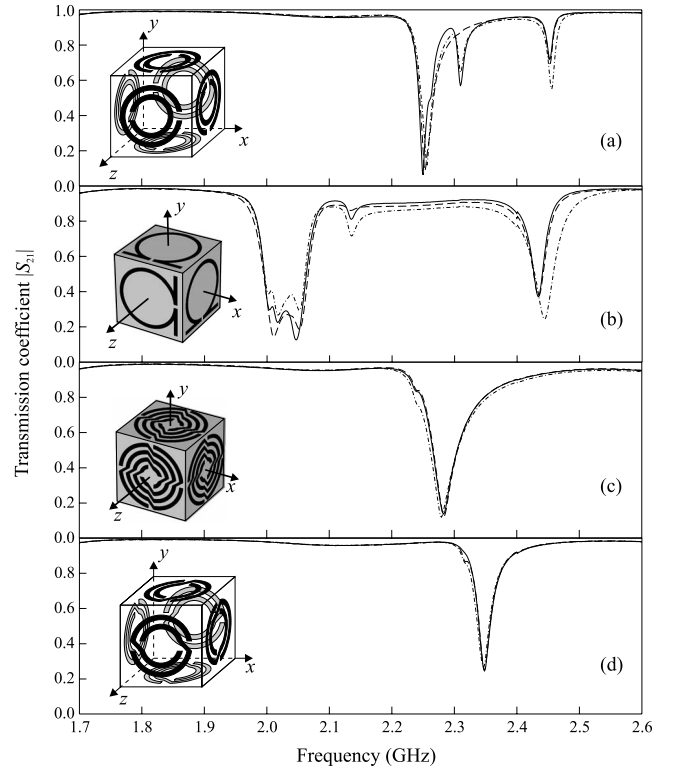

FIG. 7. Transmission coefficient ($|S_{21}|$) through a waveguide containing a cubic resonator made of (a) Pendry's SRRs, (b) Omega particles, (c) C_4-SRRs, or (d) C_2-SRRs (or NB-SRR). Solid line: the particle is oriented with its axes (x,y,z) parallel to the waveguide axes (X,Y,Z) shown in Fig. 6. Dashed line: the first orientation is rotated by 45° along the Y axis. Dash-dot line: the first orientation is rotated by 45° along the Z axis and 45° along the Y axis. The size of all cubes is $2\times2\times2$ cm^3. Dimensions of Pendry's SRRs: external radius $r_{ext}=7$ mm, width of the strip $w=1.25$ mm, distance between strips $d=0.5$ mm, and size of split gap $g=1$ mm. Dimensions of Ω: $r_{ext}=8.5$ mm, $w=1$ mm, $g=1$ mm, and the length of "legs" $l=8$ mm. Dimensions of C_4-SRR: $r_{ext}=9.25$ mm, $w=1.25$ mm, $d=0.5$ mm, and $g=1.5$ mm. Dimensions of C_2-SRR: external radius $r_{ext}=7$ mm, width of the strip $w=1.25$ mm, distance between strips $d=0.5$ mm, and size of split gap $g=1$ mm.

cient changes for different orientations. However, the number of resonance dips in Fig. 7(b) is 5 instead of 4, as previously predicted in Sec. III A. This failure of the model can be attributed to a strong electric coupling between the legs of two neighbors. In fact, it can be expected from the CR depicted in Fig. 7(b) that the electric field between legs of two omega particles on adjacent sides of the CR is comparable to the internal electric field in each omega particle. Thus, the CR should be seen as an inseparable particle instead of six RLC circuits, as assumed in Sec. III.

An important result of the reported measurements is that the relative frequency deviations between the different resonances of the CRs made of Pendry's SRRs and omega particles (10% or more with regard to the central frequency) are of the same order that the bandwidths reported for most SRR or omega based negative-μ metamaterials. Therefore, as advanced in Sec. III, it can be guessed that any metamaterial made from such configurations will show multiple reso-
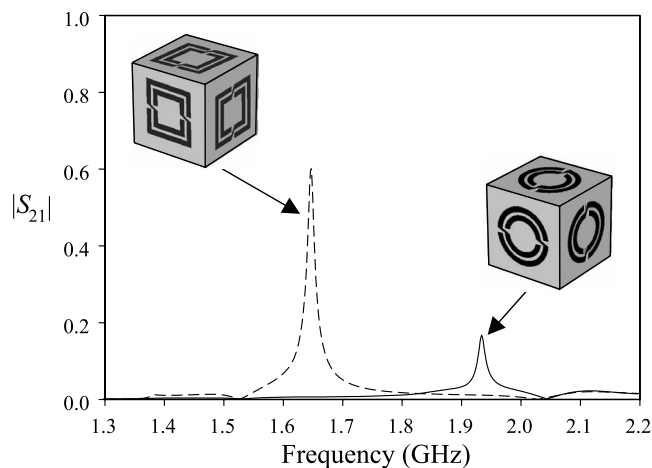
FIG. 8. Simulated transmission coefficient ($|S_{21}|$) through the cross polarization waveguide setup filled by T-CRs made of circular (solid line) and square NB-SRRs (dashed line). Dimensions of the circular NB-SRR: external diameter $2r_{ext}$=20 mm, width of the strip w=2 mm, distance between strips d=1 mm, and size of split gap g=1.6 mm. The square NB-SRRs have similar dimensions and the same external perimeter. Cube edge was 24 mm long.

nances inside the expected negative-μ frequency band, thus destroying any single-resonance Lorentzian behavior.

B. Isotropic cubes

In order to show the usefulness of spatial symmetries to provide isotropic resonators, the cubes made of C_4-SRRs and C_2-SRRs [see insets in Figs. 7(c) and 7(d)], satisfying the octahedron group O and the tetrahedron group T, respectively, have been tested. As shown in Sec. II B, both cubes are symmetric enough to be isotropic. The transmission coefficients for these CRs are shown in Figs. 7(c) and 7(d). It can be observed that the transmission does not depend on their orientations, thus demonstrating their isotropy. Besides, it can be seen that only one peak appear in both measurements, as predicted in Sec. III B. It is worth noting that a similar result will be obtained for any CR satisfying any one of the five cubic symmetry point groups (T, T_h, T_d, O, and O_h).

The cubes analyzed in this section have no inversion symmetry and, as mentioned at the end of Sec. III, they could exhibit a bi-isotropic behavior. However, from the experimental curves, it is impossible to see whether the analyzed CRs are bi-isotropic or not. To examine this possibility, electromagnetic simulations of a square waveguide loaded with T-CRs were made. The input port was fed by the TE_{10} mode, while the TE_{01} mode with orthogonal polarization was measured on the output port. The resulting cross-polarization transmission coefficient is shown in Fig. 8. The nonzero transmission means that the incident electric field can excite not only a parallel electric dipole but also a parallel magnetic dipole. From reciprocity, it is also clear that an incident magnetic field can excite both magnetic and electric dipoles parallel to the exciting field. This result clearly shows the bi-isotropic behavior of the C_2-SRR cube. In order to show that
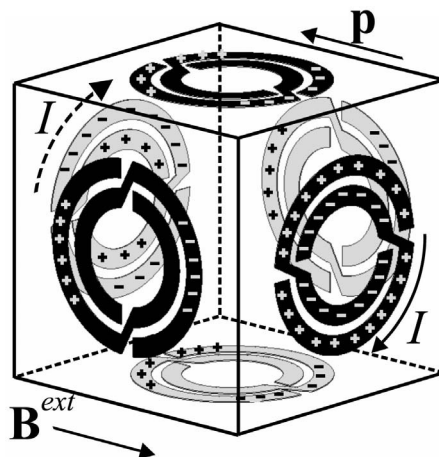

FIG. 9. Illustration of the bi-isotropic behavior of a T-CR made of NB-SRRs driven by an external magnetic field.

the bi-isotropy can be avoided by including the inversion symmetry in the configuration, a similar simulation was carried out for the T_h-CR shown in Fig. 1(d), already proposed in,[13] which possesses an inversion symmetry. The transmission coefficient, not depicted here, was almost zero and of the same order as the transmission through the waveguide without any resonator, thus showing that this last configuration is not bi-isotropic.

As already reported, the bi-isotropy of the T-CR cannot be explained by the circuit model proposed in Sec. III. The explanation of this effect seems to rely on the electric coupling between the edges of two SRR on adjacent faces of the cube. To understand this in a qualitative way, let us assume that the cube is driven by an external magnetic field feeding only two resonators in the cube, as shown in Fig. 9. This figure also depicts the current and corresponding charges induced by the external field on each NB-SRR. Due to the inversion symmetry of the NB-SRR, the electric dipole generated by the excited resonators is zero.[8] However, Fig. 9 also shows how the induced resonant charges polarize the other (not excited) rings. These are polarized in such a way that the CR acquires a net electric dipole, as sketched in the figure. This dipole does not excite an extra net current on the NB-SRR since the polarization charge symmetrically flows on both halves of the resonator. Therefore, this effect is not taken into account by the circuit model reported in Sec. III. However, it introduces a nonzero magnetoelectric polarizability that cannot be extracted from that model. According to the above explanation, it is expected that magnetoelectic coupling will increase if the electric coupling between the edges of neighboring resonators grows. To check this hypothesis, the cross-polarized transmission was also computed for square rings (see dashed line in Fig. 8). The enhancement of the magnetoelectric coupling can be clearly observed in this case.

At the end of Sec. II, it was mentioned that this bi-isotropic behavior would disappear in an fcc cubic lattice with b=$2a$ (see Fig. 3). In that section, this behavior was predicted on the basis of the particular symmetry of this specific lattice. The illustration in Fig. 9 of the bi-isotropy of an isolated CR made of six identical NB-SRRs also provides a qualitative physical interpretation of such result: if additional

SRRs were added to Fig. 9 in order to make an fcc cubic lattice, it becomes apparent that the induced charges on the nonresonant additional SRRs will cancel the total electric dipole shown in the figure.

V. CONCLUSIONS

A systematic approach to the design of isotropic magnetic metamaterials by using isotropic cubic magnetic resonators in a cubic lattice has been developed. For this purpose, cubic magnetic resonators obeying some cubic point groups of symmetry (T, T_d, T_h, O, or O_h) placed in cubic Bravais' lattice (sc, bcc, or fcc) were analyzed. Special care has been taken in the study of the symmetry of the constitutive elements (also called cubic resonators or CRs). For practical reasons, CRs made of six modified SRRs assembled over the surface of a cube were considered. The connection between the orientations of these SRRs over the cube and the cubic point groups of symmetry has been analyzed. Starting from this analysis, some particular examples of anisotropic and isotropic CRs were analyzed, manufactured, and measured. It was analytically and experimentally shown that the lack of the necessary symmetry leads to an anisotropic response. In experiments, the transmission through a waveguide loaded with the manufactured CRs was measured, getting a strong dependence of this parameter on the orientation for anisotropic CRs, while the transmission was invariant with respect to the orientation for isotropic CRs. Furthermore, the splitting of the isolated SRR resonances into several resonances was observed in anisotropic CRs. This effect is absent in isotropic CRs, which always show a single resonance. Most of these effects were theoretically explained by using an equivalent circuit model, which takes into account the electromagnetic couplings between the SRRs making the analyzed CRs.

From a practical standpoint, we have found that using some low symmetry CRs, pertaining to the tetrahedral group T or T_h, placed in a cubic Bravais lattice is enough to provide isotropy in three dimensions. Using CRs with lower symmetry results in an anisotropic behavior, even if the dipole representation of the SRRs suggests an isotropic behavior. In general, using cubic resonators pertaining to a symmetry group which does not include inversion (such as the symmetry group T) produces a bi-isotropic behavior, even if the isolated SRRs making the metamaterial do not present magnetoelectric coupling. However, this bi-isotropy can be avoided by a proper choice of the lattice. In particular, it has been shown that cubic resonators pertaining to the aforementioned T group placed in an fcc lattice with the appropriate periodicity can produce a purely magnetic isotropic behavior.

We hope that the reported results will pave the way to the design of isotropic three-dimensional periodic metamaterials with a resonant magnetic response, including negative permeability and left-handed metamaterials.

ACKNOWLEDGMENTS

APPENDIX: ELECTRIC EXCITATION OF THE CUBIC RESONATOR MADE OF PENDRY'S SPLIT RING RESONATOR

Let us assume a single SRR placed in the xy plane with its two slits along the x axis. The electromotive force can be approximated by averaging the path integral of the external electric field through the gap along the circumference of the particle, so that

$$\text{emf} = \langle \mathbf{E}^{ext} \cdot \mathbf{d}_{eff}(\varphi) \rangle = 2E_y^{ext} d_{eff} \frac{1}{\pi} \int_0^\pi \cos(\varphi - \pi/2) d\varphi$$

$$= \frac{4}{\pi} d_{eff} E_y^{ext}. \tag{A1}$$

It is worth noting that the two halves of the SRR are polarized in the same direction,[5,6] so that it justifies the factor 2 in front of the integral and its integration domain $(0, \pi)$. Now, let us generalize the electromotive force of Eq. (A1) to get the "excitation vector" for the CR made of Pendry's SRRs shown in Fig. 1(a). Taking into account the sketch of the excitation shown in Fig. 5, it easy to get the following electric excitation vector:

$$\mathbf{F}_e = \frac{4}{\pi} d_{eff}(E_z^{ext}, -E_z^{ext}, -E_x^{ext}, E_x^{ext}, -E_y^{ext}, E_y^{ext}). \tag{A2}$$

In what follows, for simplicity, the superscript ext will be avoided. By introducing Eq. (A2) in Eq. (9), we get the associated currents

$$
\begin{pmatrix} I_1 \\ I_2 \\ I_3 \\ I_4 \\ I_5 \\ I_6 \end{pmatrix} = \frac{\frac{4}{3\pi} d_{eff}}{Z_{11} - Z_{12} - Z_{13} + Z_{14}} \begin{pmatrix} E_x + E_y + 2E_z \\ -E_x - E_y - 2E_z \\ -2E_x + E_y - E_z \\ 2E_x - E_y + E_z \\ E_x - 2E_y - E_z \\ -E_x + 2E_y + E_z \end{pmatrix}
$$

$$
+ \frac{\frac{4}{3\pi} d_{eff}}{Z_{11} - Z_{12} + 2Z_{13} - 2Z_{14}} \begin{pmatrix} -E_x - E_y + E_z \\ E_x + E_y - E_z \\ -E_x - E_y + E_z \\ E_x + E_y - E_z \\ -E_x - E_y + E_z \\ E_x + E_y - E_z \end{pmatrix}.
$$

$$\tag{A3}$$

The electric dipole for a single SRR can be expressed in terms of a linear charge density λ as[5,6]

$$p_y = 2\lambda r_0 d_{eff} \int_0^\pi \cos(\varphi - \pi/2) d\varphi = 4\lambda r_0 d_{eff}, \quad \text{(A4)}$$

where d_{eff} is an effective distance between the two metallic strips forming the SRR. The charge density on the inner, I_i, and outer rings, I_o, of the SRR can be calculated by means of the charge conservation law as follows:

$$\frac{dI_{i,o}}{d\theta} = j\omega r \lambda_{i,0} \Rightarrow \lambda_{i,0} = \frac{1}{j\omega r} \frac{dI_{i,o}}{d\theta}. \quad \text{(A5)}$$

Since the SRR size is much smaller than one wavelength, we can suppose a linear variation of $I_{i,o}$ respect to the angle ϕ, taking its maximum value, I, at the center of the metal strip and zero at its ends, as in Refs. 4 and 5. Then,

$$|\lambda| = \frac{1}{j\omega r} \frac{|I|}{\pi}. \quad \text{(A6)}$$

Although I_i and I_o are not uniform through ϕ, the sum of both, $I_i + I_o$, is approximately constant and equal to the current I, which is actually the effective current associated with the averaged loop. By Eqs. (A4) and (A6), we obtain

$$|p_y| = \frac{4d_{eff}}{j\omega\pi}|I|. \quad \text{(A7)}$$

Now, we can calculate the total electric moment of the SRR cube by adding the six moments. By considering Eq. (A7) and taking into account the signs of the charges shown in Fig. 5, we obtain the electric dipole

$$\mathbf{p} = \frac{4d_{eff}}{j\omega\pi} \begin{pmatrix} I_3 - I_4 \\ I_5 - I_6 \\ I_2 - I_1 \end{pmatrix}. \quad \text{(A8)}$$

Finally, by substituting the currents of Eq. (A3) into Eq. (A8), we get the electric dipole in terms of the components of the external electric field,

$$\mathbf{p} = \frac{32d_{eff}^2}{3j\omega\pi^2} \left[\frac{1}{Z_{11} - Z_{12} - Z_{13} + Z_{14}} \begin{pmatrix} -2E_x + E_y - E_z \\ E_x - 2E_y - E_z \\ -E_x - E_y - 2E_z \end{pmatrix} \right.$$
$$\left. + \frac{1}{Z_{11} - Z_{12} + 2Z_{13} - 2Z_{14}} \begin{pmatrix} -E_x - E_y + E_z \\ -E_x - E_y + E_z \\ E_x + E_y - E_z \end{pmatrix} \right]. \quad \text{(A9)}$$

*juan_dbd@us.es

†l_jelinek@us.es

‡marques@us.es

[1] V. G. Veselago, Sov. Phys. Usp. **10**, 509 (1968).

[2] D. R. Smith, W. J. Padilla, D. C. Vier, S. C. Nemat-Naser, and S. Schultz, Phys. Rev. Lett. **84**, 4184 (2000).

[3] J. B. Pendry, A. J. Holden, D. J. Robbins, and W. J. Stewart, IEEE Trans. Microwave Theory Tech. **47**, 2075 (1999).

[4] W. Rotman, IRE Trans. Antennas Propag. **10**, 82 (1962).

[5] R. Marqués, F. Medina, and R. Rafii-El-Idrissi, Phys. Rev. B **65**, 144440 (2002).

[6] R. Marqués, F. Mesa, J. Martel, and F. Medina, IEEE Trans. Antennas Propag. **51**, 2572 (2003).

[7] J. D. Baena, R. Marqués, F. Medina, and J. Martel, Phys. Rev. B **69**, 014402 (2004).

[8] J. D. Baena, J. Bonache, F. Martín, R. Marqués, F. Falcone, T. Lopetegui, M. A. G. Laso, J. García-García, I. Gil, and M. Flores, IEEE Trans. Microwave Theory Tech. **53**, 1451 (2005).

[9] J. B. Pendry, Phys. Rev. Lett. **85**, 3966 (2000).

[10] A. L. Pokrovsky and A. L. Efros, Phys. Rev. Lett. **89**, 093901 (2002).

[11] R. Marques and D. R. Smith, Phys. Rev. Lett. **92**, 059401 (2004).

[12] P. Gay-Balmaz and O. J. F. Martin, Appl. Phys. Lett. **81**, 939 (2002).

[13] J. D. Baena, L. Jelinek, R. Marqués, and J. Zehentner, Appl. Phys. Lett. **88**, 134108 (2006).

[14] C. R. Simovski and S. He, Phys. Lett. A **311**, 254 (2003).

[15] C. R. Simovski and B. Sauviac, Radio Sci. **39**, RS2014 (2004).

[16] E. Verney, B. Sauviac, and C. R. Simovski, Phys. Lett. A **331**, 244 (2004).

[17] L. Jelinek, J. Zehentner, J. D. Baena, and R. Marqués, Proceedings of IEEE MELECON 2006, Benalmádena (Málaga), Spain, 16–19 May 2006, p. 250.

[18] Th. Koschny, L. Zhang, and C. M. Soukoulis, Phys. Rev. B **71**, 121103(R) (2005).

[19] W. J. Padilla, Opt. Express **15**, 1639 (2007).

[20] C. L. Holloway, E. F. Kuester, J. Baker-Jarvis, and P. A. Kabos, IEEE Trans. Antennas Propag. **51**, 2596 (2003).

[21] I. Vendik, O. Vendik, I. Kolmakov, and M. Odit, Opto-Electron. Rev. **14**, 179 (2006).

[22] G. V. Eleftheriades, A. K. Iyer, and P. C. Kremer, IEEE Trans. Microwave Theory Tech. **50**, 2702 (2002).

[23] W. J. R. Hoefer, P. P. M. So, D. Thompson, and M. Tentzeris, IEEE International Microwave Symposium Digest, Long Beach, CA, June 2005, pp. 313–316.

[24] A. Grbic and G. V. Eleftheriades, J. Appl. Phys. **98**, 043106 (2005).

[25] P. Alitalo, S. Maslovski, and S. Tretyakov, J. Appl. Phys. **99**, 064912 (2006).

[26] P. Alitalo, S. Maslovski, and S. Tretyakov, J. Appl. Phys. **99**, 124910 (2006).

[27] T. J. Yen, W. J. Padilla, N. Fang, D. C. Vier, D. R. Smith, J. B. Pendry, D. N. Basov, and X. Zhang, Science **303**, 1494 (2004).

[28] S. Linden, C. Enkrich, M. Wegener, J. Zhou, T. Koschny, and C. M. Soukoulis, Science **306**, 1351 (2004).

[29] S. A. Tretyakov, A. Sihvola, and L. Jylhä, Photonics Nanostruct. Fundam. Appl. **3**, 107 (2005).

[30] R. Marqués, L. Jelinek, and F. Mesa, Microwave Opt. Technol. Lett. **49**, 2606 (2007).

[31] I. V. Lindell, A. Sihvola, S. A. Tretyakov, and A. J. Viitanen, *Electromagnetic Waves in Chiral and Bi-Isotropic Media* (Artech House, Norwood, MA, 1994).

[32] N. W. Aschroft and N. D. Mermin, *Solid State Physics* (Holt, Rinehart and Winston, Philadelphia, 1976).

[33] J. F. Nye, *Physical Properties of Crystals: Their Representation by Tensors and Matrices* (Clarendon, Oxford, 1993).

[34] A. Sihvola, *Electromagnetic Mixing Formulas and Applications* (The Institution of Electrical Engineers, London, 1999).

[35] M. M. I. Saadoun and N. Engheta, Microwave Opt. Technol. Lett. **5**, 184 (1992).

[36] J. García-García, F. Martín, J. D. Baena, R. Marqués, and L. Jelinek, J. Appl. Phys. **98**, 033103 (2005).

[37] S. O'Brien and J. B. Pendry, J. Phys.: Condens. Matter **14**, 6383 (2002).

[38] C. R. Simovski, S. A. Tretyakov, A. A. Sochava, B. Sauviac, F. Mariotte, and T. G. Kharina, J. Electromagn. Waves Appl. **11**, 1509 (1997).

[39] R. F. Harrington, *Time-Harmonic Electromagnetic Fields* (McGraw-Hill, New York, 1961), p. 119.

[40] P. Gay-Balmaz and O. J. F. Martin, J. Appl. Phys. **92**, 2929 (2002).

[41] See EPAPS Document No. E-PRBMDO-76-032744 for additional information about the "Preparation of experiments." For more information on EPAPS, see http://www.aip.org/pubservs/epaps.html.

[42] See EPAPS Document No. E-PRBMDO-76-032744 for additional information about the "Identification of the resonances of the Pendry's SRR-CR." For more information on EPAPS, see http://www.aip.org/pubservs/epaps.html.

Appendix 4

This appendix contains a full text of Ref. [22]

Analytical circuit model for split ring resonators in the far infrared and optical frequency range

V. Delgado [a], O. Sydoruk [b], E. Tatartschuk [b], R. Marqués [a,*], M.J. Freire [a], L. Jelinek [a]

[a] *Microwave Group, Dept. of Electronics and Electromagnetics, University of Seville, Facultad de Fisica,*
Avda. Reina Mercedes s/n, 41012 Sevilla, Spain
[b] *Erlangen Graduate School in Advanced Optical Technologies, University of Erlangen-Nuremberg,*
Paul-Gordan Str. 6, D-91052 Erlangen, Germany

Abstract

The article proposes an LC-circuit model for single split ring resonators (SRRs) operating at far infrared and optical frequencies. Taking the effects of magnetic and kinetic inductances as well as gap and surface capacitances into account, we obtain analytical expressions for the resonant frequency of the singly, doubly, and quadruply split SRRs. Comparing the analytical results with numerical simulations, we show that the numerical simulations agree better with the present model than with the models reported previously. We also discuss a size dependent correction to the electron collision frequency which takes into account electron collisions with SRR walls.
© 2009 Elsevier B.V. All rights reserved.

Since the seminal work of Pendry et al. [1] split ring resonators (SRRs) have been intensively used for the design of metamaterials from microwaves to terahertz frequencies [2]. Due to technological constraints, the original design evolved to a single ring design for operation in the far infrared [3] and, eventually, the optical range. SRRs have the intrinsic advantage of a potentially very small electrical size at resonance, provided a strong gap and surface capacitances (see below) can be technologically achieved. The main drawback of SRRs for operation at high frequencies (far infrared and optics) is the saturation of the frequency of resonance and the simultaneous decrease of polarizability [4]. The main

aim of this article is to develop an analytical model for the description of single ring SRRs operating at infrared and optical frequencies. This model will be useful as a first step in the design, in order to identify the most relevant physical effects at such frequencies, as well as to provide insight on the potentialities of single ring SRRs for operation in the aforementioned frequency range.

The single ring SRR is shown schematically in Fig. 1, where r is the mean radius, h is the height, w is the width, and g is the gap width. The resonant properties of a metallic SRR depend on its geometry and the complex permittivity of the metal. At high frequencies, the permittivity of bulk metals is commonly approximated by a Drude model

$$\tilde{\epsilon} = \epsilon_0 \left[\epsilon_i^{(0)} - \frac{\omega_p^2}{\omega(\omega - jf_c^{(0)})} \right], \tag{1}$$
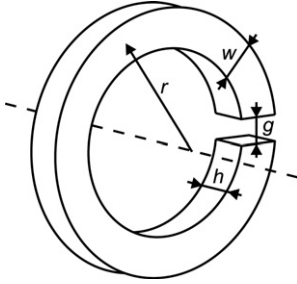
Fig. 1. Geometry of the singly split single SRR.

where $\epsilon_i^{(0)}$ is the background permittivity of the ions, ω_{p} is the plasma frequency, and $f_{\mathrm{c}}^{(0)}$ is the electron collision frequency. These parameters have a well defined physical meaning and are often assumed to be independent of frequency. However, actual behavior of the permittivity can substantially deviate from this model. These effects can be formally introduced in formula (1) by means of a phenomenological frequency dependent background permittivity ϵ_i which includes effects such as the interband transitions of electrons [5,6], as well as a phenomenological frequency of electron collision f_{c}, which may differ from the generic values $\epsilon_i^{(0)}$ and $f_{\mathrm{c}}^{(0)}$, while being of the same order of magnitude. Furthermore, when SRR is scaled down for operation at far infrared and optical frequencies, its effective permittivity becomes substantially different from the bulk metal permittivity. Although this topic has been widely studied in the past (see, for instance [7] and references therein), these studies had small impact in metamaterial theory. In metamaterial context, these effects have been studied in [9] as applied to nanorods, some experimental observations were reported in [8] with regards to U-resonators, but have not been discussed specifically for SRRs. The dielectric permittivity of small size metamaterial particles depends on the size, shape, surface roughness, environment and polarization of incident light [9]. The classical approach for the analysis of the size and shape dependence of the permittivity assumes that the effective electron collision frequency must be corrected through the equation [10,11]:

$$f_{\mathrm{c}}' = f_{\mathrm{c}} + A \frac{v_{\mathrm{F}}}{L_{\mathrm{eff}}} \tag{2}$$

where A is a dimensionless parameter usually close to unity, v_{F} is the Fermi velocity and L_{eff} an effective mean free path which takes into account the size and shape of the particle. For spherical particles, both the classical and the quantum approaches confirm the general dependence $L_{\mathrm{eff}} \sim R$, where R is the radius of the sphere (see [11] and references therein). For particles of complex shape, such
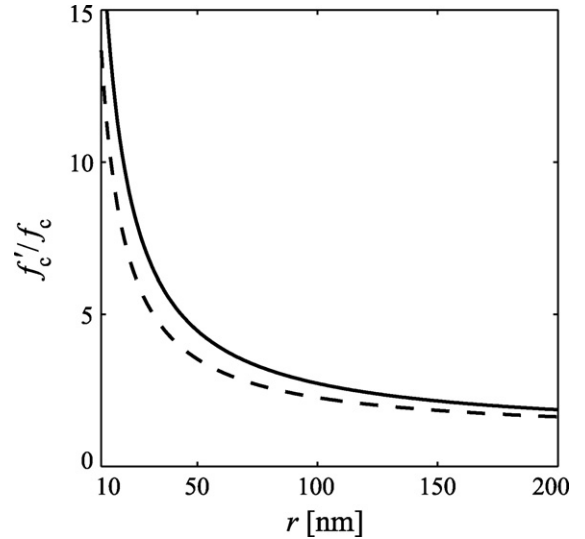
Fig. 2. Evolution of the effective electron collision frequency for a typical SRR as a function of the SRR size. The rings are made of gold (dashed line) and silver (solid line).

as the SRR, rigorous analysis is more involved and yields the expression:

$$L_{\mathrm{eff}} = \frac{4V}{S}, \tag{3}$$

where V is the volume of the particle, and S is the area of its surface [11]. Using this equation, and considering the SRR as made of a metallic wire of cross section $w \times h$ and length $2\pi r \gg w, h$ we obtain the size-dependent correction to the electron collision frequency in the form

$$f_{\mathrm{c}}' \approx f_{\mathrm{c}} + A v_{\mathrm{F}} \left(\frac{1}{2w} + \frac{1}{2h} \right)$$

$$= v_{\mathrm{F}} \left(\frac{1}{l_{\mathrm{e}}} + \frac{A}{2w} + \frac{A}{2h} \right) \tag{4}$$

where l_{e} the mean free path of electrons in the unbounded metal. In Fig. 2 the correction to the collision frequency for SRRs made of silver and gold is plotted against the SRR radius for $w = h = 0.3r$, which may be considered a reasonable aspect ratio. In this figure it has been assumed that $A = 1$ and that the frequency of collision and the mean free path are given by its low frequency values, i.e. $f_{\mathrm{c}} = f_{\mathrm{c}}^{(0)} = 27.3\,\mathrm{THz}$, $l_{\mathrm{e}} = l_{\mathrm{e}}^{(0)} = 52\,\mathrm{nm}$ for silver, and $f_{\mathrm{c}} = f_{\mathrm{c}}^{(0)} = 40.8\,\mathrm{THz}$, $l_{\mathrm{e}} = l_{\mathrm{e}}^{(0)} = 38\,\mathrm{nm}$ for gold. Fig. 2 shows that the frequency of collision grows dramatically for particle radius below $100\,\mathrm{nm}$ (i.e. for wire sections roughly of the same order as the mean free path of electrons). For larger sizes this effect is less important. There are other effects that may affect the effective frequency of collision of metamaterial ele-

ments, such as the aforementioned interband transitions, surface roughness and matrix environment (see, e.g. [9] and references therein). However, the size, and shape effects summarized in Eq. (2) usually outweigh all other factors when the structural details of the particle become smaller than the mean free path of electrons [11].

Once the frequency, size and shape dependence of the metal permittivity has been discussed, our aim is to develop an analytical circuit model for the SRR, including all relevant effects at far infrared and optical frequencies. Specifically, we will develop a closed expression for the resonant frequency of the SRR. When the dimensions of the ring's cross section approach the plasma wavelength (also tens of nanometers for most metals), inertia of conduction electrons becomes important. The inertia can be characterized by a kinetic inductance [12,13]. The kinetic inductance scales as $1/r$, whereas the magnetic inductance scales as r. For small rings, the kinetic inductance dominates over the magnetic one, and the resonant frequency of the SRR becomes independent of its size [4]. To explain the saturation of the resonant frequency of the SRRs at optical frequencies, several LC circuit models have been proposed that included the kinetic inductance in addition to the magnetic inductance and the gap capacitance [4,14,15]. The latter characterizes the parallel-plate capacitor formed by the gap. The charges in the gap, however, are not the sole source of the ring's capacitance. The charges on the ring's surfaces will also play a role. A recent study [16] took these charges into account by introducing a surface capacitance in addition to the gap capacitance. At microwave frequencies, the surface capacitance can significantly contribute to the resonant frequency of the single SRR. The question that arises now is whether the surface capacitance also plays a role at optical frequencies, and, still more important, whether the addition of this effect is enough to accurately characterize the behavior of the SRR. To answer this question, we obtain in this article an analytical expression for the resonant frequency of the SRRs taking into account all four contributions: the kinetic and magnetic inductance and the gap and surface capacitance. We will show that including the surface capacitance significantly improves the agreement between the analytical results and numerical simulations. Subsequently, we will further extend this analysis to doubly and quadruply split rings.

At far infrared and optical frequencies, we can still assume that $|\tilde{\epsilon}| \gg \epsilon_0\epsilon_i$, see Eq. (1). From the continuity of the normal component of $\mathbf{D} = j\omega\tilde{\epsilon}\mathbf{E}$ at metal–air interfaces follows that the electric field lines are strongly confined inside the ring. Therefore, we can define a total current inside the ring as $I_t \approx j\omega\tilde{\epsilon}E_r S$, where E_r is the

electric field inside the ring, and S is the area of the ring's cross section. This current includes both conduction and displacement currents and, due to the confinement effect, is approximately uniform along the ring (provided that the gap is small relative to the ring's circumference: $g \ll 2\pi r$). We can, therefore, take the magnetic inductance as that of a closed ring with the mean radius r (see, e.g. Ref [17])

$$L_{\mathrm{mag}} = \mu_0 r \left[\log \frac{8r}{h+w} - \frac{1}{2} \right]. \tag{5}$$

Because the electric field is well confined inside the ring, it has mainly the azimuthal component. Therefore, taking Eq. (1) into account, the electromotive force along the ring can be approximated by

$$\mathcal{E} = \oint \mathbf{E}d\mathbf{l} \approx \left(j\omega L_{\mathrm{kin}} + \frac{1}{j\omega C} + R \right) I_{\mathrm{t}}, \tag{6}$$

where L_{kin} the kinetic inductance, C is the total capacitance of the SRR, which includes both the gap and the surface capacitances, and R is the ohmic resistance of the ring. Because the SRR radiates, the total resistance of the ring is the contribution of ohmic and radiation losses. However, in bulk metamaterials the radiation resistance of the elements does not play a significant role due to the cancellation between the radiation fields of the different metamaterial elements. Therefore, we are only interested in the correction to ohmic losses and we will not take care of radiation losses. The ring ohmic resistance can be approximated by

$$R = \frac{(2\pi r - g)f_{\mathrm{c}}'}{S\omega_{\mathrm{p}}^2\varepsilon_0}, \tag{7}$$

and the kinetic inductance by [13]

$$L_{\mathrm{kin}} = \frac{(2\pi r - g)}{S\omega_p^2\varepsilon_0}. \tag{8}$$

As shown in Ref. [16], the total capacitance of the SRR can be presented as a sum of the gap, C_{gap}, and the surface, C_{surf}, capacitances

$$C_{\mathrm{gap}} = \varepsilon_0 \frac{hw}{g} + \varepsilon_0(h+g+w) \tag{9}$$

and

$$C_{\mathrm{surf}} = \frac{2\varepsilon_0(h+w)}{\pi} \log \frac{4r}{g}. \tag{10}$$

The final expression for the total current inside the ring is

$$\left[j\omega(L_{\text{mag}} + L_{\text{kin}}) + \frac{1}{j\omega(C_{\text{gap}} + C_{\text{surf}})} + R \right] I_t$$
$$= -j\omega\Phi_{\text{ext}} \tag{11}$$

where Φ_{ext} is the external axial magnetic flux through the SRR, and the term $j\omega L_{\text{mag}} I_t$ accounts for the internal magnetic flux through the SRR. The resonant frequency is

$$\omega_0 = \frac{1}{\sqrt{(L_{\text{mag}} + L_{\text{kin}})(C_{\text{gap}} + C_{\text{surf}})}}. \tag{12}$$

At optical frequencies, both the magnetic and kinetic inductances should be taken into account. However, when the ring is sufficiently small, the kinetic inductance dominates, and the resonant frequency saturates to the value

$$\omega_s \approx \frac{1}{\sqrt{L_{\text{kin}}(C_{\text{gap}} + C_{\text{surf}})}}. \tag{13}$$

In Fig. 3 the analytically calculated values of the resonant frequency, Eq. (12), are compared with CST simulations for two different geometries. Since $f_c^{(0)} \ll \omega/2\pi$ in the frequency range of interest, the permittivity of aluminum is mainly real. Therefore, it is not expected that the corrections to the frequency of collisions will considerably affect the resonant frequency of the SRR. Nevertheless, in order to be sure of this assumption, the simulated data were obtained using the low frequency collision frequency $f_c^{(0)} = 121.9$ THz, the corrected frequency of collision given by Eq. (4), and three times this value[1] without obtaining any meaningful deviation between them. As seen from Fig. 3, the agreement between the analytical and numerical results is much better when the surface capacitance is taken into account. For the rings of Fig. 3a, the mean difference between the analytical and numerical calculations is 55% without the surface capacitance and 13% with the surface capacitance. For the rings of Fig. 3b, the difference between the analytical and numerical results is 59% without the surface capacitance and 8% with the surface capacitance. Therefore, including the surface capacitance in the model improves considerably the agreement between the analytical and numerical results. The importance of the surface capacitance at optical frequencies is also confirmed by the numerical simulations of the ring's electric field distribution near the resonance. As shown in Fig. 4 for the ring with $r = 40$ nm, the electric field is strong

Fig. 3. Scaling of the resonant frequency of singly split SRRs: analytical calculations with the surface capacitance (solid line), without the surface capacitance (dashed line), and numerical simulations (circles). The analytical results agree much better with the numerical simulations when the surface capacitance is taken into account. The parameters are $\omega_p = 2\pi \cdot 3570$ THz and $f_c^{(0)} = 121.9$ THz; (a) $w = h = 0.3r$, $g = 0.1r$ and (b) $w = 0.1r$, $h = r$, $g = 0.1r$.

Fig. 4. Electric field distribution provided by CST simulation. The field is confined in and around the gap.

---

[1] Note that for aluminum, internal photoelectric effect occurs at wavelengths below 8 μm (see Ref. [5,6]). This requires an additional correction to calculate the dissipation properly.
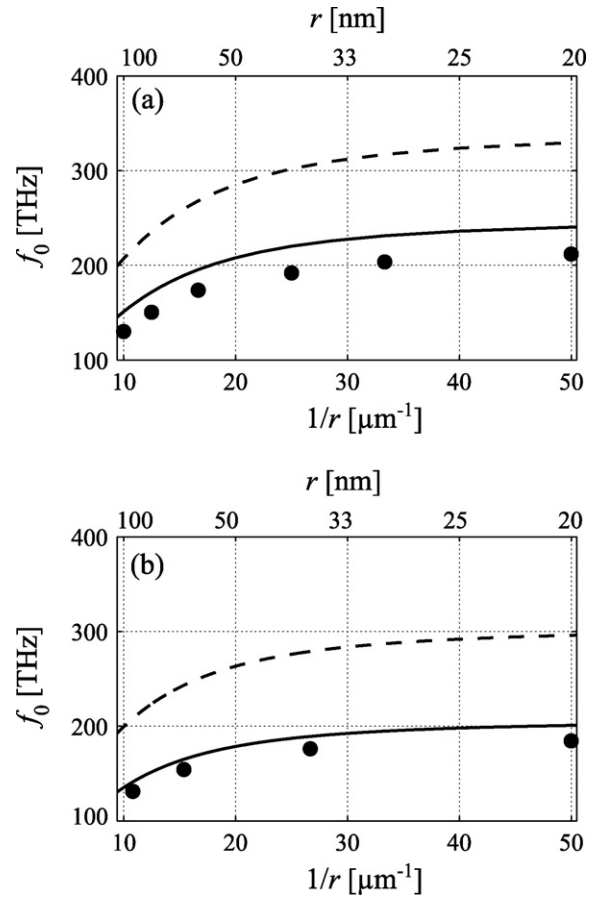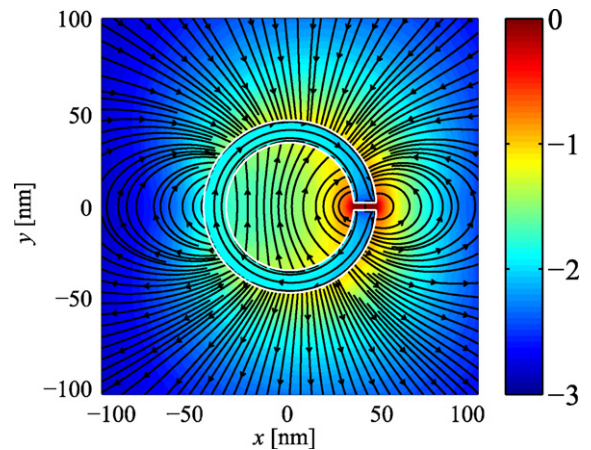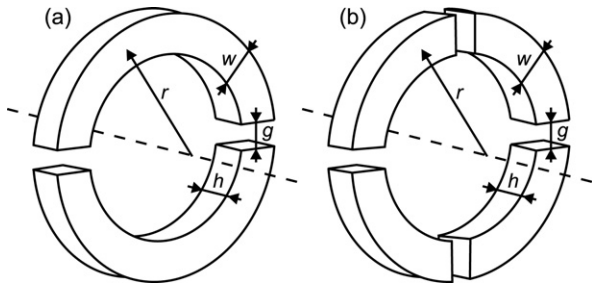
Fig. 5. Geometry of the doubly (a) and quadruply (b) split resonators.

outside the gap. This effect is taken into account by the surface capacitance.

The agreement between the numerical calculations and the analytical model with the surface capacitance is surprisingly good taking into account the nature of the approximations used to derive the expression for the surface capacitance, Eq. (10). This expression was obtained in Ref. [16] from analytical expressions for the voltage and surface charge distributions of an infinitely long thin cylinder with an infinitesimal gap [18]. It was further assumed that the surface charge distribution will be the same for a finite SRR if the SRR is sufficiently high. As can be seen in Fig. 3, the analytical results agree better with the numerical simulations for the higher and thinner ring.[2]

The expression for the surface capacitance derived in Ref. [16] is for singly split SRRs. In this paper, we extend the model by deriving expressions for the resonant frequency of doubly and quadruply split rings shown in Fig. 5. Multiply split rings, due to their high symmetry, could be used to mitigate bi-anisotropic effects [13]. As previously, we assume that the width of the gaps is small comparable to the rings' circumference. Consequently, both the magnetic and the kinetic inductances are the same as for the singly split rings, Eqs. (5) and (8). Similarly, the gap capacitance of each gap is the same as for the singly split rings, Eq. (9). The surface capacitance is, however, different. Taking the expressions for the electric field distributions of multiply split cylinders from Ref. [18] and following the approach of Ref. [16], we can derive the expressions for the surface capacitances associated with each gap of a multiply split SRR. For the doubly split rings, we obtain

$$C_{\text{surf}}^{(2\,\text{gap})} = \frac{2\varepsilon_0(h+w)}{\pi} \, \log \frac{2r}{g}, \tag{14}$$

────────
[2] Note that another contribution to the capacitance has been recently considered for SRRs at optical frequencies [19]. For the rings considered here, we found, however, that including this capacitance in the model lead to insignificant changes in the resonant frequency.
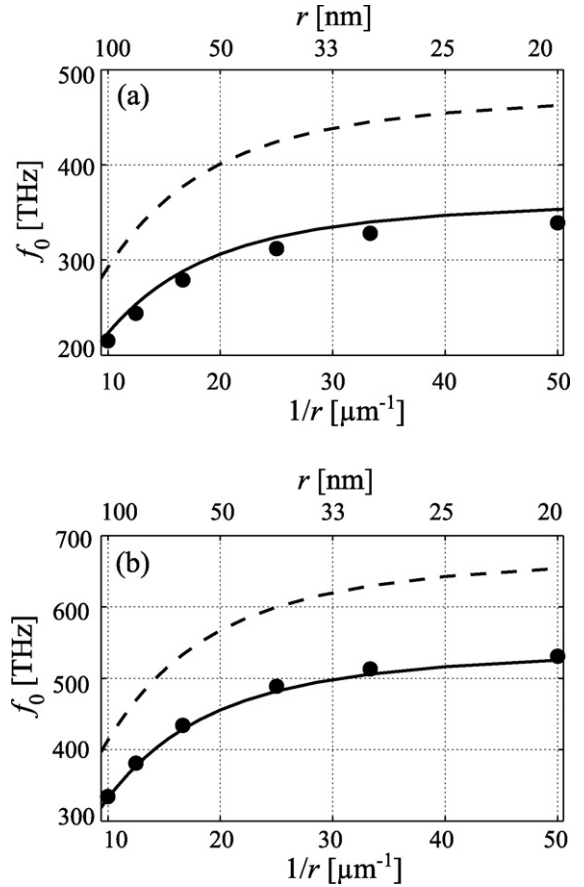
Fig. 6. Scaling of the resonant frequency of doubly (a) and quadruply (b) split SRRs: analytical calculations with the surface capacitance (solid line), without the surface capacitance (dashed line), and numerical simulations (circles). The parameters are $\omega_p = 2\pi \cdot 3570$ THz and $f_c = 121.9$ THz; $w = h = 0.3r$, $g = 0.1r$.

and for the quadruply split rings, we obtain

$$C_{\text{surf}}^{(4\,\text{gap})} = \frac{2\varepsilon_0(h+w)}{\pi} \, \log \frac{r}{g}. \tag{15}$$

The gap and surface capacitances associated with each gap are connected in series, so that the total capacitance of the doubly split SRR is

$$C_{\text{total}}^{(2\,\text{gap})} = \frac{C_{\text{gap}} + C_{\text{surf}}^{(2\,\text{gap})}}{2}. \tag{16}$$

The total capacitance of the quadruply split ring is

$$C_{\text{total}}^{(4\,\text{gap})} = \frac{C_{\text{gap}} + C_{\text{surf}}^{(4\,\text{gap})}}{4}. \tag{17}$$

To check the predictions of the analytical model, we performed numerical simulations. The results are shown in Fig. 6a for a doubly split SRR, and in Fig. 6b for a quadruply split SRR. Analogously to the singly split rings, including the surface capacitance improves

greatly the agreement between the numerical and analytical results. In fact, the difference between the analytical and numerical results for the quadruply split rings is only 1% when the surface capacitance is taken into account, whereas it is about 24% when the surface capacitance is ignored.

In summary, we have developed an analytical circuit model which takes into account the most relevant effects in single ring SRRs at far infrared and optical frequencies, including size and shape dependence of the metal permittivity, kinetic and magnetic inductances, and surface and gap capacitances. We have obtained simple analytical expressions for all these quantities for singly, doubly and quadruply split SRRs, and it has been shown that including these expressions in the model improves greatly the agreement between analytical results and numerical simulations. The accuracy of our model in determining the resonant frequency of SRRs is typically around a 10%.

Acknowledgements

References

[1] J.B. Pendry, A.J. Holden, D.J. Robbins, W.J. Stewart, Magnetism from conductors and enhanced nonlinear phenomena, IEEE Trans. Microwave Theory Tech. 47 (1999) 2075–2084.

[2] T.J. Yen, W.J. Padilla, N. Fang, D.C. Vier, D.R. Smith, J.B. Pendry, D.N. Basov, X. Zhang, Terahertz magnetic response from artificial materials, Science 303 (5663) (2004) 1494–1496.

[3] S. Linden, C. Enkrich, M. Wegener, J. Zhou, T. Koschny, C.M. Soukoulis, Magnetic response of metamaterials at 100 THz, Science 306 (2004) 1351–1353.

[4] J. Zhou, T. Koschny, M. Kafesaki, E.N. Economou, J.B. Pendry, C.M. Soukoulis, Saturation of the magnetic response of split-ring-resonators at optical frequencies, Phys. Rev. Lett. 95 (2005) 223902.

[5] R.B. Dingle, The anomalous skin effect and the reflectivity of metals: comparison between theoretical and experimental optical properties, Physica 19 (1953) 348.

[6] M.A. Ordal, et al., Optical properties of the metals Al, Co, Cu, Au, Fe, Pb, Ni, Pd, Pt, Ag, Ti, and W in the infrared and far infrared, Appl. Opt. 22 (1983) 1099.

[7] U. Kreibig, M. Vollmer, Optical Properties of Metal Clusters, Springer-Verlag, Berlin, Heidelberg, 1995.

[8] H. Guo, N. Liu, L. Fu, H. Schweizer, S. Kaiser, H. Giessen, Thickness dependence of the optical properties of split-ring resonator metamaterials, Phys. Status Solidi B 244 (2007) 1256–1261.

[9] V.P. Drachev, U.K. Chettiar, A.V. Kildishev, H.-K. Yuan, W. Cai, V.M. Shalaev, The Ag dielectric function in plasmonic metamaterials, Opt. Express 16 (2008) 1186.

[10] L. Genzel, T.P. Martin, U. Kreibig, Dielectric function and plasma resonances of small metal particles, Z. Phys. B 21 (1975) 339–346.

[11] E.A. Coronado, G.C. Schatz, Surface plasmon broadening for arbitrary shape nanoparticles: a probability approach, J. Chem. Phys. 119 (2003) 3926–3934.

[12] L. Solymar, Lectures on Electromagnetic Theory, Oxford University Press, Oxford, 1984 (Section 4.4).

[13] R. Marques, F. Martin, M. Sorolla, Metamaterials with Negative Parameters: Theory, Design and Microwave Applications, John Wiley and Sons Inc., New York, 2008.

[14] M.W. Klein, C. Enkrich, M. Wegener, C.M. Soukoulis, S. Linden, Single-slit split-ring resonators at optical frequencies: limits of size scaling, Opt. Lett. 31 (2006) 1259–1261.

[15] R. Marques, M. Freire, On the usefulness of split ring resonators for magnetic metamaterial design at infrared and optical frequencies, in: IEEE MELECON, Benalmadena (Malaga), Spain, 2005, pp. 222–224.

[16] O. Sydoruk, E. Tatartschuk, E. Shamonina, L. Solymar, Analytical formulation for the resonant frequency of split rings, J. Appl. Phys. 105 (2009) 014903.

[17] F.W. Grover, Inductance Calculations: Working Formulas and Tables, Instrument Society of America, Research Triangle Park, NC, 1981.

[18] J.E. Allen, S.E. Segre, Electric field in single-turn and multi-sector coils, Nuov. Cim. 21 (1961) 980–987.

[19] S. Tretyakov, On geometrical scaling of split-ring and double-bar resonators at optical frequencies, Metamaterials 1 (2007) 40–43.

Appendix 5

This appendix contains a full text of Ref. [24]

Artificial magnetism and left-handed media from dielectric rings and rods

L Jelinek[1,2] **and R Marqués**[2]

[1] Department of Electromagnetic Field, Czech Technical University in Prague, 166 27-Prague,
Czech Republic
[2] Departamento de Electrónica y Electromagnetismo, Universidad de Sevilla, 41012-Sevilla,
Spain

E-mail: l_jelinek@us.es

Abstract
It is shown that artificial magnetism with relatively large frequency bandwidth can be obtained
from periodic arrangements of dielectric rings. Combined with dielectric rods, dielectric rings
can provide 3D isotropic left-handed metamaterials which are an advantageous alternative to
metallic split ring resonators (SRRs) and/or metallic wires when undetectability by low
frequency external magnetic fields is desired. Furthermore it is shown that, unlike conventional
SRRs, dielectric rings can also be combined with natural plasma-like media to obtain a
left-handed metamaterial.

1. Introduction

Metamaterials, that is, artificial effective media with properties not found in Nature, such as negative magnetic permeability and/or permittivity, have recently been the subject of a big wave of scientific interest due to the unique new physical properties and promising applications (see, e.g., [1] and references therein). For the present state of the art, the most common way to artificial magnetism uses metallic rings loaded either with a lumped capacitor [2] or with a distributed capacitance [3]. This last configuration—the so called split ring resonator (SRR)—is by far the most common configuration due to its easy manufacturing by means of standard photo-etching techniques.

There can be, however, other possibilities for obtaining artificial magnetism, and, in particular, intensive research has been recently aimed at the substitution of metallic particles by purely dielectric resonators in order to reduce losses and/or minimize interactions with low frequency external magnetic fields. The overwhelming majority of these dielectric resonators are based on Mie resonances of variously shaped dielectric/plasmonic bodies such as long cylinders [4–6], cubes [7–9] and spheres [10–15].

Throughout this paper we will show that uniform dielectric rings (DRs) present unconventional LC quasi-static magnetic resonances, which can be advantageously used in the design of negative permeability effective media. It will

also be shown that connected networks of dielectric rods (DRos) can be used for the design of negative permittivity media, and that a combination of the two designs provides a left-handed behavior. The advantages of these approaches over conventional designs using dynamic Mie resonances will be discussed. The paper is organized as follows. First it will be shown that high permittivity DRs present magnetic resonances that can be described using an LC quasi-static model, in a rather similar way to that for capacitively loaded rings and/or SRRs. Then, the usefulness of these resonances for the design of negative permeability effective media will be proven and discussed. The possibility of designing left-handed metamaterials by combining DRs with other elements will also be investigated. In particular, it will be shown that combinations of DRs with a network of connected DRos, similar to conventional combinations of SRRs and wires, can provide a left-handed behavior. Finally, the effective medium properties of a combination of DRs with natural plasma-like media will be analyzed.

2. The dielectric ring

To show the principle of operation of the DR, let us assume a ring of mean radius a made of a 'dielectric wire' of radius b, as sketched in figure 1(a). Let the permittivity of the ring be $\varepsilon = \varepsilon'(1 + i \tan \delta)$ and let the ring be placed in a
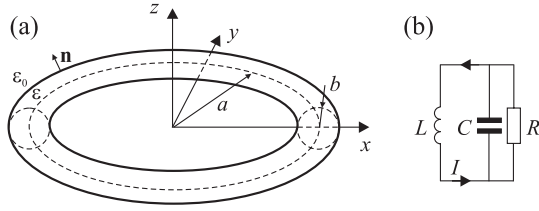
Figure 1. (a) Sketch of the proposed dielectric particle.
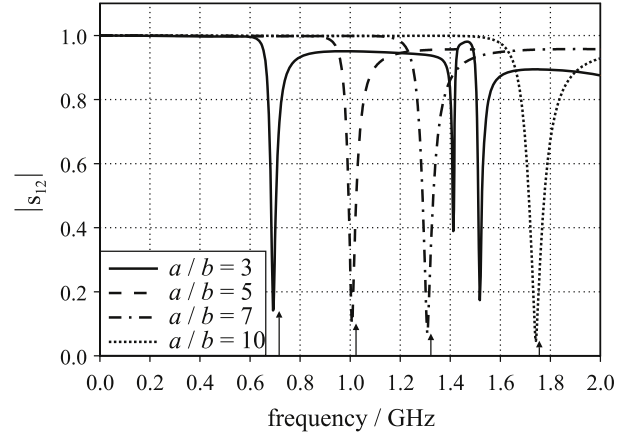(b) Equivalent circuit model.

Figure 2. Transmittances through a square TEM waveguide of lateral size $4a$ loaded with a dielectric ring resonator with $a = 15$ mm and $\epsilon_r = 250$ for several a/b ratios. Curves come from numerical simulations. Arrows show the resonances predicted from the reported analytical model.

homogeneous time varying magnetic field directed along the ring axis. For high enough permittivities, ε, it can be assumed that the electric field is strongly confined inside the ring due to the boundary condition $\mathbf{E} \cdot \mathbf{n} = \varepsilon_0/\varepsilon \mathbf{E}_0 \cdot \mathbf{n} \approx 0$ (see figure 1(a)). Therefore, assuming a uniform distribution of the electric field inside the ring, an axial magnetic field will induce an uniform displacement current in the ring given by

$$I = -i\omega\varepsilon A E_\varphi, \tag{1}$$

where $A = \pi b^2$ is the cross-section of the wire and E_φ is the angular component of the electric field, which can be determined from Faraday's law:

$$2\pi a E_\varphi = i\omega(\phi^{\text{int}} + \phi^{\text{ext}}), \tag{2}$$

where $\phi^{\text{int}} = LI$ is the internal magnetic flux due to the self-inductance of the ring and ϕ^{ext} is the external driving magnetic flux. Substituting (1) into (2) we obtain

$$\left(\frac{2\pi a}{i\omega\varepsilon A} + i\omega L\right) I = -i\omega\phi^{\text{ext}}. \tag{3}$$

In (3) the first term in the bracket can be easily recognized as the impedance $Z = (1/R - i\omega C)^{-1}$ coming from the parallel combination of a capacitor C and a resistor R:

$$C = \frac{\varepsilon' A}{2\pi a}; \qquad R = \frac{2\pi a}{A\omega\varepsilon' \tan\delta} \tag{4}$$

which formally are the capacitance and the resistance of an ideal parallel plate capacitor of plate surface equal to the wire cross-section and the distance between plates equal to the circumference of the ring. Equation (3) leads to the equivalent circuit shown in figure 1(b), where L can be evaluated as [16]

$$L = \mu_0 a[\ln(8a/b) - 7/4]. \tag{5}$$

Equation (3) can also be used to calculate the axial magnetic polarizability of the particle:

$$\alpha_{zz}^{mm} = \frac{(1 + i\tan\delta)(\pi a^2)^2/L}{(\frac{\omega_0^2}{\omega^2} - 1 - i\tan\delta)}, \tag{6}$$

where $\omega_0 = 1/\sqrt{LC}$. Therefore, the electrical size of the DR at resonance is

$$\frac{2a}{\lambda_0} = \frac{\sqrt{2}}{\pi} \frac{a/b}{\sqrt{[\ln(8a/b) - 7/4]}} \frac{1}{\sqrt{\varepsilon'_r}}. \tag{7}$$

From (7) it follows that in order to reduce the electrical size of the DR, high permittivity dielectrics and/or low a/b ratios must be used. Since losses should increase with permittivity, it will be advantageous to use a/b ratios that are as small as possible. Assuming $a/b = 3$, we can see that in order to achieve an electrical size $a/\lambda_0 \sim 0.1$, the real part of the ring permittivity must be $\varepsilon \sim 100\varepsilon_0$, which is a quite achievable value at microwave and THz frequencies.

To check our analytical results, several DRs with different a/b ratios have been designed and simulated using CST Microwave Studio[3]. To obtain the resonance frequency and the field distribution at resonance, an ideal square TEM waveguide (with upper and lower perfect electric conducting walls, and lateral perfect magnetic conducting walls) was loaded with a dielectric ring, and the scattering parameters were calculated. The dielectric ring was placed at the center of the TEM waveguide, with its axis along the incident magnetic field direction. With this configuration, any resonance of the dielectric ring will appear as a sharp dip in the transmission coefficient. Figure 2 shows the simulated transmission coefficients and the resonances predicted by our analytical model for several values of the a/b ratio. A very good agreement can be observed, even for a/b ratios as small as $a/b = 3$. The higher order DR resonances which appear in the figure for the smaller a/b ratio are electric resonances, whose description is outside the scope of our model. The electric field simulations shown in figure 3 also confirm the hypothesis underlying the model, particularly the uniformity of the field along the ring. Besides the dielectric nature, a noticeable advantage of the proposed DR is that it allows for the design of unit cells exhibiting full cubic symmetry (O_h group symmetry), thus being able to form isotropic metamaterials [17]. Such an

---

[3] In the case of figures 2, 3, 9 the time domain solver (FDTD) has been used. The structure was fed by TEM waveguide ports. In the case of figures 7 and 8 the eigensolver with the Jacobi–Davidson computation scheme has been used. In both simulations the PEC or PMC walls have been used on allowed symmetry planes. The mesh used globally 20 mesh cells per wavelength and local refinement in the rings/wires with 15 mesh cells along the wire diameter.
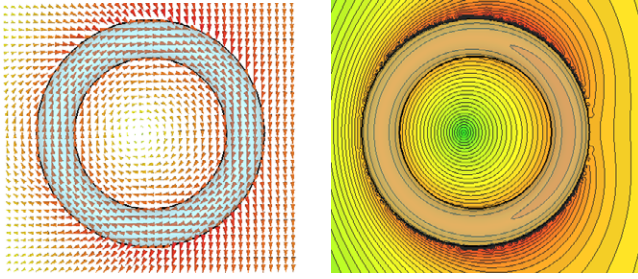
Figure 3. Vector and contour plot of the electric field intensity in the vicinity of the dielectric ring resonance. The incident wave is the TEM waveguide mode with the magnetic field along the axis of the ring. The contour plot shows the absolute value of the field. The ring and waveguide parameters are the same as in figure 2.

(This figure is in colour only in the electronic version)

isotropic composite, whose unit cell is shown in the inset of figure 4, can be described using the homogenization model developed in [18, equation 13] combined with the magnetic polarizability (6), which leads to the local effective magnetic permeability

$$\mu / \mu_0 = 1 + \frac{\frac{\alpha_0}{p^3}}{\frac{\omega_{0c}^2}{\omega^2} - 1 - \frac{2M_a}{L} - \frac{4M_c}{L} - \frac{\alpha_0}{3p^3}}, \qquad (8)$$

where p is the lattice constant, $\omega_{0c}^2 = \omega_0^2/(1 + i \tan \delta)$, $\alpha_0 = \mu_0(\pi a^2)^2/L$ and M_a and M_c are the mutual inductances of the closest rings of the same orientation, placed in the coplanar and the axial directions, respectively. Equation (8) is depicted in figure 4. The theoretical relative bandwidth of the negative permeability region shown in figure 4 is about 10%, whereas the simulated bandwidth is about 14% (see figure 7, below), more than one order of magnitude larger than in other previous designs of dielectric negative permeability media using Mie resonances of dielectric rods, cubes or spheres in free space [4–15]. The reason for this enhanced bandwidth may be the strong confinement of current in the periphery of the DR, which results in a stronger magnetic moment.

3. Dielectric rods

The high symmetry of DRs also suggests the possibility of designing a 3D isotropic left-handed medium by combining them with a connected network of metallic wires [19]. Actually, the field confinement concept underlying DR theory can also be applied in the design of a fully dielectric and isotropic left-handed metamaterial by substituting the metallic wires with dielectric rods (DRos). To keep the explanation as simple as possible, we will stick to the parallel plate waveguide model of the cubic wire medium [1, section 2.2.2]. In the framework of this model, the unit cell of such a medium is equivalent to the circuit depicted in figure 5, where $L/p = \mu_0$ is the per unit length inductance of 'vacuum', $C/p = \varepsilon$ is the per unit length capacitance of 'vacuum', Z_w is the impedance of a wire section of length p, and p is the lattice constant. In a metallic wire medium the wire exhibits an inductance that can
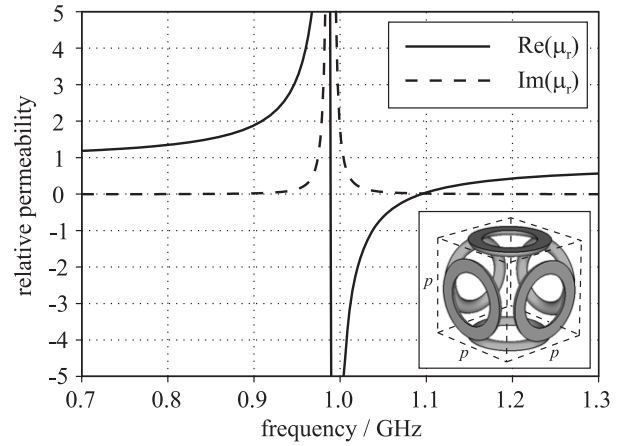
Figure 4. Effective permeability of an isotropic magnetic medium composed of DRs. The geometrical ring parameters are $a = 15$ mm and $a/b = 5$. The material is a commercially available dielectric, denoted as K-250, from TCI Ceramics, with $\epsilon_r = 250$ and $\tan \delta = 0.005$. The lattice constant is 45 mm.
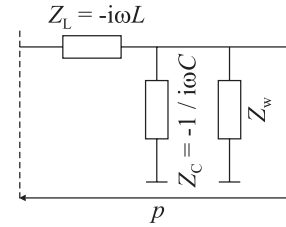
Figure 5. Equivalent circuit model of the unit cell of the connected wire medium with a cubic lattice of periodicity p.

be approximated as [19]

$$Z_w = \frac{-i\omega\mu_0 p}{2\pi} \left[\ln \left(\frac{p}{2\pi r_w} \right) + 0.5275 \right], \qquad (9)$$

where r_w is the wire radius. However, as shown at the beginning of this paper, if the wires are substituted by high permittivity DRos, they also exhibit an additional capacitance and resistance (4) which result in the impedance

$$Z = \frac{-p}{i\omega\varepsilon\pi r_w^2} \qquad (10)$$

which must be added to the impedance (9). Now, the resulting effective permittivity is

$$\varepsilon_{rw} = 1 - \frac{1}{\frac{\omega^2}{\omega_p^2} - \frac{(p/r_w)^2}{\varepsilon_r \pi}}, \qquad (11)$$

where

$$\omega_p^2 = \frac{1}{\frac{\varepsilon_0\mu_0 p^2}{2\pi} \left[\ln \left(\frac{p}{2\pi r_w} \right) + 0.5275 \right]} \qquad (12)$$

is the plasma frequency of the ordinary metallic wire medium. From (11) it can be seen that the presence of the additional wire capacitance shifts the resonance of the metallic wire medium from zero frequency to the higher frequency $\omega_r = p w_p/(r_w \sqrt{\epsilon_r \pi})$. The permittivity (11) is plotted in figure 6 for some realistic structural parameters.

Figure 6. Effective permittivity of a connected dielectric wire medium. The geometrical parameters are $p = 45$ mm and $r_w = p/15$. The material is commercially available dielectric SrTiO₃ with $\epsilon_r = 500$ and $\tan \delta = 0.01$. The unit cell is shown in the inset.
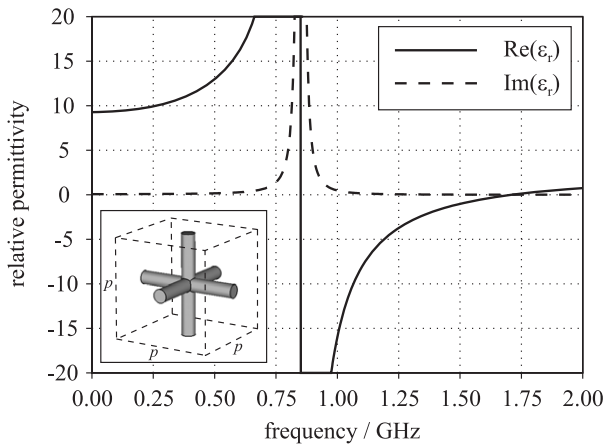

Figure 7. The band diagram of the DR + DRo medium (solid lines) with the unit cell shown in the inset and the band diagram of the DR medium alone (dashed lines). The structural parameters are the same as in figures 4 and 6; however the losses were omitted in the band-structure calculation. Note that the flat longitudinal mode in the DR band diagram will also appear in the combined structure, but has been omitted to retain the clarity of the figure.

4. The combined ring and rod medium

By combining the DR and DRo media of figures 4 and 6, the isotropic DR + DRo medium with the unit cell depicted in the inset of figure 7 is obtained. The band diagram along the Γ–X direction of this medium calculated using CST Microwave Studio is shown in figure 7, along with the band diagram for the DR medium only (losses were omitted in this calculation). A backward-wave pass band with a relative bandwidth of about 14% can be clearly observed for the DR + DRo medium. This pass band appears quite approximately at the negative permeability frequency band of the DR medium shown in figure 4. The forward pass band for the DR + DRo medium located at lower frequencies coincides almost exactly with a similar pass band for the DRo medium alone, which corresponds to the region of positive dielectric permittivity below the resonance frequency ω_r. The small numerical discrepancies in the location of the pass bands and stop bands between figures 7, 4 and 6 can be attributed to the effect of spatial dispersion, not considered in our analytical model. It should be mentioned, however, that these effects could be included in the model using the general formalism developed in [18].

5. Dielectric rings in a dielectric background

An interesting property of DRs is that, in principle, the reported expression for capacitance (4), as well as for the magnetic polarizability (6), and the results for the magnetic permeability, are independent of the characteristics of the host medium. Increasing the permittivity of the host medium however implies a smaller jump of the dielectric constant across the ring interface, and therefore a weaker field confinement, a feature that may affect the results in practice. On the other hand, as suggested in [11], the introduction of a permittivity background can lead to increased bandwidth of the negative permeability region, making such trials worthwhile. In order to test this hypothesis we have introduced the DR

Figure 8. Band diagram of the DR medium immersed in the host material with permittivity $\varepsilon = 5\varepsilon_0$. The structural parameters are equal to those of figure 7.

lattice into the host medium with $\varepsilon = 5\varepsilon_0$ and calculated the band diagram using CST Microwave Studio. The result is depicted in figure 8. As can be observed, the material still exhibits the expected stop band at around 1 GHz and indeed its fractional bandwidth increased to approximately 27%. Further increase in the background permittivity (the value of $12\varepsilon_0$ has been tested) starts to change the band structure considerably, revealing for example a left-handed pass band in the region of previous stop band. The reason for such unexpected features can however be easily explained. Although the high permittivity background does not greatly affect the ring capacitance, it considerably enlarges the electrical size of unit cell (with respect to the wavelength of the host) and we are thus in the realm of photonic crystals rather than of homogenizable media. This analysis thus shows that the addition of a positive dielectric background can enlarge the negative permeability
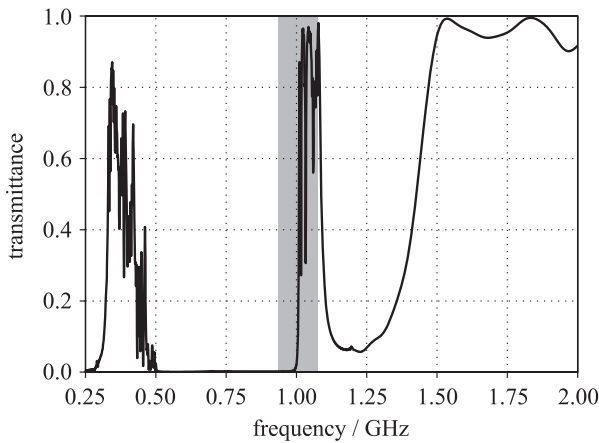
Figure 9. Transmittance through a five unit cells thick slab of DRs combined with homogeneous plasma. The plasma frequency has been set to $\omega_p = 2\pi 10^9 \sqrt{2} s^{-1}$ and the collision frequency to $f_c = \omega_p/1000$. The gray-shaded area shows the region of the stop band in figure 7 arising from negative permeability. The structural parameters are the same as for figure 4.

bandwidth. However, unless the electrical size of the DR is very small, the presence of the host dielectric may lead to strong spatial dispersion or even prevent any attempt at homogenization.

The use of a low permittivity background also raises the question of whether negative permittivity can be used. In this case however another issue may appear. It is well known [20, 21, 1] that mixing two composites of negative permittivity and permeability does not ensure a left-handed behavior. In particular, an array of SRRs immersed in a homogeneous negative permittivity medium does not provide a left-handed metamaterial, because the capacitance distributed along the SRR becomes negative (that is, in fact inductive) due to the negative permittivity of the host medium [1]. Fortunately, as mentioned in the previous paragraph, the capacity of the DR should be independent of the surrounding medium. In order to further study this property of DR composites, the transmittance through a five unit cells thick slab of the DR medium, shown in figure 4, immersed in a plasma-like medium of permittivity $\varepsilon/\varepsilon_0 = 1 - \omega_p^2/(\omega(\omega - \mathrm{i} f_c))$, has been computed using CST Microwave Studio. The result is shown in figure 9.

A clear pass band in the frequency band of negative permeability of figure 4 can be observed, in agreement with the above hypothesis. Apart from this left-handed band, the structure also exhibits a right-handed pass band at lower frequencies, which results from the plasmonic resonances supported by the ring for high values of the negative permittivity of the host medium. The ripples observed in both pass bands are Fabry–Perot resonances due to the finite width of the sample. The above results for the DR furthermore suggest that also previously proposed dielectric metamaterials based on magnetic Mie resonances would provide left-handed media when immersed in a low value negative permittivity medium.

Apart from in gaseous hot plasmas, low valued negative permittivity is present in metals and in semiconductors near its

plasma frequency. The plasma frequency of metals is beyond the optical range, where achieving the large permittivities needed for the proposed DR designs seems almost impossible. However, some semiconductors such as InSb [22], and others, present plasma frequencies and relatively low losses in the terahertz range, where the high dielectric constants needed for DR media design can be easily achieved. Therefore, a semiconductor matrix with DR inclusions seems to be a promising structure for left-handed media design at THz frequencies.

6. Conclusions

It has been shown that a high permittivity DR can resonate at microwave and terahertz frequencies, providing strong artificial magnetism with a frequency band of effective negative permeability one order of magnitude larger than for other previously proposed dielectric designs. By combining these DRs with DRos or with a plasma-like host medium, a left-handed behavior can be achieved. Combinations of DRs with DRos may be useful for the design of left-handed metamaterials when interactions with external low frequency magnetic fields should be minimized. A composite made of DR inclusions in a host semiconducting media near its plasma frequency appears to be a promising alternative for the design of left-handed media at terahertz frequencies. Lastly, it is also worth mentioning that the use of ferroelectrics in DRs or DRos can lead to significant tunability of the above proposed systems.

Acknowledgments

References

[1] Marqués R, Martín F and Sorolla M 2007 *Metamaterials with Negative Parameters: Theory and Microwave Applications* (New York: Wiley)
[2] Schelkunoff S A and Friis H T 1952 *Antennas: Theory and Practice* (New York: Wiley)
[3] Pendry J B, Holden A J, Robbins D J and Stewart W J 1999 *IEEE Trans. Microw. Theory Tech.* **47** 2075
[4] O'Brien S and Pendry J B 2002 *J. Phys.: Condens. Matter* **14** 4035
[5] Huang K C, Povinelli M L and Joannopoulos J D 2004 *Appl. Phys. Lett.* **85** 543
[6] Schuller J A, Zia R, Taubner T and Brongersma M L 2007 *Phys. Rev. Lett.* **99** 107401
[7] Zhao Q, Kang L, Du B, Zhao H, Xie Q, Huang X, Li B, Zhou J and Li L 2008 *Phys. Rev. Lett.* **101** 027402
[8] Zhao Q, Du B, Kang L, Zhao H, Xie Q, Li B, Zhang X, Zhou J, Li L and Meng Y 2008 *Appl. Phys. Lett.* **92** 051106
[9] Popa B and Cummer S A 2008 *Phys. Rev. Lett.* **100** 207401
[10] Holloway C L, Kuester E F, Baker-Jarvis J and Kabos P 2003 *IEEE Trans. Antennas Propag.* **51** 2596

[11] Yannopapas V and Moroz A 2005 *J. Phys.: Condens. Matter* **17** 3717
[12] Wheeler M S, Aitchison J S and Mojahedi M 2005 *Phys. Rev. B* **72** 193103
[13] Vendik I, Vendik O and Odit M 2006 *Microw. Opt. Technol. Lett.* **48** 2553
[14] Yannopapas V and Vitanov N V 2006 *Phys. Rev. B* **74** 193304
[15] Yannopapas V 2007 *Phys. Rev. B* **75** 035112
[16] Landau L D, Lifshitz E M and Pitaevskii L P 1984 *Electrodynamics of Continuous Media* 2nd edn (Oxford: Pergamon)
[17] Baena J D, Jelinek L and Marqués R 2007 *Phys. Rev. B* **76** 245115
[18] Baena J D, Jelinek L, Marqués R and Silveirinha M 2008 *Phys. Rev. A* **78** 013842
[19] Silveirinha M and Fernandes C A 2005 *IEEE Trans. Microw. Theory Tech.* **53** 1418
[20] Pokrovsky A L and Efros A L 2002 *Phys. Rev. Lett.* **89** 093901
[21] Marqués R and Smith D R 2004 *Phys. Rev. Lett.* **92** 059401
[22] Rivas J G, Janke C, Bolivar P H and Kurz H 2005 *Opt. Express* **13** 847

Appendix 6

This appendix contains a full text of Ref. [25]

Periodic arrangements of chiral scatterers providing negative refractive index bi-isotropic media

L. Jelinek,[1,*] R. Marqués,[1,†] F. Mesa,[2,‡] and J. D. Baena[1,3,§]

[1]*Departamento de Electrónica y Electromagnetismo, Universidad de Sevilla, 41012-Sevilla, Spain*
[2]*Departamento de Física Aplicada 1, Universidad de Sevilla, 41012-Sevilla, Spain*
[3]*Departamento de Física, Universidad Nacional de Colombia, Bogotá, Colombia*
(Received 14 April 2008; published 14 May 2008)

The main goal of this contribution is to show that periodic arrangements of chiral scatterers can be the basis for the development of three dimensional and isotropic negative refractive index artificial media. Three dimensionality and isotropy are key issues in this context since only three dimensional structures can be properly viewed as a "medium," and only in isotropic media the refractive index is unambiguously defined. The proposed arrangements are cubic lattices of chiral split ring resonators conveniently designed to yield an isotropic behavior. The reported structures are shown to provide a significant frequency band of negative refraction with good matching to free space.

I. INTRODUCTION

Isotropic negative refractive index (NRI) media were first proposed and analyzed by Veselago in 1968,[1] but its practical implementation was not envisaged until recently, after the results of Smith *et al.*[2] It should be pointed out that the refraction index can only be unambiguously defined in three dimensional isotropic media and that most reported practical realizations of media exhibiting negative refraction fall into the category of *indefinite* media[3] rather than into the category of isotropic NRI or "left-handed"[1] media. Actually, the development of an isotropic NRI medium is still a challenging issue despite the diverse efforts in this direction.[4–7] Overcoming this challenge is of interest not only from a theoretical standpoint but also from a practical one: isotropic and bi-isotropic NRI media will be useful for designing three dimensional planar focusing devices,[1,8] subdiffraction imaging devices,[9] and other applications.

Chiral scatterers are an attractive alternative for the design of NRI artificial media because of their ability for providing simultaneously negative permittivity and permeability. To the best of our knowledge, the first proposals in this direction were made by Tretyakov and co-workers.[10,11] Other proposals aimed to take advantage of chirality for NRI media design were subsequently reported.[12,13] All these proposals either neglect the issue of isotropy or propose random arrangements to address it. However, random arrangements, although conceptually appealing, are not easily reproducible and do not show a well defined electromagnetic response, mainly if the size of inclusions is not sufficiently small compared to wavelength (as usual in most artificial media). In fact, this last feature could be one of the main reasons why isotropic NRI artificial media made from chiral inclusions have not been developed further, remaining only as a theoretical possibility. By contrast, periodic arrangements are reproducible, and the eigenmodes of the structure can be unambiguously identified by using Bloch–Floquet theorem. Starting from these considerations, this paper proposes a way to the experimental realization of bi-isotropic and isotropic NRI artificial media using periodic arrangements of chiral scatterers. The paper is organized as follows. First, the basic

structure is proposed and an approximate analytical theory based on a generalization of Lorentz homogenization procedure is developed. This analysis directly provides the appropriate design parameters. Then, rigorous full-wave electromagnetic simulations are carried out in order to identify the eigenmodes of the structure and to validate the analytical theory. These simulations are also useful in order to identify the effects of spatial dispersion, which are not taken into account by the analytical theory. As will be shown, these effects are not relevant in the frequency band of interest. Next, the impedance matching to free space of the proposed structure is studied. Finally, the possibility of creating a racemic configuration is discussed.

II. BALANCED CHIRAL BI-ISOTROPIC MEDIA

Before the analysis of any specific structure, some key properties of bi-isotropic chiral media will be recalled. Bi-isotropic media can be described by the following linear constitutive relations:[14]

$$\mathbf{D} = \varepsilon_0(1 + \chi_e)\mathbf{E} + j\sqrt{\varepsilon_0\mu_0}\kappa\mathbf{H}, \tag{1}$$

$$\mathbf{B} = -j\sqrt{\varepsilon_0\mu_0}\kappa\mathbf{E} + \mu_0(1 + \chi_m)\mathbf{H}, \tag{2}$$

where χ_e, χ_m, and κ are the electric, magnetic, and cross susceptibilities, respectively, which are real quantities for lossless media. Assuming an $\exp(j\omega t)$ time dependence, the eigenwaves propagating through these media are right- and left-circularly polarized plane waves whose dispersion relation is given by[14]

$$k^{\pm} = k_0(\sqrt{\mu_r\varepsilon_r} \pm \kappa), \tag{3}$$

where $k_0 = \omega\sqrt{\varepsilon_0\mu_0}$ and $\varepsilon_r = (1 + \chi_e)$, $\mu_r = (1 + \chi_m)$. In order to reduce the forbidden bands of propagation coming from complex values of $k^{\pm}$, it is desirable that $\chi_e(\omega) \simeq \chi_m(\omega)$ so that μ_r and ϵ_r always have the same sign. It is known[11,13] that this condition also implies that

$$\chi_e(\omega) \simeq \chi_m(\omega) \simeq |\kappa(\omega)|. \tag{4}$$

The conditions for negative refraction in transparent bi-isotropic chiral media are also known.[15] In lossless bi-
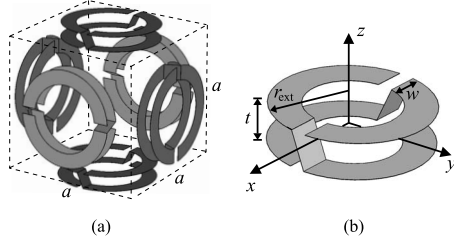
FIG. 1. (a) Cubic arrangement of chiral SRRs satisfying T group of symmetry (namely, any of the in-body diagonals is a third order rotation symmetry axis) and (b) detail of the chiral SRR design.

isotropic media satisfying the *balance* condition [Eq. (4)], these conditions reduce to

$$\chi_e < -0.5 \quad \text{and} \quad \chi_m < -0.5 \tag{5}$$

or, equivalently, $\varepsilon_r < 0.5$ and $\mu_r < 0.5$,[13] which is less restrictive than the usual condition for conventional isotropic media ($\varepsilon_r < 0$ and $\mu_r < 0$). The price to pay for this enhanced bandwidth is that only one of the eigenwaves of Eq. (3) will exhibit negative refraction, while the other will present a positive refractive index.[8,13]

Both eigenwaves have the same wave impedance given by[14]

$$Z = Z_0 \sqrt{\frac{\mu_r}{\varepsilon_r}}, \tag{6}$$

where $Z_0 = \sqrt{\mu_0/\varepsilon_0}$ is the free space impedance. However, since the refractive index is different for each eigenmode, the refracted amplitude is not necessarily the same for both eigenmodes. In general, both eigenmodes will be generated at the interface between free space (or other isotropic medium) and a chiral medium, even if the incident wave is circularly polarized. The only exception to this rule is normal incidence.

III. THEORY AND DESIGN

In a previous paper,[16] some of the authors showed that a cubic arrangement of scatterers satisfying the tetrahedral or (in Schoenflies notation) T group of symmetry provides a useful basis for the design of isotropic artificial media. Figure 1(a) shows a cubic arrangement of chiral split ring resonators (SRRs) satisfying this symmetry. It should be noticed that the SRRs on opposite sides of the cube of Fig. 1(a) are identical, which allows for the realization of an artificial medium by means of the periodic repetition of this structure. This artificial medium has a simple cubic lattice of periodicity a (the edge of the cube) and its primitive unit cell contains three chiral SRRs. Note that the proposed chiral SRR is a practical design, feasible to be manufactured by standard planar-circuit fabrication techniques.[20]

An easy way to compute the susceptibilities of the metamaterial can be obtained from a straightforward extension of Lorentz local field theory that takes into account the presence of cross polarizabilities. This simple theory leads to the following equations for the macroscopic polarizations, **P** and **M**, of the metamaterial:

$$\mathbf{P} = \frac{1}{V} \left[\langle \alpha_e \rangle \left(\mathbf{E} + \frac{\mathbf{P}}{3\varepsilon_0} \right) + \mu_0 \langle \alpha_{em} \rangle \left(\mathbf{H} + \frac{\mathbf{M}}{3} \right) \right], \tag{7}$$

$$\mathbf{M} = \frac{1}{V} \left[\mu_0 \langle \alpha_m \rangle \left(\mathbf{H} + \frac{\mathbf{M}}{3} \right) - \langle \alpha_{em} \rangle \left(\mathbf{E} + \frac{\mathbf{P}}{3\varepsilon_0} \right) \right], \tag{8}$$

where $V = a^3$ is the volume of the unit cell and $\langle \alpha_e \rangle$, $\langle \alpha_{em} \rangle$, and $\langle \alpha_m \rangle$ are the average polarizabilities of the unit cell, which are defined as

$$\mathbf{p} = \langle \alpha_e \rangle \mathbf{E}_l + \langle \alpha_{em} \rangle \mathbf{B}_l, \tag{9}$$

$$\mathbf{m} = -\langle \alpha_{em} \rangle \mathbf{E}_l + \langle \alpha_m \rangle \mathbf{B}_l, \tag{10}$$

where **p** and **m** are the electric and magnetic dipoles induced at each unit cell, $\mathbf{E}_l$ and $\mathbf{B}_l$ are the electric and magnetic local fields, and where Onsager symmetries[17] for the magneto-electric polarizabilities are explicitly introduced ($\langle \alpha_{me} \rangle = -\langle \alpha_{em} \rangle$). By using Eqs. (7) and (8), the metamaterial susceptibilities are directly obtained from their definitions, $\varepsilon_0 \chi_e = \partial \mathbf{P}/\partial \mathbf{E}$ and $\chi_m = \partial \mathbf{M}/\partial \mathbf{H}$, provided that the polarizabilities are known. These polarizabilities can be obtained from the polarizabilities of the chiral SRR. Analytical expressions for the chiral SRR polarizabilities were already reported[18] and will be here reproduced for completeness,

$$\alpha_{zz}^{mm} = \frac{\pi^2 r^4}{L} \frac{\omega^2}{\omega_0^2 - \omega^2 + j\omega R/L}, \tag{11}$$

$$\alpha_{zz}^{em} = \pm j \frac{2\pi r^2 t}{\omega_0 L} \left(\frac{\omega_0}{\omega} \right) \frac{\omega^2}{\omega_0^2 - \omega^2 + j\omega R/L}, \tag{12}$$

$$\alpha_{zz}^{ee} = \frac{4t^2}{\omega_0^2 L} \left(\frac{\omega_0}{\omega} \right)^2 \frac{\omega^2}{\omega_0^2 - \omega^2 + j\omega R/L}, \tag{13}$$

$$\alpha_{xx}^{ee} = \alpha_{yy}^{ee} = \varepsilon_0 \frac{16}{3} r_{\text{ext}}^3, \tag{14}$$

where t and r_{ext} are geometrical parameters [see Fig. 1(b)] and L, R, and ω_0 are the chiral SRR self-inductance, resistance, and frequency of resonance, respectively, which can be analytically obtained from a general procedure already developed by some of the authors.[19] From Eqs. (11)–(14), the average polarizabilities in Eqs. (9) and (10) are obtained as

$$\langle \alpha_e \rangle = \alpha_{xx}^{ee} + \alpha_{yy}^{ee} + \alpha_{zz}^{ee}, \tag{15}$$

$$\langle \alpha_{em} \rangle = \alpha_{zz}^{em}, \tag{16}$$

$$\langle \alpha_m \rangle = \alpha_{zz}^{mm}. \tag{17}$$

When the balance condition [Eq. (4)] is translated to the unit cell polarizabilities, it becomes

$$c^2 \langle \alpha_e \rangle = c |\langle \alpha_{em} \rangle| = \langle \alpha_m \rangle, \tag{18}$$

where c is the velocity of light. This condition cannot be exactly fulfilled at all frequencies using the polarizabilities from Eqs. (11)–(14) due to the presence of the static electric polarizabilities [Eq. (14)]. However, if the static electric po-
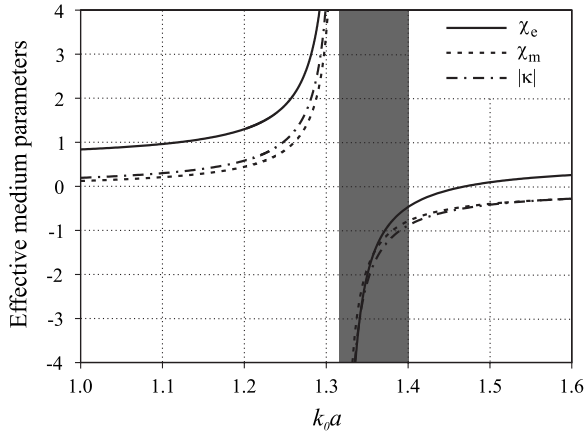
FIG. 2. Theoretical constitutive parameters χ_e, χ_m, and κ for the metamaterial made of the periodic repetition of the cubic arrangement of Fig. 1(a), forming a simple cubic lattice with periodicity a. SRR parameters are $a/r_{ext}=2.87$, $w/r_{ext}=0.4$, and $t/r_{ext}=0.47$.

FIG. 3. Theoretical dispersion curves for the eigenwaves of the metamaterial shown in Fig. 2. Dispersion curves are drawn inside the first Brillouin zone of the structure.

IV. ELECTROMAGNETIC SIMULATIONS

larizabilities are neglected (which is a reasonable hypothesis near resonance), the balance condition [Eq. (18)] is approximately satisfied provided that

$$t\lambda_0 = (\pi r)^2, \qquad (19)$$

where λ_0 is the wavelength at resonance and t and $r=r_{ext}-w/2$ are structural parameters of the chiral SRR [see Fig. 1(b)]. Although Eq. (19) is only approximate and comes from a simplified homogenization procedure, it will be shown that it is a very good design rule in the frequency band of interest.

In the following, a particular example is analyzed in order to illustrate and validate our analytical predictions. The chosen metamaterial parameters satisfy Eq. (19) and are given in the caption of Fig. 2. The frequency band of left-handed propagation, given by Eq. (5), is marked in gray. It can be seen how inside this region the balance condition [Eq. (4)] is approximately fulfilled. However, outside this region, the static nonresonant polarizabilities [Eq. (14)] dominate and the balance condition is not fulfilled. The theoretical dispersion curves for the eigenwaves of the bi-isotropic metamaterial, given by Eq. (3), are shown in Fig. 3. A frequency band of backward-wave propagation for one of the eigenwaves can be clearly observed (between points marked as 2 and 4), which corresponds to the left-handed frequency band shown in Fig. 2. Since backward-wave propagation is the signature of negative refraction,[1] this region corresponds to a NRI for the considered eigenmode. Inside this band, there is also a small forbidden band gap (marked as 3; see also the inset) that corresponds to complex values of the propagation constants [Eq. (3)]. This small band gap is due to the aforementioned approximations implicit in Eq. (19). The straight horizontal line at the frequency where the propagation constant of one of the eigenwaves vanishes (corresponding to the condition $\varepsilon_r\mu_r=\kappa^2$) represents a fully degenerate longitudinal wave with $\mathbf{k}\times\mathbf{E}=0$ and $\mathbf{k}\times\mathbf{H}=0$.
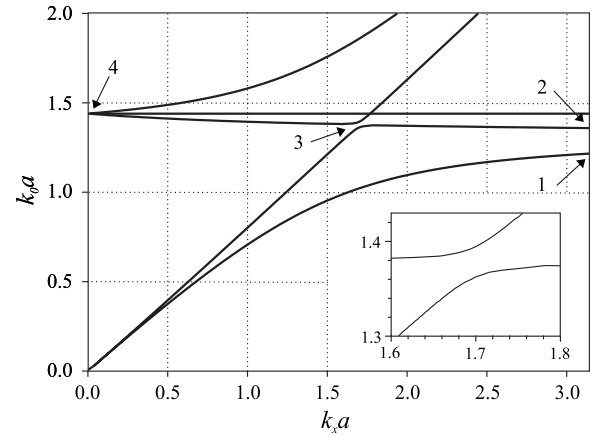
In this section, the previously studied structure is analyzed by means of the commercial electromagnetic simulator CST MICROWAVE STUDIO, giving the band structure shown in Fig. 4. A good qualitative agreement is found between Figs. 3 and 4. In both figures, a frequency band of backward-wave propagation is observed for one of the eigenwaves. Also, a small frequency stopband appears in Fig. 4 inside this backward-wave passband (because of the approximate balance condition employed) in agreement with the theoretical predictions of Fig. 3. In order to show the isotropic nature of the structure, the dispersion curves along the Γ-X, Γ-M, and Γ-R paths are shown in Fig. 5. The isotropy of the dispersion relation for the transverse modes becomes apparent from these curves, except for high values of the propagation constant (namely, close to the border of the Brillouin zone), where spatial dispersion affects the dispersion relation. The longitudinal mode of Fig. 3 also appears in Figs. 4 and 5, although now spatial dispersion destroys degeneracy and isotropy.

The main differences between Figs. 4 and 5 and the theoretical dispersion curves shown in Fig. 3 are observed at
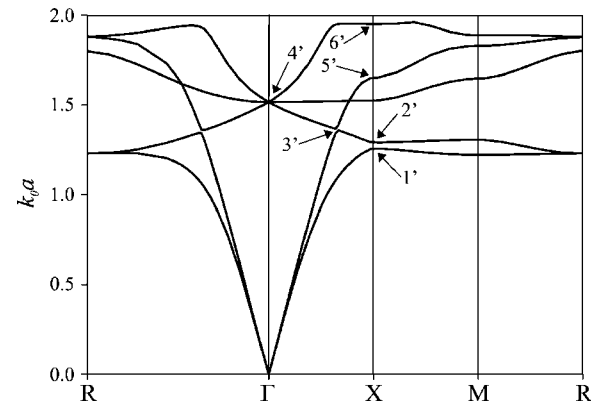
FIG. 4. Band structure and dispersion relation for the metamaterial of Fig. 2 obtained from full-wave simulations along the path R-Γ-X-M-R [Γ is the center of the k-space, $X=(\pi/a,0,0)$, $M=(\pi/a,\pi/a,0)$, and $R=(\pi/a,\pi/a,\pi/a)$].

FIG. 5. Dispersion curves along the Γ-*X*, Γ-*M*, and Γ-*R* directions for the eigenwaves of the balanced metamaterial of Figs. 2 and 3. The end of the first Brillouin zone for each direction of propagation is shown in the figure (vertical lines).

high values of k and also at high values of frequency (i.e., at high values of $k_0 a$). These differences correspond to the effect of spatial dispersion, which becomes important when the size of the unit cell is not small in comparison with the wavelength in free space and in the medium.[17] In such regions,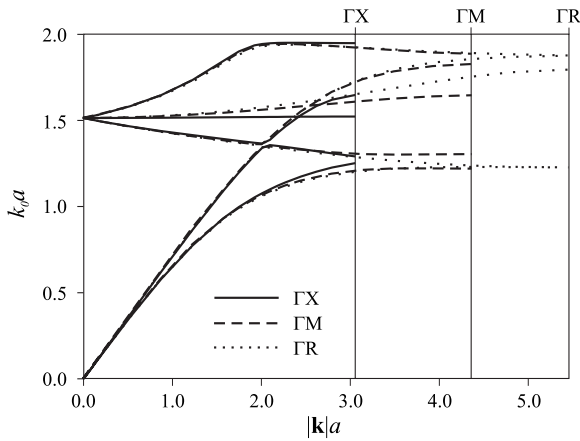 the behavior of the structure is closer to a photonic crystal than to an effective medium. However, inside the left-handed band (between points marked 2′ and 4′ in Fig. 4), spatial dispersion does not produce significant deviations from isotropy (i.e., the dispersion curves are almost equal for any direction of propagation, as can be seen in Fig. 5). This effect is even more apparent in the frequency band between the unbalanced forbidden band (marked as 3′ in Fig. 4) and the end of the left-handed band (marked as 4′ in Fig. 4).

It is illustrative to compare the band structure of the considered balanced structure with that of an unbalanced one. Thus, Fig. 6 shows the dispersion diagrams for the eigenmodes of two unbalanced structures (which were obtained by varying t in Fig. 1). It can be observed how, as t decreases, the forbidden frequency band increases until the backward-
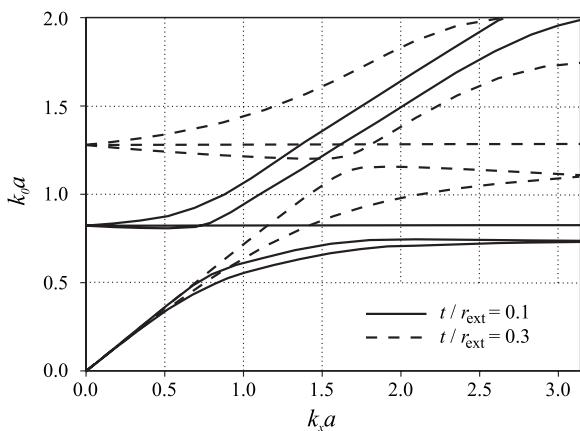

FIG. 6. Dispersion curves along the Γ-*X* direction for the eigenwaves of two unbalanced metamaterials. Parameters are the same as in Fig. 2, except for t/r_{ext}, which is taken as $t/r_{ext}=0.3$ (dashed lines) and $t/r_{ext}=0.1$ (solid lines).

FIG. 7. Simulated transmittance through a seven unit cell thick slab of the metamaterial analyzed in Figs. 2–5 for a left-circularly polarized (LCP) incident wave. Transmittance is plotted for both the co-polar (LCP wave) and the cross-polar (RCP wave) components. Points marked 1′–6′ correspond to the marks in Fig. 4.

wave region vanishes, giving a behavior similar to that of a negative-μ split ring metamaterial. Figure 6 also shows that the tolerance of condition (19) is high. It can be seen that even a change of more than 30% in the particle thickness does not strongly affect the left-handed passband.

V. PROPAGATION THROUGH A FINITE SLAB

In the practical design of a NRI medium, apart from the obvious obtaining of some amount of negative refraction, it should be required that the metamaterial has small reflectance for the beam to be refracted with a significant amplitude. Since for balanced metamaterials it is imposed that $\chi_e \simeq \chi_m$ in the frequency range of interest, it directly follows from Eq. (6) that $Z(\omega) \simeq Z_0$, which ensures a good matching to free space and constitutes an additional relevant advantage of the proposed *balanced* NRI metamaterials.

In order to illustrate the above feature, the normal incidence of a circularly polarized plane wave on a slab of the proposed chiral medium will be studied through electromagnetic simulations. First, a wave with the same polarization as the left-handed eigenmode of Figs. 4 and 5 is analyzed. The computed transmittance is shown in Fig. 7. It can be seen that the amplitude of the cross-polarized wave is almost negligible, which means that the circular polarization is maintained. The figure also shows that the medium is practically transparent for almost all the considered frequencies, as expected from the aforementioned impedance matching. However, the small ripples observed in the transmittance in Fig. 7 shows that the impedance matching is not perfect. The regions of poor transmittance, between points 1′ and 2′, and beyond 6′, exactly reproduce the corresponding band gaps in Fig. 4. There is also a smaller dip at point 3′, which corresponds to the unbalanced band gap of Fig. 4. Therefore, a useful region of backward-wave propagation ranges from point 3′ to point 4′, which includes the most useful values of ε_r and μ_r, as already mentioned.

Backward-wave propagation in the frequency band of interest will be demonstrated by plotting the phases of the

FIG. 8. Phase of the simulated transmission coefficient for the incident LCP wave through a seven unit cell thick slab (solid line) and a five unit cell thick slab (dashed line). Points marked 2'–4' correspond to the marks in Fig. 4.
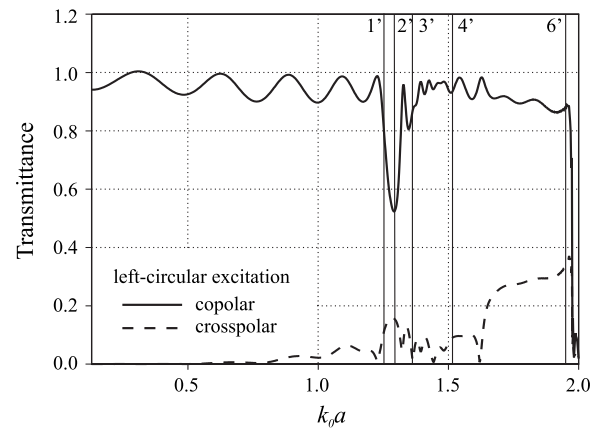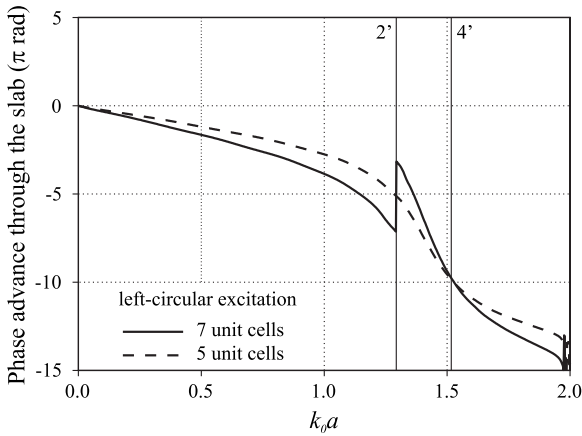

FIG. 9. Simulated transmittance through a seven unit cell thick slab of the metamaterial analyzed in Figs. 2–5 for the co-polar (RCP wave) and the cross-polar (LCP wave) components of an incident RCP eigenmode. Points marked 3' and 5' correspond to the marks in Fig. 4.

computed transmission coefficients for two slabs of different thicknesses (see Fig. 8). A zero phase shift between both transmission coefficients was imposed at zero frequency, i.e., for static fields. Also, a convenient phase shift of 4π was imposed to the phase of the seven unit cell thick slab at the onset of the left-handed band (i.e., at frequency point 2'). This shift is imposed in order to obtain a zero phase shift between both coefficients at point 4', which corresponds to the zero phase advance point for the backward-wave eigenmode of Fig. 4. As a consequence, the sign of the phase difference between both samples changes from the backward-wave region (between frequency points 2' and 4') to the forward-wave bands (between zero frequency and 2', and beyond 4'). This result is in complete agreement with the backward-wave propagation postulated for the left-circularly polarized wave (LCP) between frequency points 2' and 4'. It should be mentioned that once a zero phase shift is imposed at zero frequency and at the frequency point 4', the phase jump at 2' cannot be arbitrarily imposed. Therefore, the fact that the phase jump necessary to fulfill the aforementioned conditions equals to 4π provides an additional confirmation of the proposed theory.

Finally, the simulated transmittances for the co-polar and cross-polar componets of an incident RCP wave are shown in Fig. 9. The obtained values for this transmittance are again near unity, except for the band gaps shown in Fig. 4 for this wave, i.e., around frequency point 3' and beyond 5'.

VI. RACEMIC PERIODIC MEDIUM

Next, it will be explored the possibility of designing a racemic mixture of chiral SRRs while keeping the necessary symmetries to ensure an isotropic behavior for the metamaterial. For this purpose, it will be considered a simple cubic lattice of periodicity $2a$ made of cubes as that shown in Fig. 1(a) and another similar cubic lattice made of the same cubes but of opposite handedness. Both cubic lattices can be interleaved, as shown in the inset of Fig. 10, to give a simple cubic lattice whose unit cell is formed by two cubes of op-

posite handedness. Since the whole structure is symmetric after inversion (the centers of symmetry are the corners of the cubes), the cross susceptibility κ (which is pseudoscalar) must vanish.[17] Therefore, the whole structure is a balanced isotropic metamaterial with $\kappa=0$. Figure 10 shows the theoretical dispersion relation ($k=k_0\sqrt{\varepsilon_r\mu_r}$) of the proposed structure. A frequency band of backward-wave propagation, corresponding to the condition $\varepsilon_r, \mu_r < 0$, can be observed in the figure. Since the phase vector is now simply given by $k = \omega\sqrt{\varepsilon\mu}$, the unbalanced band gap disappears, and the width of the left-handed frequency band decreases in comparison with that of Fig. 3. The wave impedance is also given by Eq. (6). That is, it is almost equal to the free space impedance, which ensures good matching to free space for all angles of incidence. From the above considerations, we feel that these
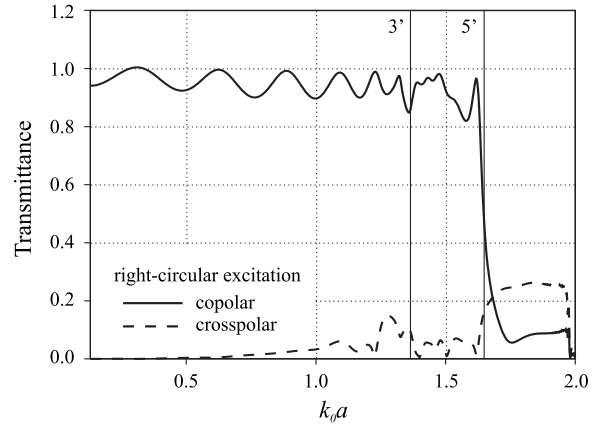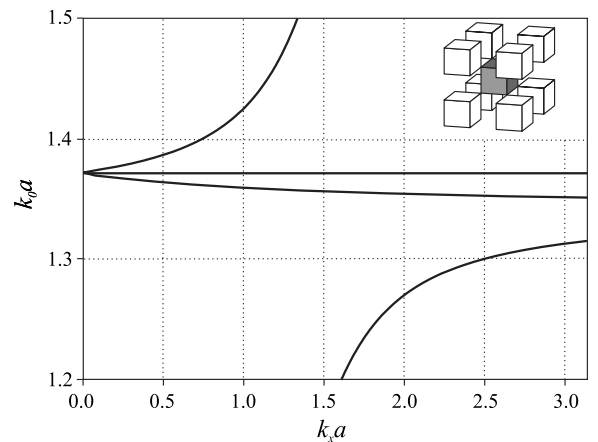
FIG. 10. Theoretical dispersion relation for plane waves propagating in the racemic metamaterial with the simple cubic lattice shown in the inset. Inset: Racemic periodic structure made of two interleaved simple cubic lattices of cubes as that of Fig. 1(a). White cubes are identical to that of Fig. 1(a) and gray cubes are similar cubes made of chiral SRRs of opposite handedness. Chiral SRR parameters are as in Fig. 3 and the periodicity of the structure is $2a$. The fully degenerate longitudinal mode is now located at $\varepsilon_r\mu_r=0$.

racemic isotropic mixtures can be very useful for the design of isotropic regular left-handed metamaterials.

VII. CONCLUSIONS

Periodic NRI metamaterials based on chiral SRRs have been proposed and demonstrated. An analytical theory has been developed for the design of such metamaterials, which has been validated by careful full-wave electromagnetic simulations. It has been shown that simple cubic lattices of chiral SRRs can provide bi-isotropic NRI metamaterials with a well defined frequency band of backward-wave propagation for one of its plane-wave eigenstates. Transmittance through a slab of finite thickness has been analyzed and good matching to free space has been demonstrated. Besides, a racemic simple cubic lattice of chiral SRRs satisfying the appropriate symmetry has been proposed in order to provide ordinary NRI isotropic left-handed metamaterials with a well defined band of backward-wave propagation for all its plane-wave eigenstates. Good matching to free space is also expected for these last designs. Besides good matching to free space, the proposed structures have the advantage of being made of a single kind of inclusions, a fact that substantially simplifies their design and fabrication. Applications of the reported concepts in the design of lenses, antennas, and other NRI metamaterial based devices can be envisaged.

ACKNOWLEDGMENTS

*l_jelinek@us.es

†marques@us.es

‡mesa@us.es

§jdbaenad@unal.edu.co

[1] V. G. Veselago, Sov. Phys. Usp. **47**, 509 (1968).

[2] D. R. Smith, W. J. Padilla, D. C. Vier, S. C. Nemat-Nasser, and S. Schultz, Phys. Rev. Lett. **84**, 4184 (2000).

[3] D. R. Smith and D. Schurig, Phys. Rev. Lett. **90**, 077405 (2003).

[4] T. Koschny, L. Zhang, and C. M. Soukoulis, Phys. Rev. B **71**, 121103(R) (2005).

[5] I. Vendik, O. Vendik, I. Kolmarov, and M. Odit, Opto-Electron. Rev. **14**, 179 (2006).

[6] A. Grbic and G. V. Eleftheriades, J. Appl. Phys. **98**, 043106 (2005).

[7] M. Zedler, C. Caloz, and P. Russer, IEEE Trans. Microwave Theory Tech. **55**, 2930 (2007).

[8] C. Monzon and D. W. Forester, Phys. Rev. Lett. **95**, 123904 (2005).

[9] J. B. Pendry, Phys. Rev. Lett. **85**, 3966 (2000).

[10] S. Tretyakov, *Analytical Modeling in Applied Electromagnetism* (Artech House, Norwood, 2003).

[11] S. A. Tretyakov, A. Sihvola, and L. Jylh, Photonics Nanostruct. Fundam. Appl. **3**, 107 (2005).

[12] J. B. Pendry, Science **306**, 1353 (2004).

[13] R. Marqués, L. Jelinek, and F. Mesa, Microwave Opt. Technol. Lett. **49**, 2006 (2006).

[14] J. A. Kong, *Electromagnetic Wave Theory* (EMW, Cambridge, 2000).

[15] T. G. Mackay, Microwave Opt. Technol. Lett. **45**, 120 (2005).

[16] J. D. Baena, L. Jelinek, and R. Marqués, Phys. Rev. B **76**, 245115 (2007).

[17] L. D. Landau, E. M. Lifshitz, and L. P. Pitaevskii, *Electrodynamics of Continuous Media*, 3rd ed. (Pergamon, New York, 1984).

[18] R. Marqués, F. Mesa, L. Jelinek, and J. D. Baena, in *Proceedings of Metamaterials 2007*, Rome, Italy (Metamorphose VI-AISBL, Louvaine-la-Neuf, Belgium, 2007), p. 214.

[19] R. Marqués, F. Mesa, J. Martel, and F. Medina, IEEE Trans. Antennas Propag. **51**, 2572 (2003).

[20] In practical designs, a very low dielectric substrate (foam, for instance) could be introduced between the rings in order to provide mechanical stability and the bridges between them substituted by standard via-hole connections.

Appendix 7

This appendix contains a full text of Ref. [26]

NEGATIVE REFRACTION FROM BALANCED QUASI-PLANAR CHIRAL INCLUSIONS

Ricardo Marqués,[1] Lukas Jelinek,[2] and Francisco Mesa[3]
[1] Department of Electronics and Electromagnetism, Facultad de Física, Avd. Reina Mercedes s/n, 41012-Seville, Spain;
Corresponding author: marques@us.es
[2] Department of Electromagnetic Field, Czech Tech University, Prague, Czech Republic
[3] Department of Applied Physics 1, ETS de Ingeniería Informática, University of Seville, Avda. Reina Mercedes s/n, 41012-Seville, Spain;
Corresponding author: mesa@us.es

ABSTRACT: *This work proposes a quasi-planar chiral resonator suitable for the design of negative refractive index metamaterials. It is presented as an analytical model to determine the metamaterial polarizabilities, which is also the basis of a further study of the viability of negative refraction in chiral and racemic arrangements of inclusions made up with the proposed quasi-planar chiral resonator. The present analysis is expected to pave the way for the design and building of feasible negative refractive index metamaterials whose inclusions can be manufactured by means of standard photo-etching techniques.* © 2007 Wiley Periodicals, Inc. Microwave Opt Technol Lett 49: 2606–2609, 2007; Published online in Wiley InterScience (www.interscience.wiley.com). DOI 10.1002/mop.22736

Key words: *negative refraction; metamaterials*

1. INTRODUCTION

The main aim of this work is to explore the possibility of obtaining negative refraction in a medium made of a random arrangement of quasi-planar chiral inclusions. Artificial bi-isotropic chiral media made of random arrangements of metallic chiral inclusions are known since long, after the works of Lindmann [1]. More recently, a mixture of such inclusions was proposed in [2] as a way to obtain negative refractive index metamaterials, a proposal further developed in [3] and [4]. Negative refraction in a mixture of chiral inclusions and resonant wires was also analyzed in [5]. The main advantage of using chiral elements to provide negative refraction is that only one kind of inclusions is necessary to obtain negative values of ε and μ simultaneously. If the design of this particle was quasi-planar, a key additional advantage would come from the possibility of using conventional printed-circuit fabrication techniques to manufacture such inclusions.

2. THE PROPOSED INCLUSION

The inclusion proposed here is depicted in Figure 1, which basically shows a broadside-coupled version of the two-turn spiral resonator (2-SR) already proposed by some of the authors in [6]. The analysis in that paper shows that the proposed element can be characterized by a quasi-static LC circuit, where L is the inductance of a single ring with the same radius and width as the inclusion, and $C = 2\pi r C_{\mathrm{pul}}$ is the total capacitance between the rings. There are, however, two main differences between the structure of Figure 1 and the 2-SR analyzed in [6]. First, due to the broadside coupling of the proposed inclusion, the distributed capacitance between the rings can be very large, thus reducing the electrical size of the inclusion near the resonance. Second, when the element is excited near the resonance, there will appear strong magnetic and electric dipoles oriented parallel to the resonator axis. The electric dipole comes from the strong electric field between the upper and lower rings that appear near the resonance.

Neglecting losses and following the analysis in [6], the circuit equation for the total current in the element (i.e., for the sum of the currents excited on both rings, which must be angle-independent [6]) can be written as

$$\left(\frac{1}{j\omega C} + j\omega L \right) I = \varepsilon, \tag{1}$$

where ε represents the external voltage excitation, given by

$$\varepsilon = \begin{cases} -j\omega\pi r 2 B_z^{\mathrm{ext}}, & \text{magnetic excitation} \\ t C_0/C E_z^{\mathrm{ext}}, & \text{electric excitation,} \end{cases} \tag{2}$$

where r is the mean radius of the inclusion, B_z^{ext} the z-component of the external magnetic field, t the substrate thickness, E_z^{ext} the z-component of the external electric field, and C_0 the total capacitance between the rings in the absence of the dielectric substrate. (The factor C_0/C is introduced to account for the multiplicative factor that modifies the electric field inside the capacitor when this is excited by a normal external field). From the above equations, the electric and magnetic moments excited in the inclusion when subjected to external electric and/or magnetic fields can be obtained following the same procedure already reported in [7]:

$$m_z = \alpha_{zz}^{\mathrm{mm}} B_z^{\mathrm{ext}} - \alpha_{zz}^{\mathrm{em}} E_z^{\mathrm{ext}} \tag{3}$$

$$p_z = \alpha_{zz}^{\mathrm{ee}} E_z^{\mathrm{ext}} + \alpha_{zz}^{\mathrm{em}} B_z^{\mathrm{ext}}, \tag{4}$$

where

$$\alpha_{zz}^{\mathrm{mm}} = \frac{\pi^2 r 4}{L} \left(\frac{\omega_0^2}{\omega^2} - 1 \right)^{-1} \tag{5}$$

$$\alpha_{zz}^{\mathrm{em}} = \pm j\pi r^2 t C_0 \frac{\omega_0^2}{\omega} \left(\frac{\omega_0^2}{\omega} - 1 \right)^{-1} \tag{6}$$

$$\alpha_{zz}^{\mathrm{ee}} = t^2 C_0^2 L \frac{\omega_0^4}{\omega^2} \left(\frac{\omega_0^2}{\omega^2} - 1 \right)^{-1}, \tag{7}$$

with $\omega_0 = \sqrt{1/LC}$ being the resonance frequency. From (5)–(7) it is found the following useful identity:

$$\alpha_{zz}^{\mathrm{mm}} \alpha_{zz}^{\mathrm{ee}} = -(\alpha_{zz}^{\mathrm{em}})^2. \tag{8}$$

It should be noted that the proposed inclusion also presents non-resonant electric polarizabilities in the transverse z-plane, $\alpha_{xx}^{\mathrm{ee}}$ and $\alpha_{yy}^{\mathrm{ee}}$, [7]. However, since these polarizabilities are almost constant with frequency and not very large, they can be neglected in a first approximation.

When N chiral inclusions are randomly assembled, the resulting medium becomes bi-isotropic with constitutive relations given by

$$\mathbf{D} = \varepsilon_0(1 + \chi_{\mathrm{e}})\mathbf{E} + j\sqrt{\varepsilon_0\mu_0}\kappa\mathbf{H} \tag{9}$$

$$\mathbf{B} = -j\sqrt{\varepsilon_0\mu_0}\kappa\mathbf{E} + \mu_0(1 + \chi_{\mathrm{m[b]}})\mathbf{H}. \tag{10}$$

The electric, χ_{e}, magnetic, χ_{m}, and cross, κ, susceptibilities are related to the inclusion polarizabilities through

$$\chi_{\mathrm{e}} = \frac{N}{\Delta \varepsilon_0} \frac{\alpha_{zz}^{\mathrm{ee}}}{3} \tag{11}$$

$$\chi_{\mathrm{m}} = \frac{N\mu_0}{\Delta} \frac{\alpha_{zz}^{\mathrm{mm}}}{3} \qquad (12)$$

$$\kappa = \pm j \frac{N}{\Delta} \sqrt{\frac{\mu_0}{\varepsilon_0}} \frac{\alpha_{zz}^{\mathrm{em}}}{3}, \qquad (13)$$

where the factor 1/3 arises from the random arrangement and Δ is a common factor that depends on the homogenization procedure. If Lorentz local field theory is used for the determination of the local field seen by each inclusion, and (8) is taken into account, this factor is given by

$$\Delta = 1 - \frac{N}{9}\left\{ \frac{\alpha_{zz}^{\mathrm{ee}}}{\varepsilon_0} + \mu_0 \alpha_{zz}^{\mathrm{mm}} \right\}. \qquad (14)$$

From (8) and (11)–(13) it follows that

$$\chi_{\mathrm{e}}(\omega)\chi_{\mathrm{m}}(\omega) = [\kappa(\omega)]^2. \qquad (15)$$

3. NEGATIVE REFRACTION

As it is well known, the general dispersion equation for plane waves in lossless chiral media is

$$k = \pm k_0 (\sqrt{(1 + \chi_{\mathrm{e}})(1 + \chi_{\mathrm{m}})} \pm \kappa), \qquad (16)$$

where $k_0 = \omega \sqrt{\varepsilon_0 \mu_0}$ is the free-space wavenumber. The four solutions of (16) correspond to right- and left-hand circularly polarized waves, depending on the sign of κ. To avoid complex solutions of (16), and therefore forbidden frequency bands for plane wave propagation, it would be desirable that $\chi_{\mathrm{e}}(\omega) = \chi_{\mathrm{m}}(\omega)$. According to (15) this implies that

$$\chi_{\mathrm{e}}(\omega) = \chi_{\mathrm{m}}(\omega) = |\kappa(\omega)|, \qquad (17)$$

namely, the electric and magnetic responses of the inclusions should be very similar [4].

The general conditions for backward-wave propagation in chiral media were analyzed in [8], and can be summarized as

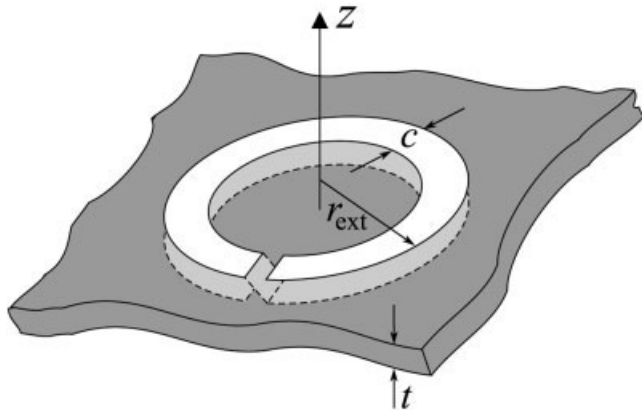$$\sqrt{\epsilon_{\mathrm{r}}\mu_{\mathrm{r}}} \pm \kappa < 0, \qquad (18)$$

Figure 1   The proposed inclusion is formed by two identical conducting rings etched on both sides of a dielectric substrate and connected by a via in order to obtain an helicoidal shape
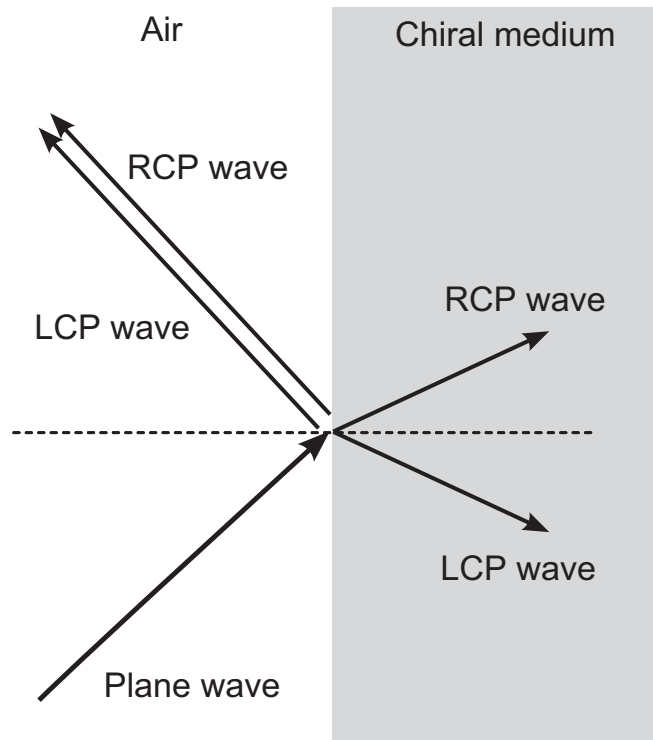

Figure 2   Illustration of the negative refraction of a linearly polarized wave at the interface with a chiral metamaterial made of inclusions such as that shown in Figure 1. Only one of the two eigenwaves that can propagate in the chiral medium shows negative refraction while the reflected wave is elliptically polarized. RCP, right-handed circularly polarized; LCP, left-handed circularly polarized

where the negative sign of the square root has to be chosen if ε_{r} and μ_{r} are both negative. According to (18), if $\kappa^2 > |\epsilon_{\mathrm{r}}\mu_{\mathrm{r}}|$, only one of the solutions of (16) can be a backward-wave and therefore will experience negative refraction at the interface with ordinary media. This is indeed the case when (17) is satisfied and both χ_{e} and χ_{m} are negative. In such case, negative refraction will take place for only one of the eigenmodes of (16) provided that $\chi_{\mathrm{e}} = \chi_{\mathrm{m}} = |\kappa| < -0.5$. This condition is less restrictive than the condition found for ordinary media (for instance, for a balanced mixture of inclusions of opposite helicity): $\chi_{\mathrm{e}}, \chi_{\mathrm{m}} < -1$. The price to pay for this bandwidth enlargement is that only one of the circularly polarized wave solutions of (16) will show negative refraction. This scenario is illustrated in Figure 2, where an incident linearly polarized plane wave is considered

Returning to the inclusions, it is found from (11)–(13) that condition (17) is satisfied provided that

$$c_0^2 \alpha_{zz}^{\mathrm{ee}}(\omega) = \alpha_{zz}^{\mathrm{mm}}(\omega) = \pm j c_0 \alpha_{zz}^{\mathrm{em}}(\omega), \qquad (19)$$

where c_0 is the velocity of light in vacuum. In principle, this condition is compatible with (5)–(7), which makes it possible to find particular designs that satisfy this condition by using the analytical expressions for L and C_{pul} reported in [7]. A substrate with permittivity similar to free space (a foam for instance) has been chosen in order to simplify the computations. With this substrate ($\varepsilon = \varepsilon_0$), a suitable design can be: width of the strips $c = 2$ mm, external radius $r_{\mathrm{ext}} = r + c/2 = 5$ mm, and separation between strips $t = 2.35$ mm. Following [7], the resonance frequency of the proposed configuration should be

about 2.3 GHz, which gives an electrical size for the inclusion ($\sim\lambda/13$) that is acceptable for a practical metamaterial design.

To validate our analytical results, the electric and magnetic polarizabilities of the inclusions have been numerically computed following the procedure described in [9]. This procedure mainly consists in placing the particle inside a TEM waveguide and to determine the polarizabilities from the loaded waveguide's reflection and transmission coefficients (see [9] for more details). The results for the meaningful quantities $\mu_0\alpha_{zz}^{mm}$ and $\alpha_{zz}^{ee}/\epsilon_0$ are plotted in Figure 3, which shows a behavior for these quantities in accordance with the predictions of our analytical model.

The frequency bandwidth for negative refraction in a metamaterial made of a random arrangement of the proposed inclusions can be computed from the values of the electric susceptibility χ_e of such medium (11) with Δ given by (14). Thus, taking the dimensions and characteristics of the inclusions as those previously reported (the number of inclusions per unit volume is set to $N = (12)^{-3}$ mm^{-3}), Figure 4 shows the analytical results together with the numerical ones obtained from the data in Figure 3. According to the previous analysis and the presented numerical results, the curves for the magnetic, χ_m, and cross, κ, susceptibilities (not shown in Fig. 3) must be quite similar. Although Figure 4 shows some differences between the analytical and numerical results, the qualitative agreement is apparent. In both cases, a significant negative refraction frequency band appears for both the random and the racemic mixtures. As already mentioned, such frequency bands are limited by the straight lines $\chi_e = -0.5$ and $\chi_e = -1$, respectively (see Fig. 4).

Since the proposed inclusions show a balanced electric and magnetic response (that is, (19) is satisfied), it follows from (17) and (16) that there are no forbidden frequency bands for plane wave propagation in the considered chiral medium. This implies that the transition from backward to forward propagation occurs through a point of zero phase velocity and nonzero group velocity, a fact that recalls the behavior of balanced right/left-handed transmission lines reported in [10]. Needless to say, a similar behavior
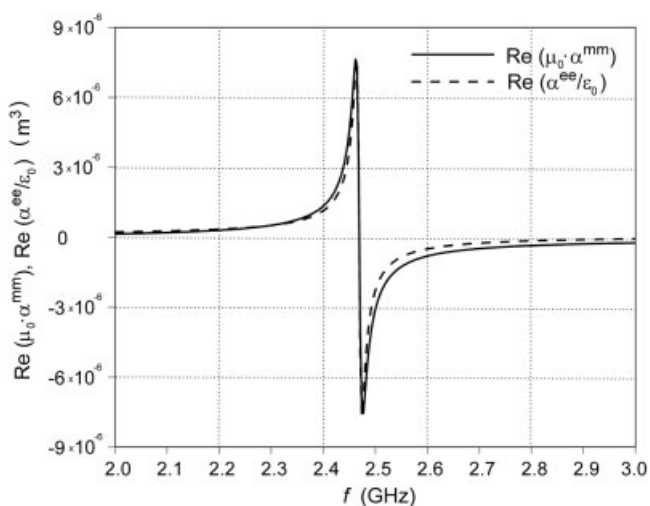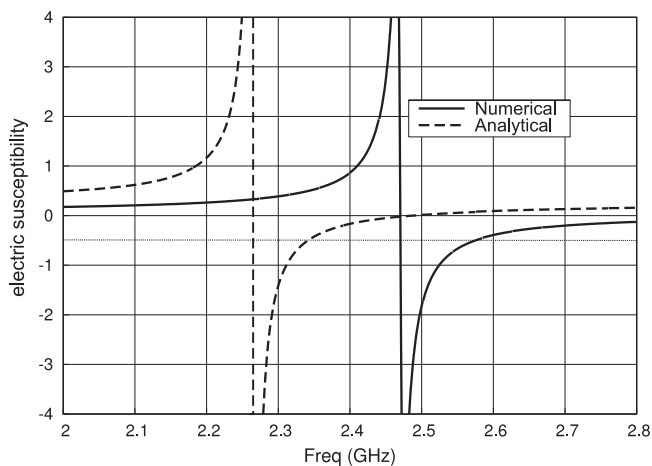

Figure 4 Analytical and numerical results for the electric susceptibility χ_e of a random arrangement of chiral inclusions as those shown in Figure 1. The parameters of the inclusions are given in the text and are the same as in Figure 3. The average volume per inclusion is $V = 12^3$ mm^3

would appear in racemic mixtures of the proposed inclusions, where the propagation constant for plane waves is given by $k = \pm k_0\sqrt{(1 + \chi_e)(1 + \chi_m)}$.

4. CONCLUSION

The feasibility of negative refractive index metamaterials made of a random arrangement of balanced chiral quasi-planar inclusions has been analyzed. It has been proposed that a specific design amenable of being easily manufactured by means of the standard photo-etching techniques. The proposed design has been found to provide the necessary behavior for all the resonant polarizabilities in order to produce a significant negative refractive index bandwidth near the resonance. Finally, it has been shown that a behavior quite similar to the previously reported balanced right/left-handed transmission lines can be achieved in three-dimensional arrangements of the proposed inclusions.

REFERENCES

1. K.F. Lindmann, Rotation polarisation of electromagnetic waves generated by the isotropic system of spiral resonators, Annalen der Physik 63 (1920), 621-644.
2. S.A. Tretyakov. Analytical modeling in applied electromagnetics, Artech House, Norwood, MA, 2003.
3. S.A. Tretyakov, I. Nefedov, A. Sihvola, S. Maslowski, and C. Simowski, Waves and energy in chiral nihility, J Electromagnetic Waves Appl 5 (2003), 695-706.
4. S.A. Tretyakov, A. Sihvola, and L. Jylh, Backward-wave regime and negative refraction in chiral composites, arXiv:cond-mat/0509287v1, 2005.
5. J.B. Pendry, A chiral route to negative refraction, Science 306 (2004), 1353-1355.
6. J.D. Baena, R. Marqués, F. Medina, and J. Martel, Artificial magnetic metamaterial design by using spiral resonators, Phys Rev B 69 (2004), 014402.
7. R. Marqués, F. Mesa, J. Martel, and F. Medina, Comparative analysis of edge and broadside coupled split ring resonators for metamaterial

Figure 3 Numerical computation of $\mu_0\alpha_{zz}^{mm}$ and $\alpha_{zz}^{ee}/\epsilon_0$ for the inclusion shown in Figure 1. Width of the strips $c = 2$ mm, external radius $r_{ext} = r + c/2 = 5$ mm, and separation between strips $t = 2.35$ mm

design, theory and experiment, IEEE Trans Ant Propag 51 (2003), 2572-2581.

8. T.G. Mackay, Plane waves with negative phase velocity in isotropic chiral mediums, Microwave Opt Tech Lett 45 (2005), 120-121.

9. L. Jelinek, J.B. Baena, R. Marqués, and J. Zehentner, Direct polarisability extraction method, Proceeding of the 36th European Microwave Conference, Manchester, England 2006, p. 983.

10. C. Caloz and T. Itoh, Electromagnetic metamaterials: Transmission line theory and microwave applications, Wiley, New York, 2006.

NUMERICAL ASPECTS IN THE ANALYSIS OF INFINITE REGULAR AND RANDOM HELIX ARRAYS

Christian Meiners and Arne F. Jacob
Institut für Hochfrequenztechnik, Technische Universität Hamburg-Harburg, Denickestr. 22, 21073 Hamburg, Germany; Corresponding author: christian.meiners@tuhh.de

ABSTRACT: *This contribution focuses on a scattering description of infinite arrays of small metallic helices. The latter are assumed to scatter like dipoles. A numerical approach is extended to account for the influence of the lattice with more precision. This is done by a simple extrapolation scheme, which accelerates the convergence of the arising series. For regular arrays, a comparison with a commercial software tool reveals a good agreement, at least as long as the distance between the particles is large enough for the dipole assumption to be valid. This also applies at resonance, the most critical case. The effects on random arrays are also investigated.* © 2007 Wiley Periodicals, Inc. Microwave Opt Technol Lett 49: 2609–2613, 2007; Published online in Wiley InterScience (www.interscience.wiley.com). DOI 10.1002/mop.22788

1. INTRODUCTION

For numerical reasons, the properties of finite but large arrays of antennas or scatterers are commonly estimated by applying periodic boundary conditions to a unit cell, i.e., considering the infinite case [1–3]. Depending on the applied numerical technique, e.g., a method of moments [4] approach, this may require a summation of the fields of the elements in the original cell and its spatial repetitions to account for mutual coupling. As these series converge very slowly in space domain, several methods have been investigated to speed up this process (see, e.g., [5–7]).

This article is mainly concerned with the case of arrays of small metallic helices. The adopted methodology follows from previous work [8]. Thereby the fields of each particle are expanded into spherical waves that render the fields of its multipole moments. Periodic boundaries are implemented by re-expanding the fields of neighboring cells into spherical waves with respect to the global origin and a subsequent summation. This series converges slowly. It is shown in the course of the present article that a simple extrapolation scheme can be effectively used to speed up the convergence of the sum in space domain. The improved accuracy of the method is illustrated by a sample regular helix configuration. A comparison with a commercial software tool using finite elements is drawn to assess the validity of the approach as well as the quality of the dipole assumption for the helices.

The evaluation of the required sum described above is independent of the arrangement of scatterers within a unit cell. Thus, we finally apply the more precise method to the setup of [8] to investigate to what extent the results are affected if randomly located inclusions are considered and a subsequent averaging procedure to homogenize the layer is applied.

2. NUMERICAL TECHNIQUE

The main focus of this section is on the method used to sum up the fields of the infinite array. The underlying scattering theory is described in [8]. Nevertheless, for clarity, the main ideas are briefly reviewed below. This is also expedient since some of the involved approximations have to be addressed.

2.1. Scattering Approach

Each helix is supposed to scatter like a dipole. This is plausible for observation points far away from the scatterer. As shown in [8], this is also a reasonable assumption if a material made of randomly oriented helices is considered and a certain minimum distance between the inclusions is preserved. This randomness does not occur here, so that the influence of this approximation is investigated later on. We use the dipole-polarizabilities of the helices to account for mutual coupling within the scattering approach. They are determined quasi-analytically from the inverse system matrix arising from the method of moments [9]. To keep the number of unknowns small, a thin-wire approximation is used. Thereby, global (harmonic) basis functions render the currents on the helix.

A number of N_c particles is arranged within a unit cell, which is then periodically repeated to form an infinite two-dimensional array. In the present context, i.e., plane wave incidence, the number of unknowns reduces to the number of spherical waves required to describe the scattering of the elements in the original unit cell centered at the global origin (in case of the dipole approximation: six per helix). In the following, this cell will be denoted as "simulated cell." If the complex spherical wave amplitudes of each particle i in the simulated cell are written as vector $\mathbf{b}_i$, they can be obtained by the following relationship [8, 10]

$$\underline{\mathbf{b}}_i = \underline{\mathbf{a}}_i + \underline{\underline{\boldsymbol{\tau}}}_i \cdot (\underline{\underline{\boldsymbol{\xi}}}^b(\underline{\mathbf{r}}_i) \cdot \underline{\mathbf{Y}} + \sum_{j=1, j \neq i}^{N_c} \underline{\underline{\boldsymbol{\xi}}}^h(\underline{\mathbf{r}}_i - \underline{\mathbf{r}}_j) \cdot \underline{\mathbf{b}}_j).$$

Here, the mutual coupling between the particles is accounted for by the matrices $\underline{\underline{\boldsymbol{\xi}}}^b$ and $\underline{\underline{\boldsymbol{\xi}}}^h$ that comprise the Cartesian components of different types of spherical waves (depending on their radial dependence) and $\underline{\underline{\boldsymbol{\tau}}}_i$, which transforms these "incident" fields into the corresponding expansion coefficients that represent the excited dipoles [8, 11]. The coefficients for the case, if only the external excitation were present, are denoted by the vector $\underline{\mathbf{a}}_i$. The vector $\underline{\mathbf{Y}}$ represents the fields of the particles positioned outside the simulated cell—the part that is obtained by summing up the fields of neighboring cells in space domain until convergence is achieved:

$$\underline{\mathbf{Y}} = \sum_{l=1}^{\infty} \underline{\underline{\boldsymbol{\alpha}}}(\underline{\mathbf{r}}_{0l}) \cdot \sum_{j=1}^{N_c} \underline{\underline{\boldsymbol{\beta}}}(\underline{\mathbf{r}}_{0j}) \cdot \underline{\mathbf{b}}_j.$$

The subscript l denotes the index of the considered cell. The index of the simulated cell is $l = 0$. In the above, the translation matrices $\underline{\underline{\boldsymbol{\beta}}}$ and $\underline{\underline{\boldsymbol{\alpha}}}$ [12] are used to re-expand the scattered fields into spherical harmonics with respect to the global origin. The expansion is performed in two steps: Firstly, the translation from each particle to the origin of the cell to which it is assigned ($\underline{\underline{\boldsymbol{\beta}}}(\underline{\mathbf{r}}_{0j})$) and

Appendix 8

This appendix contains a full text of Ref. [29]

An FET-Based Unit Cell for an Active Magnetic Metamaterial

Lukas Jelinek and Jan Machac, *Senior Member, IEEE*

Abstract—A particle that can be used to create an active magnetic metamaterial has been designed using an FET transistor loaded in its gate by a conducting ring and in its source by a parallel resonance circuit. The design procedure is discussed, and the working principle is experimentally demonstrated in the RF range.

Index Terms—Artificial materials, FET circuits, negative resistance devices, oscillators, polarizability.

I. INTRODUCTION

IN THE present state of the art, artificially made lattices of conducting rings terminated by a properly chosen impedance are considered a standard way of implementing magnetic metamaterials, i.e., artificial media with negative permeability [1], [2]. Materials made of conducting rings are also behind the practical realization of super-resolution lenses [3] and of cloaking devices [4]. Unfortunately, it is well known [4], [5] that the intrinsic losses of the rings and their loads are responsible for great degradation of lens and cloaking properties in comparison to their lossless theoretical proposals. Passive reduction of losses by a proper choice of their geometry is very limited [6], and thus active elements seem to be the only way out of this problem. The first proposal for using active elements in the ring metamaterial was published in 2001 [7] and used a negative impedance converter (NIC) as a load. The NIC in [7] was designed using an ideal operational amplifier, a component that works in a realistic implementation (with current technology) only up to the low RF range. A much simpler design of NIC has recently been used in [8]–[10]. A two-transistor implementation that offers a much wider frequency range of operation has been used in these works. In addition to loading rings with NIC, other authors have used two-port amplifiers to create an active magnetic metamaterial [11], [12]. These designs, however, suffer from the need for input and output coils, which enlarge the unit cell and are necessarily coupled. In addition, the necessary two-port monolitic amplifier and phase shifter are difficult to make at high frequencies.

The design presented in this letter uses a one-port approach, i.e., it uses a ring loaded by a one-port device offering at a given

The authors are with the Department of Electromagnetic Field, Czech Technical University in Prague, 16627 Prague, Czech Republic (e-mail: l_jelinek@us.es).
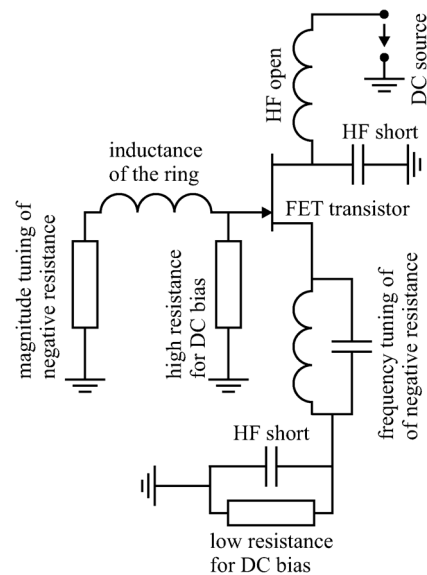
Fig. 1. Scheme of a ring loaded by a negative resistance transistor circuit. A JFET transistor is used, however any other FET transistor could be used.

frequency a negative real part of impedance. Three main principles can be used to create this negative resistance. The first principle involves the Gunn diode [13], an element that is widely used for microwave oscillators up to subterahertz range. Unfortunately, the Gunn diode needs considerable cooling, as it works with a high dc bias, and the bulky nature of the sink preclude its use for metamaterial design. The second principle uses the above-mentioned NIC, which is a two-port device that images the loading impedance Z on one port into an impedance $-Z$ on the other port [14]. A major review of possible NIC designs has been published in [15] and [16]. It is shown that at least two transistors are needed for NIC design. The third principle is the use of a single transistor loaded in its source by a proper impedance, which makes it conditionally unstable. This is a common way of making HF oscillators, and it is the principle that we employ in our design. It offers the smallest size, the simplest assembly, and even higher operating frequency than NIC.

II. DESIGN APPROACH

Our design (see Fig. 1) is mostly inspired by [17], where the structure was used for an active antenna array. As can be seen, the circuit is based on a JFET transistor connected in a common drain mode, which is loaded at its gate by a ring and by a tuning impedance, and which has a parallel resonance circuit connected to its source. On the transistor gate, the negative resistance will appear when operating above the resonance frequency (the capacitive loading of the source) and will disappear at frequencies

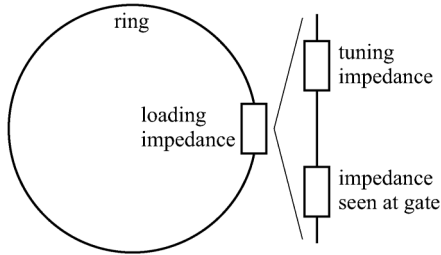Fig. 2.   Situation as seen by the ring.

Fig. 3.   Input impedance of the prototype at the transistor gate.

high enough to make a low-impedance connection between gate and source (through the internal gate-source capacitance). The negative resistance is thus limited to a given frequency band. This is important in order to preclude self-maintained oscillations of the transistor, as will be discussed later. The tuning impedance in the gate serves to compensate the total impedance of the ring circuit in order to obtain the strongest possible response. The scenario from the point of view of the ring is depicted in Fig. 2. If properly tuned, the total impedance of the ring (the self-inductance plus the load) should be small in absolute value to obtain a strong response and should have a negative real part in order to obtain a gain. The concept of Fig. 2 allows us to write the magnetic polarizability of the proposed particle as [2]

$$\alpha = -\frac{\mathrm{j}\omega S^2}{Z} = -\frac{\mathrm{j}\omega S^2}{\mathrm{j}\omega L_{\mathrm{ring}} + Z_{\mathrm{tune}} + Z_{\mathrm{gate}}} \qquad (1)$$

with S as the area of the loop. For our purposes, the polarizability will be further normalized as

$$\alpha_{\mathrm{n}} = \frac{\mu_0 \alpha}{V} = -\mathrm{j}\frac{2\pi^3 N^2 (r_0/\lambda_0)}{(Z/Z_0)(V/r_0^3)} \qquad (2)$$

where V is the volume occupied by the particle, r_0 is the mean radius of the ring, which is assumed to be made of N turns, λ_0 is a free-space wavelength at the operating frequency, and Z_0 is the free-space impedance. Using (2), a rough estimate of the permeability of a cubic lattice of such particles can be written as $\mu_{\mathrm{r}} \approx 1 + \alpha_{\mathrm{n}}$.

A. Frequency Tuning and Stability

In the frequency range of intended operation, the impedance seen at the gate of the transistor has a capacitive imaginary part. From that point of view, the situation is identical to an ordinary split-ring resonator (SRR), where an inductive loop is loaded by a capacitance. However, the presented circuit, unlike in SRR, also imposes some positive or negative (depending on frequency) real part of the impedance $\mathrm{Re}(Z)$. Denoting the frequency where $\mathrm{Im}(Z)$ crosses zero as ω_{Im}, the full list of possible responses is as follows:

$$\begin{array}{l|l}
\omega < \omega_{\mathrm{Im}} \Rightarrow \mathrm{Re}(\alpha) > 0 & \mathrm{Im}(\alpha) < 0 \text{ for } \mathrm{Re}(Z) > 0 \\
& \mathrm{Im}(\alpha) > 0 \text{ for } \mathrm{Re}(Z) < 0 \\[4pt]
\omega = \omega_{\mathrm{Im}} \Rightarrow \mathrm{Re}(\alpha) = 0 & \mathrm{Im}(\alpha) < 0 \text{ for } \mathrm{Re}(Z) > 0 \\
& \text{unstable for } \mathrm{Re}(Z) < 0 \\[4pt]
\omega > \omega_{\mathrm{Im}} \Rightarrow \mathrm{Re}(\alpha) < 0 & \mathrm{Im}(\alpha) < 0 \text{ for } \mathrm{Re}(Z) > 0 \\
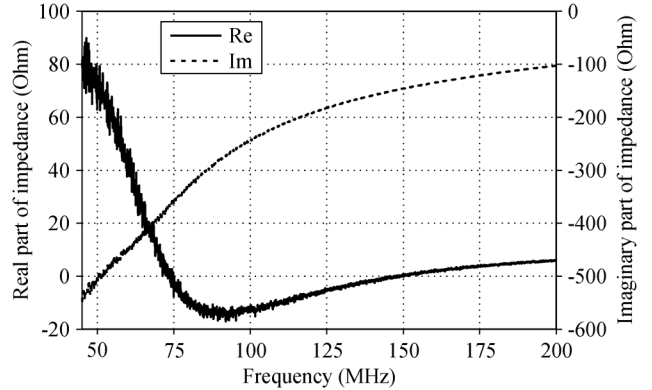& \mathrm{Im}(\alpha) > 0 \text{ for } \mathrm{Re}(Z) < 0.
\end{array} \qquad (3)$$

For our purposes (a magnetic metamaterial with negative real part of permeability), we are interested in the case of $\omega > \omega_{\mathrm{Im}}$. However, care must be taken of the stability, otherwise the particle could become a generator. In Section III, it will be shown that in the region of interest the total impedance Z can be approximated as

$$Z \approx A(\omega - \omega_{\mathrm{Re}}) + \mathrm{j}B(\omega - \omega_{\mathrm{Im}}) \qquad (4)$$

where $A < 0$, $B > 0$, and where $\omega_{\mathrm{Re}}/\omega_{\mathrm{Im}}$ are frequencies at which real/imaginary part of Z crosses zero. Substituting (4) in (1) leads to (in this frequency band)

$$\alpha \sim \frac{\mathrm{j}\omega}{\mathrm{j}\omega + p_0} \qquad (5)$$

with

$$\mathrm{Re}(p_0) = \frac{-AB(\omega_{\mathrm{Re}} - \omega_{\mathrm{Im}})}{B^2 + A^2}. \qquad (6)$$

Equation (6) implies that in order to ensure the stability $(\mathrm{Re}(p_0) > 0)$ of the proposed particle, $\omega_{\mathrm{Re}} > \omega_{\mathrm{Im}}$ must hold, i.e., the imaginary part of the total impedance needs to cross zero earlier than the real part.

III. FABRICATION AND MEASUREMENT

In order to prove the working principle of the proposed active ring, the frequency neighborhood of 100 MHz has been used, as it allows for easy handmade implementation and it is close to the frequency used in common MRI machines—one of the important fields of metamaterial applications [3], [18]. A prototype was built using a JFET J310 transistor, which is commonly used in VHF amplifiers. The parameters of the parallel resonant circuit in the source of the transistor were set to $f_{\mathrm{r}} \approx 60$ MHz, $\sqrt{L/C} \approx 30\ \Omega$, and $R \approx 50\ \Omega$. After setting the bias so that the drain-source dc current was $I_{\mathrm{DS}} \approx 12$ mA, the impedance between the transistor gate and the common node was measured through the connected SMA connector on the vector network analyzer (VNA); see Fig. 3. The negative real part of the impedance can be appreciated in the frequency interval 75–150 MHz together with the capacitive imaginary part. According to Section II-A, the imaginary part of the gate input impedance needs to be compensated just below $f \approx 73$ MHz,
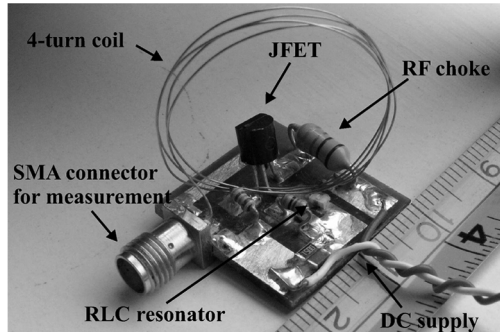
Fig. 4. Photograph of a realistic implementation of the ring loaded by a negative resistance circuit. The ring is actually a four-turn coil made of thin wire.
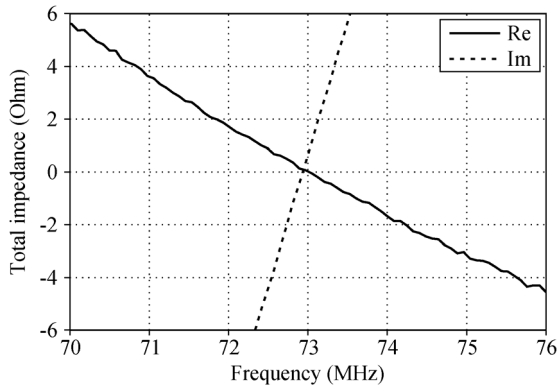

Fig. 5. Detail of the frequency band in which the real and the imaginary part of the total impedance crosses zero. Note how the imaginary part passes zero earlier than the real part.

Fig. 6. Frequency dependence of the normalized magnetic polarizability of the particle. The normalization volume was taken as a brick with the external dimensions of the prototype, which is $20 \times 20 \times 30$ mm^3.

Fig. 7. Amplitude of the reflection coefficient measured on the loop magnetically coupled to the active ring.

i.e., at a frequency just before the zero crossing of the real part. Only in this case will we get stable and strong magnetic polarizability with a negative real part and a positive imaginary part. It is also worth noting that in order to obtain low frequency dispersion and thus to make the compensation easier, the parallel resonant circuit in the source of the transistor is highly damped.

In this particular case, the compensation was made by the self-inductance of the connected ring, which was actually made by four turns of wire with diameter $d = 0.2$ mm. The diameter of the loop was $D \approx 25$ mm. The fine frequency tuning was done by a slight change in the separation of the coil turns. The tuning impedance of Fig. 1 was not needed in this case. A photograph of the prototype is shown in Fig. 4.

With the compensating coil connected to the transistor gate, the impedance as seen by the coil induced voltage was once more measured on VNA via the SMA connector. The detail of the zero crossing of the total impedance is depicted in Fig. 5, from which it can be clearly seen that the stability condition, derived in Section II-A, is satisfied. The measured total impedance was then substituted into (2), and the result is plotted in Fig. 6. The negative real part and the positive imaginary part of the normalized polarizability can be clearly observed in the figure in the frequency range of 73–150 MHz. The polarizability values show that the real part of the permeability of a cubic lattice of such particles can easily be cast below zero. Note also that in our case the electrical size of the particle is rather small ($r_0/\lambda_0 \approx 1/320$), and that according to (2) the response will

be much stronger for particles of common metamaterial sizes ($r_0/\lambda_0 \approx 1/20$).

Until now the particle has been measured by directly connected VNA and thus not in the free-space configuration in which it is intended to work in a realistic metamaterial. To this point the SMA connector has been substituted by a short. The VNA has then been coupled to the particle via a mutual inductance between the active ring and a loop of similar radius connected to the VNA port. The measured amplitude of the reflection coefficient is shown in Fig. 7, from where the amplification peak in the vicinity of 78 MHz can be seen, proving the principle proposed in this letter. In the same setup, the coupling loop has also been connected to a spectrum analyzer. It has been checked that the particle does not self generate any oscillations in the range of 9 kHz–2 GHz, and that what we have at hand is really an active metamaterial element and not a microwave generator.

IV. CONCLUSION

An active particle using a ring loaded by an FET transistor circuit and offering magnetic polarizability with a negative real part and a positive imaginary part has been proposed, designed, and measured. The measurements show that the particle is capable of being used in negative-permeability metamaterial systems, where it can remove losses or even add a gain. The use of

the proposed particle in magnetic lenses and magnetic metasurfaces is envisaged and should be studied in future.

REFERENCES

[1] R. Marqués, F. Martín, and M. Sorolla, *Metamaterials With Negative Parameters: Theory and Microwave Applications*. Hoboken, NJ: Wiley, 2007.

[2] S. Tretyakov, *Analytical Modeling in Applied Electromagnetics*. Norwood, MA: Artech House, 2003.

[3] M. J. Freire, R. Marqués, and L. Jelinek, "Experimental demonstration of a $\mu = -1$ metamaterial lens for magnetic resonance imaging," *Appl. Phys. Lett.*, vol. 93, p. 231108, 2008.

[4] D. Schurig, J. J. Mock, B. J. Justice, S. A. Cummer, J. B. Pendry, A. F. Starr, and D. R. Smith, "Metamaterial electromagnetic cloak at microwave frequencies," *Science*, vol. 314, pp. 977–980, 2006.

[5] R. Marques and J. D. Baena, "Effect of losses and dispersion on the focusing properties of left-handed media," *Microw. Opt. Technol. Lett.*, vol. 41, pp. 290–294, 2004.

[6] S. A. Cummer, B. I. Popa, and T. H. Hand, "Q-based design equations and loss limits for resonant metamaterials and experimental validation," *IEEE Trans. Antennas Propag.*, vol. 56, no. 1, pp. 127–132, Jan. 2008.

[7] S. A. Tretyakov, "Meta-materials with wideband negative permittivity and permeability," *Microw. Opt. Technol. Lett.*, vol. 31, pp. 163–165, 2001.

[8] M. Al-Azab, "Simulation and realization of an active metamaterial cell for GSM/UMTS," *Prog. Electromagn. Res.*, vol. 5, pp. 55–65, 2008.

[9] A. K. S. Hrabar and I. Krois, "Towards active dispersionless ENZ metamaterial for cloaking applications," *Metamaterials*, vol. 4, pp. 89–97, 2010.

[10] P. Jin and R. W. Ziolkowski, "Broadband, efficient, electrically small metamaterial-inspired antennas facilitated by active near-field resonant parasitic elements," *IEEE Trans. Antennas Propag.*, vol. 58, no. 2, pp. 318–327, Feb. 2010.

[11] B. Popa and S. A. Cummer, "An architecture for active metamaterial particles and experimental validation at RF," *Microw. Opt. Technol. Let.*, vol. 49, pp. 2574–2577, 2007.

[12] Y. Yuan, B. Popa, and S. A. Cummer, "Zero loss magnetic metamaterials using powered active unit cells," *Opt. Exp.*, vol. 17, pp. 16 135–16 143, 2009.

[13] J. B. Gunn, "Microwave oscillations of current in 111-V semiconductors," *Solid State Commun.*, vol. 1, pp. 88–91, 1963.

[14] J. G. Linvill, "Transistor negative-impedance converters," *Proc. IRE*, vol. 41, no. 6, pp. 725–725, Jun. 1953.

[15] S. E. Sussman-Fort, "An nic-based negative resistance circuit for microwave active filters," *Int. J. Microw. Millim.*, vol. 4, pp. 130–139, 1994.

[16] S. E. Sussman-Fort, "Gyrator-based biquad filters and negative impedance converters for microwaves," *Int. J. RF Microw. C. E.*, vol. 8, pp. 86–101, 1998.

[17] S. Chung, S. Chen, and Y. Lee, "A novel bi-directional amplifier with applications in active Van Atta retrodirective arrays," *IEEE Trans. Microw. Theory Tech.*, vol. 51, no. 2, pp. 542–547, Feb. 2003.

[18] M. C. K. Wiltshire, J. B. Pendry, I. R. Young, D. J. Larkman, D. J. Gilderdale, and J. V. Hajnal, "Microstructured magnetic materials for RF flux guides in magnetic resonance imaging," *Science*, vol. 291, p. 849, 2001.

Appendix 9

This appendix contains a full text of Ref. [35]

Unified homogenization theory for magnetoinductive and electromagnetic waves in split-ring metamaterials

J. D. Baena,[1,2,*] L. Jelinek,[1,†] R. Marqués,[1,‡] and M. Silveirinha[3,§]

[1]*Departamento de Electrónica y Electromagnetismo, Universidad de Sevilla, 41012 Sevilla, Spain*
[2]*Departamento de Física, Universidad Nacional de Colombia, Bogotá, Colombia*
[3]*Departamento de Engenharia Electrotécnica, Instituto de Telecomunicações, Universidade de Coimbra, 3030 Coimbra, Portugal*

A unified homogenization procedure for split-ring metamaterials taking into account time and spatial dispersion is introduced. It is shown that electromagnetic and magnetoinductive waves propagating in the metamaterial are obtained from this analysis. Therefore, the proposed time and spatially dispersive permeability accounts for the characterization of the complete spectrum of waves of the metamaterial. Finally, it is shown that the proposed theory is in good quantitative and qualitative agreement with full wave simulations.

I. INTRODUCTION

Diamagnetic properties of systems of conducting rings have long been known by physicists. In 1852 Wilhem Weber [1] tried to explain natural diamagnetism (discovered by Faraday some years before) as a consequence of the excitation of induced currents in some hypothetical conducting loops that supposedly existed in diamagnetic materials. In order to enhance the magnetic properties of artificial media (or metamaterials in modern terminology) made from metallic conducting rings, Shelkunoff proposed in 1952 to introduce a capacitor [2], so that the rings become resonant. More recently Pendry *et al.* [3] proposed to replace the capacitively loaded rings by planar split-ring resonators (SRRs) which substitute the lumped capacitor with a distributed capacitance between the rings. Because Pendry's SRRs can be easily manufactured by using standard printed circuit technologies, this design opened the way to manufacturing true magnetic metamaterials made of many individual elements (SRRs) at many laboratories around the world. As a consequence of this resonant behavior, capacitively loaded rings and/or SRRs can produce metamaterials with negative magnetic permeability above resonance. It is also well known [4–6] that when a system of these elements is properly combined with another system of elements (metallic wires or plates, for instance) producing a negative electric permittivity [7], a metamaterial with simultaneously negative permittivity and permeability (or left-handed metamaterial [8]) arises in the frequency band where both subsystems present negative parameters. Remarkably, the electric and magnetic properties of such combinations are, quite approximately, the superposition of the electric and magnetic properties of each subsystem. This superposition hypothesis is not apparent at all (see, for instance, Refs. [9,10]) and, for the specific SRRs and wire configuration proposed in Ref. [4], it can be admitted that it is valid provided the elements of both subsystems

are placed in such a way that their quasistatic fields do not interact or interact weakly [10,11]. Almost simultaneously, other analyses and experiments [12,13] did show that SRR-based metamaterials also support, in some frequency bands, slow waves based on short-range interactions between the SRRs: the so-called magnetoinductive (MI) waves, which cannot be deduced from the usually assumed local magnetic permeability of the metamaterial. Interestingly, many of the physical effects expected in negative permeability and left-handed metamaterials, such as frequency band gaps and frequency bands of backward-wave propagation, also come out from the analysis when the coupling between electromagnetic and MI waves in SRR systems is considered [14], thus providing an alternative explanation for such effects. Although the analysis in Ref. [14] has a great heuristic value, it cannot be considered as fully satisfactory because it only considers one-dimensional systems in the nearest-neighbor approximation. On the other hand, the presence of waves which cannot be deduced from a local time dispersive magnetic permeability in split-ring metamaterials can be expected from the fact that its periodicity is usually not smaller than one tenth of a wavelength. As is well known [15], when the periodicity of a given medium approaches the wavelength of the electromagnetic radiation, it becomes not only time dispersive but also spatially dispersive. Therefore, it can be expected that both electromagnetic and MI waves would come out from the analysis if spatial dispersion in split ring metamaterials were taken into account. In fact, the main purpose of this paper is to develop a spatially dispersive homogenization procedure able to describe both types of waves.

II. ANALYSIS

In order to simplify the analysis, we will consider an ideal metamaterial made of a cubic arrangement of LC circuits supporting current loops as sketched in Fig. 1(a) for a unit cell. We define the current vector $\mathbf{I^n}$ on each unit cell as $\mathbf{I^n} = (I_x^{\mathbf{n}}, I_y^{\mathbf{n}}, I_z^{\mathbf{n}})$, where $\mathbf{n} = (n_x, n_y, n_z)$ specifies the location of each unit cell in the lattice and $I_i^{\mathbf{n}}$ denotes the current along the loop located in the face normal to the i direction of the unit cell of index $\mathbf{n}$. The time dependence is assumed to be of

*juan_dbd@us.es
†l_jelinek@us.es
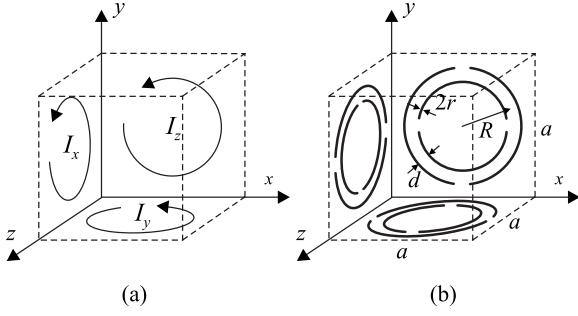‡marques@us.es
§mario.silveirinha@co.it.pt

FIG. 1. (a) Unit cell of a material formed by a cubic array of current loops. Each unit cell has three current loops centered at the faces of the cube. (b) Similar to (a) but for a realistic metamaterial formed by edge coupled SRRs with two splits. The SRRs are formed by circular wires with radius r. The distance between the inner and outer rings is d and the average radius of the particle is R.

the form $\mathbf{I^n} \propto \exp(j\omega t)$. Each component of the current vector is governed by the equation

$$\left(j\omega L + \frac{1}{j\omega C} \right) I_i^{\mathbf{n}} = -j\omega \Phi_i^{\mathbf{n}}, \tag{1}$$

where L, C are self-inductance and self-capacitance of the circuit (losses are neglected by simplicity, although they can be easily introduced in the analysis through a ring resistance). In Eq. (1) $\Phi_i^{\mathbf{n}}$ is the total magnetic flux through the considered loop which, using Lorentz local field approximation, can be calculated as

$$\Phi_i^{\mathbf{n}} = A\mu_0 \left(H_i + \frac{M_i}{3} \right) + \sum_{(\mathbf{m} \neq \mathbf{n}) \wedge (j \neq i)}^{r<R} M_{ij}^{\mathbf{nm}} I_j^{\mathbf{m}}, \tag{2}$$

where A is the area of the loop, $\mathbf{H}$, $\mathbf{M}$ are the macroscopic magnetic field and magnetization on the ring, and $M_{ij}^{\mathbf{nm}}$ are the mutual inductances between the loops oriented along the i and j axes in unit cells with indexes $\mathbf{n}$ and $\mathbf{m}$. The summation is extended to the cells inside a sphere centered around the nth unit cell and with radius R sufficiently large so that the region outside can be approximated by a continuous material but such that R is smaller than the wavelength to guarantee that the Lorentz approximation can be used. Therefore, in Eq. (2) the first term accounts for the contribution of all rings outside the sphere which, according to the standard Lorentz local field theory, are considered as a "continuous medium," whereas the summation accounts for the detailed contribution of each ring inside the sphere.

In the following we will assume a spatial field dependence of the kind $\{\mathbf{H}, \mathbf{M}\} = \{\mathbf{H}_0, \mathbf{M}_0\} \exp(-j\mathbf{k} \cdot \mathbf{r})$ and $\mathbf{I^n} = \mathbf{I}_0 \exp(-ja\mathbf{k} \cdot \mathbf{n})$, where a is the lattice periodicity and $\mathbf{I}_0$, $\mathbf{H}_0$, $\mathbf{M}_0$ are constant vectors. With the assumed time and space dependence, the macroscopic Maxwell equations lead to

$$(k_m^2 - k^2)\mathbf{H}_0 + (k_m^2 - \mathbf{k}\mathbf{k} \cdot)\mathbf{M}_0 = 0, \tag{3}$$

with $k_m = k_0\sqrt{\epsilon_r} = \omega\sqrt{\epsilon_r \epsilon_0 \mu_0}$, where ϵ_r is the macroscopic relative dielectric constant of the metamaterial. By combining Eqs. (1) and (2) the following equation for $\mathbf{I}_0$ is obtained:

$$\bar{\bar{Z}}(\mathbf{k}, \omega) \cdot \mathbf{I}_0 = -j\omega A\mu_0 \left(\mathbf{H}_0 + \frac{\mathbf{M}_0}{3} \right), \tag{4}$$

where $\bar{\bar{Z}}(\mathbf{k}, \omega)$ is an impedance matrix which incorporates all the magnetoinductive effects between the neighboring rings. Explicit expressions for the diagonal and the off-diagonal terms of $\bar{\bar{Z}}$ are

$$Z_{ii} = j\omega L \left\{ 1 - \frac{\omega_0^2}{\omega^2} + \sum_{\mathbf{n} \neq \mathbf{0}}^{r<R} \frac{M_{ii}^{\mathbf{0n}}}{L} e^{-ja\mathbf{k} \cdot \mathbf{n}} \right\}, \tag{5}$$

$$Z_{ij} = Z_{ji} = j\omega L \sum_{\mathbf{n}}^{r<R} \frac{M_{ij}^{\mathbf{0n}}}{L} e^{-ja\mathbf{k} \cdot \mathbf{n}}, \quad i \neq j, \tag{6}$$

where $\omega_0 = 1/\sqrt{LC}$ is the frequency of resonance of the rings. Taking into account that $\mathbf{M}_0 = A\mathbf{I}_0/a^3$, it is possible to combine Eq. (3) with Eq. (4) which gives

$$\left\{ \bar{\bar{Z}}(\mathbf{k}, \omega) - \frac{j\omega\mu_0 A^2}{3a^3} \frac{2k_m^2 + k^2 - 3\mathbf{k}\mathbf{k}}{k_m^2 - k^2} \right\} \cdot \mathbf{I}_0 = 0. \tag{7}$$

The dispersion relation for plane waves in the metamaterial is obtained by equating the determinant of Eq. (7) to zero. In the most general case this equation can be only solved numerically. However, in some cases, it is possible to give analytical solutions. In particular, for propagation along one of the coordinate axes (for $\mathbf{k} = k\hat{\mathbf{x}}$, for instance) the summation in Eq. (6) vanishes because all unit cells in planes perpendicular to the x axis are in phase and mutual inductances cancel out couple by couple (for instance, the mutual inductances between the ring marked I_x and the rings placed on the top and lower faces of the cube of Fig. 1(a) cancel each other, and so on). Therefore, the matrix $\bar{\bar{Z}}(\mathbf{k}, \omega)$ becomes diagonal, and Eq. (7) can be easily solved. This gives two branches: a longitudinal wave with $\mathbf{I}_0 = I_{0x}\hat{\mathbf{x}}$ given by

$$Z_{xx} - \frac{2}{3} \frac{j\omega\mu_0 A^2}{a^3} = 0 \tag{8}$$

and a transverse wave with $\mathbf{I}_0 = I_{0y}\hat{\mathbf{y}} + I_{0z}\hat{\mathbf{z}}$ given by

$$Z_{yy} - \frac{j\omega\mu_0 A^2}{3a^3} \frac{2k_m^2 + k_x^2}{k_m^2 - k_x^2} = 0. \tag{9}$$

If only interactions with the closest rings are considered for the computation of the summations in Eqs. (5) and (6) the dispersion equation for the longitudinal wave becomes

$$\frac{\omega_0^2}{\omega^2} = 1 + 2\frac{M_a}{L}\cos(ak_x) + 4\frac{M_c}{L} - \frac{2}{3}\frac{\alpha_0}{a^3}, \tag{10}$$

where $\alpha_0 = \mu_0 A^2/L$ and M_a and M_c are the mutual inductances between closest rings of the same orientation, placed in the axial and the coplanar directions, respectively. It can be easily recognized that Eq. (10) corresponds to the dispersion relation for longitudinal magnetoinductive waves [12], with some small corrections, which take into account the effects of the rings other than the nearest neighbors in the axial direction. In the same approximation the dispersion equation for transverse waves can be written as

$$\frac{k_x^2}{k_m^2} - 1 = \frac{\dfrac{\alpha_0}{a^3}}{\dfrac{\omega_0^2}{\omega^2} - 1 - \dfrac{2M_c}{L}\cos(ak_x) - \dfrac{2(M_a + M_c)}{L} - \dfrac{\alpha_0}{3a^3}}.$$

(11)

For high values of k_x ($k_x \gg k_m$) this equation reduces to

$$\frac{\omega_0^2}{\omega^2} = 1 + \frac{2M_c}{L}\cos(ak_x) + \frac{2(M_a + M_c)}{L} + \frac{\alpha_0}{3a^3},$$

(12)

which corresponds to the dispersion relation for transverse magnetoinductive waves [12]. On the other hand, in the long wavelength limit ($ak_x \ll 1$) Eq. (11) reduces to

$$\chi(\omega) = \frac{k_x^2}{k_m^2} - 1 = \frac{\dfrac{\alpha_0}{a^3}}{\dfrac{\omega_0^2}{\omega^2} - 1 - \dfrac{2M_a}{L} - \dfrac{4M_c}{L} - \dfrac{\alpha_0}{3a^3}}.$$

(13)

This equation gives the value for the magnetic susceptibility that is obtained when the Lorentz homogenization procedure is applied to the metamaterial with the ring magnetic polarizabilities $\alpha = \alpha_0(\omega_0^2/\omega^2 - 1)^{-1}$ already proposed in Ref. [16], except for a small correction term $2M_a/L + 4M_c/L$ accounting for the effect of the closest rings. Actually, if such a correction term is calculated by assuming a magnetic dipole approximation for the rings, it can be easily shown that it vanishes, thus giving exactly the Clausius-Mossotti formula for the susceptibility. Therefore, we can conclude that in the long wavelength limit, the transverse waves (9) correspond to the electromagnetic waves that are obtained from the local time-dispersive permeability $\mu = \mu_0\{1 + \chi(\omega)\}$. Conversely, in the short wavelength limit ($k_x \gg k_m$), they converge to the transverse magnetoinductive waves (12). Furthermore, from $\mathbf{M}_0 = A\mathbf{I}_0/a^3$ and Eq. (4)

$$\mathbf{M}_0 = \left\{ \frac{ja^3}{\mu_0\omega A^2}\bar{\bar{Z}}(\mathbf{k},\omega) - \frac{1}{3} \right\}^{-1} \cdot \mathbf{H}_0 = \bar{\bar{\chi}}(\mathbf{k},\omega) \cdot \mathbf{H}_0 \quad (14)$$

can be obtained. Now in Eq. (3) $\mathbf{M}_0$ can be replaced by Eq. (14) leading to

$$\{(-k^2 + k_m^2) + (-\mathbf{k}\mathbf{k} + k_m^2) \cdot \bar{\bar{\chi}}(\mathbf{k},\omega)\} \cdot \mathbf{H}_0 = 0, \quad (15)$$

which gives the same dispersion equation as Eq. (7). Therefore we can conclude that the nonlocal (i.e., time and spatially dispersive) magnetic permeability

$$\bar{\bar{\mu}}(\mathbf{k},\omega) = \mu_0\left(1 + \left\{ \frac{ja^3}{\mu_0\omega A^2}\bar{\bar{Z}}(\mathbf{k},\omega) - \frac{1}{3} \right\}^{-1}\right) \quad (16)$$

provides a complete characterization of the metamaterial, accounting for all kinds of waves propagating through it. In the long wavelength limit ($a|\mathbf{k}| \ll 1$) all the exponential terms in $\bar{\bar{Z}}(\mathbf{k},\omega)$ can be equated to unity and the magnetic permeability (14) reduces to the scalar time-dispersive permeability $\mu = \mu_0[1 + \chi(\omega)]$ with $\chi(\omega)$ given by Eq. (13). Alternatively, following Landau's description [15], the metamaterial can be also described by an equivalent spatially dispersive permit-
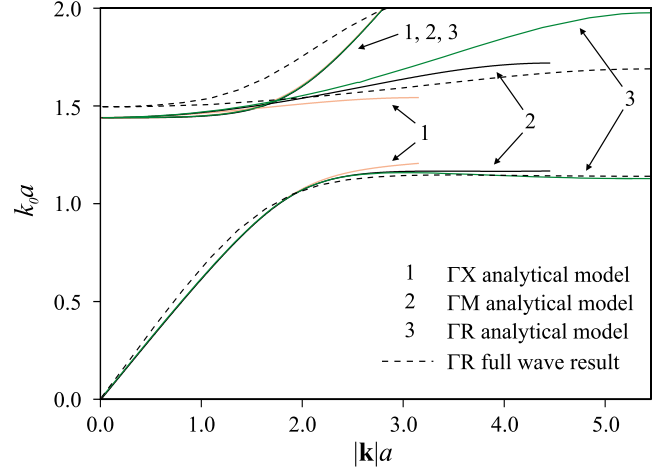

FIG. 2. (Color online) Dispersion diagram along Γ-X, Γ-M, Γ-R directions obtained from the analytical model (lines 1, 2, 3) and from a full-wave simulation (dashed line). The coordinates of selected points are $\Gamma = (0,0,0)$, $X = (\pi/a, 0, 0)$, $M = (\pi/a, \pi/a, 0)$, $R = (\pi/a, \pi/a, \pi/a)$.

tivity $\bar{\bar{\epsilon}}(\mathbf{k},\omega)$. The relation between this dielectric permittivity and the proposed magnetic permeability Eq. (16) is given by Eq. (43) in Ref. [17].

III. NUMERICAL EXAMPLE

As a numerical example, we have studied the propagation of electromagnetic waves in a metamaterial formed by the simple cubic lattice of split-ring resonators whose unit cell is depicted in Fig. 1(b). The capacitance C and self-inductance L were calculated following the ideas of Ref. [18] but for the case of a SRR made of wires instead of planar strips. This calculation was carried out by using well-known formulas [19] as explained in Ref. [20]. The mutual inductances $M_{ij}^{\mathbf{nm}}$ were calculated numerically using Neumann's formula including time retardation. The macroscopic permittivity was evaluated by substituting the SRRs by planar conducting disks of the same external radius, and by using the static Lorentz homogenization theory [21]. This approach yielded the approximate value $\epsilon_r = 2.5$. Using Eq. (7) and the first neighbor approximation, the dispersion characteristic of the electromagnetic modes supported by the metamaterial along different directions of the first Brillouin zone was calculated. The result for the geometry associated with $R = 0.44a$, $r = 0.005a$, and $d = 0.03a$ [see Fig. 1(b)] is depicted in Fig. 2. It can be seen that the band structure is formed by three branches and contains a band gap for all the depicted directions of $\mathbf{k}$. For $\mathbf{k}$ along Γ-X, the first and third branches correspond to the transversal mode described by Eq. (9) and the second branch corresponds to the longitudinal mode described by Eq. (8). Figure 2 also shows the high isotropy of the transversal mode even for moderate values of $\mathbf{k}$, a fact that is expected from the tetrahedral symmetry of the system [22].

To assess the accuracy of the proposed analytical model, we have also numerically computed the exact band structure of the aforementioned periodic material using the hybrid-
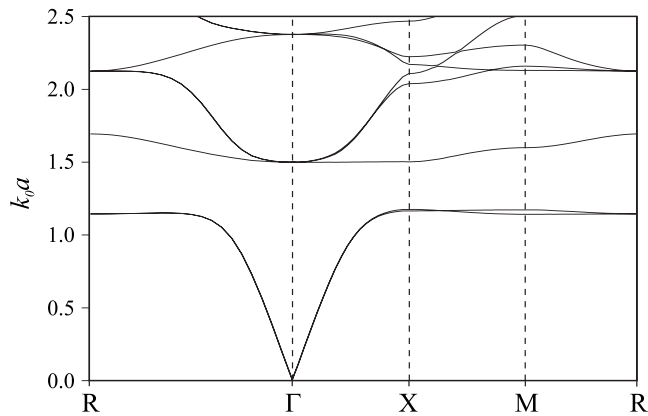
FIG. 3. Dispersion diagram along the closed path *R*-Γ-*X*-*M*-*R* obtained from full-wave simulation. The horizontal axis shows a projection of **k** on the corresponding line on the boundary of the Brillouin zone.

plane-wave-integral-equation formalism introduced in Ref. [23]. The result of the numerical simulation is presented in Fig. 2 for the specific direction Γ-*R*, and in Fig. 3 for the closed path *R*-Γ-*X*-*M*-*R*. Good qualitative agreement between theory and simulation can be seen from Fig. 2. We think that the quantitative disagreement for high values of k in the second branch can be attributed to the specific local field approximation considered in Eq. (2), which is strictly valid only for small values of k. In the case of the third branch, the disagreement is due to the proximity of the second resonance of the SRRs, which is not taken into account in the model. This effect is more visible in Fig. 3, where higher frequency branches are included. This figure also shows a complete electromagnetic band gap in the range $1.18 < k_0 a < 1.50$, in agreement with the hypothesis of a negative permeability in such a frequency band. It is worth noting that the effect of the substitution $k_m^2 \rightarrow -k_m^2$ (or equivalently $\epsilon_r \rightarrow -\epsilon_r$) into Eq. (11) is the onset of a backward wave pass-band in the frequency range of the stop-band of Fig. 3, as well as the conversion of the pass-bands of Fig. 2 into stop-bands. Therefore, the proposed model will be also use-

ful for the analysis of isotropic left-handed media made of SRRs and wires or any other elements providing a macroscopic negative permittivity (provided the conditions for the validity of the superposition hypothesis previously discussed in Ref. [10] are fulfilled). Work in this direction is in progress.

IV. CONCLUSIONS

A homogenization procedure for split-ring metamaterials taking into account spatial dispersion has been developed. The spatially dispersive permeability arising from this homogenization accounts for all the electromagnetic spectra observed in these composites, including electromagnetic and magnetoinductive waves. It has been also shown that this spatially dispersive permeability continuously approaches to the Lorentz local permeability in the long wavelength limit. From this analysis follows that transverse magnetoinductive waves are the continuation, at short wavelengths, of the well known transverse electromagnetic waves that can be found in the long wavelength limit. However, longitudinal magnetoinductive waves are not related to electromagnetic waves but to the collective oscillations of the metamaterial arising at $\mu=0$ in the long wavelength limit. It has been also observed that, when a macroscopic negative permittivity is imposed to the metamaterial, a typical left-handed pass-band appears at those frequencies where the magnetic permeability becomes negative. Therefore, we feel that the proposed homogenization procedure provides a complete macroscopic characterization of negative-μ and left-handed split-ring metamaterials.

[1] W. Weber, Ann. Phys. **87**, 145 (1852).

[2] S. A. Shelkunoff and H. T. Friis, *Antennas Theory and Practice* (Wiley, New York, 1952).

[3] J. B. Pendry, A. J. Holden, D. J. Robbins, and W. J. Stewart, IEEE Trans. Microwave Theory Tech. **47**, 2075 (1999).

[4] D. R. Smith, W. J. Padilla, D. C. Vier, S. C. Nemat-Nasser, and S. Schultz, Phys. Rev. Lett. **84**, 4184 (2000).

[5] R. A. Shelby, D. R. Smith, S. C. Nemat-Nasser, and S. Schultz, Appl. Phys. Lett. **78**, 489 (2001).

[6] R. Marqués, J. Martel, F. Mesa, and F. Medina, Microw. Opt. Technol. Lett. **35**, 405 (2002).

[7] W. Rotman, IRE Trans. Antennas Propag. **10**, 82 (1962).

[8] V. G. Veselago, Sov. Phys. Usp. **10**, 509 (1968).

[9] A. L. Pokrovsky and A. L. Efros, Phys. Rev. Lett. **89**, 093901 (2002).

[10] R. Marqués and D. R. Smith, Phys. Rev. Lett. **92**, 059401 (2004).

[11] M. G. Silveirinha, Phys. Rev. B **75**, 115104 (2007).

[12] E. Shamonina, V. A. Kalinin, K. H. Ringhofer, and L. Solymar, J. Appl. Phys. **92**, 6252 (2002).

[13] P. A. Belov and C. R. Simovski, Phys. Rev. E **72**, 026615 (2005).

[14] R. R. A. Syms, E. Shamonina, V. Kalinin, and L. Solymar, J. Appl. Phys. **97**, 064909 (2005).

[15] L. D. Landau, E. M. Lifshitz, and L. P. Pitaevskii, *Electrodynamics of Continuous Media*, 3rd ed. (Pergamon, Oxford, 1984).

[16] R. Marqués, F. Medina, and R. Rafii-El-Idrissi, Phys. Rev. B **65**, 144440 (2002).

[17] M. G. Silveirinha, Phys. Rev. B **76**, 245117 (2007).

[18] R. Marqués, F. Mesa, J. Martel, and F. Medina, IEEE Trans. Antennas Propag. **51**, 2572 (2003).

[19] J. D. Jackson, *Classical Electrodynamics*, 3rd ed. (Wiley, New York, 2001).

[20] In this case the total capacitance of the SRR can be estimated as $C=\frac{1}{8}\pi R C_{\mathrm{PUL}}=\pi^2\epsilon_0 R/[4\cosh^{-1}(\frac{d^2}{2r^2}-1)]$, where C_{PUL} is the per unit length capacitance of two parallel wires given in Ref. [19] (p. 88). The self-inductance of the SRR was approximated by the self-inductance of a torus with large radius R and small radius r [19] (p. 233): $L=\mu_0 R[\ln(8\frac{R}{r})-2]$.

[21] R. E. Collin, *Field Theory of Guided Waves*, 2nd ed. (IEEE Press, London, 1991).

[22] J. D. Baena, L. Jelinek, and R. Marqués, Phys. Rev. B **76**, 245115 (2007).

[23] M. Silveirinha and C. A. Fernandes, IEEE Trans. Microwave Theory Tech. **52**, 889 (2004).

Appendix 10

This appendix contains a full text of Ref. [36]

Metamaterials

ELSEVIER

Nonlocal homogenization of an array of cubic particles made of resonant rings

M.G. Silveirinha [a,*], J.D. Baena [b], L. Jelinek [c], R. Marqués [c]

[a] *Department of Electrical Engineering – Instituto de Telecomunicações, University of Coimbra, 3030 Coimbra, Portugal*
[b] *Departamento de Física, Universidad Nacional de Colombia, Carrera 30 No 45-30 Bogotá D.C., Colombia*
[c] *Departamento de Electrónica y Electromagnetismo, Universidad de Sevilla, 41012 Sevilla, Spain*

Abstract

Here, we develop a nonlocal homogenization model to characterize the electrodynamics of an array of cubic particles made of resonant rings. The effective parameters are calculated from the microscopic fields produced by a periodic external excitation. It is confirmed that the spatial dispersion effects cannot be neglected in the regime where $\mu \approx 0$. We demonstrate that when the array of resonant rings is combined with a triple wire medium formed by connected wires, the structure may behave approximately as an isotropic left-handed material.
© 2009 Elsevier B.V. All rights reserved.

1. Introduction

Structured materials with a strong magnetic response have been under intense research in recent years [1–10], mainly due to their potential applications in the design of imaging systems with improved resolution [2–5]. In particular, it was recently demonstrated that a metamaterial lens formed by split-ring resonators (SRRs) boosts the sensitivity of the coil used in magnetic resonance imaging when operated in the regime $\mu = -1$ [6].

In most of the studies published in the literature, it is typically assumed from the outset that the response of the metamaterial is local, and, based on that assumption the effective parameters are usually calculated using the retrieval procedure reported in Ref. [11] (inversion of the scattering parameter data). Recently, in Ref. [12] the Lorentz local field theory was used to homogenize a metamaterial formed by an array of cubic particles with tetrahedral symmetry formed by split-ring resonators (a topology similar to that considered here), and the nonlocal magnetic permeability was calculated. It was demonstrated that the spatially dispersive model provides a unified description of the transverse electromagnetic waves and of the so-called magnetoinductive waves [13], demonstrating in this manner that the latter are a short-wavelength continuation of the former. In this work, we investigate a problem closely related to

* Corresponding author. Tel.: +351 239 796268;
fax: +351 239 796293.
E-mail addresses: mario.silveirinha@co.it.pt (M.G. Silveirinha),
jdbaenad@unal.edu.co (J.D. Baena), l.jelinek@us.es (L. Jelinek),
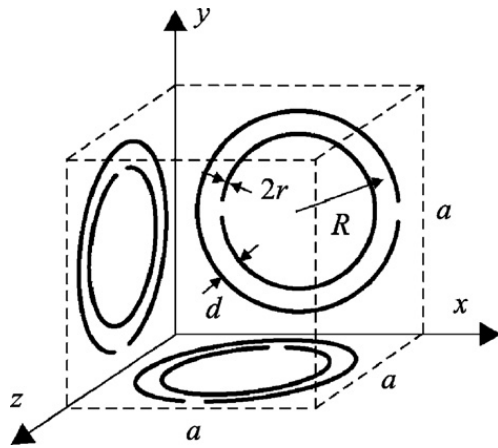marques@us.es (R. Marqués).

Fig. 1. Geometry of the unit cell of a structured material formed by resonant rings. The figure depicts the particular case in which the resonant particles are SRRs.

that considered in Ref. [12] but from a different perspective. Instead of applying the Lorentz's local field theory, we compute the nonlocal parameters using the homogenization method proposed in the works [14,15], which is based on the idea of exciting the metamaterial with a periodic source with suitable phase-shift. We obtain the exact solution (taking into account the interaction between all the particles in lattice) of the homogenization problem under the approximation that the response of the inclusions can be described using the dipole approximation, and an explicit formula for the nonlocal magnetic permeability is derived. The results of the analytical model are compared with the effective parameters obtained with full wave simulations that take into account all the details of the microstructure of the material. Finally, we study the electrodynamics of a system formed by the array of SRRs and a connected array of wires. It should be mentioned that other previous works (e.g. Ref. [16]) have studied the homogenization of arrays of SRRs taking into account rigorously the mutual effects and lattice ordering. The main contribution of our analysis, which extends our previous work [12], is the characterization of the spatial dispersion effects.

2. Homogenization

A representative geometry of the unit cell of the material under analysis is shown in Fig. 1. The unit cell contains three different resonant metallic rings, being each ring normal to one of the Cartesian axes. The lattice is simple cubic with lattice constant a. Clearly, each basic inclusion has an anisotropic response, but in the long wavelength limit the response of the composite material is approximately isotropic due to the spatial arrangement and orientation of the particles. The ith resonant ring in

the unit cell is by definition normal to the unit vector $\hat{\mathbf{u}}_i$ ($i = x, y, z$), and is centered at the point $\mathbf{r}_{0,i} = -(a/2)\,\hat{\mathbf{u}}_i$.

The resonant rings are generic planar (or quasi-planar) inclusions, which may be produced by some lumped or distributed capacitance. We suppose that the rings can be characterized by an impedance $Z_0 = j\omega L + 1/(j\omega C)$ obtained from a circuit model (for simplicity the effect of metallic loss is neglected; see Refs. [17,18] for the particular case of SRRs). The resonant rings will be modeled as dipole-type magnetic particles characterized by a uniaxial magnetic polarizability dyadic (tensor). The magnetic polarizability dyadic of the ith ring is

$$\bar{\bar{\alpha}}_i = \alpha_m \hat{\mathbf{u}}_i \hat{\mathbf{u}}_i, \tag{1}$$

where $\hat{\mathbf{u}}_i \hat{\mathbf{u}}_i \equiv \hat{\mathbf{u}}_i \otimes \hat{\mathbf{u}}_i$ represents the dyadic (tensor) product of two vectors. The parameter α_m (with unities $[m^3]$) is related to the impedance Z_0 as follows (including the effect of the radiation loss)

$$
\begin{aligned}
\alpha_m^{-1} &= \frac{Z_0}{-j\omega A^2 \mu_0} + j\frac{1}{6\pi}\left(\frac{\omega}{c}\right)^3 \\
&= \alpha_0^{-1}\left[\left(\frac{\omega_r}{\omega}\right)^2 - 1\right] + j\frac{1}{6\pi}\left(\frac{\omega}{c}\right)^3,
\end{aligned} \tag{2}
$$

where $\alpha_0^{-1} = L/\mu_0 A^2$, A is the area of the ring and $\omega_r = 1/\sqrt{LC}$.

For simplicity, it will be assumed that the rings do not have an electric response (i.e. that the electric polarizability vanishes; in Section 3, we will discuss how to incorporate the electric response in the model). Thus, at a microscopic level, the magnetic dipole moment of the ith particle in the unit cell, $\mathbf{p}_i$, must verify:

$$\frac{\mathbf{p}_i}{\mu_0} = \bar{\bar{\alpha}}_i \cdot \mathbf{H}_{\text{loc}}\left(\mathbf{r}_{0,i}\right), \quad i = x, y, z, \tag{3}$$

where $\mathbf{H}_{\text{loc}}$ is the local magnetic field that polarizes the pertinent ring. The magnetic dipole $\mathbf{p}_i$ as defined above is related to the more traditional definition given in textbooks (e.g. Ref. [19]) as $\mathbf{m} = \mathbf{p}_i/\mu_0$.

2.1. Two models for the response of the rings

It is possible to model the response of the resonant rings using two alternative approaches. The first model takes into account that the rings are metallic particles, and thus that an external field induces a microscopic *electric current density* in each ring. Since it is assumed that the rings only have a magnetic response, which is necessarily caused by the vortex part of the induced electric current (artificial magnetism), the induced current is related to the magnetic dipole moments as follows (see

Ref. [15] for a related result)

$$\mathbf{J}_{e,\mathrm{dip}} = \nabla \times \left\{ \sum_{i=1,2,3} \sum_{\mathbf{I}} \delta(\mathbf{r} - \mathbf{r_I} - \mathbf{r}_{0,i}) \frac{\mathbf{p}_i}{\mu_0} e^{-j\mathbf{k}\cdot\mathbf{r_I}} \right\},$$

(4)

where $\mathbf{r_I} = a(i_1, i_2, i_3)$ represents a generic lattice point, $\mathbf{I} = (i_1, i_2, i_3)$ is a triple index of integers, and $\mathbf{p}_i$ is the magnetic dipole moment of the ith particle in the unit cell. Following the works [14,15], the unbounded metamaterial can be characterized by a dielectric function of the type $\bar{\bar{\varepsilon}} = \bar{\bar{\varepsilon}}(\omega, \mathbf{k})$, where ω is the angular frequency and $\mathbf{k} = (k_x, k_y, k_z)$ is the wave vector. The procedure to compute the dielectric function for a given ω and $\mathbf{k}$ is to excite the metamaterial with an external Floquet-type electric current density $\mathbf{J}_{e,\mathrm{ext}} = \mathbf{J}_{e,\mathrm{av}} e^{-j\mathbf{k}\cdot\mathbf{r}}$, where $\mathbf{J}_{e,\mathrm{av}}$ is a constant vector [14]. Then, one needs to solve the corresponding source-driven electromagnetic problem and calculate the microscopic fields. The averaged macroscopic fields and the generalized electric polarization vector are computed using the microscopic fields. Finally, the unknown dielectric function $\bar{\bar{\varepsilon}}(\omega, \mathbf{k})$ is obtained from the macroscopic fields and from the generalized polarization vector [14]. This approach is further developed in Appendix A.

The second model is based on the observation that since the resonant rings only have a magnetic response, they may be as well regarded as pure magnetic particles which, when excited by an external field, originate a *magnetic current density* given by:

$$\mathbf{J}_{m,\mathrm{dip}} = \sum_{i=1,2,3} \left(\sum_{\mathbf{I}} \delta\left(\mathbf{r} - \mathbf{r_I} - \mathbf{r}_{0,i}\right) j\omega\mathbf{p}_i e^{-j\mathbf{k}\cdot\mathbf{r_I}} \right),$$

(5)

i.e. the second model for the response of the rings regards the inclusions as magnetic particles characterized by a magnetic current density (instead of an electric current density as in Eq. (4)). Such model may seem less rigorous than the model associated with Eq. (4), but as discussed below, they actually lead to equivalent results after proper homogenization.

It is important to note that the homogenization method introduced in Ref. [14] assumes that the inclusions are either dielectric or metallic materials with constant permeability ($\mu = \mu_0$), i.e. the particles must have exclusively an electric response (even though, as mentioned before, magnetic effects may occur due to the eddy part of the electric current). Thus, the method of Ref. [14] cannot be directly applied to characterize a material formed by pure magnetic particles, for which the response is

characterized by a magnetic current density as in Eq. (5). However, evidently a structured material formed by magnetic-type inclusions is the electromagnetic dual of a material formed by electric-type inclusions, and thus it is trivial to modify and generalize the method of Ref. [14] to such configurations. It should be clear that such modified homogenization approach is based on the introduction of a magnetic function of the type $\bar{\bar{\mu}} = \bar{\bar{\mu}}(\omega, \mathbf{k})$, which, as detailed below, can be calculated by exciting the metamaterial with an external magnetic current density $\mathbf{J}_{m,\mathrm{ext}} = \mathbf{J}_{m,\mathrm{av}} e^{-j\mathbf{k}\cdot\mathbf{r}}$.

One important point is the relation between the dielectric function $\bar{\bar{\varepsilon}}(\omega, \mathbf{k})$ calculated within the framework of the first model (developed in Appendix A), and the magnetic function $\bar{\bar{\mu}} = \bar{\bar{\mu}}(\omega, \mathbf{k})$ calculated within the framework of the second model (developed in Section 2.2). From the results of Appendix A, it turns out that:

$$\frac{\bar{\bar{\varepsilon}}(\omega, \mathbf{k})}{\varepsilon_0} = \bar{\bar{\mathbf{I}}} + c^2 \frac{\mathbf{k}}{\omega} \times \left(\mu_0 \bar{\bar{\mu}}^{-1} - \bar{\bar{\mathbf{I}}} \right) \times \frac{\mathbf{k}}{\omega},$$

(6)

where $\bar{\bar{\mathbf{I}}}$ is the identity dyadic and c is the speed of light in the host medium (assumed vacuum for simplicity). Interestingly, in Refs. [14,15,20,21] it is demonstrated that an unbounded material characterized by a given magnetic permeability $\bar{\bar{\mu}}$ and an electric permittivity $\varepsilon = \varepsilon_0$, can be as well characterized by a nonlocal dielectric function defined as in Eq. (6) (in the sense that the plane wave dispersion characteristic and the associated electric field polarizations are the same independent of the adopted constitutive relations). Thus, Eq. (6) demonstrates that the two models described in this section yield equivalent results. We will adopt the second model in the following sections to calculate an explicit expression for $\bar{\bar{\mu}} = \bar{\bar{\mu}}(\omega, \mathbf{k})$.

2.2. The homogenization problem

Following the discussion of Section 2.1, here we assume that the rings can be modeled as pure magnetic particles, whose response to an external field originates a magnetic current density given by Eq. (5). In order to determine the unknown $\bar{\bar{\mu}} = \bar{\bar{\mu}}(\omega, \mathbf{k})$, we excite the electromagnetic crystal with an external (magnetic-type) source such that

$$\mathbf{J}_{m,\mathrm{ext}} = j\omega \frac{\mathbf{p}_{\mathrm{ext}}}{V_{\mathrm{cell}}} e^{-j\mathbf{k}\cdot\mathbf{r}},$$

(7)

where $V_{\mathrm{cell}} = a^3$ is the volume of the unit cell, and $\mathbf{p}_{\mathrm{ext}}$ is a constant vector that determines the applied current.

The microscopic fields $(\mathbf{E}, \mathbf{H})$ are the solution of the electromagnetic problem

$$\nabla \times \mathbf{E} = -j\omega\mu_0\mathbf{H} - \mathbf{J}_{m,\text{ext}} - \mathbf{J}_{m,\text{dip}} \qquad (8a)$$

$$\nabla \times \mathbf{H} = j\omega\varepsilon_0\mathbf{E}, \qquad (8b)$$

where $\mathbf{J}_{m,\text{dip}}$ is given by Eq. (5), and is written in terms of the unknown magnetic dipole moments of the particles in the unit cell $\mathbf{p}_i$ (which obviously depend on the external field). Notice that since the current source $\mathbf{J}_{m,\text{ext}}$ has the Floquet property and the material is periodic, it is clear that both $(\mathbf{E}, \mathbf{H})$ and $\mathbf{J}_{m,\text{dip}}$ have the Floquet property as well (this actually justifies formula (5)). It is important to emphasize that system (8) is a source driven problem and not an eigenvalue problem. Notice also that in this formulation all the microscopic currents are purely magnetic, because the rings are modeled as true magnetic particles.

The solution of (8) can be written in a straightforward manner in terms of the Green dyadic $\bar{\bar{\mathbf{G}}}_p\left(\mathbf{r} | \mathbf{r}'; \omega, \mathbf{k}\right) = \left(\bar{\bar{\mathbf{I}}} + c^2/\omega^2\nabla\nabla\right)\Phi_p\left(\mathbf{r} | \mathbf{r}'; \omega, \mathbf{k}\right)$ introduced in Refs. [14,15], being Φ_p the lattice Green function [22]. The Green dyadic verifies $\nabla \times \nabla \times \bar{\bar{\mathbf{G}}}_p\left(\mathbf{r} | \mathbf{r}'\right) - (\omega/c)^2\bar{\bar{\mathbf{G}}}_p\left(\mathbf{r} | \mathbf{r}'\right) = \bar{\bar{\mathbf{I}}}\left(\sum_{\mathbf{I}}\delta\left(\mathbf{r} - \mathbf{r}' - \mathbf{r_I}\right)e^{-j\mathbf{k}\cdot\mathbf{r}}\right)$. Thus, it is simple to verify that the solution of system (8) is such that:

$$\mathbf{H}\left(\mathbf{r}\right) = (-j\omega\varepsilon_0)\sum_{i=1,2,3}\bar{\bar{\mathbf{G}}}_p\left(\mathbf{r} | \mathbf{r}_{0,i}\right)\cdot j\omega\mathbf{p}_i$$
$$+ (-j\omega\varepsilon_0)\bar{\bar{\mathbf{G}}}_{\text{av}}\cdot j\omega\mathbf{p}_{\text{ext}}\,e^{-j\mathbf{k}\cdot\mathbf{r}}, \qquad (9)$$

where $\bar{\bar{\mathbf{G}}}_{\text{av}}$ is the dyadic

$$\bar{\bar{\mathbf{G}}}_{\text{av}} = \frac{1}{V_{\text{cell}}}\frac{\bar{\bar{\mathbf{I}}} - c^2/\omega^2\mathbf{kk}}{k^2 - (\omega/c)^2}, \qquad (10)$$

with $k^2 = \mathbf{k}\cdot\mathbf{k}$ and $\mathbf{kk} = \mathbf{k}\otimes\mathbf{k}$. The first term in the right-hand side of Eq. (9) corresponds to the field created by the induced magnetic dipoles, whereas the second terms corresponds to the field created by the external source $\mathbf{J}_{m,\text{ext}}$. It is interesting to note that $\bar{\bar{\mathbf{G}}}_{\text{av}}$ is the spatial average of the Green dyadic:

$$\bar{\bar{\mathbf{G}}}_{\text{av}} = \frac{1}{V_{\text{cell}}}\int_{\text{cell}}\bar{\bar{\mathbf{G}}}_p\left(\mathbf{r} | \mathbf{r}'\right)e^{+j\mathbf{k}\cdot(\mathbf{r}-\mathbf{r}')}d^3\mathbf{r}'. \qquad (11)$$

To obtain the complete solution of (8) we still have to determine the magnetic dipole moments, $\mathbf{p}_i$ $(i = 1, 2, 3)$, of the rings in the unit cell. This can be done using the microscopic relations (3). It is clear from Eq. (9) that the

local field on the ith ring is

$$\mathbf{H}_{\text{loc},i} = \left(\frac{\omega}{c}\right)^2\overline{\overline{\mathbf{G}'_p}}\left(0 | 0\right)\cdot\frac{\mathbf{p}_i}{\mu_0}$$
$$+ \sum_{j \neq i}\left(\frac{\omega}{c}\right)^2\bar{\bar{\mathbf{G}}}_p(\mathbf{r}_{0,i}|\mathbf{r}_{0,j})\cdot\frac{\mathbf{p}_j}{\mu_0}$$
$$+ \left(\frac{\omega}{c}\right)^2\bar{\bar{\mathbf{G}}}_{\text{av}}\cdot\frac{\mathbf{p}_{\text{ext}}}{\mu_0}e^{-j\mathbf{k}\cdot\mathbf{r}_{0,i}}, \qquad (12)$$

where by definition

$$\overline{\overline{\mathbf{G}'_p}}\left(\mathbf{r} | \mathbf{r}'\right) = \bar{\bar{\mathbf{G}}}_p\left(\mathbf{r} | \mathbf{r}'\right) - \overline{\overline{\mathbf{G}_0}}\left(\mathbf{r} | \mathbf{r}'\right) \qquad (13)$$

and $\overline{\overline{\mathbf{G}_0}}\left(\mathbf{r} | \mathbf{r}'\right)$ is the free-space Green dyadic. Using now the microscopic relations (3) and the fact that $\mathbf{p}_i = p_i\hat{\mathbf{u}}_i$, it is readily found that for $i = 1, 2, 3$

$$\alpha_m^{-1}\frac{p_i}{\mu_0} = \left(\frac{\omega}{c}\right)^2\left(\hat{\mathbf{u}}_i\cdot\overline{\overline{\mathbf{G}'_p}}\left(0 | 0\right)\cdot\hat{\mathbf{u}}_i\frac{p_i}{\mu_0}\right.$$
$$+ \sum_{j \neq i}\hat{\mathbf{u}}_i\cdot\bar{\bar{\mathbf{G}}}_p\left(\mathbf{r}_{0,i} | \mathbf{r}_{0,j}\right)\cdot\hat{\mathbf{u}}_j\frac{p_j}{\mu_0}$$
$$\left. + \hat{\mathbf{u}}_i\cdot\bar{\bar{\mathbf{G}}}_{\text{av}}\cdot\frac{\mathbf{p}_{\text{ext}}}{\mu_0}e^{-j\mathbf{k}\cdot\mathbf{r}_{0,i}}\right). \qquad (14)$$

The above equation can be written in matrix notation as follows:

$$[a_{ij}]\cdot\begin{pmatrix}p_1e^{+j\mathbf{k}\cdot\mathbf{r}_{0,1}}\\p_2e^{+j\mathbf{k}\cdot\mathbf{r}_{0,2}}\\p_3e^{+j\mathbf{k}\cdot\mathbf{r}_{0,3}}\end{pmatrix} = \left(\frac{\omega}{c}\right)^2\overline{\overline{\mathbf{G}}}_{\text{av}}\cdot\mathbf{p}_{\text{ext}}, \qquad (15)$$

where the matrix entries are defined as $a_{ii} = \alpha_m^{-1} - \hat{\mathbf{u}}_i\cdot(\omega/c)^2\overline{\overline{\mathbf{G}'_p}}\left(0 | 0\right)\cdot\hat{\mathbf{u}}_i$, and $a_{ij} = -\hat{\mathbf{u}}_i\cdot(\omega/c)^2\bar{\bar{\mathbf{G}}}_p\left(\mathbf{r}_{0,i} | \mathbf{r}_{0,j}\right)e^{j\mathbf{k}\cdot(\mathbf{r}_{0,i}-\mathbf{r}_{0,j})}\cdot\hat{\mathbf{u}}_j$ for $i \neq j$. Eq. (15) formally relates the amplitudes of the induced magnetic dipole moments p_i $(i = 1, 2, 3)$ with the external source $(\mathbf{p}_{\text{ext}})$. Thus, the microscopic fields are completely determined by the solution of Eq. (15).

We are now in a position to determine the magnetic function $\bar{\bar{\mu}} = \bar{\bar{\mu}}\left(\omega, \mathbf{k}\right)$ of the metamaterial. To begin with, we introduce the macroscopic averaged electric and magnetic fields, which for the present homogenization problem where all the particles are purely magnetic, should be defined as

$$\mathbf{E}_{\text{av}} = \frac{1}{V_{\text{cell}}}\int_{\text{cell}}\mathbf{E}\left(\mathbf{r}\right)e^{+j\mathbf{k}\cdot\mathbf{r}}d^3\mathbf{r},$$

$$\mathbf{H}_{\text{av}} = \frac{1}{V_{\text{cell}}}\int_{\text{cell}}\mathbf{H}\left(\mathbf{r}\right)e^{+j\mathbf{k}\cdot\mathbf{r}}d^3\mathbf{r}. \qquad (16)$$

It is simple to verify that the Maxwell equations (8) imply that

$$\omega\mu_0\mathbf{H}_{\mathrm{av}} - \mathbf{k} \times \mathbf{E}_{\mathrm{av}} = -\omega\frac{\mathbf{p}_{\mathrm{ext}}}{V_{\mathrm{cell}}} - \omega\mu_0\mathbf{M} \qquad (17a)$$

$$\mathbf{k} \times \mathbf{H}_{\mathrm{av}} + \omega\varepsilon_0\mathbf{E}_{\mathrm{av}} = 0, \qquad (17b)$$

where the magnetization vector $\mathbf{M}$ was defined as

$$\mathbf{M} \equiv \frac{\left(\mathbf{J}_{m,\mathrm{dip}}\right)_{\mathrm{av}}}{j\omega\mu_0} = \frac{1}{V_{\mathrm{cell}}} \sum_{i=1,2,3} \frac{\mathbf{p}_i}{\mu_0} e^{j\mathbf{k}\cdot\mathbf{r}_{0,i}} \qquad (18)$$

and we used the fact that $(\mathbf{J}_{m,\mathrm{ext}})_{\mathrm{av}} = j\omega\mathbf{p}_{\mathrm{ext}}/V_{\mathrm{cell}}$, being $(\mathbf{J}_{m,\mathrm{dip}})_{\mathrm{av}}$ and $(\mathbf{J}_{m,\mathrm{ext}})_{\mathrm{av}}$ defined consistently with Eq. (16).

The magnetic function $\bar{\bar{\mu}}$ must ideally be such that, independent of the external excitation, one has $\mathbf{B}_{\mathrm{av}} = \bar{\bar{\mu}} \cdot \mathbf{H}_{\mathrm{av}}$ where by definition the macroscopic induction field is given by $\mathbf{B}_{\mathrm{av}} \equiv \mu_0(\mathbf{H}_{\mathrm{av}} + \mathbf{M})$, consistently with the classical formula. Thus, $\bar{\bar{\mu}}$ must be such that $\left(\bar{\bar{\mu}}/\mu_0 - \bar{\bar{\mathbf{I}}}\right) \cdot \mathbf{H}_{\mathrm{av}} = \mathbf{M}$, for arbitrary $\mathbf{p}_{\mathrm{ext}}$.

One interesting aspect implicit in the previous discussion is that when the metamaterial is formed by purely magnetic particles, as considered in this section, the fundamental field entity (obtained from averaging the microscopic field) is the magnetic field intensity ($\mathbf{H}$), whereas the derived field is the induction field ($\mathbf{B}$). Indeed, this a trivial consequence of the formulation of Ref. [14], noting that $\mathbf{H}$ is the electromagnetic dual of $\mathbf{E}$, and $\mathbf{B}$ is the electromagnetic dual of $\mathbf{D}$. Quite differently, when all the particles only have an electric response (e.g. standard dielectrics or metals) the fundamental field quantity is the induction field, whereas in those conditions the magnetic field should be regarded as the derived quantity [14] (see also Appendix A).

In order to calculate $\bar{\bar{\mu}}$ we substitute (17b) into (17a) and solve the resulting equation with respect to $\mathbf{p}_{\mathrm{ext}}$. It may be easily verified that:

$$\frac{\mathbf{p}_{\mathrm{ext}}}{\mu_0} = -\mathbf{M}V_{\mathrm{cell}} + \frac{c^2}{\omega^2}\bar{\bar{\mathbf{G}}}_{\mathrm{av}}^{-1} \cdot \mathbf{H}_{\mathrm{av}}, \qquad (19)$$

$(p_1 e^{+j\mathbf{k}\cdot\mathbf{r}_{0,1}}, p_2 e^{+j\mathbf{k}\cdot\mathbf{r}_{0,2}}, p_3 e^{+j\mathbf{k}\cdot\mathbf{r}_{0,3}})$, it is found that:

$$\left[a_{ij}\right] \cdot \mathbf{M} = -\left(\frac{\omega}{c}\right)^2 \bar{\bar{\mathbf{G}}}_{\mathrm{av}} \cdot \mathbf{M} + \frac{1}{V_{\mathrm{cell}}}\mathbf{H}_{\mathrm{av}}. \qquad (20)$$

Therefore, it is clear that in order that $\left(\bar{\bar{\mu}}/\mu_0 - \bar{\bar{\mathbf{I}}}\right) \cdot \mathbf{H}_{\mathrm{av}} = \mathbf{M}$, $\bar{\bar{\mu}}$ should verify

$$\frac{\bar{\bar{\mu}}}{\mu_0} = \bar{\bar{\mathbf{I}}} + \frac{1}{V_{\mathrm{cell}}}\bar{\bar{\chi}}^{-1}, \qquad (21)$$

where the dyadic $\bar{\bar{\chi}}$ is such that (with $\chi_{ij} = \hat{\mathbf{u}}_i \cdot \bar{\bar{\chi}} \cdot \hat{\mathbf{u}}_j$),

$$\chi_{ii} = \alpha_m^{-1} - \hat{\mathbf{u}}_i \cdot \bar{\bar{\mathbf{C}}}_{\mathrm{int}} \cdot \hat{\mathbf{u}}_i \qquad (22a)$$

$$\chi_{ij} = -\hat{\mathbf{u}}_i \cdot \bar{\bar{\mathbf{D}}}_{\mathrm{int}}\left(\mathbf{r}_{0,i}\,\middle|\,\mathbf{r}_{0,j}\right) \cdot \hat{\mathbf{u}}_j, \quad \text{for } i \neq j \qquad (22b)$$

and $\bar{\bar{\mathbf{C}}}_{\mathrm{int}}$ and $\bar{\bar{\mathbf{D}}}_{\mathrm{int}}$ are defined by

$$\bar{\bar{\mathbf{C}}}_{\mathrm{int}}(\omega, \mathbf{k}) = \left(\frac{\omega}{c}\right)^2 \left(\overline{\overline{\mathbf{G}'_p}}(0\,|\,0) - \bar{\bar{\mathbf{G}}}_{\mathrm{av}}\right) \qquad (23a)$$

$$\bar{\bar{\mathbf{D}}}_{\mathrm{int}}\left(\mathbf{r}\,|\,\mathbf{r}'; \omega, \mathbf{k}\right) = \left(\frac{\omega}{c}\right)^2 \left(\overline{\overline{\mathbf{G}_p}}(\mathbf{r}|\mathbf{r}')e^{j\mathbf{k}\cdot(\mathbf{r}-\mathbf{r}')} - \bar{\bar{\mathbf{G}}}_{\mathrm{av}}\right). \qquad (23b)$$

Eq. (21) establishes that the magnetic function (i.e. the spatially dispersive permeability) of the material can be written exclusively in terms of magnetic polarizability of the basic particles and of the *interaction* dyadics $\bar{\bar{\mathbf{C}}}_{\mathrm{int}}$ and $\bar{\bar{\mathbf{D}}}_{\mathrm{int}}$. The dyadic $\bar{\bar{\mathbf{C}}}_{\mathrm{int}}$ describes the interaction between rings with the same orientation, whereas $\bar{\bar{\mathbf{D}}}_{\mathrm{int}}$ describes the interaction between rings with different orientations. In general, these dyadics need to be numerically evaluated (using for example the mixed-domain Green function representation of Ref. [22]). It is interesting to mention that $\bar{\bar{\mathbf{C}}}_{\mathrm{int}}$ is precisely the same dyadic that was obtained in Ref. [15]. Specifically, $\bar{\bar{\mathbf{C}}}_{\mathrm{int}}$ relates the local fields and the macroscopic fields for point dipole particles (Lorentz–Lorenz formulas). In particular, it was demonstrated in Ref. [15] that for a simple cubic lattice (as the one considered in this work), we have that to a first approximation:

$$C_{11}(\omega, \mathbf{k}) \equiv \hat{\mathbf{u}}_1 \cdot \mathrm{Re}\left\{\bar{\bar{\mathbf{C}}}_{\mathrm{int}}\right\} \cdot \hat{\mathbf{u}}_1 \approx \frac{1}{a^3}\left[\frac{1}{3} - 0.15\left(\frac{\omega}{c}a\right)^2 + 0.052\left(\cos\left(k_x a\right) - 1\right)\right.$$
$$\left. -0.026\left(\cos\left(k_y a\right) - 1\right) - 0.026\left(\cos\left(k_z a\right) - 1\right)\right] \qquad (24)$$

where $\bar{\bar{\mathbf{G}}}_{\mathrm{av}}^{-1}$ is the inverse of the dyadic defined by Eq. (10). Now, substituting the above equation into Eq. (15), and noting that since $\mathbf{p}_i = p_i\hat{\mathbf{u}}_i$ the magnetization vector is such that $\mu_0 V_{\mathrm{cell}}\mathbf{M} =$

The interaction constants C_{22} and C_{33} are defined similarly, by permutating the wave vector components k_x, k_y and k_z. The imaginary part of the interaction dyadic verifies $\mathrm{Im}\left\{\bar{\bar{\mathbf{C}}}_{\mathrm{int}}\right\} = \frac{1}{6\pi}(\omega/c)^3\bar{\bar{\mathbf{I}}}$ [15]. The first term in

Eq. (24) is the familiar static interaction constant, $1/3a^3$, for a simple cubic lattice. The second term in Eq. (24) is a frequency correction of the static term. The remaining terms, whose amplitude is evidently quite small, are related to structural spatial dispersion effects [15]. In general these small corrections are negligible, except near to a resonance of the electric/magnetic response of the particles where they may play an important role [15,23].

On the other hand, it can be shown that because of symmetry reasons $\mathrm{Im}\left\{\bar{\bar{\mathbf{D}}}_{\mathrm{int}}\left(\mathbf{r}_{0,i}\middle|\mathbf{r}_{0,j}\right)\right\}=0$, $i\neq j$. Moreover, $D_{\mathrm{int},ij}=\hat{\mathbf{u}}_i\cdot\bar{\bar{\mathbf{D}}}_{\mathrm{int}}\left(\mathbf{r}_{0,i}\middle|\mathbf{r}_{0,j}\right)\cdot\hat{\mathbf{u}}_j$, can be very accurately represented by the following Taylor series in powers of k_i, k_j and (ω/c) $(i\neq j)$

$$D_{\mathrm{int},ij}\left(\omega,\mathbf{k}\right)\approx\frac{k_i k_j}{a}\left[-0.1936-0.01188\left(\frac{\omega}{c}a\right)^2+0.005902\,a^2\left(k_i^{\,2}+k_j^{\,2}\right)\right],\qquad(25)$$

even when the wave vector is close to the boundary of the Brillouin zone or when the frequency is moderately large. It is interesting to note that $D_{\mathrm{int},ij}=0$ (for arbitrary i,j, with $i\neq j$) when the wave vector $\mathbf{k}$ is directed along one of the coordinate axes, i.e. in these conditions the coupling between the resonant rings in the unit cell is mutually cancelled.

It is clear that Eqs. (24) and (25) imply that in the very long wavelength limit, when $|ka|\ll 1$ and $|\omega a/c|\ll 1$, the dyadic $\bar{\bar{\chi}}$ is approximately diagonal and verifies $\bar{\bar{\chi}}=\left(Re\left\{\alpha_m^{-1}\right\}-1/3a^3\right)\bar{\bar{\mathbf{I}}}$. Thus, within such approximations the nonlocal permeability reduces to the classical Clausius–Mossotti formula

$$\frac{\bar{\bar{\mu}}}{\mu_0}\approx\left(1+\frac{1}{V_{\mathrm{cell}}}\frac{1}{Re\left\{\alpha_m^{-1}\right\}-1/3a^3}\right)\bar{\bar{\mathbf{I}}}.\qquad(26)$$

This result confirms that in the very long wavelength limit the material response is isotropic, as could be expected from the symmetry of the lattice. Other materials formed by uniaxial resonators, suitably oriented along different directions in order to yield an isotropic response, have been as well considered in Refs. [24–26]. It will be shown below that such simple result

(which neglects the nonlocal effects) is in general invalid, particularly when the effective permeability is near zero.

2.3. Comparison with the model of Ref. [12]

In our previous paper (Ref. [12]) an array of cubic particles made of SRRs was homogenized using a local field approach, and the nonlocal permeability was written in terms of an impedance matrix that incorporates all the magnetoinductive effects between the rings. The case of wave propagation along one of the Cartesian axes was analyzed in particular detail and it was shown that for propagation along the x-direction ($k_y=k_z=0$), the yy-component of the permeability dyadic is [12]

$$\left.\frac{\mu_{yy}}{\mu_0}\right|_{k_y=k_z=0}\approx 1+\frac{1}{a^3}\frac{1}{Re\left\{\alpha_m^{-1}\right\}-\left(\alpha_0^{-1}2M_c/L\left(\cos\left(k_x a\right)-1\right)+\alpha_0^{-1}\left(2M_a/L+4M_c/L\right)\right)-1/3a^3},\qquad(27)$$

where M_a and M_c are the mutual inductances between closest rings of the same orientation, placed in the axial and the coplanar directions, respectively, and α_0 is defined as in Eq. (2). For the particular case of magnetic dipole-type inclusions, straightforward calculations (using the fact that the magnetic field created by a magnetic dipole is $\mathbf{B}=(\mu_0/4\pi)(3\hat{\mathbf{r}}\hat{\mathbf{r}}\cdot\mathbf{m}-\mathbf{m}/r^3)$ [19]) show that in the quasi-static limit $M_a+2M_c=0$ and $\alpha_0^{-1}(2M_c/L)=2M_c/\mu_0 A^2=(-1/2\pi)(1/a^3)=-0.16/a^3$. Therefore, Eq. (27) simplifies to:

$$\left.\frac{\mu_{yy}}{\mu_0}\right|_{k_y=k_z=0}$$
$$\approx 1+\frac{1}{a^3}\frac{1}{Re\{\alpha_m^{-1}\}+0.16/a^3(\cos(k_x a)-1)-1/3a^3}\qquad(28)$$

It is interesting to compare the above formula with the magnetic permeability derived in Section 2.2. Since for $k_y=k_z=0$ we have $D_{\mathrm{int},ij}=0$ and it is clear that Eq. (21) implies that the magnetic permeability function is diagonal and such that $\mu_{yy}|_{k_y=k_z=0}=\mu_0\left(1+1/\left(a^3\chi_{22}\right)\right)$, or equivalently:

$$\left.\frac{\mu_{yy}}{\mu_0}\right|_{k_y=k_z=0}=1+\frac{1}{a^3}\frac{1}{Re\left\{\alpha_m^{-1}\right\}+0.026/a^3\left(\cos\left(k_x a\right)-1\right)-1/a^3\left(1/3-0.15(\omega a/c)^2\right)}\qquad(29)$$

Comparing Eqs. (28) and (29) two differences are detected. The first difference is the frequency correction of the static interaction constant (the term $0.15(\omega a/c)^2$), which was not considered in Ref. [12]. The second

difference is the coefficient that multiplies the term $(\cos(k_x a) - 1)$, which is responsible for the spatial dispersion effects. Apparently, the theory of our previous paper [12] (when applied to the particular case of magnetic dipoles) overestimates this coefficient by nearly one order of magnitude. A possible reason for this disagreement is that formula (28) is based on the nearest neighbor approximation, while the formula derived in this work takes into account the coupling between all the particles in the lattice. Indeed, the nearest neighbor approximation may be more useful when the mutual coupling between adjacent rings is large (which was the case studied in our previous work [12], where the resonant rings have larger diameters), whereas it may not be so accurate for dipole-type particles with a comparatively weaker mutual coupling.

3. Plane wave dispersion characteristic

Next, we apply the developed homogenization model to characterize the dispersion characteristic of plane

$$\left.\frac{\mu_{xx}}{\mu_0}\right|_{k_y=k_z=0} = 1 + \frac{1}{a^3 \operatorname{Re}\left\{\alpha_m^{-1}\right\} - 1/a^3 \left(1/3 - 0.15(\omega a/c)^2 + 0.052 \left(\cos\left(k_x a\right) - 1\right)\right)} \tag{32}$$

waves. To begin with, we remind that the model introduced in Section 2 supposes that the rings only have a magnetic response. Actually, this is a very rough approximation, since it is well known that in general resonant rings have as well an electric response (see for example Ref. [17]). As in Ref. [12], we will assume that the electric response of the rings can be taken into account by considering that the effective permittivity is equal to ε_{SRR}. Within this approximation the metamaterial is characterized by a local effective permittivity (ε_{SRR}) and by the nonlocal magnetic function (21) ($\bar{\bar{\mu}}(\omega, \mathbf{k})$).[1] It is interesting to note that this hypothesis is nothing more than assuming that the electric and magnetic responses are decoupled. Indeed, ε_{SRR} may be easily related to the electric polarizability of the particles using a homogenization approach similar to that of Section 2 (in general ε_{SRR} may also depend on the wave vector, however since the electric resonance occurs at a frequency significantly higher than the magnetic resonance, that dependence is expected to be small for frequencies comparable or smaller than the frequency associated with the magnetic resonance, which is the case of interest in this work).

From Eq. (17), setting $\mathbf{p}_{\text{ext}} = 0$, i.e. removing the external source, using $\mathbf{M} = \left(\bar{\bar{\mu}}/\mu_0 - \bar{\bar{\mathbf{I}}}\right) \cdot \mathbf{H}_{\text{av}}$, and replacing ε_0 by ε_{SRR}, it is readily found after some manipulations that

$$\left(\omega^2 \varepsilon_{SRR} \bar{\bar{\mu}} - k^2 \bar{\bar{\mathbf{I}}} + \mathbf{kk}\right) \cdot \mathbf{H}_{\text{av}} = 0. \tag{30}$$

3.1. Propagation along the coordinate axes

First we will analyze the case of propagation along the one of the coordinate axes, let us say the x-axis ($k_y = k_z = 0$). For this case the modes can be classified as longitudinal modes and transverse modes. The longitudinal modes are such that the magnetic field is parallel to the wavevector ($\mathbf{H}_{\text{av}} \sim \mathbf{k}$), which from Eq. (30) implies that

$$\bar{\bar{\mu}}(\omega, \mathbf{k}) \cdot \mathbf{k} = 0. \tag{31}$$

As discussed in Section 2, for propagation along the coordinate axes the magnetic function is diagonal, and thus the above relation is equivalent to $\mu_{xx} = 0$. Using Eq. (21) and the fact that $D_{\text{int},ij} = 0$, we find that

Thus, the dispersion relation of the longitudinal mode is:

$$a^3 \operatorname{Re}\left\{\alpha_m^{-1}\right\} + \frac{2}{3} + 0.15\left(\frac{\omega}{c}a\right)^2$$
$$- 0.052 \left(\cos\left(k_x a\right) - 1\right) = 0. \tag{33}$$

On the other hand, the metamaterial also supports transverse modes for which $\mathbf{H}_{\text{av}} \cdot \mathbf{k} = 0$. It is simple to verify that for propagation along the x-direction the dispersion relation of the transverse modes is

$$\omega^2 \varepsilon_{SRR} \mu_{yy}(\omega, k_x) = k_x^2, \tag{34}$$

being μ_{yy} given by Eq. (29).

3.2. Propagation along the main diagonal

It is also interesting to analyze the propagation properties along the "main diagonal" of the unit cell, namely along the ΓR direction, being Γ the origin of the Brillouin zone and $R = (\pi/a, \pi/a, \pi/a)$. It is thus clear that $k_x = k_y = k_z$, and therefore from Eqs. (22a) and (24) it follows that $\chi_{ii} = \operatorname{Re}\left\{\alpha_m^{-1}\right\} - 1/a^3 \left(1/3 - 0.15(\omega a/c)^2\right)$, for $i = 1, 2, 3$. On the other hand, from Eqs. (22b) and (25) it is obvious that χ_{ij} is

---

[1] Alternatively, the metamaterial could as well be characterized by the nonlocal dielectric function (6) with the first term in the right-hand side ($\bar{\bar{\mathbf{I}}}$) replaced by $(\varepsilon_{SRR}/\varepsilon_0) \bar{\bar{\mathbf{I}}}$, and by $\mu = \mu_0$.

independent of the values of i and j for $i \neq j$. Based on these properties it can be verified that the magnetic function is such that:

$$\bar{\bar{\mu}}|_{k_x = k_y = k_z} = \left(\bar{\bar{\mathbf{I}}} - \frac{\mathbf{kk}}{k^2}\right)\mu_t + \frac{\mathbf{kk}}{k^2}\mu_l \quad (35a)$$

$$\mu_t = \mu_0\left(1 + \frac{1}{V_{\text{cell}}}\frac{1}{\chi_{11} - \chi_{12}}\right);$$

$$\mu_l = \mu_0\left(1 + \frac{1}{V_{\text{cell}}}\frac{1}{\chi_{11} + 2\chi_{12}}\right), \quad (35b)$$

with $\quad \chi_{12} = -k^2/3a\left[-0.1936 - 0.01188(\omega a/c)^2 + 0.005902\,a^2 2k^2/3\right]$, and $\quad k^2 = \mathbf{k} \cdot \mathbf{k} = k_x^2 + k_y^2 + k_z^2$. It is clear that the above expression implies that the electromagnetic modes can also be classified as longitudinal and transverse modes. Using Eq. (31), it follows that the dispersion characteristic of the longitudinal mode (for propagation in the ΓR direction) is $\mu_l = 0$, or equivalently

$$a^3\text{Re}\left\{\alpha_m^{-1}\right\} + \frac{2}{3} + 0.15\left(\frac{\omega}{c}a\right)^2 + 2a^3\chi_{12} = 0. \quad (36)$$

On the other hand, the dispersion characteristic of the transverse modes is obviously

$$\omega^2\varepsilon_{SRR}\mu_t(\omega, k) = k^2. \quad (37)$$

4. Numerical example and discussion

In order to describe the implications of the theory developed in Section 3, we will analyze the case where the resonant rings are the edge-side coupled (EC) SRRs originally proposed by Pendry [1]. To ease the numerical and analytical modeling it is assumed that the SRRs are formed by thin wires with radius $r = 0.01a$ (see Fig. 1), instead of planar particles. The mean radius of the outer (inner) ring is $R + d/2$ ($R - d/2$), where $d = 0.1607R$ is the mean distance between rings, and $R = 0.4a$ is the average radius. Each ring has a split that covers an angular sector of $\varphi_{gap} = 10°$. It can be shown that the self-inductance and capacitance of the EC-SRRs may be estimated using the following formulas (see Refs. [12,17,23] for closely related results)

$$C = \frac{\varepsilon_0\pi R\left(\pi - \varphi_{gap}\right)}{\cosh^{-1}\left(d^2/2r^2 - 1\right)},$$

$$L = \mu_0 R\left[\ln\left(\frac{8R}{r}\right) - 2\right]. \quad (38)$$

The SRRs are oriented as shown in Fig. 1, consistent with the proposal of Ref. [27]. Such structure,
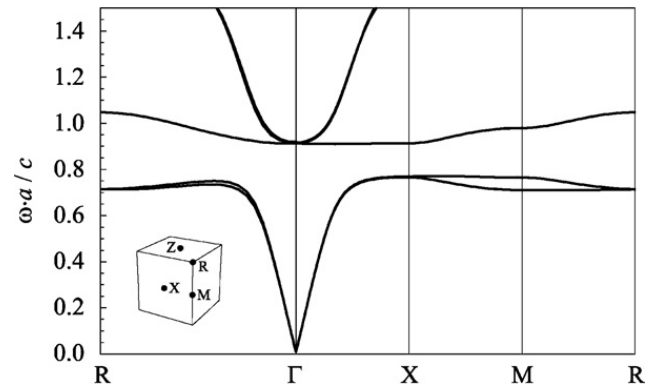

Fig. 2. Band structure of a material formed EC-SRRs with unit cell as in Fig. 1. The inset shows the first Brillouin zone and the high-symmetry points $X = (\pi/a, 0, 0)$, $M = (\pi/a, \pi/a, 0)$ and $R = (\pi/a, \pi/a, \pi/a)$.

unlike an ideal lattice of point magnetic dipoles, cannot be truly regarded as an isotropic magnetic material. Indeed, as discussed in Ref. [27], to ensure that a regular arrangement of particles is isotropic, the unit cell should be invariant under the application of proper rotations of the regular tetrahedron (cubic point group T), and the structure of Fig. 1 does not have such symmetry.[2] Moreover, the material also does not have inversion symmetry since SRRs in opposite faces of the cube have the same orientation due to the translational symmetry, and thus bianisotropic effects may occur [17]. Despite these problems, it will be shown below that the metamaterial (formed by very thin and closely spaced rings) has approximately an isotropic response.

The band structure of the array of SRR resonators was calculated using the hybrid integral equation-plane wave method described in Ref. [28], and is reported in Fig. 2. It can be seen that the structured material has a complete band gap that occurs due to the strong magnetic response of the rings. Below the magnetic resonance (normalized frequency $\omega a/c \approx 0.77$), the material supports only two electromagnetic modes (TEM waves), whose dispersion characteristic is nearly degenerated.

On the other hand, above the magnetic plasma frequency ($\omega a/c \approx 0.91$, i.e. the frequency where the propagation is resumed), the material supports three different modes. One of the modes is expected to be a longitudinal wave (the so-called longitudinal magne-

---

[2] The unit cell of Fig. 1 is invariant under the rotation $\mathbf{4}_x \cdot \mathbf{4}_z$, where $\mathbf{4}_i$ ($i = x, y, z$) represents a 4-fold (90-degree) rotation with respect to the ith axis. Thus, the metamaterial is invariant under $\pm 120°$ rotations with respect to the diagonal of the cube along $(1, -1, 1)$. However, it has not the same property along the other three diagonals, as would be required so that it would be invariant under the application of the T cubic point group.
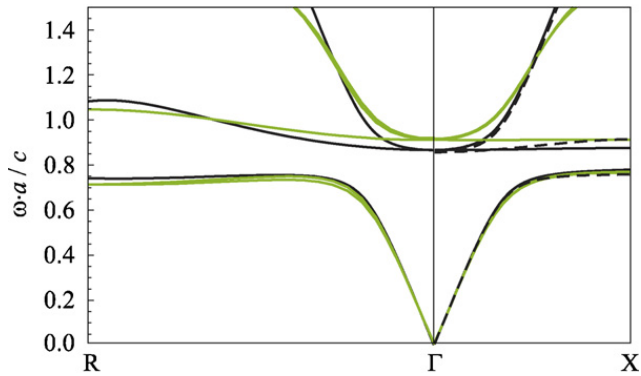
Fig. 3. Dispersion characteristic along the directions ΓR and ΓX. Black solid line: dipole based model proposed in this work. Black dashed line: model proposed in Ref. [12] (ΓX propagation), adapted for the case of point dipoles. Green (thick) lines: full wave electromagnetic simulations. (For interpretation of the references to colour in this figure legend, the reader is referred to the web version of the article.)

toinductive wave [13]) and has a nearly flat dispersion characteristic. The other two modes are approximately TEM waves and are nearly degenerated. The dispersion curves confirm that the response of the material below the magnetic resonance is to a good approximation isotropic. However, it can be seen that near the magnetic plasma frequency the dispersion characteristic of the longitudinal magnetoinductive wave depends significantly on the direction of the wave vector, having a much larger slope along the direction ΓR than along the direction ΓX. Similar results have been reported in our previous work (Ref. [12]) for the case where the inclusions are SRRs with two splits (unit cell with tetrahedral symmetry). Thus, the direction dependent properties of the longitudinal magnetoinductive wave can only be explained in terms of the emergence of nonlocal effects [21], induced by the granularity of the material.

We have calculated the theoretical dispersion characteristic using the analytical formulas reported in Sections 3.1 and 3.2, with the static effective permittivity $\varepsilon_{SRR} = 2.1\varepsilon_0$. This value was numerically computed using the homogenization approach of Ref. [14] for $\omega = 0$. The calculated dispersion curves are plotted in Fig. 3 (solid black lines) superposed on the numerical results (green thick lines). Despite the simplicity of the analytical model (which treats the SRRs as magnetic point dipoles), a fairly good agreement is revealed. In particular, below the magnetic resonance the analytical model concurs very well with the full wave simulations. Near the magnetic plasma frequency, the quantitative agreement is coarser, but the qualitative agreement remains good. Consistent with the full wave simulations, the analytical model predicts that for propagation along ΓX the dispersion characteristic of the longitudinal magne-

toinductive wave is flat, whereas for propagation along ΓR the dispersion curve has a significant dispersion. This supports that indeed the lack of isotropy of the longitudinal mode is due to the emergence of nonlocal effects, more specifically due to the relatively large values of $D_{int,ij} = -\chi_{ij}$ (see Eq. (36)), which characterizes the interaction between magnetic particles with different orientations.

Fig. 3 also reports (black dashed line) the results yielded by the model proposed in our previous work, Ref. [12], (adapted for the case of point dipoles: see Section 2.3) for propagation along the ΓX-direction. Consistent with the discussion of Section 2.3, it is seen that the model of Ref. [12] tends to overestimate the slope of the longitudinal model along the ΓX-direction. Apart from that discrepancy, the general agreement between the model proposed here and the results of Ref. [12] is good.

It is important to underline that in a local material (i.e. in the absence of spatial dispersion) the longitudinal wave should have a completely flat dispersion characteristic, independent of the direction of the wave vector. It seems that one of the most common manifestations of nonlocal effects in structured media is that the longitudinal wave is highly dispersive. This implies that unlike in a local material the longitudinal mode can be excited by an external source and represent an additional propagation channel. In an array of cubic particles made of EC-SRRs the nonlocal effects are dominant for propagation along the ΓR direction. Similar nonlocal effects have also been reported for arrays of uniaxial SRRs [23,29], for connected wire media [30–33], and for plasmonic nanorods [34].

The effects of spatial dispersion in the longitudinal mode can be tamed by decreasing the electrical size of the particles at the resonance, for example by increasing the capacitance of the rings. Indeed, from Eqs. (2) and (36) it is found that to a first order approximation (neglecting powers of both $(\omega a/c)^2$ and $(ka)^4$) the dispersion of the longitudinal mode along ΓR is

$$\left(\frac{\omega}{\omega_{mp}}\right)^2 \approx \frac{1}{1 + \left(1 - \omega_{mp}^2/\omega_r^2\right) 0.1936(ka)^2}, \quad (39)$$

where the magnetic plasma frequency (which defines the onset of propagation of the longitudinal mode) is approximately $\omega_{mp} \approx \omega_r/\sqrt{1 - 2/\left(3a^3\alpha_0^{-1}\right)}$. Let us estimate the range of wave vectors for which $\left|(\omega - \omega_{mp})/\omega_{mp}\right| < \delta$, where δ is some small number. Using Eq. (39) it can be easily seen that the solution is of the form $k < C/a$, where C is some constant that only
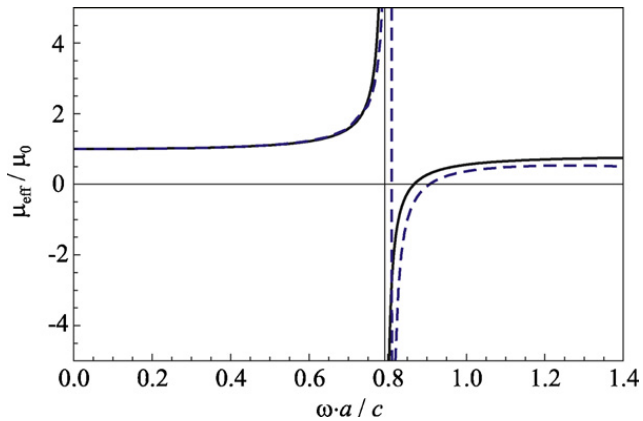
Fig. 4. Effective permeability of the array of cubic particles made of EC-SRRs as a function of frequency. Dashed blue line: full wave result extracted using the method reported in Ref. [14]. Solid black line: analytical result, $\mu(\omega, \mathbf{k}=0)$, calculated using formula (29). (For interpretation of the references to colour in this figure legend, the reader is referred to the web version of the article.)

depends on δ and on ω_{mp}/ω_r. But, for a fixed fill fraction (i.e. for R/a and r/a fixed) the ratio ω_{mp}/ω_r is independent of a. Moreover, the electrical size of the unit cell at the plasma frequency $\omega_{mp}a/c$ may be decreased by increasing the capacitance of the rings (e.g. by decreasing the inter-ring distance d). Thus, the range of wave vectors for which the condition $\left|(\omega - \omega_{mp})/\omega_{mp}\right| < \delta$ is observed verifies $kc/\omega_{mp} < C/(\omega_{mp}\, a/c)$, where C only depends on the fill fraction and δ, and $\omega_{mp}a/c$ is determined by the electrical size of the unit cell. Therefore, the values of k (normalized to the frequency of operation) for which the dispersion of the longitudinal mode is below some given threshold is broader when the electrical cell size of the unit cell is smaller, showing that in these conditions the nonlocal effects are less important.
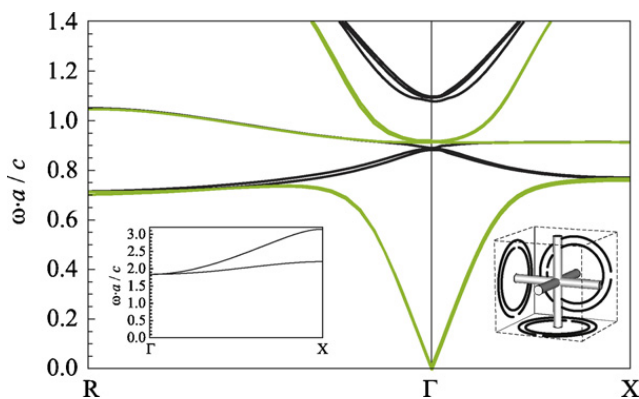

Fig. 5. Band structure of an array of cubic particles made of SRRs and connected wires (solid black lines; see geometry of the unit cell in the small right-hand side inset), superposed on the band structure of the array of SRRs (green lighter lines). The left-hand side inset shows the dispersion characteristic of the connected wire medium (without SRRs). (For interpretation of the references to colour in this figure legend, the reader is referred to the web version of the article.)

In order to further reveal other possible nonlocal effects, we have numerically calculated (with a full wave simulation) the effective permeability of the array of EC-SRRs using the approach described in Ref. [14]. The effective permeability is written in terms of the second order derivatives of the nonlocal dielectric function with respect to the wave vector [14]. The extraction procedure is only meaningful if the material's response is approximately local. The computed results are represented in Fig. 4 (dashed blue line), superposed on the results obtained with the analytical model (29), $\mu(\omega, \mathbf{k}=0)$ (solid black line). It is seen that the curves are nearly coincident, except for a small shift in frequency above the resonance. Given that the dashed line was extracted under the hypothesis that the material's response is local, these results suggest that, except for the dispersive longitudinal mode, the spatial dispersion effects are relatively weak, especially for $\mathbf{k}$ near the origin of the Brillouin zone.

5. Array of SRRs combined with a triple wire medium

Given the contemporary interest in materials with simultaneously negative permittivity and permeability [2,26,35], it is pertinent to study the electromagnetic response of a metamaterial formed by an array of SRRs combined with an array of connected wires [30–33,36,37] (see the geometry of the unit cell in the right-hand side inset of Fig. 5). Based on the results of the seminal work [35], it seems plausible that such structure may behave to some approximation as a nearly isotropic left-handed material. It is expected that the magnetic response of the composite material will be determined by the SRRs, whereas the electric response is mainly determined by the array of connected wires.

It was shown in Refs. [30,31] that the triple wire medium (with no SRRs) can be accurately characterized by the following nonlocal dielectric function (assuming perfectly conducting wires and that the host material is air):

$$\bar{\bar{\varepsilon}}(\omega, \mathbf{k}) = \varepsilon_{t,WM}(\omega)\left(\bar{\bar{\mathbf{I}}} - \frac{\mathbf{kk}}{k^2}\right) + \varepsilon_{l,WM}(\omega, k)\frac{\mathbf{kk}}{k^2},$$ (40a)

where the transverse and longitudinal components of the dielectric function are

$$\frac{\varepsilon_{t,WM}}{\varepsilon_0}(\omega) = 1 - \frac{\beta_p^2 c^2}{\omega^2}$$ (40b)

$$\frac{\varepsilon_{l,WM}}{\varepsilon_0}(\omega, k) = 1 - \frac{\beta_p^2}{\omega^2/c^2 - k^2/l_0}. \qquad (40c)$$

Above, $\beta_p = \left[2\pi / (\ln(a/2\pi r_w) + 0.5275)\right]^{1/2} / a$ is the plasma wavenumber, r_w is the radius of the wires, and l_0 is a constant defined in Refs. [30,31] that depends on the radius of the wires. The connected wire medium imitates to some extent a plasma characterized by a Drude type dispersion model, except for the longitudinal mode, which similar to the results of Section 4, may be highly dispersive [30,31].

If one assumes that the array of wires interacts weakly with the SRRs, as suggested by the symmetry of the material, by the results of Ref. [35] and also discussed in our previous work [12], it is straightforward to obtain a homogenization model for the composite material formed by SRRs and metallic wires. In fact, since the connected wire medium does not have a magnetic response, it follows that the magnetic function of the composite medium is the same as that of the array of cubic particles formed by EC-SRRs [Eq. (21)]. On the other hand, the effective permittivity of the composite medium should verify $\bar{\bar{\varepsilon}}_{WM+SRR} = \varepsilon_0 \bar{\bar{\mathbf{I}}} + (\varepsilon_{SRR} - \varepsilon_0) \bar{\bar{\mathbf{I}}} + \left(\bar{\bar{\varepsilon}}_{WM} - \varepsilon_0 \bar{\bar{\mathbf{I}}}\right)$, where ε_{SRR}, already defined in section III, is the effective permittivity of the array of EC-SRRs. Thus, within the considered hypothesis it is found that

$$\bar{\bar{\varepsilon}}(\omega, \mathbf{k}) = \varepsilon_{t,WM+SRR}(\omega)\left(\bar{\bar{\mathbf{I}}} - \frac{\mathbf{kk}}{k^2}\right)$$

$$+ \varepsilon_{l,WM+SRR}(\omega, k)\frac{\mathbf{kk}}{k^2} \qquad (41a)$$

$$\frac{\varepsilon_{t,WM+SRR}}{\varepsilon_0}(\omega) = \varepsilon_{SRR,r} - \frac{\beta_p^2 c^2}{\omega^2} \qquad (41b)$$

$$\frac{\varepsilon_{l,WM+SRR}}{\varepsilon_0}(\omega, k) = \varepsilon_{SRR,r} - \frac{\beta_p^2}{\omega^2/c^2 - k^2/l_0}. \qquad (41c)$$

where $\varepsilon_{SRR,r} = \varepsilon_{SRR}/\varepsilon_0$. It is important to emphasize that the magnetic effects of the composite medium are not included in the nonlocal dielectric function, and are described separately by $\bar{\bar{\mu}}(\omega, \mathbf{k})$, given by Eq. (21) [the magnetic effects could be easily incorporated into the dielectric function using a formula similar to (6); however, here it is preferable to separate the electric and magnetic responses since such framework is necessary to study the longitudinal magnetoinductive wave for which $\mu_l = 0$ [21].

Using the hybrid integral equation-plane wave method of Ref. [28], we have computed the band structure of the composite material formed by connected wires and EC-SRRs. The geometry of the EC-SRRs is the

same as that considered in section IV, and the triple wire medium is formed by wires with radius $r_w = 0.05a$. The calculated band structure is represented in Fig. 5 (solid black lines) for the directions ΓR and ΓX of the Brillouin zone. It is seen that the material supports backward waves for $0.77 < \omega a/c < 0.89$, i.e. roughly in the same frequency band where the array of EC-SRRs is characterized by a complete band gap (the band structure of the array of EC-SRRs is represented with green lines in Fig. 5). This supports the hypothesis that the composite material formed by wires and SRRs behaves as a left-handed medium. Quite interesting, the upper frequency of the backward wave regime is slightly below the magnetic plasma frequency of the array of EC-SRRs. Most likely this is a consequence of some residual bianisotropic effects, consistent with the theory of Ref. [17].

Besides the two backward wave (TEM) modes, the composite material also supports a longitudinal mode at the magnetic plasma frequency. Remarkably, except very near to the Γ point, the dispersion of the longitudinal mode cannot be distinguished from the dispersion of the longitudinal magnetoinductive wave identified in Section 4 (nearly flat green line in Fig. 5). This behavior completely supports the hypothesis that the triple wire medium interacts weakly with the array of SRRs. Indeed, the dispersion of the longitudinal mode is determined by condition (31), $[\bar{\bar{\mu}}(\omega, \mathbf{k}) \cdot \mathbf{k} = 0]$, which is completely independent of the dielectric function $\bar{\bar{\varepsilon}}(\omega, \mathbf{k})$ of the composite material (because the magnetoinductive longitudinal mode is associated with a trivial macroscopic electric field: $\mathbf{E}_{av} = 0$). This explains why the dispersion characteristic of this mode remains nearly invariant when the triple wire medium is added to the array of EC-SRRs.

The composite material formed by SRRs and wires has a band gap above the magnetic plasma frequency. The propagation is resumed at $\omega a/c \approx 1.08$, which supposedly corresponds to the electric plasma frequency for which $\varepsilon_{WM+SRR} \approx 0$. The theoretical value of the electric plasma frequency may be estimated using Eq. (41b) and is $\omega_{ep}/c = \beta_p / \sqrt{\varepsilon_{SRR,r}}$. Since, for wires with $r_w = 0.05a$ we have that $\beta_p = 1.93/a$, using $\varepsilon_{SRR,r} = 2.1$ (see Section 4) we obtain the theoretical value, $\omega_{ep}a/c = 1.33$, which is slightly larger than the more precise value obtained from the band structure of the material. Most likely the reason for the discrepancy is that $\varepsilon_{SRR,r} = 2.1$ is the static permittivity of the array of SRRs, and thus our model may underestimate $\varepsilon_{SRR,r}$ at the electric plasma frequency.

Above the electric plasma frequency the metamaterial supports three electromagnetic modes. Two of the modes are expected to be associated with TEM waves, whereas the other mode is expected to be associated with an

electric-type longitudinal mode. Curiously, it can be seen in Fig. 5 that the dispersion characteristic of these three modes is nearly coincident. This contrasts markedly with the case where the metallic wires stand alone in the lattice (see the left-hand side inset of Fig. 5), for which the dispersion of the longitudinal mode is much smaller than that of the transverse modes. To explain this curious phenomenon, we note that near the plasma frequency the magnetic response of the SRRs is expected to be relatively weak (see Fig. 4) [i.e. $\bar{\bar{\mu}}(\omega, \mathbf{k}) \approx \mu_0 \bar{\bar{\mathbf{I}}}$], and thus to a first a approximation the composite metamaterial may be described using only the nonlocal dielectric function $\bar{\bar{\varepsilon}}(\omega, \mathbf{k})$. It should be clear that Eq. (41) implies that the metamaterial supports two transverse modes with dispersion characteristic $k^2 = \varepsilon_{t,WM+SRR} \, \mu_0 \, \omega^2$, i.e.

$$\frac{\omega^2}{c^2} = \frac{\beta_p^2}{\varepsilon_{SRR,r}} + \frac{k^2}{\varepsilon_{SRR,r}} \tag{42a}$$

and a longitudinal mode with dispersion characteristic $\varepsilon_{l,WM+SRR} = 0$, i.e.

$$\frac{\omega^2}{c^2} = \frac{\beta_p^2}{\varepsilon_{SRR,r}} + \frac{k^2}{l_0}. \tag{42b}$$

Comparing Eqs. (42a) and (42b), it is seen that the dispersion of the transverse and longitudinal modes is the same when $\varepsilon_{SRR,r} \approx l_0$. But for a triple wire medium with $r_w = 0.05a$ we have that $l_0 \approx 2.03$ (see Refs. [30,31]), and thus the condition $\varepsilon_{SRR,r} \approx l_0$ seems to be verified in our problem. This coincidence explains the similarity of the dispersion characteristics of the transverse and longitudinal modes above the electric plasma frequency.

6. Conclusion

Using nonlocal homogenization methods we have calculated theoretically the magnetic function of an array of cubic magnetic resonators, under the approximation that the inclusions can be modeled using the magnetic dipole approximation. The proposed model complements the analysis of our previous work [12], and takes into account all interactions between the particles (i.e. magnetic dipoles), and both frequency and spatial dispersion. It was shown that the properties of the longitudinal magnetoinductive wave are determined by nonlocal effects, which are caused by the interaction of the magnetic resonators with different orientations. Our results suggest that except in the regime where $\mu \approx 0$, the effects of spatial dispersion may be relatively weak, especially if $\mathbf{k}$ is near the origin of the Brillouin zone. In addition, we studied the propagation properties in

a composite material formed by EC-SRRs and a triple wire medium. It was shown that such material supports a backward wave regime, where it may behave as a nearly isotropic left-handed material. In addition, it also supports both magnetic-type and electric-type longitudinal modes, and two TEM modes above the electric plasma frequency. It is hoped that the present study contributes for the understanding of nonlocal homogenization techniques, and stimulates the study of truly isotropic local left-handed metamaterials.

Appendix A.

In this appendix we briefly describe the solution of the homogenization problem when the resonant rings are modeled as particles with an electric response. As discussed in Section 2.1, in these circumstances the magnetic effects are related to the vortex part of the induced electric current density.

Following Ref. [14], the nonlocal dielectric function is calculated by exciting the metamaterial with an external electric current density, $\mathbf{J}_{e,\text{ext}} = j\omega \left(\mathbf{p}_{\text{ext}}^{(e)} / V_{\text{cell}} \right) e^{-j\mathbf{k}\cdot\mathbf{r}}$, where $\mathbf{p}_{\text{ext}}^{(e)}$ is a constant vector. Thus, the microscopic electromagnetic fields, $(\mathbf{E}, \mathbf{B})$, verify:

$$\nabla \times \mathbf{E} = -j\omega \mathbf{B} \tag{A1a}$$

$$\nabla \times \frac{\mathbf{B}}{\mu_0} = j\omega\varepsilon_0 \mathbf{E} + \mathbf{J}_{e,\text{ext}} + \mathbf{J}_{e,\text{dip}}, \tag{A1b}$$

where the microscopic electric current density, $\mathbf{J}_{e,\text{dip}}$, is given by Eq. (4), and is written in terms of the unknown magnetic dipole moments of the particles in the unit cell $\mathbf{p}_i$. It is important to emphasize that when the response of the particles is characterized by an electric current density, as considered here, the microscopic fields are the electric field intensity ($\mathbf{E}$) and the magnetic induction ($\mathbf{B}$). Quite differently, from duality, when the response of the particles is characterized by a magnetic current density the microscopic fields are the electric field inten-

sity (**E**) and the magnetic field intensity (**H**) (see Section 2.2).

It may be easily shown that the solution of Eq. (A1) is:

$$\mathbf{E}(\mathbf{r}) = (-j\omega\mu_0) \sum_{i=1,2,3} \nabla \times \bar{\bar{\mathbf{G}}}_p \left(\mathbf{r}|\,\mathbf{r}_{0,i}\right) \cdot \frac{\mathbf{p}_i}{\mu_0}$$
$$+ (-j\omega\mu_0)\bar{\bar{\mathbf{G}}}_{\mathrm{av}} \cdot j\omega\mathbf{p}_{\mathrm{ext}}^{(e)}\, e^{-j\mathbf{k}\cdot\mathbf{r}}. \qquad (A2)$$

Thus, the local electric field in the immediate vicinity of the ith ring is

$$\mathbf{E}_{\mathrm{loc},i}(\mathbf{r}) = -j\omega\nabla \times \overline{\overline{\mathbf{G}'_p}}\left(\mathbf{r}|\,\mathbf{r}_{0,i}\right) \cdot \mathbf{p}_i$$
$$- j\omega \sum_{j \neq i} \nabla \times \bar{\bar{\mathbf{G}}}_p \left(\mathbf{r}|\,\mathbf{r}_{0,j}\right) \cdot \mathbf{p}_j$$
$$+ \omega^2 \mu_0 \bar{\bar{\mathbf{G}}}_{\mathrm{av}} \cdot \mathbf{p}_{\mathrm{ext}}^{(e)} e^{-j\mathbf{k}\cdot\mathbf{r}}, \qquad (A3)$$

whereas the local induction field, $\mathbf{B}_{\mathrm{loc},i} = \nabla \times \mathbf{E}_{\mathrm{loc},i}/(-j\omega)$, is

$$\mathbf{B}_{\mathrm{loc},i}(\mathbf{r}) = \left(\frac{\omega}{c}\right)^2 \overline{\overline{\mathbf{G}'_p}}\left(\mathbf{r}|\,\mathbf{r}_{0,i}\right) \cdot \mathbf{p}_i$$
$$+ \sum_{j \neq i} \left(\frac{\omega}{c}\right)^2 \bar{\bar{\mathbf{G}}}_p\left(\mathbf{r}|\,\mathbf{r}_{0,j}\right) \cdot \mathbf{p}_j$$
$$+ \omega\mu_0 \mathbf{k} \times \bar{\bar{\mathbf{G}}}_{\mathrm{av}} \cdot \mathbf{p}_{\mathrm{ext}}^{(e)} e^{-j\mathbf{k}\cdot\mathbf{r}}, \qquad (A4)$$

being $\overline{\overline{\mathbf{G}'_p}}$ defined as in Eq. (13). It should be clear that in the present context $\mathbf{H}_{\mathrm{loc}}$ in Eq. (3) should be identified with $\mathbf{B}_{\mathrm{loc}}/\mu_0$. Thus, using the auxiliary relation $\mathbf{k} \times \bar{\bar{\mathbf{G}}}_{\mathrm{av}} = \bar{\bar{\mathbf{G}}}_{\mathrm{av}} \times \mathbf{k} = \bar{\bar{\mathbf{G}}}_{\mathrm{av}} \cdot (\mathbf{k} \times \bar{\bar{\mathbf{I}}})$, [see Eq. (10)], and the property $\mathbf{p}_i = p_i\hat{\mathbf{u}}_i$, it is found that for $i = 1, 2, 3$

$$\alpha_m^{-1}\frac{p_i}{\mu_0} = \left(\frac{\omega}{c}\right)^2 \left(\hat{\mathbf{u}}_i \cdot \overline{\overline{\mathbf{G}'_p}}(0|0) \cdot \hat{\mathbf{u}}_i \frac{p_i}{\mu_0}\right.$$
$$+ \sum_{j \neq i} \hat{\mathbf{u}}_i \cdot \overline{\overline{\mathbf{G}}}_p \left(\mathbf{r}_{0,i}|\,\mathbf{r}_{0,j}\right) \cdot \hat{\mathbf{u}}_j \frac{p_j}{\mu_0}$$
$$+ \hat{\mathbf{u}}_i \cdot \bar{\bar{\mathbf{G}}}_{\mathrm{av}} \cdot \left(\frac{c^2\mathbf{k}}{\omega} \times \mathbf{p}_{\mathrm{ext}}^{(e)}\right) e^{-j\mathbf{k}\cdot\mathbf{r}_{0,i}}\right). \qquad (A5)$$

Interestingly, the above result is equivalent to Eq. (14), provided we make the identification $\mathbf{p}_{\mathrm{ext}} = \mathbf{k} \times \mathbf{p}_{\mathrm{ext}}^{(e)}/\omega\varepsilon_0$. Therefore, making manipulations similar to

those of Section 2.2, we conclude that

$$\bar{\bar{\chi}} \cdot \mathbf{M} = \left(\frac{\omega}{c}\right)^2 \bar{\bar{\mathbf{G}}}_{\mathrm{av}} \cdot \left(\mathbf{M} + \frac{1}{V_{\mathrm{cell}}}\frac{c^2\mathbf{k}}{\omega} \times \mathbf{p}_{\mathrm{ext}}^{(e)}\right), \qquad (A6)$$

where the magnetization vector $\mathbf{M}$ is defined as in Eq. (18), and the dyadic $\bar{\bar{\chi}}$ is defined as in Eq. (22).

The dielectric function must verify $\left(\bar{\bar{\varepsilon}}(\omega, \mathbf{k}) - \varepsilon_0\bar{\bar{\mathbf{I}}}\right) \cdot \mathbf{E}_{\mathrm{av}} = \mathbf{P}_g$, independent of the applied current density, where $\mathbf{P}_g$ is the generalized electric polarization vector given by [14]:

$$\mathbf{P}_g = \frac{1}{V_{\mathrm{cell}}\,j\omega} \int_{\mathrm{cell}} \mathbf{J}_{e,\mathrm{dip}}(\mathbf{r})\, e^{+j\mathbf{k}\cdot\mathbf{r}} d^3\mathbf{r} = -\frac{\mathbf{k}}{\omega} \times \mathbf{M}. \qquad (A7)$$

By averaging the microscopic Maxwell's equations (A1) [see Eqs. (9) and (14) of Ref. [14]], it can be easily shown that the macroscopic electric field must be such that:

$$\mathbf{E}_{\mathrm{av}} = \omega^2 \mu_0 V_{\mathrm{cell}} \bar{\bar{\mathbf{G}}}_{\mathrm{av}} \cdot \left(\mathbf{P}_g + \frac{\mathbf{p}_{\mathrm{ext}}^{(e)}}{V_{\mathrm{cell}}}\right). \qquad (A8)$$

Thus, using again the result $\mathbf{k} \times \bar{\bar{\mathbf{G}}}_{\mathrm{av}} = \bar{\bar{\mathbf{G}}}_{\mathrm{av}} \times \mathbf{k}$ and Eq. (A7), it is found after some algebra that:

$$\frac{\mathbf{k}}{\mu_0\omega} \times \mathbf{E}_{\mathrm{av}}$$
$$= \mathbf{M} + \frac{\omega^2}{c^2} V_{\mathrm{cell}} \bar{\bar{\mathbf{G}}}_{\mathrm{av}} \cdot \left(\mathbf{M} + \frac{1}{V_{\mathrm{cell}}}\frac{c^2\mathbf{k}}{\omega} \times \mathbf{p}_{\mathrm{ext}}^{(e)}\right). \qquad (A9)$$

Substituting now the above formula into Eq. (A6), it follows the magnetization vector is related to the macroscopic electric field as

$$\mathbf{M} = -\left(\mu_0\bar{\bar{\mu}}^{-1} - \bar{\bar{\mathbf{I}}}\right) \cdot \left(\frac{\mathbf{k}}{\mu_0\omega} \times \mathbf{E}_{\mathrm{av}}\right), \qquad (A10)$$

where $\bar{\bar{\mu}}$ is defined as in Eq. (21), and we have used the property $\bar{\bar{\mu}}^{-1} = \bar{\bar{\mathbf{I}}} - \left(\bar{\bar{\mathbf{I}}} + V_{\mathrm{cell}}\bar{\bar{\chi}}\right)^{-1}$. Finally, using the property $\left(\bar{\bar{\varepsilon}}(\omega, \mathbf{k}) - \varepsilon_0\bar{\bar{\mathbf{I}}}\right) \cdot \mathbf{E}_{\mathrm{av}} = \mathbf{P}_g$ and Eqs. (A7) and (A10), it is found that the nonlocal dielectric function of the metamaterial verifies, indeed, Eq. (6), as we wanted to prove.

References

[1] J. Pendry, A. Holden, D. Robbins, W. Stewart, IEEE Trans. Microwave Theory Tech. 47 (1999) 2075.
[2] J.B. Pendry, Phys. Rev. Lett. 85 (2000) 3966.
[3] J. Freire, R. Marques, Appl. Phys. Lett. 86 (2005) 182505.

[4] M.C.K. Wiltshire, J.B. Pendry, I.R. Young, D.J. Larkman, D.J. Gilderdale, J.V. Hajnal, Science 291 (2001) 849.

[5] M.C.K. Wiltshire, J.V. Hajnal, J.B. Pendry, D.J. Edwards, C.J. Stevens, Opt. Exp. 11 (2003) 709.

[6] M.J. Freire, R. Marques, L. Jelinek, Appl. Phys. Lett. 93 (2008) 231108.

[7] C.R. Simovski, S.A. Tretyakov, Phys. Rev. B 79 (2009) 045111.

[8] A. Alù, A. Salandrino, N. Engheta, Opt. Exp. 14 (2006) 1557.

[9] A. Alù, N. Engheta, Phys. Rev. B 75 (2007) 024304.

[10] A. Alù, N. Engheta, Phys. Rev. B 78 (2008) 085112.

[11] D.R. Smith, S. Schultz, P. Markos, C.M. Soukoulis, Phys. Rev. B 65 (2002) 195104.

[12] J.D. Baena, L. Jelinek, R. Marqués, M. Silveirinha, Phys. Rev. A 78 (2008) 013842.

[13] E. Shamonina, V.A. Kalinin, K.H. Ringhofer, L. Solymar, J. Appl. Phys. 92 (2002) 6252.

[14] M.G. Silveirinha, Phys. Rev. B 75 (2007) 115104.

[15] M.G. Silveirinha, Phys. Rev. B 76 (2007) 245117.

[16] M. Gorkunov, M. Lapine, E. Shamonina, K.H. Ringhofer, Eur. Phys. J. B 28 (2002) 263–269.

[17] R. Marqués, F. Medina, R. Rafii-El-Idrissi, Phys. Rev. B 65 (2002) 144440.

[18] R. Marqués, F. Mesa, J. Martel, F. Medina, IEEE Trans. Antennas Propagat. 51 (2003) 2572.

[19] J.D. Jackson, Classical Electrodynamics, Wiley, 1998.

[20] V.M. Agranovich, Y.R. Shen, R.H. Baughman, A.A. Zakhidov, Phys. Rev. B 69 (2004) 165112.

[21] V.M. Agranovich, Metamaterials 3 (2009) 1.

[22] M.G. Silveirinha, C.A. Fernandes, IEEE Trans. Antennas Propagat. 53 (2005) 347–355.

[23] M.G. Silveirinha, P.A. Belov, Phys. Rev. B 77 (2008) 233104.

[24] C.R. Simovski, S. He, Phys. Lett. A 311 (2003) 254.

[25] C.R. Simovski, B. Sauviac, Radio Sci. 39 (2004) RS2014.

[26] L. Jelinek, R. Marqués, F. Mesa, J.D. Baena, Phys. Rev. B 77 (2008) 205110.

[27] J.D. Baena, L. Jelinek, R. Marqués, Phys. Rev. B 76 (2007) 245115.

[28] M.G. Silveirinha, C.A. Fernandes, IEEE Trans. Microw. Theory Tech. 52 (2004) 889–902.

[29] P.A. Belov, C.R. Simovski, Phys. Rev. E 72 (2005) 026615.

[30] M.G. Silveirinha, C.A. Fernandes, IEEE Trans. Microw. Theory Tech. 53 (2005) 1418–1430.

[31] M.G. Silveirinha, Phys. Rev. B 79 (2009) 035118.

[32] M.A. Shapiro, G. Shvets, J.R. Sirigiri, R.J. Temkin, Opt. Lett. 31 (2006) 2051–2053.

[33] A. Demetriadou, J.B. Pendry, J. Phys. Condens. Matter 20 (2008) 295222.

[34] R.J. Pollard, A. Murphy, W.R. Hendren, P.R. Evans, R. Atkinson, G.A. Wurtz, A.V. Zayats, V.A. Podolskiy, Phys. Rev. Lett. 102 (2009) 127405.

[35] D.R. Smith, J. Willie, D.C. Padilla, S.C. Vier, S. Nemat-Nasser, Schultz, Phys. Rev. Lett. 84 (2000) 4184.

[36] J. Pendry, A.J. Holden, W.J. Stewart, I. Youngs, Phys. Rev. Lett. 76 (1996) 4773.

[37] M. Hudlicka, J. Machác, I.S. Nefedov, Prog. Electromagnet. Res. 65 (2006) 233–246.

Appendix 11

This appendix contains a full text of Ref. [43]

Surface mesoscopic effects in finite metamaterials

Mikhail Lapine,[1,*] **Lukas Jelinek,**[2] **and Ricardo Marqués**[3]

[1]*CUDOS, School of Physics, University of Sydney, Australia*
[2]*Department of Electromagnetic Field, Czech Technical University in Prague, Czech Republic*
[3]*Department of Electronics and Electromagnetism, University of Seville, Spain*

[*]*mlapine@physics.usyd.edu.au*

Abstract: While the effective medium treatment of unbounded metamaterials appears to be well established and firmly proven, related phenomena in finite structures have not received sufficient attention. We report on mesoscopic effects associated with the boundaries of finite discrete metamaterial samples, which can invalidate an effective medium description. We show how to avoid such effects by proper choice of boundary configuration. As all metamaterial implementations are naturally finite, we are confident that our findings are crucial for future metamaterial research.

© 2012 Optical Society of America

References and links

1. C. R. Simovski, "Material parameters of metamaterials," Opt. Spectrosc. **107**, 726–753 (2009).
2. S. A. Schelkunoff and H. T. Friis, *Antennas Theory and Practice* (Wiley, 1966).
3. J. B. Pendry, A. J. Holden, D. J. Robbins, and W. J. Stewart, "Magnetism from conductors and enhanced nonlinear phenomena," IEEE Trans. Microw. Theory Tech. **47**, 2075–2084 (1999).
4. M. Gorkunov, M. Lapine, E. Shamonina, and K. H. Ringhofer, "Effective magnetic properties of a composite material with circular conductive elements," Eur. Phys. J. B **28**, 263–269 (2002).
5. R. Marqués, F. Medina, and R. Rafii-El-Idrissi, "Role of bianisotropy in negative permeability and left-handed metamaterials," Phys. Rev. B **65**, 144440 (2002).
6. E. Shamonina, V. A. Kalinin, K. H. Ringhofer, and L. Solymar, "Magnetoinductive waves in one, two, and three dimensions," J. Appl. Phys. **92**, 6252–6261 (2002).
7. R. R. A. Syms, E. Shamonina, V. Kalinin, and L. Solymar, "A theory of metamaterials based on periodically loaded transmission lines: interaction between magnetoinductive and electromagnetic waves," J. Appl. Phys. **97**, 064909 (2005).
8. J. D. Baena, L. Jelinek, R. Marqués, and M. Silveirinha, "Unified homogenization theory for magnetoinductive and electromagnetic waves in split-ring metamaterials," Phys. Rev. A **78**, 013842 (2008).
9. M. Silveirinha, J. Baena, L. Jelinek, and R. Marques, "Nonlocal homogenization of an array of cubic particles made of resonant rings," Metamaterials **3**, 115–128 (2009).
10. V. M. Agranovich and Y. N. Gartstein, "Electrodynamics of metamaterials and the Landau–Lifshitz approach to the magnetic permeability," Metamaterials **3**, 1–9 (2009).
11. C. R. Simovski, "Analytical modelling of double-negative composites," Metamaterials **2**, 169–185 (2008).
12. P. A. Belov and C. R. Simovski, "Boundary conditions for interfaces of electromagnetic crystals and the generalized Ewald-Oseen extinction principle," Phys. Rev. B **73**, 045102 (2006).
13. M. Albooyeh, D. Morits, and C. R. Simovski, "Electromagnetic characterization of substrated metasurfaces," Metamaterials **5**, 178–205 (2011).
14. M. Silveirinha, "Metamaterial homogenization approach with application to the characterization of microstructured composites with negative parameters," Phys. Rev. B **75**, 115104 (2007).
15. A. Alù, "First-principles homogenization theory for periodic metamaterials," Phys. Rev. B **84**, 075153 (2011).
16. M. Gorkunov, S. A. Gredeskul, I. V. Shadrivov, and Y. S. Kivshar, "Effect of microscopic disorder on magnetic properties of metamaterials," Phys. Rev. E **73**, 056605 (2006).

17. J. Rico-García, J. López-Alonso, and A. Aradian, "Toy model to describe the effect of positional blocklike disorder in metamaterials composites," J. Opt. Soc. Am. B **29**, 53–67 (2012).
18. R. R. A. Syms, O. Sydoruk, and L. Solymar, "Lossy metamaterials: no effective medium properties without noise," Phys. Rev. B **84**, 235150 (2011).
19. A. P. Vinogradov, D. P. Makhnovskii, and K. N. Rozanov, "Effective boundary layer in composite materials," J. Communication Technol. Electron. **44**, 317–322 (1999).
20. O. N. Gadomskii and S. V. Sukhov, "Microscopic theory of a transition layer on the ideal surface of semiinfinite dielectric media and the near-field effect," Opt. Spectrosc. **89**, 261–266 (2000).
21. M. Lapine, S. Tretyakov, "Contemporary notes on metamaterials," IET Microw. Antenn. Propag. **1**, 3–11 (2007).
22. O. Zhuromskyy, E. Shamonina, and L. Solymar, "2D metamaterials with hexagonal structure: spatial resonances and near field imaging," Opt. Express **13**, 9299–9309 (2005).
23. R. Marqués, L. Jelinek, M. Freire, J. Baena, and M. Lapine, "Bulk metamaterials made of resonant rings," Proc. IEEE **99**, 1660–1668 (2011).
24. A. M. Nicolson and G. F. Ross, "Measurement of the intrinsic properties of materials by time-domain techniques," IEEE Trans. Instrum. Meas. **IM–19**, 377–382 (1970).
25. W. B. Weir, "Automatic measurement of complex dielectric constant and permeability at microwave frequencies," Proc. IEEE **62**, 33–36 (1974).
26. X.-X. Liu, D. A. Powell, and A. Alù, "Correcting the Fabry-Perot artifacts in metamaterial retrieval procedures," Phys. Rev. B **84**, 235106 (2011).
27. O. Luukkonen, S. I. Maslovski, and S. A. Tretyakov, "A stepwise Nicolson–Ross–Weir–based material parameter extraction method," IEEE Antenn. Wireless Propag. Lett. **10**, 1295–1298 (2011).
28. M. Lapine, L. Jelinek, R. Marqués, and M. Freire, "Exact modelling method for discrete finite metamaterial lens," IET Microw. Antenn. Propag. **4**, 1132–1139 (2010).
29. H. Wallén, H. Kettunen, and A. Sihvola, "Surface modes of negative-parameter interfaces and the importance of rounding sharp corners," Metamaterials **2**, 113–121 (2008).

1. Introduction

Metamaterials — artificial media engineered with various structural units which play the role of atoms — have been in the focus of active research for more than a decade. One of the milestones in understanding metamaterial properties is the effective medium theory (EMT), which aims to describe metamaterials in terms of effective parameters: permittivity and permeability [1]. In particular, EMT has been essential for the lattices of split-ring-resonators (SRRs) — the key structure for obtaining an artificial magnetic response [2]. Approaches for determining the effective permeability of bulk SRR-metamaterials were attempted prior to metamaterials outburst [3]. Subsequently, fruitful theoretical procedures were developed to account for mutual interaction [4], bianisotropy [5], magnetoinductive waves [6] and their interaction with the electromagnetic spectrum [7, 8], spatial dispersion [8–10], mutual interaction between the electric and magnetic subsystems [11], specificity of boundary conditions [12, 13], arbitrary geometry of elements [14], multipole expansion [15], disorder [16, 17] and noise [18].

However, effective medium theories, in principle, consider unbounded lattices, whereas all practical metamaterials are of finite size. For conventional materials, it is well known [13, 19, 20] that at the boundaries a transition layer is formed, with properties different from those of the bulk (see the historical introduction in [13] for a detailed background). For large samples, however, transition layer does not significantly affect the overall macroscopic properties, and only manifests itself under specific conditions such as strongly oblique incidence, with surface modes not affecting the bulk considerably. But metamaterials are often constructed with a much fewer number of elements than reasonable pieces of conventional materials, so a comparison to atomic clusters might be more appropriate. At the same time, internal structure of metamaterials is often more complex than that of natural materials, in a sense that metamaterial elements may be quite densely arranged, be of different types or form geometrically independent sublattices [21]. This raises an issue of pronounced surface and spatial resonances which may appear in finite structures even in a quasi-static regime [22, 23].

For metamaterial slabs, having a finite size in one dimension (and the same applies to the small samples placed inside a waveguide, which is equivalent to a system infinite in transverse
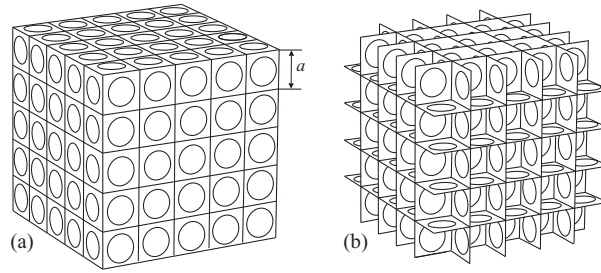
Fig. 1. Scheme of a symmetric finite cube with discrete structure, showing two options of surface configuration (for the same unit cell in the bulk): "flat" geometry (a) and "ragged" geometry (b). Note that the actual number of elements is not necessarily reflected here.

direction), bulk effective parameters can be, with certain precautions, extracted from transmission and reflection characteristics [24, 25] (see e.g. [26, 27] for a recent update on the methodology). On this way, it is known that the effective properties extracted for the slabs of finite thickness quickly converge to the EMT predictions when the number of unit cells across the slab increases, and for most structures with low spatial dispersion a thickness of a few unit cells is sufficient to yield the bulk properties.

In this paper, we address the most general case of practical relevance: metamaterials with finite size in all three dimensions, observed in free space. We will analyse whether such metamaterials can be described with EMT parameters, and what are the requirements for such a description to be valid. It turns out that while for a slab of metamaterial a few unit cells across the slab are sufficient for EMT to work well, for the finite size in 3D it may be not sufficient to take several unit cells in each direction, and that a dramatic effect is caused by the ambiguity in the boundary structure (see Fig. 1).

Indeed, a unit cell of the isotropic system shown in Fig. 1 contains three resonant loops non-symmetrically positioned with respect to the geometrical centre of the cell: three sides of the cube carry resonators, and the other three do not (as those resonators belong to the adjacent unit cells). This makes no difference in the middle of the structure. However, at the boundaries, overall symmetry of the sample can be achieved either by adding extra surface resonators on the three sides, Fig. 1(a), or, less trivially, by removing the unnecessary resonators on the opposite sides, Fig. 1(b). We will further refer to these methods of assembly as "flat" and "ragged".

We should note that early analysis [4] confirmed that anisotropic stacks of uniformly oriented SRRs (all having parallel axes), with about one thousand elements can be successfully described with EMT; however that structure has no ambiguity of the kind described above.

2. Results and discussion

We will now analyse metamaterial cubes with isotropic cubic unit cells, and having different surface geometry as discussed above, and compare their characteristics to those of homogeneous pieces of a bulk material with the corresponding effective parameters [8]. In order to avoid any complications related to spatial dispersion and fit well into the EMT domain, we study a system with deeply subwavelength and strongly interacting resonant current loops: $k_{res}a \approx 0.02$ and $a/r_0 \approx 3.1$ (where k_{res} is the value of the free space wavenumber k_0 at resonance, a is the lattice constant and r_0 is the mean radius of the loop). A high quality factor of the resonators, $Q \approx 500$, has been chosen in order to present more illustrative results.

The finite size in all three directions does not permit a consistent study in terms of transmission characteristics, but there is a convenient macroscopic characteristic that can be attributed
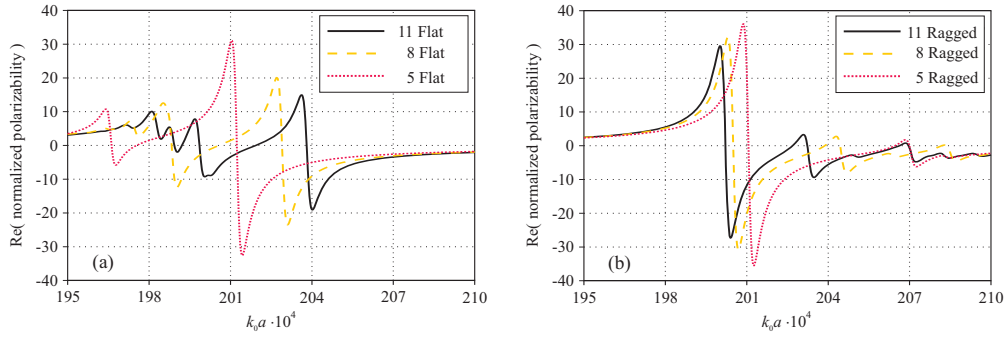
Fig. 2. Real part of the normalised polarisability (arbitrary units) of discrete cubes with 5, 8 or 11 layers of resonators in each direction, having either a "flat" geometry (a) or a "ragged" geometry (b).

to finite samples: normalised polarisability, i.e. the total magnetic moment of the sample per unit external magnetic field and per unit volume. For subwavelength objects made of a homogeneous isotropic medium, this quantity is a scalar independent of the size. To find the polarisability of our discrete cubes, we solved a system of circuit equations for coupled resonators [6, 28], assuming a uniform external magnetic field perpendicular to the face of the cube; note that taking all the mutual interactions into account is essential for such analysis. The total magnetic moment is then computed by summing the individual magnetic moments of each ring.

In Fig. 2, we compare the normalised polarisabilities of several metamaterial samples with various number of layers in each direction, calculated for either "flat" or "ragged" boundary. The normalised polarisability of the discrete cubes changes remarkably as the number of elements grows (unlike what we would expect for a homogeneous material), and it does not show a trend towards similarity between "flat" and "ragged" versions. However, the results obtained for the "ragged" geometry show more uniformity than those obtained for "flat" cubes.

Further distinctions are revealed (Fig. 3) by comparing discrete cubes with an equivalent cube made of a homogeneous medium, with the permeability given by Eq. (13) of [8],

$$\mu = 1 + \frac{\gamma}{(k_{\text{res}}a)^2/(k_0a)^2 - 1 - 2\varkappa_{\text{a}} - 4\varkappa_{\text{c}} - \gamma/3},\tag{1}$$

where $\gamma = 0.162$ is a coefficient related to the polarisability of a ring (determined by its geometry), $\varkappa_{\text{a}} = 0.0195$ and $\varkappa_{\text{c}} = -0.0173$ are inductive coupling coefficients to the axial and coplanar nearest neighbours; the numerical values specified here, correspond to the example used in our illustrations. Note that, although it is generally necessary to take more remote neighbours into account as well [4], for an unbounded cubic lattice taking only the nearest neighbours explicitly and then using Lorentz correction for farther neighbours [8] provides a sufficiently good accuracy. The polarisability of the homogeneous cube was found using the CST "Microwave Studio" commercial package. In order to avoid the appearance of multiple non-physical resonances, the edges and corners of the homogeneous cube must be rounded [29]. We have used a rounding radius corresponding to one half of the unit cell size of the discrete cubes. Such rounding leads to a minor difference between the simulation results for cubes of various absolute sizes, but this difference is very small in comparison with discrete cubes, and is not of a qualitative nature. Figure 3 shows that the polarisability of the "ragged" cube is significantly closer to that of the homogeneous cube, than the polarisability of the "flat" cube.

These results can be understood in view of the essential role of surface elements [13, 20], since they do not have the same surroundings as the elements in the bulk and form transition
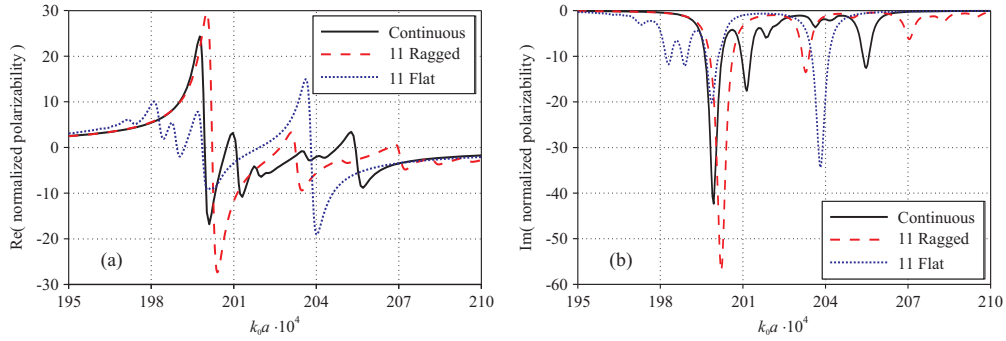
Fig. 3. Real (a) and imaginary (b) parts of the normalised polarisability (arbitrary units) of discrete cubes with 11 layers in each direction, having either a "flat" geometry (dashed lines) or "ragged" geometry (dotted lines), in comparison with the polarizability of a homogeneous cube (solid lines).

layers with different properties. Then the difference between a "flat" structure and a "ragged" structure can be qualitatively assessed by noting that the elements of a "flat" surface do not have 5 out of 14 nearest neighbours, as compared to fully immersed rings, while in "ragged" surfaces, only 3 of the nearest neighbours are absent. This suggests that the behaviour of the "ragged" cube should be closer to the behaviour of an unbounded piece.

Although the considered metamaterial samples are formed by hundreds or even thousands of elements, they still behave like mesoscopic systems. The reason for this is that the number of periods is relatively small, so the surface excitations do not sufficiently dissipate within the sample, making a consistent macroscopic field averaging unreliable. However, we can attempt to extract the effective permeability directly from the polarisability of our cubic samples, as these quantities must be related. For this purpose, we assume that the functional form of the polarisability of a cube is similar to that of a sphere $\alpha_o = 3(\mu - 1)/(\mu + 2)$. So, we formally express the polarisability of a cube as

$$\alpha = A \cdot (\mu - 1)/(\mu + C), \tag{2}$$

where A and C are real frequency-dependent coefficients (see Fig. 4 for an example of their functional form). But for a homogeneous cube we know both the permeability function μ given
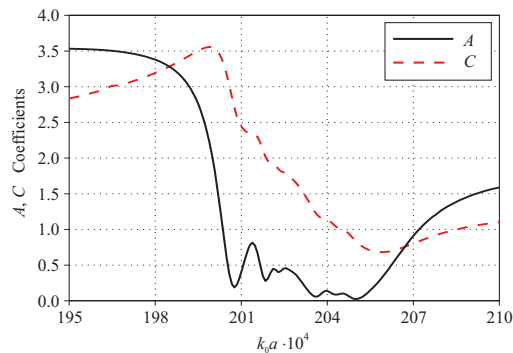

Fig. 4. Frequency dependence of the A and C coefficients calculated with Eq. (3) based on the effective permeability μ of a homogeneous cube Eq. (1) and its polarisability α, obtained from numerical simulations.
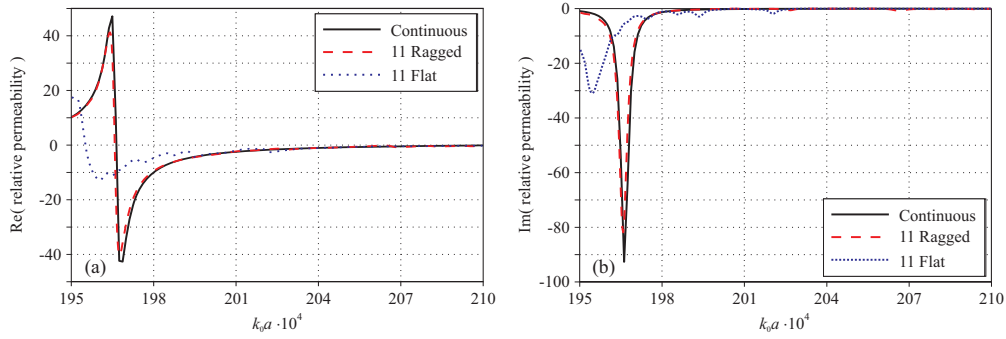
Fig. 5. A comparison between the permeability μ of a homogeneous cube (solid line) and the effective permeability $\mu^{\#}$ obtained for 11-layer discrete cubes with a "flat" geometry (dashed lines) or a "ragged" geometry (dotted lines); real (a) and imaginary (b) parts.

by Eq. (1), and the polarisability α (which was computed numerically and shown with solid lines in Fig. 3). Thus, we can uniquely calculate A and C (shown in Fig. 4) as

$$C = \frac{|\mu|^2 - \mathrm{Re}\,\mu - \dfrac{\mathrm{Re}\,\alpha}{\mathrm{Im}\,\alpha}\,\mathrm{Im}\,\mu}{1 - \mathrm{Re}\,\mu + \dfrac{\mathrm{Re}\,\alpha}{\mathrm{Im}\,\alpha}\,\mathrm{Im}\,\mu}, \qquad A = \frac{(\mathrm{Re}\,\mu + C)^2 + (\mathrm{Im}\,\mu)^2}{\mathrm{Im}\,\mu \cdot (C+1)}\,\mathrm{Im}\,\alpha. \qquad (3)$$

Now, these A and C coefficients can be used to evaluate the effective permeability of discrete cubes from their polarisability $\alpha^{\#}$ which is available from our analysis (shown with the dashed and dotted lines in Fig. 3), using an inverse of equation (2):

$$\mu^{\#} = (A + C\alpha^{\#})/(A - \alpha^{\#}). \qquad (4)$$

The result of this procedure is shown in Fig. 5: the curve corresponding to the "ragged" cube is very similar to the actual permeability of a homogeneous cube, unlike the curve of the "flat" cube. This result can be regarded as a strong argument in favour of the "ragged" configuration, in a sense that its effective permeability retrieved through the above procedure, matches the EMT prediction, whereas for the "flat" configuration such retrieval fails.

3. Conclusions

We have shown that the behaviour of finite metamaterial samples can deviate significantly from continuous medium expectations. We conclude that for isotropic SRR-metamaterials with up to several thousands of elements, the "ragged" boundary structure should be used for practical applications to permit a description in terms of the effective parameters of an unbounded metamaterial. We are confident that, for the size range in which most practical metamaterials fit, our results provide valuable information and design guidelines, allowing for to control the properties of finite metamaterial structures. Our results can be also of interest for the general theory of mesoscopic electromagnetic systems.

Acknowledgment

Appendix 12

This appendix contains a full text of Ref. [45]

Experimental demonstration of a $\mu=-1$ metamaterial lens for magnetic resonance imaging

Manuel J. Freire,[a] Ricardo Marques, and Lukas Jelinek
Departamento de Electronica y Electromagnetismo, Facultad de Fisica, Universidad de Sevilla,
Avda. Reina Mercedes s/n, E 41012 Sevilla, Spain

In this work a $\mu=-1$ metamaterial (MM) lens for magnetic resonance imaging (MRI) is demonstrated. MRI uses surface coils to detect the radio frequency (rf) energy absorbed and emitted by the nuclear spins in the imaged object. The proposed MM lens manipulates the rf field detected by these surface coils so that the coil sensitivity and spatial localization are substantially improved. Beyond this specific application, we feel that the reported results are the experimental confirmation of a new concept for the manipulation of rf field in MRI, which paves the way to many other interesting applications. © 2008 American Institute of Physics. [DOI: 10.1063/1.3043725]

After the demonstration of the ability of a slab of an ideal negative refractive index metamaterial (MM) with $\varepsilon=-1$ and $\mu=-1$ to obtain subdiffraction images,[1] the issue of optical subwavelength imaging through the direct manipulation of the electromagnetic field has attracted a lot of attention. This effect has been shown in the optical frequency range,[2] in the microwave range,[3,4] and in the radio frequency (rf) range[5,6] by using different devices. However, the ability to image objects smaller than the wavelength is not a recent concept. It is something well known since long in magnetic resonance imaging (MRI), where imaged objects are very small as compared to the wavelength of the rf fields used to obtain the image. As it is well known, the generation of images in MRI is based on the detection of spatial variations in the phase and frequency of the rf energy absorbed and emitted by the nuclear spins of the imaged object.[7] These spatial variations are induced by some static magnetic field gradients, and the image is built from signals measured by a receiving coil that has no information about the relative location of the emitting magnetic dipoles. Conventional MRI involves many repeated measurements and then signal processing (inverse Fourier transforming) before obtaining an image of a single slice of tissue. Therefore, conventional subwavelength MRI is based on signal processing and does not involve any optical means such as focusing or collimation. At this point a question arises in a natural way: would it be possible to combine both signal processing and optical means so that the ability of MM devices to directly obtain subwavelength images could be used to improve conventional MRI? The application of microstructured MM in MRI was already explored to some extension by Wiltshire *et al.*[8] In Ref. 8 a magnetic flux guide with high permeability was used to guide the rf flux to a remote coil. This work clearly showed the compatibility of microstructured MMs with conventional MRI machines, as well as their potential usefulness in the frame of this technology, thus encouraging our search for a rf lens with application in MRI.

In a recent work[9] some of the authors proposed to use a subdiffraction MM lens to improve the images obtained by surface coils in MRI. Surface MRI coils are usually placed just on the skin of the patient and are used to obtain images of tissues in the proximity of the coil. Due to its higher sensitivity, surface coils provide a signal-to-noise ratio (SNR) much larger than that obtained with whole-volume coils or body coils. However, whereas the sensitivity of body coils is uniform, the sensitivity of surface coils, as well as the SNR, decreases rapidly with the distance from the coil. Due to Lorentz reciprocity, the sensitivity of a coil is directly proportional to the intensity of the magnetic field created by the coil inside the body of the patient for a standard value of the current on the coil.[10] Figure 1(a) shows a typical plot of the sensitivity (i.e., the normalized magnetic field intensity)
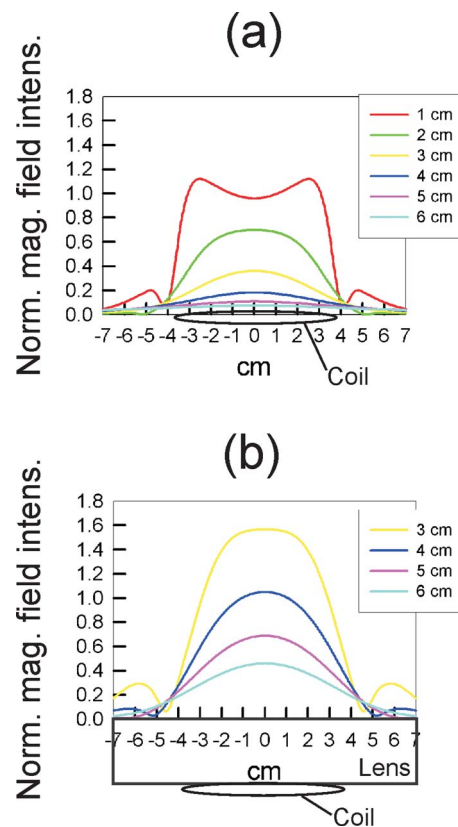

FIG. 1. (Color online) Calculation of the normalized magnetic field intensity (sensitivity) for different distances in centimeter of (a) a standard surface coil of 3 in. in diameter and (b) of the same coil placed on the lens. Units are arbitrary.

[a]Electronic mail: freire@us.es.

93, 231108-1

of a circular coil placed on the skin of the patient. As can be seen, this sensitivity decays with the distance from the coil, making the coil useless for obtaining images of tissues located at distances into the body deeper than the coil dimensions, typically. Let us now imagine that an ideal MM lens of thickness d is placed between the coil and the skin of the patient. An ideal MM lens of thickness d has the ability of focusing the electromagnetic field, translating the field distribution on the plane of the coil to another plane at a distance $2d$ from the coil, and vice versa.[1] Therefore, this configuration would increase the coil sensitivity, making it possible to obtain images of deeper tissues. Before going further with the design, we must consider that rf fields used for MRI have an associated wavelength much higher than the dimensions of any practical coil. Therefore, we are in the realm of the quasimagnetostatics, and a slab of a microstructured MM with $\mu = -1$ should be enough for manufacturing the lens. Figure 1(b) shows the sensitivity of a coil in the presence of such a lens with $\mu \approx -1$ [actually, the permeability of this MM lens corresponds to that computed according to Eq. (13) of Ref. 11 for the lens manufactured for this work]. As it can be seen, the theory predicts a substantial increase in the coil sensitivity and SNR inside the body of the patient. It is worth mentioning here that the same effect would appear if the lens is placed not directly on the coil but at some distance from it. In this case the only difference will be that the coil sensitivity in the space between the coil and the lens will not be affected by the presence of the lens.

For the practical implementation of the aforementioned ideas, the ideal $\mu = -1$ lens was mimicked by a slab consisting of a three-dimensional (3D) array of copper metallic rings loaded with nonmagnetic capacitors. Capacitively loaded rings (CLRs) were previously proposed by Schelkunoff and Friis[12] in order to design artificial media with strong magnetic response. In our case they were placed in a simple cubic lattice in order to obtain an isotropic artificial medium with $\mu = -1$. The magnetic permeability of this medium was computed from Eq. (13) of Ref. 11 as a function of the periodicity, the ring resistance, the ring self-inductance, and the frequency of resonance. The fabricated MM lens was a two unit cell thick slab of this artificial medium. A sketch of the proposed lens is shown in Fig. 2(a). Before proceeding with the description of the experiments, some additional words will be devoted to the modeling of the lens. It is apparent that a slab made of only two layers of unit cells can hardly be considered as a continuous medium. Therefore, the detailed description of this structure deserves a deeper discussion. Actually, the authors have recently developed a homogenization procedure for thin slabs made of resonant metallic rings.[13,14] A conclusion of this analysis was that for the specific configuration proposed in this report, the continuous medium approach gives a good description of the behavior of the lens. Only a small shift in the frequency of operation of the lens with regard to the continuous medium model was detected. This conclusion was confirmed by additional electromagnetic simulations made by using the commercial software package CST MICROWAVE STUDIO. Additional design corrections were necessary as a consequence of the finite size of the capacitors, which was not taken into account by the models. Finally, the lens was manufactured for operation in a MRI system of 1.5 T (i.e., for a frequency of operation of 63.85 MHz). Figure 2(b) shows a sketch of a CLR of the lens whose dimensions and design parameters are external radius
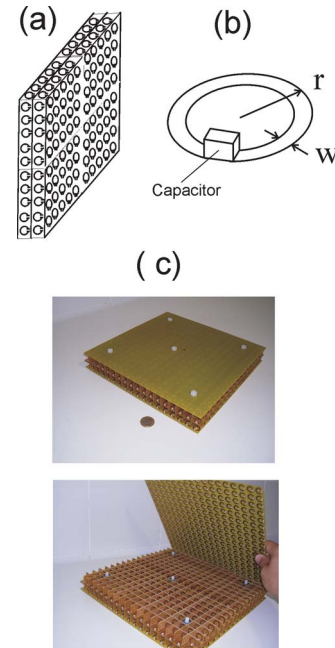

FIG. 2. (Color online) (a) Sketch of the lens: a 3D array of CLRs. (b) Sketch of a CLR with dimensions. Parameters of the fabricated CLRs: $w = 2.17$ mm, $r = 6.02$ mm, self-inductance of 13.45 nH, capacitance of $470 \pm 1\%$ pF, resonance frequency of 63.28 MHz, and quality factor of $Q = 115$. (c) Photographs of the fabricated lens consisting of a 3D array of $18 \times 18 \times 2$ cubic cells with a periodicity of 15 mm. The total number of CLRs is 2196. The height and width of the lens are both 27 cm and the thickness is 3 cm.

of the rings $r = 6.02$ mm, ring width $w = 2.17$ mm, ring self-inductance of 13.45 nH, and ring capacitance of $470 \pm 1\%$ pF, which gives a resonance frequency of 63.28 MHz and a quality factor of 115. Finally, Fig. 2(c) shows two photographs of the final device consisting of a 3D array of $18 \times 18 \times 2$ cubic cells with a periodicity of 15 mm and a total number of CLRs of 2196. The dimensions of the lens are $27 \times 27 \times 3$ cm^3. The capacitors were low-loss nonmagnetic capacitors of the series ATC100B specially designed by the company American Technical Ceramics Corp. (NY, USA) for MRI applications and manufactured with low tolerance for our application. The rings were photoetched on a FR4 substrate by the company Circuitronica S. L. (Seville, Spain) and the capacitors were inserted by the company Silicium S. L. (Seville, Spain).

The fabricated lens was tested in a General Electric Signa 1.5T MRI machine using a standard 3 in. circular surface coil 1.5T model M1085GA manufactured by ETL for General Electric. In the experiment, one of the authors was lying on the MRI machine and the coil was placed beside one of his knees. In our study, axial images (i.e., images of a plane normal to the bore of the magnet) of type T1 were acquired using a standard spin-echo sequence typical of T1 acquisitions. The repetition time between signals was 220 ms and the echo time was 10 ms. The field of view was 34×34 cm^2 with a 256×192 data matrix. Two acquisitions with averaging were used in all cases. Figure 3(a) shows an axial image of the knees without the lens so that both knees are touching. In this figure, the knee on the right of the image is closer to the coil and is clearly visible, whereas the knee on the left is hardly visible, as it is expected from the fact that the sensitivity of the coil drops off rapidly with distance. Figure 3(b) shows also an axial image of both knees with the
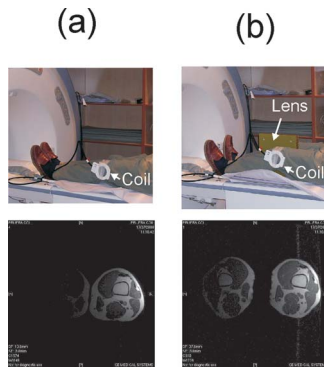
FIG. 3. (Color online) Axial T1 image of the knees of one of the authors (a) without the lens and (b) with the lens between the knees. It must be noted that the magnetic resonance images are inverted with respect to the photographs, and that this is inherent to the MRI acquisition process.

lens being placed between them (with this configuration it is not necessary to retune the coil, and a direct comparison with the previous image is possible using the same coil). In spite of the fact that the distance between the coil and the knee on the left of the image is larger than in the absence of the lens, this knee is now more visible due to the presence of the lens. This makes apparent that the lens increases the sensitivity of the coil. We feel that this is a completely new result that relies on the specific design of the lens, which mimics a $\mu=-1$ medium. We also feel that this result introduces a new concept in MRI, showing that a $\mu=-1$ MM lens can be applied in the frame of conventional MRI technology in order to improve the sensitivity of surface coils.

Up to now we have shown that MM lenses can be useful in MRI technology due to their ability of focusing the rf magnetic field lines of force. Specifically, we have shown that MM lenses can be applied to improve the sensitivity of surface coils, thus resulting in an improvement in image quality, reduction in acquisition time, and/or increase in spatial localization. Since MM lenses can translate the field distribution in a plane behind the lens to another "equivalent" plane in front of the lens, they can be also useful for obtaining images of deeper tissues. We feel that the reported results provide a sufficient "proof of concept" for the reported effect. Other MM lens configurations different from the manufactured CLR lens, as that proposed in Ref. 15, could be also useful for this application. Regarding further applications of this new concept, we feel that it may also find application in *parallel imaging* MRI technology,[16] as suggested in Ref. 15.

MRI parallel imaging techniques use several surface coils and take advantage of the spatial localization of the images detected by each coil[17] to reduce acquisition time. The spatial localization of the images detected by the different coils would be substantially increased if the coils were placed on the equivalent plane of the imaged slice of tissue. In the limit, this technique could make possible to avoid the phase encoding process following the technique reported in Ref. 18, thus opening the way to real time image acquisition of deep tissues.

[1] J. B. Pendry, Phys. Rev. Lett. **85**, 3966 (2000).
[2] N. Fang, H. Lee, C. Sun, and X. Zhang, Science **308**, 534 (2005).
[3] A. Grbic and G. Eleftheriades, Phys. Rev. Lett. **92**, 117403 (2004).
[4] M. J. Freire and R. Marques, Appl. Phys. Lett. **86**, 182505 (2005).
[5] M. C. K. Wiltshire, J. B. Pendry, and J. V. Hajnal, J. Phys.: Condens. Matter **18**, L315 (2006).
[6] M. J. Freire and R. Marques, J. Appl. Phys. **100**, 063105 (2006).
[7] P. C. Lauterbur, Nature (London) **242**, 190 (1973).
[8] M. C. K. Wiltshire, J. B. Pendry, I. R. Young, D. J. Larkman, D. J. Gilderdale, and J. V. Hajnal, Science **291**, 849 (2001).
[9] M. J. Freire and R. Marques, Proceedings of the Second International Congress on Advanced Electromagnetic Materials in Microwaves and Optics, Pamplona, Spain, 21–26 September 2008 (unpublished), pp. 639–640.
[10] E. K. Insko, M. A. Elliott, J. C. Schotland, and J. S. Leigh, J. Magn. Reson. **131**, 111 (1998).
[11] J. D. Baena, L. Jelinek, R. Marques, and M. G. Silveirinha, Phys. Rev. A **78**, 013842 (2008).
[12] S. A. Schelkunoff and H. T. Friis, *Antennas Theory and Practice* (Wiley, New York, 1952).
[13] L. Jelinek and R. Marques, Proceedings of the Second International Congress on Advanced Electromagnetic Materials in Microwaves and Optics, Pamplona, Spain, 21–26 September 2008 (unpublished), pp. 629–631.
[14] L. Jelinek, R. Marques, and M. J. Freire, "Accurate modeling of split ring metamaterial lenses for magnetic resonance imaging applications," J. Appl. Phys. (submitted).
[15] M. J. Freire and R. Marques, J. Appl. Phys. **103**, 013115 (2008).
[16] K. P. Pruessmann, M. Weiger, M. B. Scheidegger, and P. Boesiger, Magn. Reson. Med. **42**, 952 (1999).
[17] M. A. Griswold, P. M. Jakob, M. Nittka, J. W. Goldfarb, and A. Haase, Magn. Reson. Med. **44**, 602 (2000).
[18] M. P. McDougall and S. M. Wright, Magn. Reson. Med. **54**, 386 (2005).

Appendix 13

This appendix contains a full text of Ref. [46]

Accurate modeling of split ring metamaterial lenses for magnetic resonance imaging applications

L. Jelinek,[a)] R. Marqués,[b)] and M. J. Freire[c)]
Departamento de Electrónica y Electromagnetismo, Universidad de Sevilla, Sevilla 41012, Spain

The usefulness of thin split ring metamaterial slabs for imaging applications, including magnetic resonance imaging applications, has attracted some attention in the past years. However, the small number of unit cells across these thin slabs prevents the direct application of continuous medium models for its characterization. The main aim of this contribution is to provide a rigorous model for these structures, also clarifying the usefulness of continuous medium approach for their characterization. The proposed model is a generalization of the classical Lorentz procedure to two dimensions and is able to deal with electrically thin slabs made of small resonant closed current loops. The obtained results are validated by full-wave electromagnetic simulations and compared with the continuous model approximation of the slab. © *2009 American Institute of Physics.* [DOI: 10.1063/1.3067788]

I. INTRODUCTION

One of the most promising applications of left-handed metamaterials is the Veselago–Pendry lens[1,2] made of a single slab of thickness d showing relative electric permittivity and magnetic permeability both equal to minus unity. In principle, this device will be able to reproduce, with any desired resolution, including subdiffraction resolution, the electromagnetic field on a given plane (source plane) located in front of the lens onto another plane (image plane) located behind the lens at a distance $2d$ from the source plane.[2] However, this effect is strongly limited by losses, which in practice reduces it to a near field effect. In fact, it can be shown (see Ref. 3 and references therein) that the minimum resolution attainable from a lossy slab, having the real parts of μ_r and ϵ_r both equal to minus unity, is given by

$$\Delta \geq \frac{2\pi d}{\ln(2/\delta)}, \tag{1}$$

where δ is the loss tangent of the slab. It is clear from Eq. (1) that $\Delta > d$ for any realistic metamaterial. This means that in order to obtain subdiffraction resolution ($\Delta < \lambda$) the slab thickness must be substantially smaller than the wavelength. In such case, electric and magnetic effects are decoupled and we are in the realm of the quasielectrostatics or the quasimagnetostatics. Therefore, only slabs with $\mu_r = -1$ or $\epsilon_r = -1$ are necessary in order to obtain subdiffraction resolution in the near field. The first possibility was actually analyzed in Ref. 2 and then experimentally demonstrated using a thin silver slab in Ref. 4. The second one was demonstrated in Ref. 5 using a ferrite slab.

Regarding imaging in the quasimagnetostatic limit, a promising application of metamaterial structures can be found in magnetic resonance imaging (MRI) for medical applications.[6–10] In Ref. 6 a hexagonal array of metallic Swiss rolls was used as a "magnetic flux guide" in order to translate MRI images from a source to a distant receiving coil. In Ref. 7 a Swiss roll $\mu_r = -1$ lens was proposed for MRI applications. In Refs. 8 and 9 the applications of split ring magnetoinductive lenses[8] for medical MRI were discussed. Later, a $\mu_r = -1$ lens made of split rings was proposed for the same application.[10] These applications include improvement of surface coil sensitivity and acceleration of measurement time in the frame of a parallel imaging process. Split ring lenses with $\mu_r = -1$ (Ref. 10) have the key advantages over Swiss-roll lenses[7] of three-dimensional (3D) isotropy and sensitivity to axial magnetic fields. With regard to magnetoinductive lenses,[8,9] split ring $\mu_r = -1$ lenses[10] have more complicated design, but this may be compensated by smaller losses and improved sensitivity coming from the fact that they do not operate at the split ring resonance, but well above it, in the negative permeability frequency range.

Since nuclear MRI takes place in the megahertz frequency range, a cubic array of capacitively loaded rings (CLRs) (Ref. 11) is a suitable design in order to approach ideal $\mu_r = -1$ lenses in practice (CLRs were already used for magnetoinductive lenses[8] operating in the same frequency range). Since losses in the metamaterial are essentially given by losses in its constitutive elements and vary inversely with the electrical size of these elements,[12] it is desirable from this point of view to use electrically big CLRs for the design. On the other hand, since according to Eq. (1) the minimum resolution cannot be made smaller than the slab thickness, there is no reason to use more than two or three periods along the slab width. From these considerations it comes out that the better design for the implementation of an artificial $\mu_r = -1$ lens for MRI applications contains only a few periods along the slab thickness. Such system, however, can hardly be considered as a continuous medium and a specific description must be developed in order to rigorously model its behavior.

According to the previous discussion, the main aim of this work will be to develop a specific model for the analysis of electrically thin periodic slabs of resonant split rings

---
[a)]Electronic mail: l_jelinek@us.es.
[b)]Electronic mail: marques@us.es.
[c)]Electronic mail: freire@us.es.
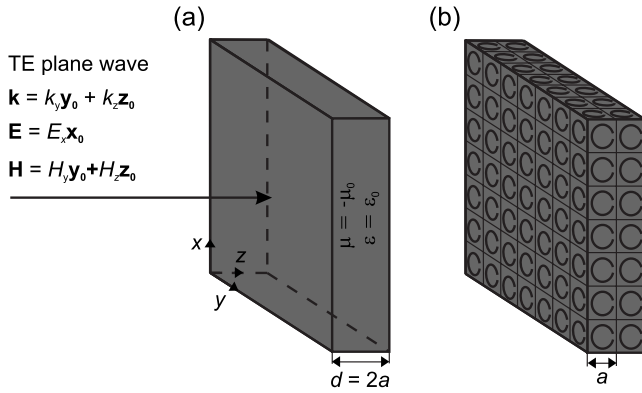
105, 024907-1

FIG. 1. (a) Ideal slab of an effective magnetic medium with $\mu = -\mu_0$. (b) A sketch of the proposed CLR implementation.

[which may include the aforementioned CLRs, as well as split ring resonators (SRRs) (Ref. 13) or other similar elements] with the sight on imaging applications. At the present state of the art it is possible to find, apart from the specific models developed for the analysis of magnetoinductive lenses,[8,9] some attempts of homogenization of thin metamaterial slabs or layers. One of the directions is the analytical calculation of the interaction constant inside double dipole arrays,[14,15] which finally leads to the definition of the effective material parameters for thin metamaterial slabs.[16] This method is not appropriate for the proposed application because it only takes into account normal incidence. Furthermore, it was developed for point dipole scatterers, which is not appropriate for the analysis of practical lenses with strongly coupled elements. Other possibility of homogenization of thin slabs was proposed in Ref. 17. This method derives the effective material parameters of a slab from the effective material parameters of a 3D infinite lattice. Also this method has two drawbacks for our purpose. First, the homogenization of a 3D lattice is in many cases of the same difficulty as the homogenization of a slab. Second, in order to calculate the transmission and reflection by a slab, spatial dispersion has to be taken into account.

To overcome the difficulties of the aforementioned approaches we will develop a model, which essentially is a kind of two-dimensional (2D) generalized Lorentz procedure including a detailed analysis of the magnetoinductive couplings between nearest neighbors. The results obtained from this model will be compared with those obtained from full-wave electromagnetic simulations in order to validate the analysis. They will also be compared with the results obtained from the continuous medium approach in order to find the limits of such approximation.

II. THE CONTINUOUS MEDIUM APPROACH

Figure 1(a) shows an ideal $\mu_r = -1$ lens for MRI applications. A practical implementation of this lens using CLRs, which, according to our previous discussion, has only two periods along the slab thickness, is sketched in Fig. 1(b). In order to find the effective parameters of the ideal lens in Fig. 1(a) we can follow the homogenization procedure developed in Ref. 18 [Eq. (13)], which takes into account magnetoinductive couplings between rings. Let us then suppose that

this homogenization procedure applies and let us compute the transfer function of the lens, that is, the transmission coefficient between two planes at opposite sides of the lens, separated by a distance $2d$, where d is the lens width. Clearly, in the ideal case of $\mu_r = -1$, this transfer function must be equal to unity for any value of the transverse wave number k_y of the incident wave.

As mentioned above, the lens is supposed to operate in the quasimagnetostatic limit, where all fields are almost purely composed of evanescent TE modes. Let us then analyze the incidence of a TE plane wave, evanescent in the z-direction, on the slab in Fig. 1(a). Fields of such wave are

$$\mathbf{E}_0^{\text{inc}} = E_0^{\text{inc}} e^{j(k_y y + k_z z)} \mathbf{x}_0,$$

$$\mathbf{H}_0^{\text{inc}} = \frac{E_0^{\text{inc}}}{\omega \mu_0} (-k_z \mathbf{y}_0 + k_y \mathbf{z}_0) e^{j(k_y y + k_z z)}, \quad (2)$$

where $k_z = \sqrt{k_0^2 - k_y^2}$, with $\text{Re}(k_z) < 0$ and $\text{Im}(k_z) > 0$. Taking the reference planes on the source and image planes (i.e., at two parallel planes located at both sides of the lens and separated by a distance $2d = 4a$) the transmission coefficient of the lens can be written as

$$T = \frac{4\mu_r \dfrac{k_{zs}}{k_z} e^{jk_z d}}{\left(\dfrac{k_{zs}}{k_z} + \mu_r\right)^2 e^{-jk_{zs}d} - \left(\dfrac{k_{zs}}{k_z} - \mu_r\right)^2 e^{jk_{zs}d}}, \quad (3)$$

where $k_{zs} = \sqrt{\mu_r k_0^2 - k_y^2}$ is the longitudinal wave number inside the slab with $\text{Re}(k_{zs}) < 0$ and $\text{Im}(k_{zs}) > 0$. Making use of this approach, we have designed a $\mu_r = -1$ split ring lens for operation in a MRI 1.5 T machine ($f \approx 63.85$ MHz) according to the design sketched in Fig. 1(b) with the lattice constant $a = 15$ mm. The CLRs were made of copper with metallic strips etched on a nonmagnetic dielectric board. The CLRs were loaded with lumped capacitors with normalized capacitance $C/(a\epsilon_0) = 354$ (470 pF). The normalized mean radius of the CLRs was $r_0/a = 0.329$ (4.935 mm) and the normalized width of the strips was $w/a = 0.145$ (2.17 mm). The self-inductance of the CLRs was obtained from the measured value of the frequency of resonance in free space, whose normalized value was $k_0 a = 0.0199$ (63.28 MHz). From this value, the CLR self-inductance $L = \omega_0^2/C$ was computed, having the normalized value $L/(a\mu_0) = 0.714$ (13.5 nH). By measurement of the quality factor of the resonator, the normalized resistance $R/(\omega_0 L) = 0.008\,69$ (0.0465 Ω), which includes the effects of the ring and the capacitor, was obtained. The permeability of a simple cubic lattice of such SRRs was then calculated using the homogenization procedure developed in Ref. 18 [Eq. (13)], and introduced in Eq. (3) in order to compute the transfer function of the lens. It is worth to note that strictly speaking, the analyzed CLR arrangement is not isotropic as it does not follow the necessary symmetries[19] due to the asymmetric location of the capacitors on the rings. However, the electrical size of the CLRs is so small (diameter/$\lambda = 1/394$) that they can be practically seen as resonant closed current loops, supporting a uniform current distribution. Therefore, the analysis reported in Ref. 18 can be applied to the proposed structure.
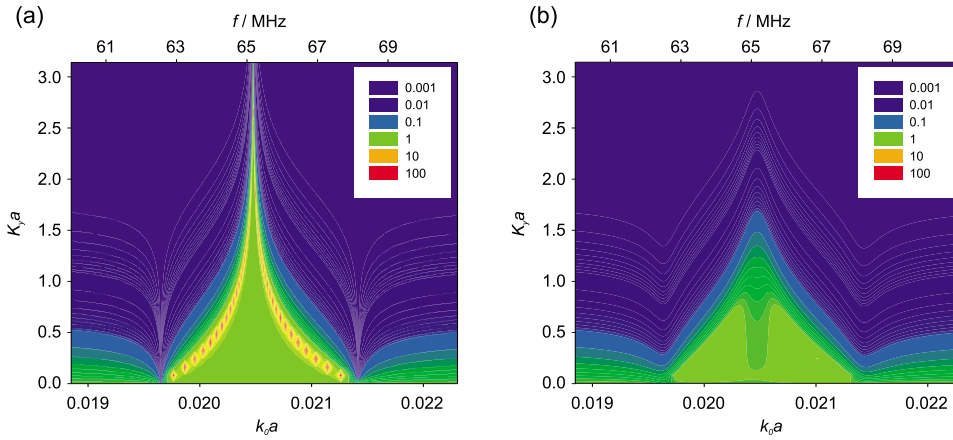
FIG. 2. (Color online) Transfer function through the $\mu_r=-1$ lens of Fig. 1 calculated using the continuous medium model in Ref. 18. (a) Losses are ignored ($R=0\ \Omega$). (b) Realistic losses ($R=0.0465\ \Omega$) are included in the model.

The computed amplitude of the transmission coefficient (3) is plotted in Fig. 2, as a function of the normalized frequency k_0a and the normalized transverse wave number k_ya. In the lossless case it can be seen that the transmission coefficient forms a flat valley between two steep cliffs, which corresponds to the surface waves that can be excited at both interfaces of the lens.[8] The frequency bandwidth of the valley increases from zero width at $k_ya=\pi$ to some finite width when the incident wave exhibits normal incidence. The transmission coefficient inside the entire valley has a value very close to unity, which reflects the imaging properties of the slab. The middle frequency of the valley corresponds to permeability $\mu_r=-1$. When realistic losses are included, the transfer function is strongly affected: both cliffs disappear (for smaller losses, for instance, $R=0.01\ \Omega$, we can still find some trace of them) and the spatial bandwidth (the allowed values of k_ya) becomes smaller. Since the resolution of the lens is limited by the minimum value of the allowed transverse wavelength $\lambda_y=2\pi/k_y$, the presence of losses reduces the resolution of the lens in agreement with our previous discussion. Nevertheless, the results shown in Fig. 2 are still very promising for MRI applications, as it will be shown in Sec. IV. However, as it was mentioned above, this conclusion is conditioned by the validity of the continuous medium model, which is not clear for the analyzed structure. In Sec. III we will develop a more accurate model and compare the results with those obtained in this section.

III. THE THIN SLAB MODEL

In this section a theoretical model of electrically thin slabs made of 2D periodic arrays of SRRs will be developed. The model will be particularized for the specific geometry discussed in Sec. II. However, it will become apparent that the analysis can be easily generalized to other similar configurations, including one or more layers of resonant current loops. The only limitations are a small electrical size of the loops and slab thickness. In our particular example, the slab is composed of a regular array of the unit cells shown in Fig. 3, which are periodically arranged in a square lattice of periodicity a over the x-y plane. It can be seen that each unit cell contains seven resonators (in our specific example they are CLRs, but other configurations, such as small SRRs, can also be considered). Figure 3(b) shows the current loop

model of the real structure in Fig. 3(a), where it is assumed that each loop forms an RLC circuit[20] having self-impedance $Z_0=1/(j\omega C)+j\omega L+R$.

A. Circuit model of the slab

Let us assume now the incident wave (2) impinging on the slab. This polarization was selected due to the particular purpose of the example; however the analysis can be easily modified for incident plane waves of any polarization and phase shift in any direction. According to the model, each unit cell of the slab is described by a current vector $\mathbf{I}^{mn}$, where superindices m and n indicate the location of the unit cell in the x-y plane. Due to the assumed form of the incident field it is $\mathbf{I}^{mn}=\mathbf{I}^{00}e^{jk_yna}$. The currents in the unit cell at origin are driven by the magnetic flux across the different loops according to

$$Z_0I_i^{00}=-j\omega\Phi_i^{00}, \quad i=1,\dots,7, \tag{4}$$

where the magnetic flux Φ_i^{00} through the loops includes the flux of the external magnetic field as well as the magnetic flux created by all other loops in the lattice. Therefore, it can be then written that

$$\Phi_i^{00}=\Phi_i^{\text{ext}}+\sum_{j\neq i}M_{ij}^{00}I_j^{00}+\sum_{mn\neq00}\sum_j M_{ij}^{mn}I_j^{mn}, \tag{5}$$

where M_{ij}^{mn} is the mutual inductance between ith loop in 00th cell and jth loop in mnth cell, and the summations extend over all the unit cells. Although Eq. (5) is formally correct, the last series are only conditionally convergent and cannot be used in practice. To overcome this difficulty, the well known Lorentz local field procedure[21] will be applied. This procedure, which for 3D structures leads to the well known
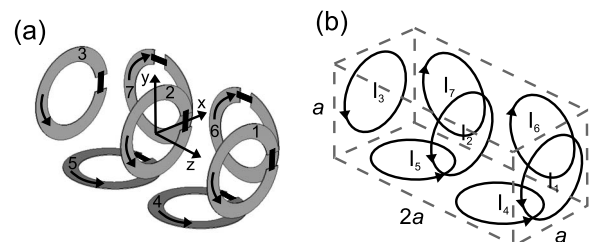

FIG. 3. (a) Considered unit cell made of CLRs. (b) Current loop model of the unit cell.

Clausius–Mossotti formula, has been successfully applied in the past to the analysis of 3D metamaterial structures (see, for instance, Ref. 3 and references therein) and, more recently, it has been applied to the analysis of 3D metamaterials made of resonant current loops.[18] In this paper, a straightforward generalization of this procedure to the analyzed 2D structure will be applied to compute the last summation in Eq. (5).

Following the aforementioned Lorentz approach, the whole metamaterial is divided in two regions: inside and outside a circle (actually a flat cylinder) of radius R around the 00th unit cell, i.e.,

$$\Phi_i^{00} = \Phi_i^{\text{ext}} + \sum_{j \neq i} M_{ij}^{00} I_j^{00} + \sum_j I_j^{00} \sum_{\substack{mn \neq 00 \\ m^2+n^2 < R^2/a^2}} M_{ij}^{mn} e^{jk_y na}$$
$$+ \sum_j M_{ij}^{\infty} I_j^{00}, \tag{6}$$

where the term $\sum_j \sqrt{M_{ij}^{\infty} I^{00}}$ represents the magnetic flux coming from all the loops outside the circle.

Substitution of Eq. (6) into Eq. (4) then gives

$$(Z_0 \overline{\mathbf{1}} + j\omega \overline{\mathbf{M}} + j\omega \overline{\mathbf{M}}^{\infty}) \mathbf{I}^{00} = -j\omega \Phi^{\text{ext}},$$

$$M_{ii} = \sum_{\substack{mn \neq 00 \\ m^2+n^2 < R^2/a^2}} M_{ii}^{mn} e^{jk_y na},$$

$$M_{i \neq j}^{ij} = M_{ij}^{00} + \sum_{\substack{mn \neq 00 \\ m^2+n^2 < R^2/a^2}} M_{ij}^{mn} e^{jk_y na}. \tag{7}$$

This equation can be solved provided $\overline{\mathbf{M}}$, $\overline{\mathbf{M}}^{\infty}$, and the external magnetic flux Φ^{ext} are known. Calculation of matrix $\overline{\mathbf{M}}$ is straightforward as its terms are given by summations of mutual inductances between two current loops, which are explicitly calculated in Appendix A. The expression for $\overline{\mathbf{M}}^{\infty}$ will be given in Sec. III C, assuming that the radius R is big enough so that the contribution coming from all the unit cells outside the circle can be seen as a continuous distribution of magnetization. The details of these computations are left to Sec. III C and to Appendix B; however, it is worth to mention that the proposed procedure avoids all the problems related to the slow convergence of the last summation in Eq. (5) because all series and integrals involved in the final expressions will be finite.

B. Transmission and reflection coefficient of the slab

The scattering of a plane wave by the considered slab is characterized by the transmission T and reflection R coefficients. At the present stage of the analysis, Eq. (7) only gives the currents on the loops along the periodic array. In order to calculate T and R, the far field radiated by the loops has to be calculated. In the far field region, the lens can be seen as seven parallel magnetized surfaces, each of them carrying the magnetization connected to each one of the seven loops in the unit cell, altogether with its periodic repetitions along the slab. Magnetization of each surface has the form

$$\mathbf{M} = \mathbf{M}_0 e^{jk_y y} \delta(z - z_i), \tag{8}$$

where z_i stands for the location of the layer along the z axis, that is, $z_1 = a$, $z_2 = 0$, $z_3 = -a$, $z_4 = z_6 = a/2$, and $z_5 = z_7 = -a/2$.

Radiation of these sources can be easily obtained by direct inversion of Maxwell equations. Assuming a magnetization layer at $z = z_i$ and $\mathbf{B} = \mu_0(\mathbf{H} + \mathbf{M})$, this results in

$$E_x = \frac{j\omega\mu_0}{2}\left(\frac{k_y M_{0z}}{k_z} - M_{0y}\, \text{sgn}(z - z_i)\right)e^{jk_y y}e^{jk_z|z-z_i|},$$

$$E_y = \frac{jk_0^2 M_{0x}}{2\omega\varepsilon_0}\text{sgn}(z - z_i)e^{jk_y y}e^{jk_z|z-z_i|},$$

$$E_z = -\frac{jk_y k_0^2 M_{0x}}{2\omega\varepsilon_0 k_z}e^{jk_y y}e^{jk_z|z-z_i|},$$

$$H_x = \frac{-k_0^2 M_{0x}}{2jk_z}e^{jk_y y}e^{jk_z|z-z_i|},$$

$$H_y = \frac{j}{2}[-k_y M_{0z}\, \text{sgn}(z - z_i) + k_z M_{0y}]e^{jk_y y}e^{jk_z|z-z_i|},$$

$$H_z = \frac{jk_y}{2}\left(\frac{k_y M_{0z}}{k_z} - M_{0y}\, \text{sgn}(z - z_i)\right)e^{jk_y y}e^{jk_z|z-z_i|}$$
$$- M_{0z}e^{jk_y y}\delta(z - z_i). \tag{9}$$

Now, according to the indices in Fig. 3(b), it can be easily realized that only surfaces corresponding to loops 1, 2, 3, 4, and 5 contribute to the radiated E_x field component through

$$E_x^{1,2,3,4,5} = \frac{j\omega\mu_0 A}{2a^2}\left[\frac{k_y}{k_z}I_1 e^{jk_z|z-a|} + \frac{k_y}{k_z}I_2 e^{jk_z|z|} + \frac{k_y}{k_z}I_3 e^{jk_z|z+a|}\right.$$
$$- \text{sgn}\left(z - \frac{a}{2}\right)I_4 e^{jk_z|z-a/2|}$$
$$\left. - \text{sgn}\left(z + \frac{a}{2}\right)I_5 e^{jk_z|z+a/2|}\right]e^{jk_y y}, \tag{10}$$

and only surfaces corresponding to loops 6 and 7 contribute to the radiated E_y and E_z field components through

$$E_y^{6,7} = \frac{jk_0^2 A}{2\omega\varepsilon_0 a^2}e^{jk_y y}\left[\text{sgn}\left(z - \frac{a}{2}\right)I_6 e^{jk_z|z-a/2|}\right.$$
$$\left. + \text{sgn}\left(z + \frac{a}{2}\right)I_7 e^{jk_z|z+a/2|}\right],$$

$$E_z^{6,7} = -\frac{jk_y k_0^2 A}{2\omega\varepsilon_0 k_z a^2}e^{jk_y y}(I_6 e^{jk_z|z-a/2|} + I_7 e^{jk_z|z+a/2|}), \tag{11}$$

where A states for the surface of the current loop.

Now, taking into account the presence of the incident wave, the reflection and transmission coefficients for the reference planes $z = -2a$ and $z = 2a$ are given by

$$R^{xx} = \frac{E_x^{1,2,3,4,5}(z=-2a)}{E_0^{\text{inc}}e^{j(k_y y - 2k_z a)}} = \frac{j\omega\mu_0 A}{2a^2 E_0^{\text{inc}}}\left(\frac{k_y}{k_z}I_1 e^{2jk_z a} + \frac{k_y}{k_z}I_2 e^{jk_z a}\right.$$

$$\left. + \frac{k_y}{k_z}I_3 + I_4 e^{3jk_z a/2} + I_5 e^{jk_z a/2}\right)e^{3jk_z a},$$

$$R^{yx} = \frac{E_y^{6,7}(z=-2a)}{E_0^{\text{inc}}e^{j(k_y y - 2k_z a)}} = \frac{-jk_0^2 A}{2\omega\varepsilon_0 a^2 E_0^{\text{inc}}}(I_6 e^{-jk_z a/2} + I_7 e^{jk_z a/2}),$$

$$R^{zx} = \frac{E_z^{6,7}(z=-2a)}{E_0^{\text{inc}}e^{j(k_y y - 2k_z a)}} = \frac{jk_y k_0^2 A}{2\omega\varepsilon_0 k_z a^2 E_0^{\text{inc}}}(I_6 e^{-jk_z a/2} + I_7 e^{jk_z a/2}),$$

$$T^{xx} = \frac{E_x^{1,2,3,4,5}(z=2a) + E_0^{\text{inc}}e^{j(k_y y + 2k_z a)}}{E_0^{\text{inc}}e^{j(k_y y - 2k_z a)}}$$

$$= \frac{j\omega\mu_0 A}{2a^2 E_0^{\text{inc}}}\left(\frac{k_y}{k_z}I_1 + \frac{k_y}{k_z}I_2 e^{jk_z a} + \frac{k_y}{k_z}I_3 e^{2jk_z a} - I_4 e^{jk_z a/2}\right.$$

$$\left. - I_5 e^{3jk_z a/2}\right)e^{3jk_z a} + e^{4jk_z a},$$

$$T^{yx} = \frac{E_y^{6,7}(z=2a)}{E_0^{\text{inc}}e^{j(k_y y - 2k_z a)}} = -R^{yx}e^{4jk_z a},$$

$$T^{zx} = \frac{E_z^{6,7}(z=2a)}{E_0^{\text{inc}}e^{j(k_y y - 2k_z a)}} = R^{zx}e^{4jk_z a}. \tag{12}$$

In Eq. (12) superindices sign the co- and cross-polar components. The presence of cross-polar components, not found in homogeneous material slabs, is a consequence of the lack of periodicity in the z-direction. The transmission and reflection coefficients for the cross-polarized wave are, however, very small in the analyzed structure, as it will be shown in Sec. IV.

C. Calculation of the magnetic flux created by far neighbors

The last step before using Eq. (7) to calculate the induced currents and, subsequently, T^{ij} and R^{ij} coefficients, is the calculation of matrix $\overline{\mathbf{M}}^\infty$, which represents the coupling of each unit cell with its far neighbors. For this purpose we must evaluate the magnetic field over the unit cell at origin created by unit cells outside a circular hole of radius R. This situation is illustrated in Fig. 4.

Let us assume, following the procedure outlined in Sec. III A, that the hole is big in comparison to unit cell ($R\gg a$), that the unit cell is electrically small ($k_0 a\ll 1$, $k_y a\ll 1$), and that the slab is electrically thin ($k_0 d\ll 1$). In such case it is possible to say that the field over the unit cell at origin, created by neighbors outside of the hole, is almost uniform. Therefore, the magnetic flux through the loops of the unit cell will be $\Phi_i\approx A\mu_0\mathbf{n}_i\cdot\mathbf{H}^M(0,0,0)$, where $\mathbf{n}_i$ is the normal to the ith loop and $\mathbf{H}^M(0,0,0)$ is the magnetic intensity at origin. Furthermore, since the slab is electrically thin, it can be said that the field $\mathbf{H}^M(0,0,0)$ is radiated by a surface with magnetization
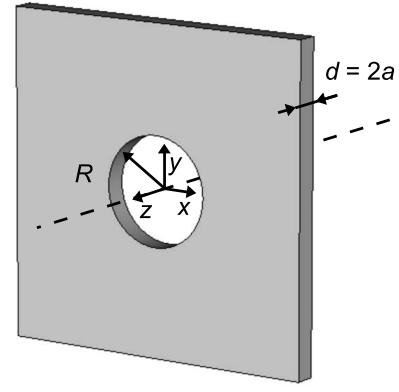

FIG. 4. Illustration of the slab with a hole of radius R.

$$\mathbf{M} = A\frac{(I_6+I_7)\mathbf{x}_0 + (I_4+I_5)\mathbf{y}_0 + (I_1+I_2+I_3)\mathbf{z}_0}{a^2}e^{jk_y y}\delta(z)$$

$$= \mathbf{M}_0 e^{jk_y y}\delta(z), \tag{13}$$

having a circular hole of radius R at the center. It may seem that the field $\mathbf{H}^M$ can be calculated by using free space Green's function for magnetic currents[22] and integrating over the surface with the hole. Although this is possible, it has to be taken into account that such approach leads to very poorly convergent integrals that prevent any numerical solution. This approach was used, for example, in Ref. 23 in case of $k_y=0$, where the poor convergence was overcome by finding an analytical solution. Unfortunately, in the general case of $k_y\neq 0$ there is no closed form solution of such integrals, which prevents the generalization of such procedure. There is, however, another possible approach that can be described as follows: calculate the field created by a magnetized annulus of outer radius R and inner radius ϵ and subtract it from the field created by a magnetized surface with a hole of radius ϵ, assuming that ϵ is negligibly small. Making then the limit $\epsilon\to 0$ leads to the desired field $\mathbf{H}^M$. This procedure slightly differs from the standard Lorentz procedure since the field created by a surface of uniform magnetization has a singularity on the surface. This singularity is avoided by the subtraction of the fields created by a small circle of radius $\epsilon\to 0$. The advantage of this procedure is that since $\epsilon\to 0$, the magnetization of this last disk can be considered uniform, and therefore the fields can be easily computed. The mathematical details of outlined procedure can be found in Appendix B, where it is shown that

$$\overline{\mathbf{M}}^\infty = \frac{\mu_0 A^2}{a^2}\begin{bmatrix} F_z^\infty & F_z^\infty & F_z^\infty & 0 & 0 & 0 & 0 \\ F_z^\infty & F_z^\infty & F_z^\infty & 0 & 0 & 0 & 0 \\ F_z^\infty & F_z^\infty & F_z^\infty & 0 & 0 & 0 & 0 \\ 0 & 0 & 0 & F_y^\infty & F_y^\infty & 0 & 0 \\ 0 & 0 & 0 & F_y^\infty & F_y^\infty & 0 & 0 \\ 0 & 0 & 0 & 0 & 0 & F_x^\infty & F_x^\infty \\ 0 & 0 & 0 & 0 & 0 & F_x^\infty & F_x^\infty \end{bmatrix}, \tag{14}$$

where F_x^∞, F_y^∞, and F_z^∞ are given by integrals (B8), which can be easily evaluated.
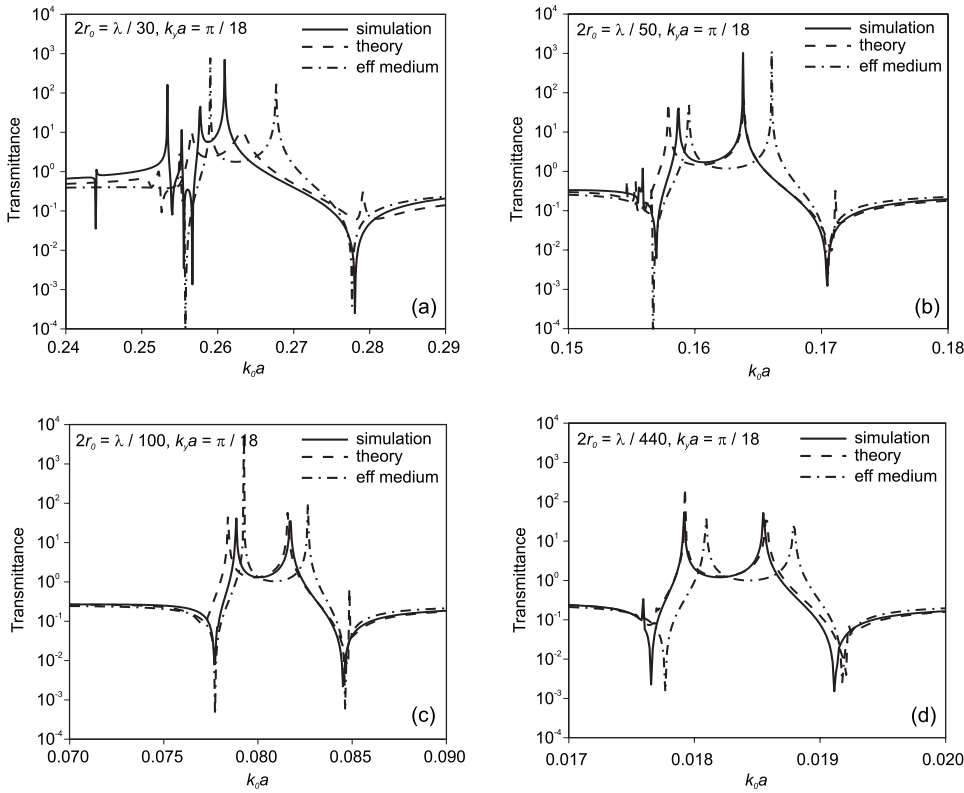
FIG. 5. Amplitude of the transmission coefficient for several electrical sizes of the CLRs in the lens of Fig. 1(b). The transmission coefficient was obtained by simulation (solid lines), theoretical model of Sec. III (dashed lines), and effective medium model (dashed-doted lines). The considered normalized transversal wave number is $k_y a = \pi / 18$ in all figures.

IV. NUMERICAL VALIDATION AND COMPARISON WITH THE CONTINUOUS MEDIUM MODEL

In this section the results of the model developed through Sec. III will be compared to full-wave numerical simulations, carried out by the numerical *CST Microwave Studio* electromagnetic solver. The comparison will be provided via the calculated transmission coefficient between planes $z=-2a$ and $z=2a$ and the reflection coefficient at plane $z=-2a$. For all the following calculations of the coupling matrices $\overline{\mathbf{M}}^\infty$ and $\overline{\mathbf{M}}$ a radius $R=10a$ will be used. The simulated slab is made of CLRs with normalized mean radius $r_0/a=0.34$ and normalized width $w/a=0.13$. The normalized self-inductance $L=\omega^2/C$ was computed from the simulated frequency of resonance for several values of the capacitance C, and the value $L/(a\mu_0)=0.79$ was obtained. The losses in CLRs will be neglected at this moment so that all the resonance peaks are well visible.

First of all, the limits of the proposed model will be studied. For this purpose the capacitance of the CLRs is varied so that the mean diameter of the CLRs at resonance is $d/\lambda=1/30$, 1/50, 1/100, and 1/440. The transmission coefficients for all the above situations obtained from the theoretical model, full-wave simulations, and effective medium model (see Sec. II) are depicted in Fig. 5. In all plots of Fig. 5 a normalized transversal wave number $k_y a = \pi/18$ was imposed. The plots for CLRs with $d/\lambda=1/30$ are depicted in Fig. 5(a). It can be seen that although the theoretical model reproduces the simulation better than the effective medium model, the quantitative agreement is very poor. This is expected since it is known[24] that the current induced on a conducting loop can be considered approximately uniform only if the circumference of the loop is smaller than $\lambda/10$. There-

fore, the quantitative disagreements can be attributed to the imprecise assumption of a uniform current over the CLRs. This hypothesis is confirmed by the remaining panels of Fig. 5, where it can be clearly observed that as the CLRs become electrically smaller, the quantitative agreement between theory and simulation improves, reaching a practically perfect matching in Fig. 5(d). Noticeably, Fig. 5 also shows that the effective medium model provides a reasonable first order approximation for small CLRs, even though it shows a systematic frequency shift with regard to simulations. This frequency shift is present for any electrical size of the CLRs. Therefore it seems to be a consequence of the small number of unit cells through the slab, regardless of the size of the CRLs.

After the validation of the proposed model, the analysis will be focused on the slab made of CLRs with $d/\lambda=1/440$, which is close to the slab proposed in Sec. II for MRI applications. To study the imaging properties of this slab, the transmission coefficient will be plotted for several values of the transversal phase shift. Figure 6(a) shows the result of the effective medium model and Fig. 6(b) shows the results of the model of Sec. III. As it was already mentioned in Sec. II, a $T\approx1$ valley appears between two peaks in both cases. These peaks are approaching each other when the transverse phase shift increases; however it can be seen that there is always a region common to all curves. When dealing with effective medium model, this common region precisely corresponds with permeability around $\mu_r=-1$ and lies just in the middle between both peaks. The model in Sec. III corrects this scenario, showing that this common region is shifted to lower frequencies when the transverse phase shift increases and it is no more centered. However, in both cases,
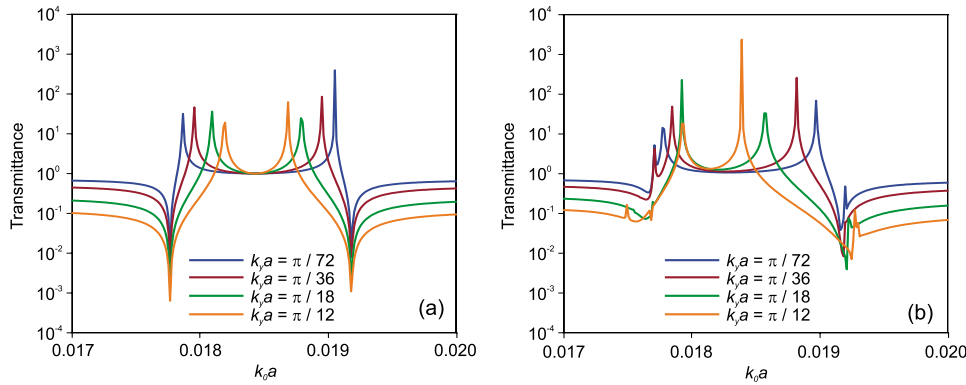
FIG. 6. (Color online) Amplitude of transmission coefficient for various transversal wave numbers obtained from the effective (a) medium model and the (b) model of Sec. III.

a frequency band of $T=1$ is present for moderate values of the transverse phase shift, which confirms the usefulness of the proposed design for MRI applications. Figure 7 shows the transmission and reflection coefficient of the lens. It reveals that an optimal point of minimum reflection appears just at the expected frequency of operation of the lens.

Finally, cross-polarization effects will be investigated. As it was already mentioned in Sec. III B, the analyzed slab produces not only copolar but also cross-polar components of the transmitted and reflected waves, as it can be seen from Eq. (12). In order to illustrate this effect, the transmission coefficients T^{xx} and T^{yx} are plotted in Fig. 8 for a normalized transversal wave number $k_y a = \pi/18$. It can be observed that especially in the region of interest, the cross-polar component is approximately two orders of magnitude smaller that the copolar one, having thus a negligible influence. Similar conclusions are reached for other transversal wave numbers.

V. CONCLUSION

A rigorous model has been proposed for the description of electrically thin metamaterial slabs made of resonant current loops. This includes electrically small capacitively loaded loops, SRRs, and other related configurations. This model allows for the computation of the transmission and reflection coefficients of any kind of propagative and/or evanescent incident plane wave, and is specifically well suited for the analysis of imaging applications of such slabs.

The reported model has been compared with numerical full-wave electromagnetic computations, and a good agreement has been found provided the hypothesis underlying the approximation is fulfilled. Specifically, it has been found that the proposed model remains valid, provided the size of the current loops is small enough to guarantee an approximately uniform current distribution along the loop. It has been also compared with the continuous medium model of the slab. The main conclusion of this comparison is that this last model provides a qualitative description of the electromagnetic behavior of the slab, even for thicknesses including a number of unit cells so small as two. Quantitatively, the continuous medium model fails by a small amount even for very small current loops, as a consequence of the small number of unit cells across the slab. In such situations, the main drawback of the continuous medium model is a non-negligible frequency shift in the transmission and reflection coefficients through the slab.

Applications of the above concepts in the design of metamaterial magnetic superlenses are envisaged. Specifically, medical applications in MRI can be foreseen. These applications could result in a meaningful increasing of the sensitivity of surface coils, reduction in image acquisition times, and improvement of parallel imaging techniques.
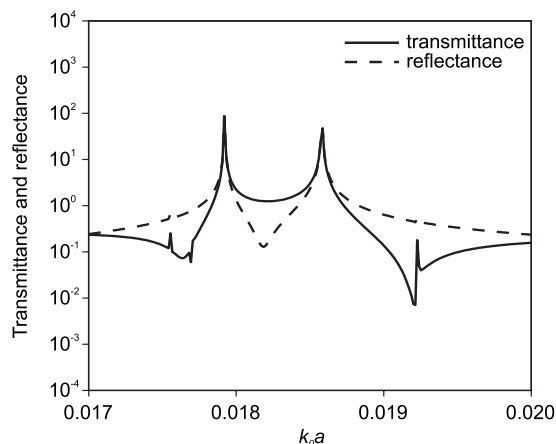

FIG. 7. Amplitude of transmission and reflection coefficient obtained from the model of Sec. III. The normalized transversal wave number is $k_y a = \pi/18$.
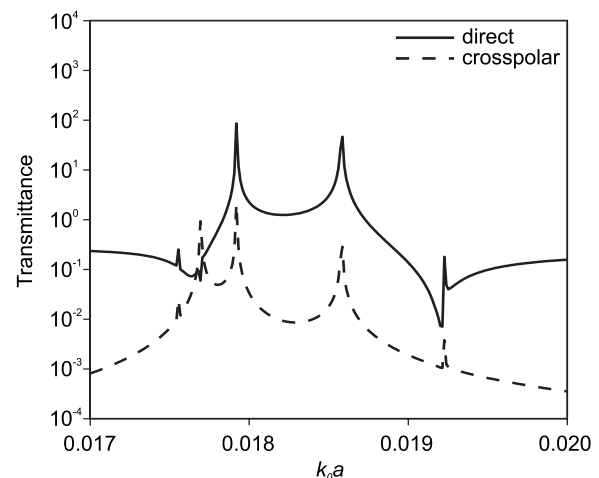

FIG. 8. Amplitude of transmission coefficient obtained from the model of Sec. III. The solid line represents direct copolar transmission, while dashed line represents transmission through cross-polar component. The normalized transversal wave number is $k_y a = \pi/18$.

ACKNOWLEDGMENTS

APPENDIX A: MUTUAL INDUCTANCE OF TWO CURRENT LOOPS

For orthogonally oriented loops the parametrization of each current loop can be written as

$$x = r_0(n_z \cos \alpha + n_y \sin \alpha) + x_s,$$

$$y = r_0(n_z \sin \alpha - n_x \sin \alpha) + y_s,$$

$$z = r_0(n_y \cos \alpha + n_x \cos \alpha) + z_s,$$

$$\alpha \in (0, 2\pi), \tag{A1}$$

where n_x, n_y, and n_z are the components of the unit vector normal to the loop; x_s, y_s, and z_s are the coordinates of its center; and r_0 is the radius of the loop. The element of length in parametrization (A1) is given by

$$\mathbf{dl} = r_0[\mathbf{x}_0(-n_z \sin \alpha + n_y \cos \alpha) + \mathbf{y}_0(n_z \cos \alpha - n_x \cos \alpha) - \mathbf{z}_0(n_y \sin \alpha + n_x \sin \alpha)]d\alpha. \tag{A2}$$

The mutual inductance between two loops can now be calculated using the Neumann formula[22] as

$$M = \frac{\mu_0}{4\pi} \int_{l_2} \int_{l_1} \frac{e^{-jk_0\rho}}{\rho} \mathbf{dl}_1 \cdot \mathbf{dl}_2,$$

$$\rho = \sqrt{[x_1(\alpha_1) - x_2(\alpha_2)]^2 + [y_1(\alpha_1) - y_2(\alpha_2)]^2 + [z_1(\alpha_1) - z_2(\alpha_2)]^2}. \tag{A3}$$

For numerical calculations it is very convenient to rewrite Eq. (A3) as

$$M = \frac{\mu_0}{4\pi} \int_{l_2} \int_{l_1} \frac{e^{-jk_0\rho} - 1}{\rho} \mathbf{dl}_1 \cdot \mathbf{dl}_2 + \frac{\mu_0}{4\pi} \int_{l_2} \int_{l_1} \frac{1}{\rho} \mathbf{dl}_1 \cdot \mathbf{dl}_2. \tag{A4}$$

In Eq. (A4) the second integral (static part) does not depend on frequency and can be evaluated only once in whole frequency sweep. The first integral (dynamic part) has to be evaluated for each frequency. However the integrand is a very slow varying function (especially when $k_0\rho < \pi/2$, the integrand is practically a linear function), so only a few integration points are needed, which drastically fasten the calculation.

APPENDIX B: CALCULATION OF THE FIELD $\mathbf{H}^M(0,0,0)$

Let us assume a problem of negligibly small hole of radius ϵ cut in the magnetized surface. Such problem can be solved by subtracting the field of a disk of radius ϵ from the field of a full magnetization surface given by Eq. (9). Since the disk is negligibly small it is $k_y\epsilon \ll 1$, and the field in its center can be approximated by the field of a uniformly magnetized disk, a problem that is solved in Appendix C. It can be found that the field at the center of such disk is

$$H_x^{\text{disk } \epsilon} = \frac{-jk_0 M_{0x}}{2} + \frac{1}{4}\left(jk_0 - \frac{1}{\epsilon}\right)M_{0x}e^{-jk_0\epsilon},$$

$$H_y^{\text{disk } \epsilon} = \frac{-jk_0 M_{0y}}{2} + \frac{1}{4}\left(jk_0 - \frac{1}{\epsilon}\right)M_{0y}e^{-jk_0\epsilon},$$

$$H_z^{\text{disk } \epsilon} = -M_{0z}\delta(z=0) + \frac{1}{2}\left(jk_0 + \frac{1}{\epsilon}\right)M_{0z}e^{-jk_0\epsilon}. \tag{B1}$$

In Eq. (B1) it can be seen that the z-component of the field is divergent. However, it will be shown that this fact does not introduce any difficulty if the term $\delta(z=0)$ is treaded in symbolic way. Subtracting Eq. (B1) from Eq. (9) we can write the field in the center of hole of radius ϵ as

$$H_x^{\text{hole } \varepsilon} = \frac{-k_0^2 M_{0x}}{2jk_z} + \frac{jk_0 M_{0x}}{2} - \frac{1}{4}\left(jk_0 - \frac{1}{\varepsilon}\right)M_{0x}e^{-jk_0\varepsilon},$$

$$H_y^{\text{hole } \varepsilon} = \frac{j}{2}[-k_y M_{0z} \text{ sgn}(z=0) + k_z M_{0y}] + \frac{jk_0 M_{0y}}{2} - \frac{1}{4}\left(jk_0 - \frac{1}{\varepsilon}\right)M_{0y}e^{-jk_0\varepsilon},$$

$$H_z^{\text{hole } \varepsilon} = \frac{jk_y}{2}\left(\frac{k_y M_{0z}}{k_z} - M_{0y} \text{ sgn}(z=0)\right) - \frac{1}{2}\left(jk_0 + \frac{1}{\varepsilon}\right)M_{0z}e^{-jk_0\varepsilon}. \tag{B2}$$

The problem of the terms $\text{sgn}(z=0)$ in Eq. (B2) can be solved as follows: assume that there is only magnetization M_{0z}. In such case there is an x-y magnetic wall at $z=0$ and H_y must vanish on it. This means that we can take $\text{sgn}(z=0)=0$ for H_y components. In a similar way, when there is only magnetization M_{0y}, there must be an x-y electric wall at $z=0$ and H_z must vanish on it. This means that we can take $\text{sgn}(z=0)=0$ for H_z component. Finally we obtain

$$H_x^{\text{hole }\varepsilon} = \left[\frac{jk_0^2}{2k_z} + \frac{jk_0}{2} - \frac{1}{4}\left(jk_0 - \frac{1}{\varepsilon}\right)e^{-jk_0\varepsilon} \right] M_{0x},$$

$$H_y^{\text{hole }\varepsilon} = \left[\frac{jk_z}{2} + \frac{jk_0}{2} - \frac{1}{4}\left(jk_0 - \frac{1}{\varepsilon}\right)e^{-jk_0\varepsilon} \right] M_{0y},$$

$$H_z^{\text{hole }\varepsilon} = \left[\frac{jk_y^2}{2k_z} - \frac{1}{2}\left(jk_0 + \frac{1}{\varepsilon}\right)e^{-jk_0\varepsilon} \right] M_{0z}. \tag{B3}$$

The final step is now to subtract from Eq. (B3) the field in the center of an annulus with outer radius R and inner radius ϵ. The field of such annulus can be solved by direct integration of the magnetic current Green's function, which leads to

$$H_x^{\text{annulus}} = \frac{M_{0x}}{2} \int_\varepsilon^R \left\{ k_0^2\left(J_0(k_y\rho) - \frac{J_1(k_y\rho)}{k_y\rho}\right) \right.$$
$$\left. + \frac{(1+jk_0\rho)}{\rho^2}\left(3\frac{J_1(k_y\rho)}{k_y\rho} - J_0(k_y\rho)\right) \right\}e^{-jk_0\rho}d\rho,$$

$$H_y^{\text{annulus}} = \frac{M_{0y}}{2} \int_\varepsilon^R \left\{ k_0^2\frac{J_1(k_y\rho)}{k_y\rho} + \frac{(1+jk_0\rho)}{\rho^2}\left(2J_0(k_y\rho)\right. \right.$$
$$\left.\left. - \frac{3J_1(k_y\rho)}{k_y\rho}\right) \right\}e^{-jk_0\rho}d\rho,$$

$$H_z^{\text{annulus}} = \frac{M_{0z}}{2} \int_\varepsilon^R \left\{ k_0^2 - \frac{(1+jk_0\rho)}{\rho^2} \right\}J_0(k_y\rho)e^{-jk_0\rho}d\rho. \tag{B4}$$

Subtraction of Eq. (B4) from Eq. (B3) gives the field $H^M(0,0,0)$ at the center of the circular hole of radius R. The integrals in Eq. (B4) can be solved numerically; however the numerical solution is difficult due to the divergent behavior of the integrands for $\rho=0$ (note that it is assumed that $k_y\epsilon \ll 1$). However, this problem can be easily solved. The integrals in Eq. (B4) have a closed form solution in the case of $k_y=0$, which reads

$$G_x = \frac{M_{0x}}{4} \int_\varepsilon^R \left\{ k_0^2 + \frac{(1+jk_0\rho)}{\rho^2} \right\}e^{-jk_0\rho}d\rho = \frac{M_{0x}}{4}\left\{ \left(jk_0 \right.\right.$$
$$\left.\left. - \frac{1}{R}\right)e^{-jk_0R} + \left(-jk_0 + \frac{1}{\varepsilon}\right)e^{-jk_0\varepsilon} \right\},$$

$$G_y = \frac{M_{0y}}{4} \int_\varepsilon^R \left\{ k_0^2 + \frac{(1+jk_0\rho)}{\rho^2} \right\}e^{-jk_0\rho}d\rho = \frac{M_{0y}}{4}\left\{ \left(jk_0 \right.\right.$$
$$\left.\left. - \frac{1}{R}\right)e^{-jk_0R} + \left(-jk_0 + \frac{1}{\varepsilon}\right)e^{-jk_0\varepsilon} \right\},$$

$$G_z = \frac{M_{0z}}{2} \int_\varepsilon^R \left\{ k_0^2 - \frac{(1+jk_0\rho)}{\rho^2} \right\}e^{-jk_0\rho}d\rho = \frac{M_{0z}}{2}\left\{ \left(jk_0 \right.\right.$$
$$\left.\left. + \frac{1}{R}\right)e^{-jk_0R} + \left(-jk_0 - \frac{1}{\varepsilon}\right)e^{-jk_0\varepsilon} \right\}. \tag{B5}$$

Now, we can add the right-hand part and subtract the left-hand part of Eq. (B5) from Eq. (B4), which leads to

$$H_x^{\text{annulus}} = \frac{M_{0x}}{2} \int_\varepsilon^R \left\{ k_0^2\left(J_0(k_y\rho) - \frac{J_1(k_y\rho)}{k_y\rho} - \frac{1}{2}\right) \right.$$
$$+ \frac{(1+jk_0\rho)}{\rho^2}\left(3\frac{J_1(k_y\rho)}{k_y\rho} - J_0(k_y\rho)\right.$$
$$\left.\left. - \frac{1}{2}\right) \right\}e^{-jk_0\rho}d\rho + \frac{M_{0x}}{4}\left\{ \left(jk_0 - \frac{1}{R}\right)e^{-jk_0R} + \right.$$
$$\left. \left(-jk_0 + \frac{1}{\varepsilon}\right)e^{-jk_0\varepsilon} \right\},$$

$$H_y^{\text{annulus}} = \frac{M_{0y}}{2} \int_\varepsilon^R \left\{ k_0^2\left(\frac{J_1(k_y\rho)}{k_y\rho} - \frac{1}{2}\right) \right.$$
$$+ \frac{(1+jk_0\rho)}{\rho^2}\left(2J_0(k_y\rho) - \frac{3J_1(k_y\rho)}{k_y\rho}\right.$$
$$\left.\left. - \frac{1}{2}\right) \right\}e^{-jk_0\rho}d\rho + \frac{M_{0y}}{4}\left\{ \left(jk_0 - \frac{1}{R}\right)e^{-jk_0R} + \right.$$
$$\left. \left(-jk_0 + \frac{1}{\varepsilon}\right)e^{-jk_0\varepsilon} \right\},$$

$$H_z^{\text{annulus}} = \frac{M_{0z}}{2} \int_\varepsilon^R \left\{ k_0^2 - \frac{(1+jk_0\rho)}{\rho^2} \right\}\{J_0(k_y\rho) - 1\}e^{-jk_0\rho}d\rho$$
$$+ \frac{M_{0z}}{2}\left\{ \left(jk_0 + \frac{1}{R}\right)e^{-jk_0R} + \left(-jk_0 - \frac{1}{\varepsilon}\right)e^{-jk_0\varepsilon} \right\}. \tag{B6}$$

Field (B6) is identical to Eq. (B4), but now all the integrands tend to zero for $\rho\to 0$ and all integrals in Eq. (B6) can be numerically evaluated without difficulty. Finally the subtraction of Eq. (B6) from Eq. (B3), taking into account Eq. (13), leads to

$$\overline{\mathbf{M}}^\infty = \frac{\mu_0 A^2}{a^2} \begin{bmatrix} F_z^\infty & F_z^\infty & F_z^\infty & 0 & 0 & 0 & 0 \\ F_z^\infty & F_z^\infty & F_z^\infty & 0 & 0 & 0 & 0 \\ F_z^\infty & F_z^\infty & F_z^\infty & 0 & 0 & 0 & 0 \\ 0 & 0 & 0 & F_y^\infty & F_y^\infty & 0 & 0 \\ 0 & 0 & 0 & F_y^\infty & F_y^\infty & 0 & 0 \\ 0 & 0 & 0 & 0 & 0 & F_x^\infty & F_x^\infty \\ 0 & 0 & 0 & 0 & 0 & F_x^\infty & F_x^\infty \end{bmatrix}, \tag{B7}$$

where

$$F_x^\infty = \left\{ \left[\frac{jk_0^2}{2k_z} + \frac{jk_0}{2} - \frac{1}{4}\left(jk_0 - \frac{1}{R}\right)e^{-jk_0R} \right] \right.$$
$$- \frac{1}{2}\int_\varepsilon^R \left\{ k_0^2\left[J_0(k_y\rho) - \frac{J_1(k_y\rho)}{k_y\rho} - \frac{1}{2}\right] \right.$$
$$\left.\left. + \frac{(1+jk_0\rho)}{\rho^2}\left[3\frac{J_1(k_y\rho)}{k_y\rho} - J_0(k_y\rho) - \frac{1}{2}\right] \right\}e^{-jk_0\rho}d\rho \right\},$$

$$F_y^\infty = \left\{ \left[\frac{jk_z}{2} + \frac{jk_0}{2} - \frac{1}{4}\left(jk_0 - \frac{1}{R}\right)e^{-jk_0R} \right] \right.$$
$$- \frac{1}{2}\int_\varepsilon^R \left\{ k_0^2 \left[\frac{J_1(k_y\rho)}{k_y\rho} - \frac{1}{2} \right] + \frac{(1+jk_0\rho)}{\rho^2}\left[2J_0(k_y\rho) \right.\right.$$
$$\left.\left.\left. - \frac{3J_1(k_y\rho)}{k_y\rho} - \frac{1}{2} \right] \right\} e^{-jk_0\rho}d\rho \right\},$$

$$F_z^\infty = \left\{ \left[\frac{jk_y^2}{2k_z} - \frac{1}{2}\left(jk_0 + \frac{1}{R}\right)e^{-jk_0R} \right] - \frac{1}{2}\int_\varepsilon^R \left[k_0^2 \right.\right.$$
$$\left.\left. - \frac{(1+jk_0\rho)}{\rho^2} \right][J_0(k_y\rho) - 1]e^{-jk_0\rho}d\rho \right\}. \quad (B8)$$

All integrals in Eq. (B8) converge even for $\epsilon = 0$. Making $\epsilon \to 0$ leads to the exact solution.

APPENDIX C: MAGNETIC FIELD IN THE MIDDLE OF A UNIFORMLY MAGNETIZED DISK

Assume that the disk of radius ϵ carries a uniform magnetization

$$\mathbf{M} = \mathbf{M}_0\delta(z). \quad (C1)$$

The magnetic intensity produced in the disk center will be obtained in two steps. First of all, setting $k_y = 0$ in Eq. (9), we obtain the magnetic field intensity radiated by an infinite surface of magnetization $\mathbf{M}$,

$$H_x = \frac{-jk_0M_{0x}}{2}e^{-jk_0|z|},$$

$$H_y = \frac{-jk_0M_{0y}}{2}e^{-jk_0|z|},$$

$$H_z = -M_{0z}\delta(z). \quad (C2)$$

Then, it is assumed that there is a circular hole of radius ϵ on the surface of magnetization (C1). Since $k_y = 0$, this problem can be solved directly by integration of the magnetic Green's function. Introducing polar coordinates and using the identity

$$\frac{\partial}{\partial\rho}\left(\frac{e^{-jk_0\rho}}{\rho} \right) = -\frac{1+jk_0\rho}{\rho^2}e^{-jk_0\rho},$$

it is found that the magnetic field intensity in the middle of the hole is

$$\mathbf{H} = \frac{1}{4}\left\{ -jk_0\begin{bmatrix} 1 & 0 & 0 \\ 0 & 1 & 0 \\ 0 & 0 & 2 \end{bmatrix} + \frac{1}{\epsilon}\begin{bmatrix} 1 & 0 & 0 \\ 0 & 1 & 0 \\ 0 & 0 & -2 \end{bmatrix} \right\}\mathbf{M}_0 e^{-jk_0\epsilon}. \quad (C3)$$

Now, by subtracting Eq. (C3) from Eq. (C2) we can easily obtain the field in the middle of uniformly magnetized disk of radius ϵ.

[1] V. G. Veselago, Sov. Phys. Usp. **10**, 509 (1968).
[2] J. B. Pendry, Phys. Rev. Lett. **85**, 3966 (2000).
[3] R. Marqués, F. Martín, and M. Sorolla, *Metamaterials with Negative Parameters: Theory and Microwave Applications* (Wiley, New York, 2008).
[4] N. Fang, H. Lee, C. Sun, and X. Zhang, Science **308**, 534 (2005).
[5] R. Marqués, F. Mesa, and F. Medina, Appl. Phys. Lett. **86**, 023505 (2005).
[6] M. C. K. Wiltshire, J. B. Pendry, I. R. Young, D. J. Larkman, D. J. Gilderdale, and J. V. Hajnal, Science **291**, 849 (2001).
[7] M. C. K. Wiltshire, J. B. Pendry, and J. V. Hajnal, J. Phys.: Condens. Matter **18**, L315 (2006).
[8] M. J. Freire and R. Marqués, J. Appl. Phys. **100**, 063105 (2006).
[9] M. J. Freire and R. Marqués, J. Appl. Phys. **103**, 013115 (2008).
[10] M. Freire and R. Marqués, Proceedings of Metamaterials, Pamplona, Spain, 23–26 September 2008 (unpublished).
[11] S. A. Schelkunoff and H. T. Friis, *Antennas: Theory and Practice* (Wiley, New York, 1952).
[12] S. A. Cummer, B. I. Popa, and T. H. Hand, IEEE Trans. Antennas Propag. **56**, 127 (2008).
[13] J. B. Pendry, A. J. Holden, D. J. Robbins, and W. J. Stewart, IEEE Trans. Microwave Theory Tech. **47**, 2075 (1999).
[14] V. V. Yatsenko, S. I. Maslovski, S. A. Tretyakov, S. L. Prosvirnin, and S. Zouhdi, IEEE Trans. Antennas Propag. **51**, 2 (2003).
[15] S. Tretyakov, *Analytical Modeling in Applied Electromagnetics* (Artech House, Boston, MA, 2003).
[16] E. Saenz, P. Ikonen, R. Gonzalo, and S. Tretyakov, J. Appl. Phys. **101**, 114910 (2007).
[17] M. G. Silveirinha and C. A. Fernandes, Phys. Rev. E **75**, 036613 (2007).
[18] J. D. Baena, L. Jelinek, R. Marqués, and M. Silveirinha, Phys. Rev. A **78**, 013842 (2008).
[19] J. D. Baena, L. Jelinek, and R. Marqués, Phys. Rev. B **76**, 245115 (2007).
[20] R. Marqués, F. Medina, and R. Rafii-El-Idrissi, Phys. Rev. B **65**, 144440 (2002).
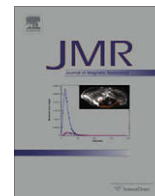[21] H. S. Lorentz, Ann. Phys. **9**, 641 (1880).
[22] J. D. Jackson, *Classical Electrodynamics*, 3rd ed. (Wiley, New York, 1998).
[23] S. I. Maslovski and S. A. Tretyakov, AEU, Int. J. Electron. Commun. **53**, 135 (1999).
[24] C. A. Balanis, *Antenna Theory: Analysis and Design*, 2nd ed. (Wiley, New York, 1997), p. 950.

Appendix 14

This appendix contains a full text of Ref. [47]

On the applications of $\mu_r = -1$ metamaterial lenses for magnetic resonance imaging

Manuel J. Freire *, Lukas Jelinek, Ricardo Marques, Mikhail Lapine

Departamento de Electronica y Electromagnetismo, Universidad de Sevilla, Facultad de Fisica, Avda. Reina Mercedes s/n, 41012 Sevilla, Spain

ARTICLE INFO

ABSTRACT

In this work some possible applications of negative permeability magnetic metamaterial lenses for magnetic resonance imaging (MRI) are analyzed. It is shown that using magnetic metamaterials lenses it is possible to manipulate the spatial distribution of the radio-frequency (RF) field used in MR systems and, under some circumstances, improve the sensitivity of surface coils. Furthermore a collimation of the RF field, phenomenon that may find application in parallel imaging, is presented. MR images of real tissues are shown in order to prove the suitability of the theoretical analysis for practical applications.

© 2009 Elsevier Inc. All rights reserved.

1. Introduction

Metamaterials are artificial composites whose electromagnetic properties can be engineered to achieve extraordinary phenomena not observed in natural materials as, for instance, negative effective permittivity and/or permeability [1]. Effective permittivity and permeability of metamaterials arise from their structure rather than from the nature of their components, which usually are conventional conductors and dielectrics. Metamaterials are usually manufactured by means of the repetition of resonant elements to constitute a periodic structure. An essential characteristic of metamaterials is that both the size of these elements and the periodicity are smaller than the wavelength of the electromagnetic fields that propagate through the structure, so that an effective permittivity and permeability can be defined through the appropriate homogenization procedure [2]. One of the most striking properties of metamaterials is the ability of a metamaterial slab with relative permittivity ε_r and relative permeability μ_r, both equal to −1, to behave as a "super-lens" with sub-wavelength resolution [3], that is, with a resolution smaller than the free-space wavelength of the impinging radiation. Although this effect is severely limited by losses, it is now well supported by many experiments and theoretical calculations (see, for instance, [2] and references therein). Interestingly, if the frequency of operation is sufficiently low, as it happens in MRI, we are in the realm of the quasi-statics, and we only need a metamaterial slab with $\varepsilon_r = -1$

or $\mu_r = -1$ (depending on the electric or magnetic nature of the quasi-static field) in order to observe this effect [3]. Therefore, if we place a $\mu_r = -1$ metamaterial slab between a RF magnetic field source (for instance an oscillating magnetic dipole) and a receiving device (for instance a MR surface coil) the slab will image the source towards the receiver, which will "see" the source closer than it actually is, thus detecting a stronger signal. It is clear that this mechanism can be applied to improve the sensitivity of MR surface coils as far as the additional noise introduced by the device will not compensate the gain in the signal. As it has been just explained, $\mu_r = -1$ metamaterial slabs have the ability to virtually "approach" the source to the detector. As it will be shown in this paper, this can be useful not only to improve the signal, but also to provide a better localization of the field of view (FOV) of the detector, with potential applications in parallel imaging. Of course, in order to take advantage of all these capabilities, metamaterials should not interact with the static magnetic fields used to codify the oscillating magnetic dipoles in MRI. Fortunately, as it was already mentioned, metamaterials are usually made of conventional dielectric and conductors, so that the compatibility with static MR magnetic fields can be achieved by using non-magnetic conductors.

The interesting properties of most metamaterials occur in a very narrow band of frequencies due to the resonant nature of the elements that constitute the periodic structure. This narrow bandwidth is usually cited as one of the main limitations for metamaterial applications. However, it is not a problem for MRI applications, because MR images are acquired by measuring RF signals inside a relatively narrow bandwidth of a few tens of kilohertz. In addition, since the wavelength associated with RF fields is of the order of the meters, it is possible to use conventional printed circuit techniques to develop quasi-continuous metamaterials

---

* Corresponding author. Fax: +34 954239434.
E-mail address: freire@us.es (M.J. Freire).
URL: http://alojamientos.us.es/gmicronda/Miembros/Freire/freire.htm (M.J. Freire).

with constituent elements and periodicities two orders of magnitude smaller than the wavelength.

Application of metamaterials in MRI has been explored previously in several works [4–11]. Basically, two types of metamaterials which correspond to two different resonant elements have been used for MRI applications. The first group are swiss roll metamaterials [4–8]. A swiss roll consists of a conductive layer which is wound on a spiral path around a cylinder with an insulator separating consecutive turns. Reported experiments [4,5] proved that swiss roll metamaterials can guide the RF flux from a sample to a remote coil. The guiding behavior is due to the high effective permeability of the metamaterial. The reported experiments also proved that these metamaterial guides can be employed in imaging [4] and spectroscopic [5] experiments for excitation as well as reception. In all these applications, the swiss rolls metamaterials mimic a medium with very high magnetic permeability at the proper frequency. A 2D log-pile structure of swiss rolls, which mimics a two-dimensional $\mu_r = -1$ medium was also used to demonstrate sub-wavelength imaging of a pair of parallel wire currents [6], but no direct application to MRI of this device has been reported up to the date. The other group of metamaterials which have been applied to MRI are capacitively-loaded split ring metamaterials [9–11]. A capacitively-loaded split ring is a small open ring of copper which is loaded in the gap with a capacitor. Of course, this capacitor has to be non-magnetic for MRI applications. Split rings have the key advantage over swiss rolls of providing three-dimensional (3D) isotropy when they form a cubic lattice [9,10], which is an essential property if the device has to image 3D sources. A split ring is similar to a very small parasitic MR coil. However, whereas a MR coil works at resonance, the working frequency of split rings in a $\mu_r = -1$ metamaterial lens differs from its frequency of resonance [9,10], which also helps to reduce losses and noise. It is the collective behaviour of split rings what provides the relative effective permeability equal to -1 [10]. Split rings were used as the constituent elements of a 3D lens that was fabricated and tested in a 1.5 T MRI system [9]. Fig. 1 shows a photograph of this device. Almost simultaneously, an accurate model for this design was developed, which showed the consistency of the continuous medium description of the device [10]. The goal of this design was to provide a permeability $\mu_r = -1$ at the Larmor frequency of the MRI system. The reported experiment [9] showed the capability of a $\mu_r = -1$ metamaterial lens to improve the signal detected by a surface coil for a pa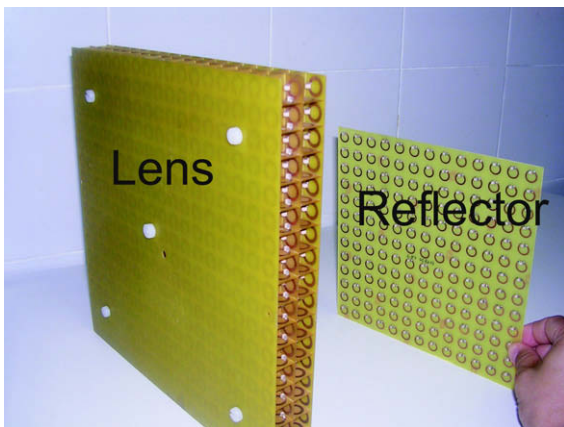rticular configuration, but did not provide a systematic analysis of the capabilities of such metamaterial lenses for MRI applications. The main aim of this work is to provide this analysis.

The paper is organized as follows: first, a theoretical model based on a continuous medium approach is developed. Using this model, the sensitivity, the signal-to-noise ratio (SNR) and the FOV localization provided by $\mu_r = -1$ metamaterial lenses are analyzed in several situations. Inspired by this analysis some experiments were designed and carried out in order to test the conclusions derived from the analysis. Finally, potential future applications of metamaterial lenses for MRI will be discussed.

2. Model

The main aim of this section is to develop a method for the computation of the signal, the noise, and then the SNR detected by a surface coil in the presence of a metamaterial slab placed at several distances. The analysis will include configurations that mimic the experiments reported in [9] and [11], as well as other potentially useful configurations. Through the analysis it will be assumed that the metamaterial slab behaves as an effective homogeneous medium with some effective permittivity and permeability. To demonstrate that the device shown in Fig. 1 actually behaves as an effective homogeneous medium is outside the scope of this paper, and furthermore this was shown in detail in our previous work [9–11]. Although the analysis could be done, in principle, by using a conventional electromagnetic solver, our experience is that these solvers have difficulties to deal with effective media of negative permeability, particularly those close to $\mu_r = -1$. Therefore, a specific code has been developed for this analysis. In order to simplify the following discussion, Fig. 2 shows the structure under analysis. This structure includes a coil of average radius ρ_0 made of a lossless metallic strip of width w and negligible thickness. The coil is placed at certain distance of a piecewise homogeneous multilayered medium with the coil axis perpendicular to the layers. The layers have a thickness t and an arbitrary complex permittivity ε and permeability μ, and depending on the values of these parameters they can model either the $\mu_r = -1$ lens, a specific tissue, or air. This simplified model has the advantage of an easy analytical solution, and we feel that it retains the most salient features of real experiments, at least qualitatively.

The first step in the analysis is the computation of the signal received by the coil. According to reciprocity theorem this signal is proportional to the B_1 magnetic field produced by the detector when it is driven by a unit current [12]. We begin with the calculation of the B_1 field by considering a current density given by

$$J_\varphi(\rho, z) = K_\varphi(\rho)\delta(z) \tag{1}$$

Fig. 1. Photograph of the metamaterial lens and reflector. The lens consists of a 3D array of capacitively-loaded copper rings with $18 \times 18 \times 2$ cubic unit cells containing a total of 2196 rings. It has been designed to exhibit a permeability equal to -1 at the Larmor frequency of 63.87 MHz in a 1.5 T system. The reflector consists of a 2D array of 14×14 rings which constitutes the first layer of a high permeability metamaterial slab.
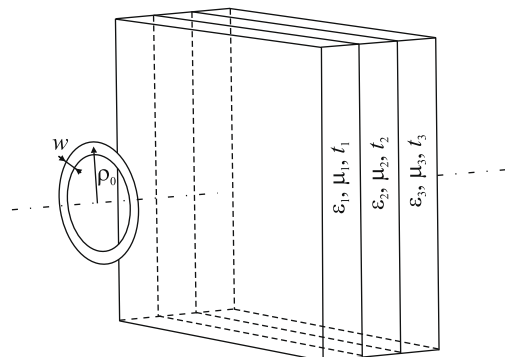

Fig. 2. Model for the analysis of the sensitivity and the SNR of a circular coil in presence of a metamaterial slab and one or more samples. The coil is modelled by a flat perfect conducting strip. The complex permittivity and/or permeability of each layer of thickness t models either the metamaterial lens or the tissue.

where $K_\varphi(\rho)$ is the surface current density on the ring. This surface current density is approximated by a Maxwellian distribution in the ring cross-section as

$$K_\varphi = K_0 \left(1 - \left(\frac{\rho - \rho_0}{w/2} \right)^2 \right)^{-1/2} \tag{2}$$

which gives quite good approximation for the actual current distribution on the metallic strip provided that the ring radius is not too small.

In order to compute the magnetic field, the equation for the vector potential **A** must be solved

$$\Delta \mathbf{A} + k^2 \mathbf{A} = -\mu_r \mu_0 \mathbf{J} \tag{3}$$

where k accounts for the wavenumber. This equation has to be solved at each layer and the boundary conditions have to be satisfied. Since the studied system has angular symmetry, Eq. (3) can be easily solved with the help of a Hankel transformation of the first order. Particularly, in the layer containing the coil, the transformed equation has the following shape

$$\frac{\partial^2 \widetilde{A}_\varphi}{\partial z^2} + k_z^2 \widetilde{A}_\varphi = -\delta(z) \mu_r \mu_0 \widetilde{K}_\varphi \tag{4}$$

where

$$k_z^2 = k^2 - k_\rho^2 \tag{5}$$

and k_ρ is the spectral wavenumber associated with the transverse coordinates x, y, and the tilde above the quantities denotes Hankel transformation. Eq. (4) can be easily solved giving

$$\widetilde{A}_\varphi(k_\rho, z) = -\frac{j\mu_r\mu_0}{2k_z} e^{-jk_z|z|} \widetilde{K}_\varphi(k_\rho) + C^-(k_\rho)e^{jk_z z} \tag{6}$$

where the first summand in the second term of Eq. (6) represents the excitation, and the second one represents the reflected wave. In the remaining layers, the corresponding equation is the expression in Eq. (4) without the source term, and the solution is

$$\widetilde{A}_\varphi = C^+(k_\rho)e^{-jk_z z} + C^-(k_\rho)e^{jk_z z}. \tag{7}$$

The unknown coefficients $C^+(k_\rho), C^-(k_\rho)$ can be determined for each layer by imposing the appropriate boundary conditions, specifically, by enforcing the continuity of the tangential components of the electric and magnetic fields on each boundary. After the unknown coefficients $C^+(k_\rho), C^-(k_\rho)$ have been determined, the magnetic field is know at every point in space.

As it was already mentioned, the signal is proportional to the B_1 magnetic field produced by the coil when it is driven by a unit current. On the other hand, the MR noise is proportional to the square root of the noise resistance R associated with the sample [13]. In our analysis the coil is assumed to be lossless, which means that both the coil losses and the MRI system losses are excluded from the analysis. Therefore the computed noise will be a sort of intrinsic noise [14]. Since we are interested in the comparison of the SNR given by different configurations, taking into account that the SNR is proportional to $B_1/\sqrt{R}$, in our analysis we will compute and compare this quantity for the different configurations. This quantity can be seen as a sort of normalized SNR. For the sake of simplicity, we will term SNR to the quantity $B_1/\sqrt{R}$, but the previous considerations must be taken into account in order to get a correct interpretation of the results.

Once the magnetic field is calculated, the next step is the computation of the noise resistance R. Usually, this resistance is calculated from the power dissipated by the eddy currents $\mathbf{J}^s$ induced in the sample as:

$$R = \frac{1}{|I|^2} \mathrm{Re} \left[\int_V \mathbf{J}^s \cdot \mathbf{E}^c dV \right] \tag{8}$$

where $\mathbf{E}^c$ is the electric field induced by the coil, and I is the current intensity, which is set equal to unity. In our analysis, we use reciprocity theorem ([15], pp. 116) to obtain this resistance from the reaction between the current in the coil $\mathbf{J}^c$ and the electric field reflected by the sample $\mathbf{E}^r$, which is defined as the field created by all currents in the multilayer medium (that is, all currents in the system, except the imposed current on the coil):

$$R = -\frac{1}{|I|^2} \mathrm{Re} \left[\int_V \mathbf{J}^c \cdot \mathbf{E}^r dV \right]. \tag{9}$$

Particularly, for the case presented above, this resistance can be calculated as

$$R = -\frac{2\pi}{|I|^2} \mathrm{Re} \left[\int_0^\infty K_\varphi \cdot E_\varphi^r \, \rho \, d\rho \right] \tag{10}$$

which can be advantageously rewritten using Plancherel–Parseval theorem as

$$R = -\frac{2\pi}{|I|^2} \mathrm{Re} \left[\int_0^\infty \widetilde{K}_\varphi \cdot \widetilde{E}_\varphi^r \, k_\rho \, dk_\rho \right]. \tag{11}$$

Once the noise resistance R has been computed, the normalized SNR given by $B_1/\sqrt{R}$, can be readily computed, which ends our analysis.

3. Results

3.1. Numerical results

Following the method described above, the signal and the SNR for a surface coil of 3 inch in diameter and a strip width of 1 cm, have been computed at the frequency of 63.87 MHz corresponding to the Larmor frequency of a 1.5 T MRI system, which is the type of system used in the experiments reported in this work. According to the previous analysis, the sample is modelled as a lossy layer with a complex permittivity whose real and imaginary parts are given by the mean values corresponding to human tissues [16]. The lens is modelled as a layer with a complex permeability whose imaginary part accounts for the losses. Fig. 3 shows on the left side a sketch of the two different configurations analyzed in this section. In one of them the coil is placed at certain distance d of a semi-infinite lossy media (*no lens* case in the figure) which models the sample. In the other configuration the coil is placed at the same distance d from the lens and this lens is in contact with the sample. In our calculations the lens was modelled as a 3 cm thick slab with a complex permeability $\mu_r = -1 - j0.25$, which corresponds to the realistic values calculated for the lens shown in Fig. 1 from previously developed models [10,17]. The sample was modelled by using an average value for the permittivity of human tissues, $\varepsilon_r = 90 - j197$, whose imaginary part corresponds to a conductivity of 0.7 S/m at 63.87 MHz [16].

Fig. 3a shows the signal (the axial magnetic field) along the coil axis for a distance $d = 1$ cm. The solid line in Fig. 3a (*no lens* case) corresponds to the signal provided by the coil in the absence of the lens. The dashed line (*realistic lens* case) corresponds to the signal provided by the coil with the lens placed between the coil and the lossy media. Finally, the dotted line (*low-loss* case) corresponds to the signal provided by the coil in front of a hypothetical lens with an imaginary part of the permeability one order of magnitude smaller than for the realistic lens. As expected, the comparison between the different curves shows that the signal with the lens is always larger that the signal without the lens for the same distance d. The dip in the signal observed for the *low-loss* case is due to the strong oscillations of the magnetic field at the output interface of
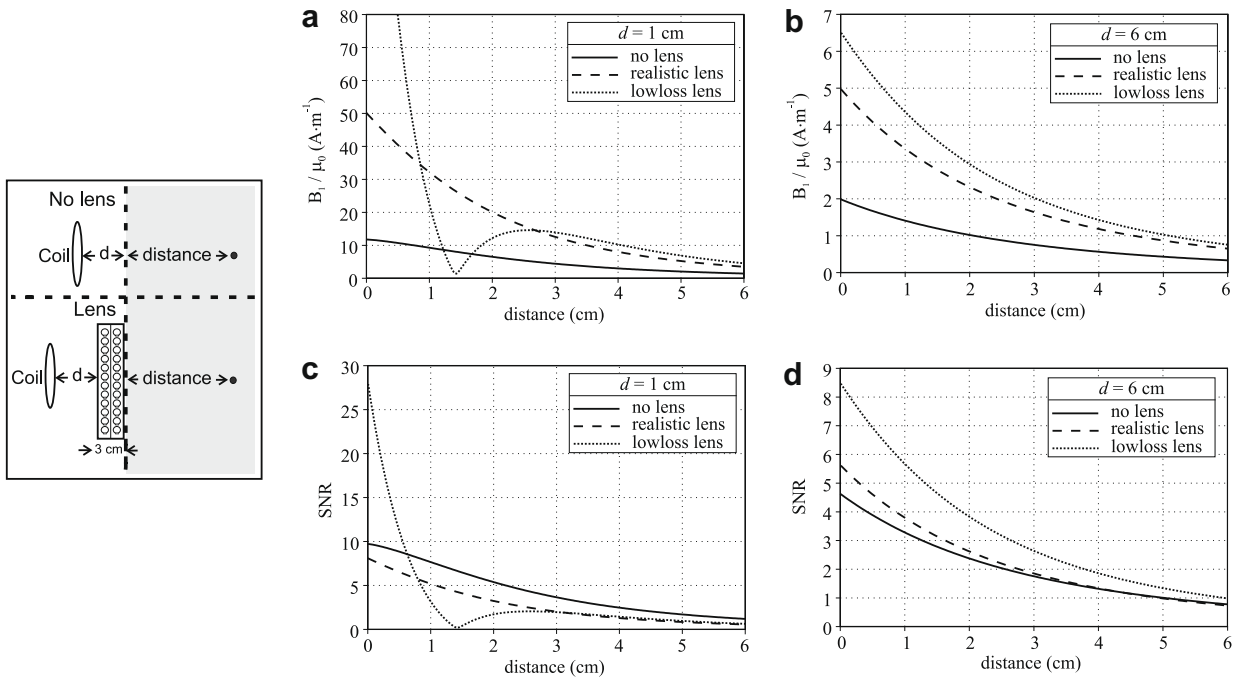
Fig. 3. On the left side it is shown a sketch of the configurations which are theoretically analyzed, a coil of 3 inch in diameter with a strip width of 1 cm at certain distance d of a semi-infinite lossy media and the coil at the same distance from a lens, which is placed in contact with the lossy media. On the right side it is shown the calculation of the magnetic field per unit current along the coil axis in these configurations for (a) $d = 1$ cm and (b) $d = 6$ cm. The SNR of the coil is also shown for (c) $d = 1$ cm and (d) $d = 6$ cm. The lens is modelled as a slab with a complex permeability $\mu_r = -1 - j0.25$ and the lossy media has a complex permittivity $\varepsilon_r = 90 - j197$. The frequency is 63.87 MHz.

the lens [2]. Fig. 3b shows the signal for a distance $d = 6$ cm, with a qualitative behavior similar to that shown in Fig. 3a.

The normalized SNR corresponding to the cases analyzed in Fig. 3a and b are shown in Fig. 3c and d, respectively. It can be seen that for the smaller distance, $d = 1$ cm, the SNR is lower in the presence of the lens than in the absence of it. However, for larger distances, such as $d = 6$ cm, the SNR becomes systematically higher when the lens is present (numerical computations not shown here prove that this improvement is even better for higher distances). It is worth to mention that this behavior is almost unchanged when losses in the lens are reduced by an order of magnitude, as it is shown in Fig. 3d. Only at very small distances of the lens there is a systematic improvement of the SNR, associated to the aforementioned oscillations of the field. Therefore, reducing lens losses—for instance, using superconducting split rings [18] (in this case the different temperature of the sample and the lens should be taken into account in the analysis)—is not enough to systematically improve the SNR over the *no lens* case when the coil is near the lens (and the lens near the sample). From field computations we have realized that this fact is related to the very high values of the induced fields at the interface between the lens and the sample that appear in the low-loss configuration. These strong fields cause a strong dissipation in the sample, and therefore a substantial increase of noise. The presence of such strong fields at the lens-sample interface is a well known effect in low-loss metamaterial lenses (see, for instance, [2] and references therein) which is related to the strong variations of the magnetic field at the input lens interface (the interface closer to the coil) when the coil is near this interface.

From the results reported in Fig. 3 and from the above considerations, it can be concluded that, as far as the lens can be modelled as a continuous medium with $\mu_r = -1$, the presence of the lens always improves the signal, but (except very near the lens) it only improves the SNR when the coil is placed at some distance of the lens. When the coil is placed near the lens, the SNR is not im-

proved, although it remains of the same order as in the absence of the lens.

From systematic numerical calculations and experiments (not shown in this work) it is concluded that, as a rule of thumb, the distance between the coil and the lens should be at least equal to the diameter of the coil in order to ensure an improvement of the SNR. Since the configuration in the experiment previously reported by the authors [9] fulfils this requirement, the analysis is now oriented to a configuration that resembles this experiment. The experiment consisted of placing the lens between the knees of a volunteer in order to image both knees with a 3-inch coil placed near one of the knees. Fig. 4 shows in logarithmic scale the normalized SNR for the same coil geometry as in Fig. 3 but with the lens placed between two lossy slabs (noted as tissue in the figure) which may represent the knees in the reported experiment [9] or any other tissue. The curves in the figure show that the SNR in the slab closer to the coil is the same regardless the lens is present or not. However, the SNR is highly improved for the slab beyond the lens in comparison with the situation where the lens has been
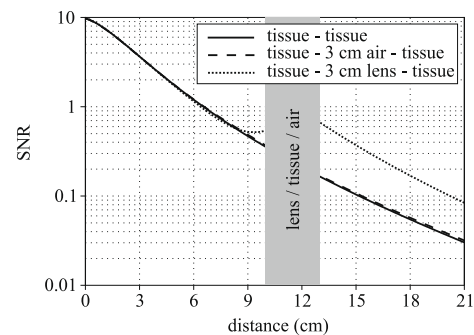

Fig. 4. SNR along the axis of a coil placed in front of two lossy slabs of 10 cm of thickness separated by a lens of 3 cm.

replaced by an air layer of the same thickness. The reported results clearly show the improvement of the SNR when the lens is placed between the lossy layers.

Since the sensitivity of surface coils strongly decays with distance, it will be useful if, on the basis of the previous concepts, it can be developed some way of reducing this decay. This can be possible by backing the lens with a magnetic wall, that is, a medium with a large value of the permeability (which, in practice, could also be another metamaterial slab). According to image theory in electromagnetism, this configuration will create an "image" beyond the magnetic wall composed by an identical lens and an identical coil, carrying the same current as the original one. Therefore, the magnetic field (and the signal) in the region of interest will be increased by the presence of these additional coil and lens. Fig. 5 shows the SNR along the coil axis for this configuration when the lens is backed by a magnetic wall and when the lens and the magnetic wall have been removed. The comparison between both results makes clear the increasing of the SNR in the region between the coil and the lens at distances where the coil sensitivity has decayed appreciably in the absence of the lens. This result is experimentally checked in the following section.

Probably the most studied property of metamaterial lenses is their ability to improve the discrimination between the fields coming from two independent sources [3]. Translated to MRI terminology, this property implies an improved localization of the FOV of each coil in an array of surface coils, a fact that could find application in parallel imaging [19]. Some numerical computations carried out using the method described in the previous section are shown in Fig. 6. This figure shows the B_1 field produced at 6 cm inside a lossy semi-infinite media by two rectangular coils with dimensions of 7×23 cm^2 and with their centers separated 10 cm. These dimensions correspond to the coil geometry used in [19]. The coil array is placed at 1.5 cm from the sample and at the same distance of the lens analyzed in this work, which is then placed on the sample, as it is shown in Fig. 6a. The results in Fig. 6b and c shows that the field pattern of each coil can be distinguished much better when the lens is present than when it is not. In other words, the lens improves the localization of the FOV of each coil in the array. As it is expected from the previous results—Fig. 3c—this should not imply a significant loss in the SNR.

3.2. Experimental results

First, for the purpose of illustrating how a $\mu_r = -1$ metamaterial lens does really transfer the field pattern of a source beyond the lens, Fig. 7 shows a sketch of a simple experiment and the MR images obtained in this experiment where a coil of 16 cm in diameter is placed on a saline solution phantom—Fig. 7a—and then a lens of 3 cm in thickness is placed between the coil and the phantom—Fig. 7b. The MR images were obtained in a Siemens Avanto
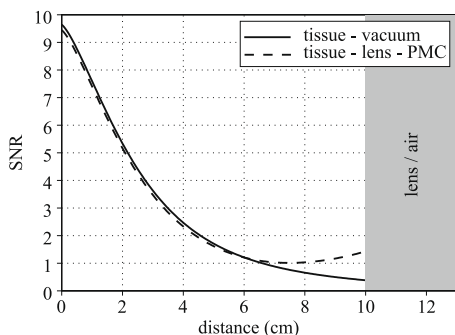

Fig. 5. SNR along the axis of a coil with a lossy slab of 10 cm of thickness placed between the coil and the lens backed by a reflector.
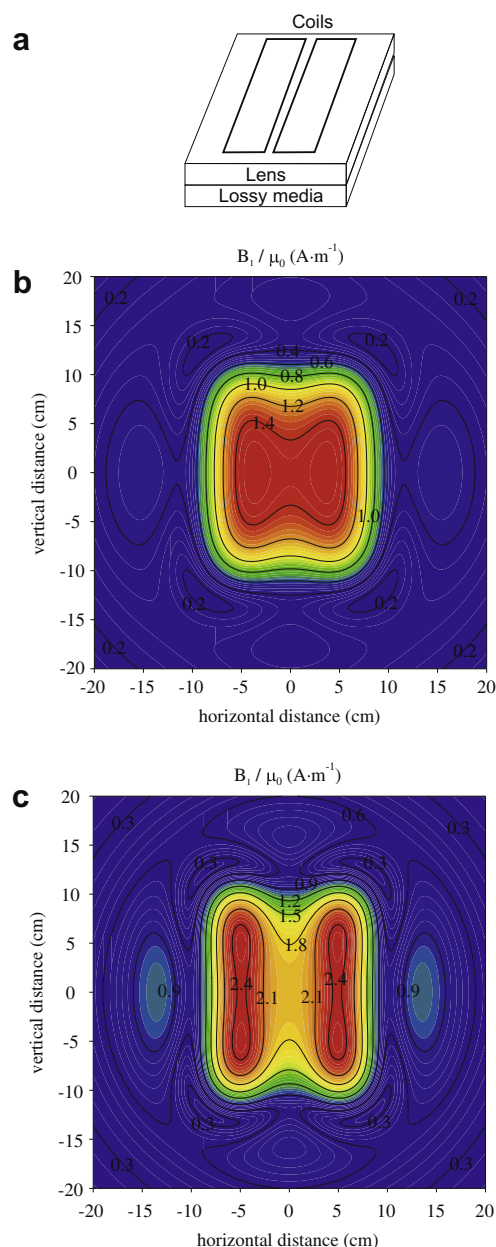

Fig. 6. Plots of the calculated sensitivity at 6 cm inside a lossy semi-infinite slab ($\varepsilon_r = 90 - j197$) for two rectangular coils with dimensions of 7×23 cm—dimensions of the coil geometry used for PILS demonstration [19]—and with their centers separated 10 cm. (a) Sketch of the configuration. (b and c) Images when the coils are placed at 1.5 cm from (a) the sample and (b) when they are placed at the same distance from the lens. The field pattern of each coil can be distinguished much better when the lens is present, which suggests the use of the lens for parallel imaging.

1.5 T system (Siemens Medical Systems, Erlangen, Germany) sited at the Department of Experimental Physics 5 (Biophysics) of the University of Würzburg (Würzburg, Germany). The coil was used in transmit/receive mode of operation. The pulse sequence used was a typical rf field mapping sequence, i.e., a high flip angle preparation pulse followed by a rapid image acquisition module. This allows to visualize the field lines pattern produced by the coil. A field line in the MR image shown in Fig. 7a has been marked with a cross. The equivalent field line in Fig. 7b appears shifted into the phantom a distance of 3 cm, which is the thickness of the lens. This experiment clearly illustrates the ability of the metamaterial lens to translate the field profile of the coil deeper into the sample.
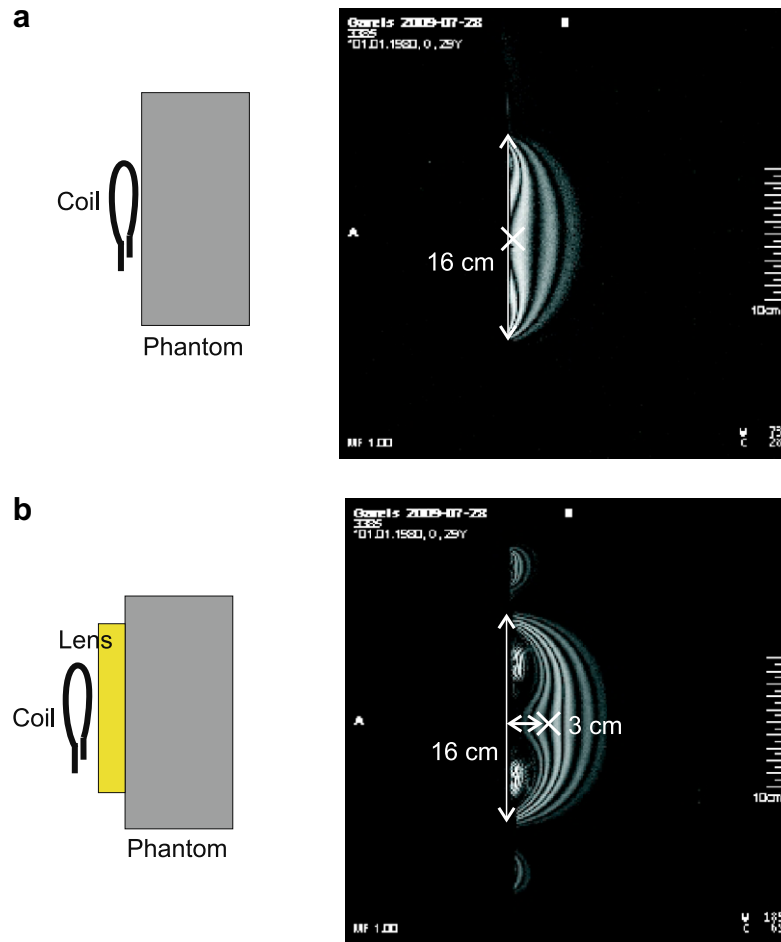
Fig. 7. MR images obtained for a circular coil of 16 cm in diameter by using a RF field sequence when (a) it is placed on a water saline phantom and (b) when a two unit cell (3 cm) thick lens is placed between the coil and the phantom. The field lines in case (a) appear in case (b) shifted inside the phantom a distance which is similar to the thickness of the lens.

Fig. 8a–c shows MR images of a phantom when a coil of 5-inch in diameter is placed in contact with the phantom. Fig. 8d–f shows MR images of the phantom when a lens is introduced between the coil and the phantom (that is, the coil is placed directly on the lens). The sagittal images in Fig. 8a and d contains the axis direction of the coil. The coronal images were obtained at distances of 1 cm (Fig. 8b and e) and 4 cm (Fig. 8c and f) inside the phantom (there is an additional distance of 0.5 cm between the lens and the phantom, as it is explained in the caption of the figure). T1-weighted pulse sequences with FOV = 26 × 26 cm², data matrix 256 × 160, TE = 10 ms, TR = 180 ms, and slice thickness 3 mm were used. The images were obtained in a GE Signa LX 1.5T system (General Electric, Milwaukee, USA) sited at PET Cartuja (Seville, Spain). The comparison between the images shows that the lens produces a compression of the image, which is in agreement with the discussion in the previous section about the parallel imaging application of the lens. In the coronal images, an estimation of the SNR in a small circular ROI placed as shown in the figures was derived from the ratio between the mean signal to the standard deviation (SD). The SNR at a distance of 4 cm inside the phantom is lower when the lens is present in Fig. 8f (mean/SD = 43.26) than when it is absent in Fig. 8c (mean/SD = 69.06), in agreement with the general conclusion arising from the analysis shown in the first section (see Fig. 3). However, at the distance of 1 cm inside the phantom (i.e. 1.5 cm from the lens) an increase in the SNR is observed in Fig. 8e with the lens (mean/SD = 75.46) in comparison with the value measured in Fig. 8b without the lens (mean/SD = 56). This in-

crease in the SNR cannot be explained by the model shown in this paper since this model assumes that the lens is a continuous slab of metamaterial and in practice the lens is a discrete structure, so that at distances from the lens of the order of the periodicity (15 mm) the continuous medium approach is not appropriate.

This unexpected increase in the SNR at very short distances has been checked theoretically by means of field calculations with an "ad hoc" numerical code which takes into account the discrete nature of the lens. This code, whose numerical details will be presented elsewhere [20,21], is based on the direct computation of the self and mutual inductances between the rings of the lens, and between these rings and the surface coil. Even taking into account all symmetries, the code involves the computation of thousands of mutual inductances, which are obtained by using some numerical tricks that are described in [21]. Both realistic widths and resistances of the rings were taking into account in the computation but the effect of the conductivity of the human body must be neglected to simplify the calculations, so that the fields are computed in vacuum. Fig. 9 shows the axial magnetic field generated in air by the coil and the lens of three layers of Fig. 8. In Fig. 9 the field is computed along the coil axis by using the continuous medium model (dotted line) described in Section 2 and the "ad hoc" model or discrete model (solid and dashed lines). With the discrete model, the field was computed for two cases: the coil axis contains the axis of a ring in the lens interface (dashed line) or the coil axis is off the axis of a ring (solid line), as it is shown in the inset. The results of this figure clearly show that there is an increase
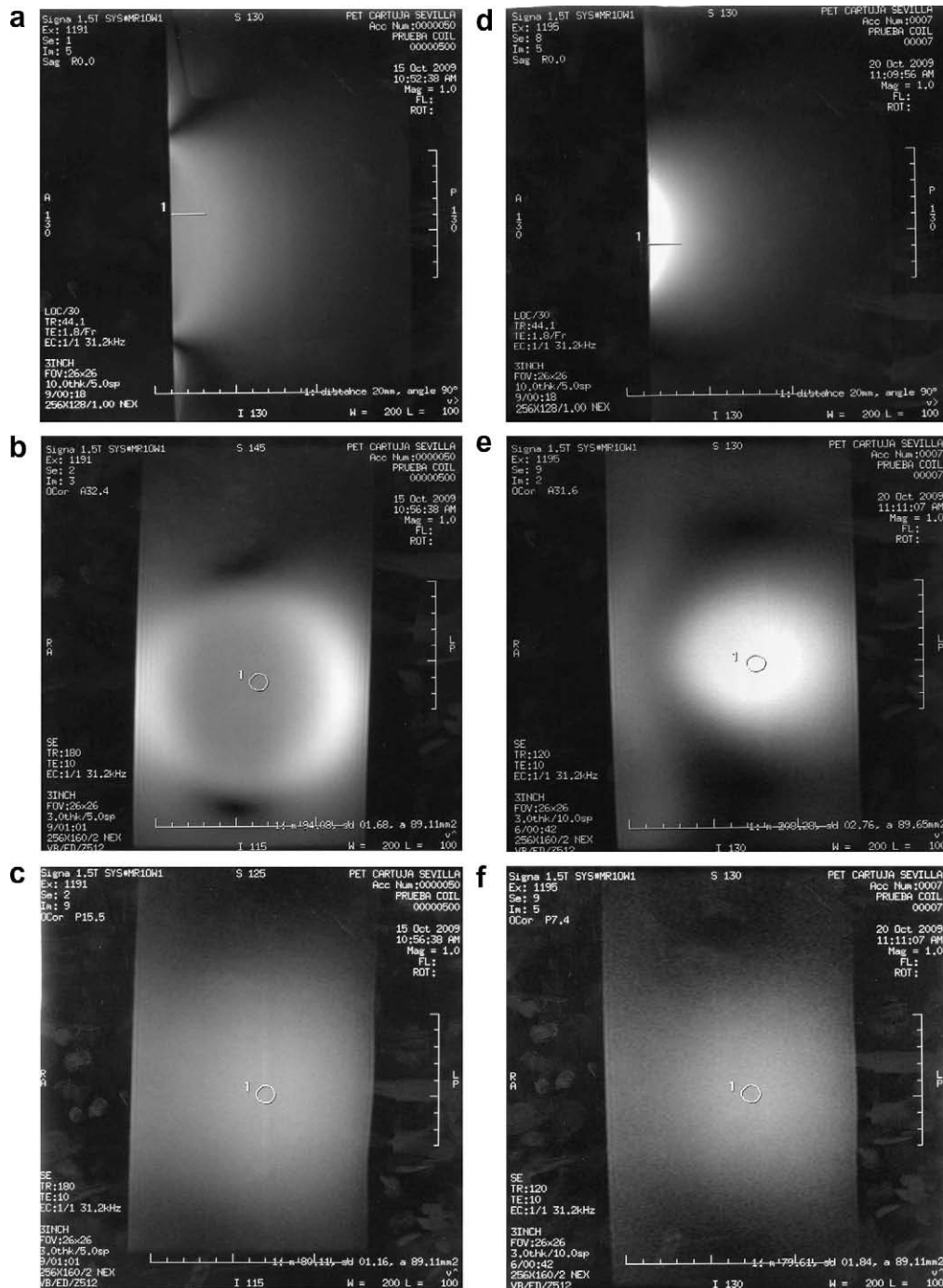
Fig. 8. MR images obtained for a circular coil of 5-inch in diameter when (a–c) the coil is placed on a water saline phantom and (d–f) a three unit cells thick lens (thickness is 4.5 cm) is introduced between the coil and the phantom. A pulse sequence with FOV = 26 × 26 cm², data matrix 256 × 160, TE = 10 ms, TR = 180 ms, and slice thickness of 3 mm was used. (a and d) Sagittal images containing the axis of the coil. (b and e) Coronal images at a distance of 1 cm inside the phantom. (c and f) Coronal images at a distance of 4 cm inside the phantom (there is, however, an additional distance between the phantom and the lens, due to the plastic screws that can be seen in Fig. 1, so that the actual distances between the images and the first plane of rings is of 1.5 cm and 4.5 cm, respectively).

of the coil signal of about a 40% at 1.5 cm of the lens (the distance for the image of Fig. 8e) with regard to the continuous medium model, which we feel can explain the observed increase in the SNR. Small discrepancies between the models at larger distances can be attributed to the finite size of the lens itself, not taken into account by the continuous model which considers the lens as an infinite slab of homogeneous permeability.

Next, other conclusions arising from the theoretical analysis shown in the previous section will be tested by means of experiments. The results shown in Fig. 4 are in agreement with the re-

sults of the previous experiment reported by the authors [9]. It is of interest to illustrate the present work with other MR images corresponding to a different coil geometry, and to include in the results a quantitative evaluation of the increase in the SNR, which was not provided in [9]. Fig. 10 shows a sketch of the experimental setup and the MR images obtained for this purpose. The MR images were obtained in a Siemens Simphony 1.5 T system (Siemens Medical Systems, Erlangen, Germany) sited at Virgen Macarena University Hospital (Seville, Spain). One of the elements of a double loop array coil (Siemens Medical Systems, Erlangen, Germany) was used
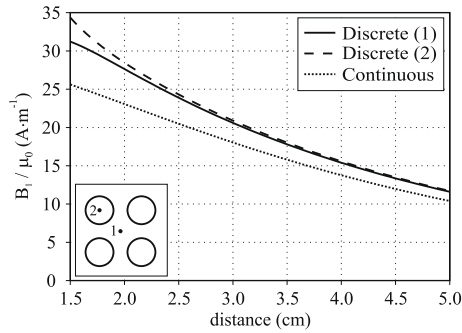
Fig. 9. Magnitude of the axial magnetic field generated in air by the coil and the lens of three layers of Fig. 8. The field is computed along the coil axis by using the continuous medium model (dotted line) described in Section 2 and an "ad hoc" model or discrete model which accounts for the discrete nature of the lens (solid and dashed lines). The discrete model involves the computation of all the mutual inductances between the 3132 rings of the lens of Fig. 8 and between the coil and these rings. With the discrete model, the field was computed for two cases: the coil axis contains the axis of a ring in the lens interface (dashed line) or the coil axis is off the axis of a ring (solid line), as it is shown in the inset.

as detector. This array is usually applied for imaging of the temporo mandibular joints, eyes and wrists, and it was used in the experiments for imaging the ankles of one of the authors. A fat-

suppression pulse sequence with FOV = 219×250 mm^2, data matrix 224×256, TE = 7.7 ms, TR = 371 ms and slice thickness 3 mm was used and axial MR images were obtained. The comparison between the MR images shows that the presence of the lens increases the SNR in the ankle which is far from the coil. An estimation of the SNR was derived from the ratio between the mean signal to the standard deviation (SD) of a small circular ROI placed as shown in the figure. The ratio mean/SD in the presence of the lens was $56.3/5.1 = 11$ and it was $15.7/3.7 = 4.2$ without the lens, that is, the SNR provided by the lens in the observed ROI was 2.6 times larger than without the lens. This gain is of the same order as the gain predicted in Fig. 4 for a similar situation, which was approximately 3.5 times along all the region behind the lens. Therefore, there exists a qualitative agreement between these experimental results and the theoretical results shown in Fig. 4 (quantitative predictions of the SNR are out of the scope of this work since noise depends on the specific structure of the tissues, which cannot be accounted for quantitatively by the simple model developed in the previous section).

At this stage it would be worth to mention that a similar enhancement of the SNR could be obtained by using a resonant coil instead of the metamaterial lens [22]. The physics behind this last technique is, however, quite different from the physics behind the analyzed device, and also performances are different. Unlike a resonant coil, the metamaterial lens is not a resonant device (the frequency of resonance of the individual coils of the lens is
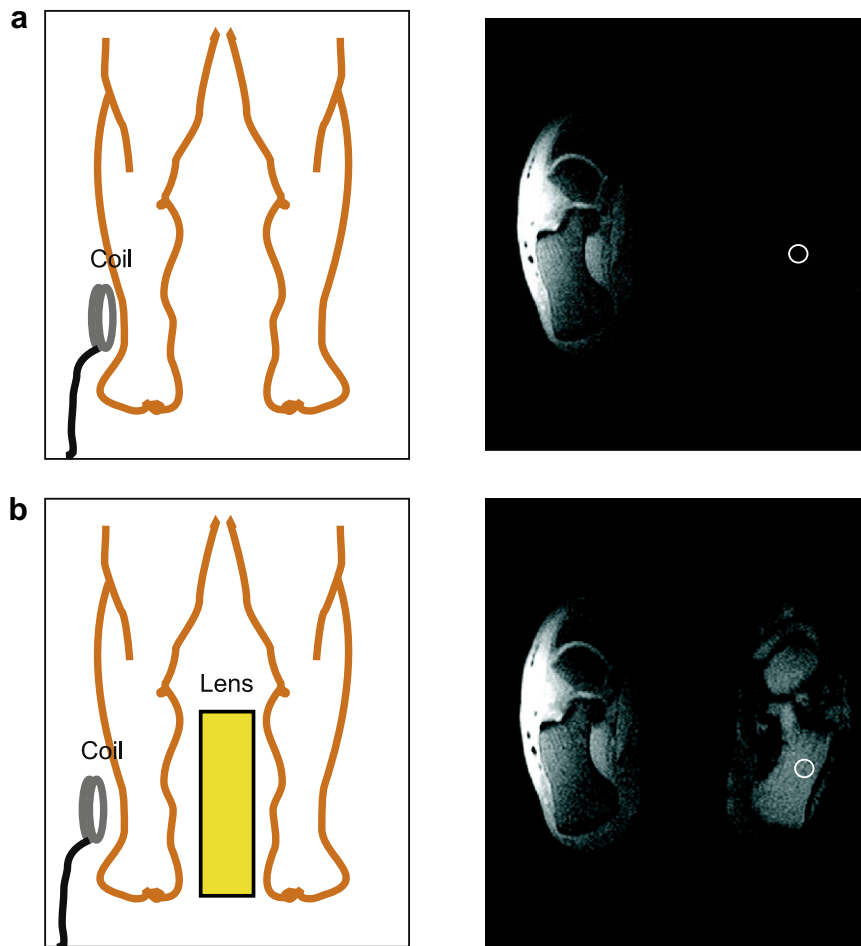

Fig. 10. Sketch of the experiment carried out in a 1.5 T Simphony system from SIEMENS (Siemens Medical Solutions, Erlangen, Germany) in the Virgen Macarena University Hospital (Seville, Spain) using an element of a double loop array coil (Siemens Medical Systems, Erlangen, Germany) as detector. A fat-suppression pulse sequence with FOV = 219×250 mm^2, data matrix 224×256, TE = 7.7 ms, TR = 371 ms, and slice thickness of 3 mm was used. Axial MR images of the ankles of one of the authors were obtained with and without a two unit cell (3 cm) thick lens. A small ROI for determination and comparison of the SNR in both situations is shown in the images. The SNR was increased 2.6 times with the lens.

63.28 MHz, which is far from the frequency of operation of 63.87 MHz in the 1.5 T system in comparison with the typical bandwidth of tens of KHz of the MRI acquisition). This makes a key difference since the metamaterial lens presents a much less interaction with the strong RF field emitted by the body coil, a fact that can be advantageous in some situations. On the other hand, owing to the intrinsic properties of metamaterial lenses [1,2], the sensitivity in the region between the receiving coil and the lens is not significantly affected by the presence of the lens, as it is shown in Fig. 4. This also implies that the metamaterial lens does not strongly interact with the receiving coil. It is quite apparent that this behavior will not be shared by a resonant coil (unless it is very small), which will equally affect the field at its both sides, and eventually could strongly interact with the receiving coil [22].

Next, an experiment was designed to validate the conclusion arising from the analysis shown in Fig. 5 for the combination of a lens with a magnetic wall. A theoretical magnetic wall is given by a semi-infinite medium with an infinite permeability. In practice, a magnetic wall can be implemented by means of a thick slab exhibiting a high permeability. In a first approach we simply fabricated a 2D array of split rings corresponding to the outer interface of this metamaterial slab. Since magnetic fields do not penetrate into the infinite permeability medium, it can be guess that this single layer will mimic to some extent the above mentioned metamaterial slab [11]. A photograph of this device, which has been termed "reflector" by the authors, is shown in Fig. 1 besides the lens. Fig. 11 shows a sketch of the experiment, as well as the axial and sagittal MR images obtained with the lens and the reflector. The pulse sequence was the same as that used for the results shown in the previous figure. With the lens and the reflector an increasing of the SNR is observed in the ankle placed between

the coil and the lens. The ratio mean/SD in the circular ROI indicated in the axial images corresponds to $30.9/4.6 = 6.7$ for the case without lens and $62.4/7.7 = 8.1$ for the case where the reflector-backed lens is used, so that this combined device provides a relative increasing of 20% in the SNR at that point. This result can be probably improved by optimizing the implementation of the magnetic wall (for example, by using a 3D array of split rings exhibiting a high permeability instead of a single 2D array). Anyway, the authors think that the reported experiment clearly shows the validity of the proposed concept.

4. Conclusions

Along this paper a theoretical model for the analysis of the sensitivity, the SNR and the FOV of MR coils in the presence of $\mu_r = -1$ metamaterial lenses has been developed. Our analysis has shown that metamaterial lenses usually improve the signal and the localization of the FOV of surface coils. However, except very near the lens, the SNR is only systematically improved if the lens is placed at a distance from the coil which, as a rule of thumb, should be larger than the coil diameter. A combination of a lens with a metamaterial mimicking a magnetic wall may behave as a reflector, increasing the signal received by a coil located at the opposite side of a given organ or tissue. These conclusions have been checked successfully by "in situ" MR experiments. Although a similar increase of the SNR could be achieved by means of other passive devices, such as additional parasitic resonant coils [22], we feel that the metamaterial lens could provide an useful alternative to such devices due to its non-resonant nature, which implies a lower interaction with the RF field coming from the body coil, as well as a lower interaction with the receiving coil.
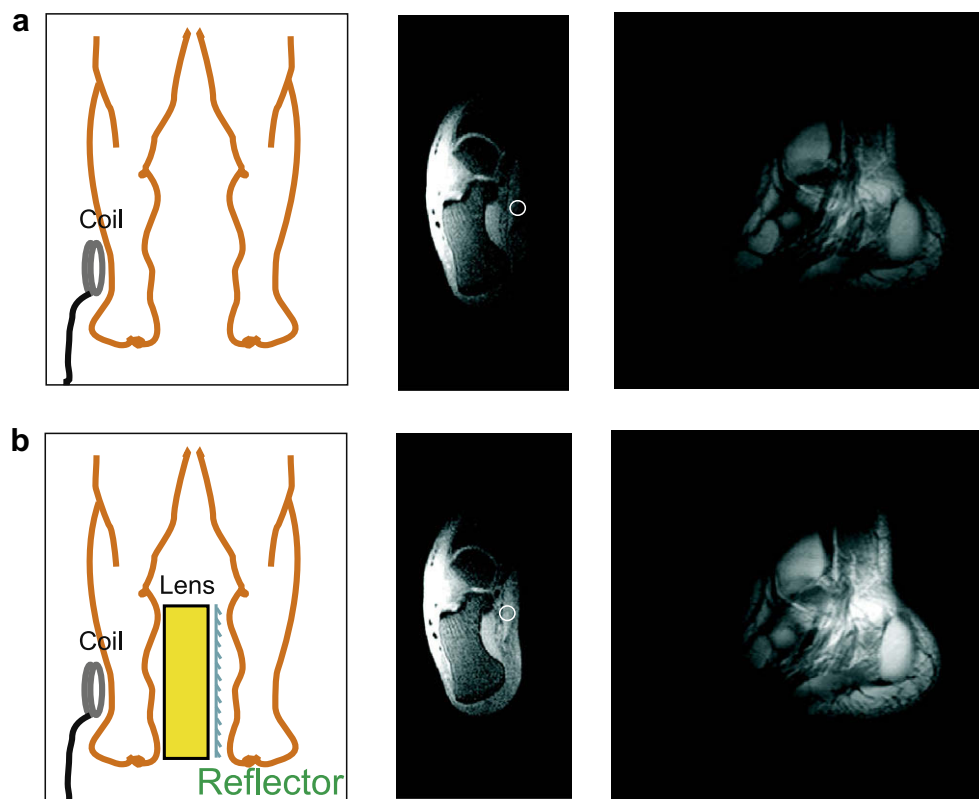

Fig. 11. With the same experimental setup as in Fig. 5, axial and sagittal MR images were obtained by using the lens backed by the reflector. The images show that the SNR is increased in the ankle placed between the detector and the reflector-backed lens. Direct measurements of the SNR in the small ROI indicated in the images show an increase of 20% by using the lens and the reflector.

Another interesting application for metamaterial lenses is related with the techniques of parallel imaging. Thus, for example, in the PILS technique [19] it is essential that the FOV of each coil is well localized and restricted to a finite region of space. However, in conventional coil arrays, this localization takes place only at distances close to the array because the field produced by the coils spread out at farther distances. Since the lens can help to discriminate the fields produced by individual coils at deeper distances inside the patient body, this device could be advantageously used in PILS and other parallel imaging techniques in order to obtain a better localization of the FOV of the receiving coils. This better localization will be achieved without significant loss in the SNR, or even with gain in the SNR at small distances of the lens. Computer simulations and experiments reported along this paper support these conclusions.

In summary, the authors feel that, in general, the emerging technology of metamaterials could help to improve several aspects of MR imaging by providing new concepts for the advancement of the MR technology, and that split ring $\mu_r = -1$ metamaterial lenses could play an important role in this direction.

Acknowledgments

References

[1] V.G. Veselago, The electrodynamics of substances with simultaneously negative values of ε and μ, Sov. Phys. Usp. 10 (1968) 509.

[2] R. Marques, F. Martin, M. Sorolla, Metamaterilas with Negative Parameters: Theory and Microwave Applications, Wiley, Hoboken, New Jersey, 2008.

[3] J.B. Pendry, Negative refraction makes a perfect lens, Phys. Rev. Lett. 85 (2000) 3966–3969.

[4] M.C.K. Wiltshire, J.B. Pendry, I.R. Young, D.J. Larkman, D.J. Gilderdale, J.V. Hajnal, Microstructured magnetic materials for RF flux guides in magnetic resonance imaging, Science 291 (2001) 849–851.

[5] V.C. Behr, A. Haase, P.M. Jakob, RF flux guides for excitation and reception in ^{31}P spectroscopic and imaging experiments at 2 Tesla, Concepts Magn. Reson. Part B (Magn. Reson. Eng.) 23B (1) (2004) 44–49.

[6] M.C.K. Wiltshire, Radio frequency (RF) metamaterials, Phys. Status Solidi B 244 (2007) 1227–1236.

[7] M. Allard, M.C.K. Wiltshire, J.V. Hajnal, R.M. Henkelman, Improved signal detection with metamaterial magnetic yoke, Proc. Intl. Soc. Mag. Reson. Med. 13 (2005) 871.

[8] A. Mathieu, R.M. Henkelman, Using metamaterial yokes in NMR measurements, J. Magn. Reson. 182 (2006) 200–207.

[9] M.J. Freire, R. Marques, L. Jelinek, Experimental demonstration of a $\mu = -1$ metamaterial lens for magnetic resonance imaging, Appl. Phys. Lett. 93 (2008) 231108 1–231108 3.

[10] L. Jelinek, R. Marques, M.J. Freire, Accurate modelling of split ring metamaterial lenses for magnetic resonance imaging applications, J. Appl. Phys. 105 (2009) 024907 1–024907 10.

[11] M.J. Freire, R. Marques, L. Jelinek, V. Delgado, Potential applications of $\mu = -1$ metamaterial superlenses for magnetic resonance imaging, in: Metamaterials 2009, 3rd International Congress on Advanced Electromagnetic Materials in Microwaves and Optics, London, UK, Aug 30th–Sept 4th, 2009.

[12] D.I. Hoult, R.E. Richards, The signal-to-noise ratio of the nuclear magnetic resonance experiment, J. Magn. Reson. 24 (1976) 71–85.

[13] D.I. Hoult, P.C. Lauterbur, The sensitivity of the zeugmatographic experiment involving human samples, J. Magn. Reson. 34 (1979) 425–433.

[14] W.A. Edelstein, G.H. Glover, C.J. Hardy, R.W. Redington, The intrinsic signal-to-noise ratio in NMR imaging, Magn. Reson. Med. 3 (1986) 604–618.

[15] R.F. Harrington, Time Harmonic Electromagnetic Field, McGraw-Hill, New York, 1961.

[16] M.E. Kowalski, J.M. Jin, J. Chen, Computation of the signal-to-noise ratio of high-frequency magnetic resonance imagers, IEEE Trans. Biomed. Eng. 47 (2000) 1525–1533.

[17] J.D. Baena, L. Jelinek, R. Marques, M.G. Silveirinha, Unified homogenization theory for magnetoinductive and electromagnetic waves in split-ring metamaterials, Phys. Rev. A 78 (2008) 013842 1–013842 5.

[18] R.D. Black, P.B. Roemer, O.M. Mueller, Electronics for a high temperature superconducting receiver system for magnetic resonance microimaging, IEEE Trans. Biomed. Eng. 41 (1994) 195–197.

[19] M.A. Griswold, P.M. Jakob, M. Nittka, J.W. Goldfarb, A. Haase, Partially parallel imaging with localized sensitivities (PILS), Magn. Reson. Med. 44 (2000) 602–609.

[20] M. Lapine, L. Jelinek, R. Marques, M.J. Freire, Discreteness effects in metamaterial lens, accepted communication to be presented at META'10, in: 2nd International Conference on Metamaterials, Photonic Crystals and Plasmonics, February 22–25, 2010, Cairo, Egypt.

[21] M. Lapine, L. Jelinek, R. Marques, M.J. Freire, Exact modelling method for discrete finite metamaterial lens, invited paper submitted to IET Transactions on Microwaves, Antennas and Propagation, special issue on: Microwave Metamaterials.

[22] R.R. Harman, P.C. Butson, A.S. Hall, I.R. Young, G.M. Bydder, Some observations of the design of RF coils for human internal use, Magn. Reson. Med. 6 (1988) 49–62.

Appendix 15

This appendix contains a full text of Ref. [48]

Exact modelling method for discrete finite metamaterial lens

M. Lapine[1]   L. Jelinek[2]   R. Marqués[1]   M.J. Freire[1]

[1]Department of Electronics and Electromagnetics, Faculty of Physics, University of Seville, 41015 Seville, Spain
[2]Department of Electromagnetic Field, Czech Technical University in Prague, 16627 Prague, Czech Republic
E-mail: mlapine@uos.de

Abstract: The authors analyse the properties of metamaterial lens composed of capacitively loaded ring resonators, with the help of an efficient rigorous model suitable for calculating the properties of finite metamaterial samples. This approach takes into account the discrete structure and finite extent of realistic metamaterials. The authors show that the discrete model reveals the effects, which can be missed by a continuous model based on effective parameters and that the results are in close agreement with the experimental data.

1 Introduction

For the last decade, metamaterials [1, 2] are in the focus of research attention in theoretical and applied electrodynamics. Even though no commonly accepted definition is available [3, 4], this research direction experiences a boom encompassing a wide span of areas ranging from microwave engineering to non-linear optics. One of the well-known suggestions for applications was formulated as a 'perfect lens' [5], making use of negative effective material parameters and providing imaging with subwavelength resolution. The idea of super-resolution was subsequently analysed and developed in a number of ways [6–8] and even realised in practice (speaking about three-dimensional (3D) systems) using split-ring resonators (SRRs) [9, 10], or transmission-line networks [11, 12].

Arguably the closest approach to practice offered by metamaterials, is related to magnetic resonance imaging (MRI). For example, rotational resonance of magnetoinductive waves [13] was suggested for parametric amplification of MRI signals [14] or enhanced detection with flexible ring resonators [15]. Alternatively, applications were promised with using 'swiss-rolls' [16] or employing channelling effect with wire media [17, 18]. Naturally, superlens concept is also promising in this area: an isotropic lens based on capacitively loaded single-ring resonators was experimentally tested specifically for MRI [19].

Such a metamaterial lens is intended to operate at the value of effective permeability $\mu = -1$. In theory, for modelling such metamaterials (based on SRRs), one can exploit an effective medium approach, taking care of numerous limitations related to general restrictions of homogenisation [20] as well as to specific peculiarities caused by resonant nature of the structural elements [21]. Universally, all the structure details (size of the elements and lattice constants) must be much smaller than the wavelength, whereas the total number of elements in metamaterial should be sufficiently large to make homogenisation meaningful. In addition, spatial dispersion effects can be rather remarkable in metamaterials and impose further restrictions on effective medium treatment, prohibiting that in certain frequency bands [21, 22].

Unless one opts for a completely numerical homogenisation method [23], generally applicable to almost arbitrary structures, a model have to be developed to describe adequately the effective medium properties. In SRR-type metamaterials, near-field mutual interaction between the elements significantly differs from dipole interaction adopted in many models; this is particularly relevant for dense arrays. The first rigorous analysis of such metamaterials was given early in [24], where the effective permeability has been derived given the properties of individual elements and lattice parameters, through the classical procedure of averaging the microscopic fields. In

that approach, mutual inductances between a large number of neighbours are taken into account, revealing the importance of lattice effects. This approach, however, is limited to quasi-static conditions and requires wavelength to be much larger than any structural details. Later on, a similar method, accounting also for spatial dispersion, was elaborated for isotropic lattices of resonant rings [22, 25]. The latter approach employs a nearest-neighbour approximation as otherwise full analytical treatment becomes impractical.

The above theoretical approaches provide the effective parameters for 'infinite' structures (which in practice implies the structures sufficiently large in all three dimensions). The lens of [10], however, contains just a few elements across the slab. Specifically for this case, a method was developed to calculate the transmission properties for a thin infinite slab [26], providing rather realistic predictions for the lens properties in most cases.

Nevertheless, it is clear that a number of peculiar effects caused by the discrete structure of the lens as well as its finite size, cannot be reliably assessed with the above models, as the lens is too small for an effective medium treatment. On the other hand, it is large enough to make an analysis with full-wave commercial software practically impossible. For this reason, an optimal solution to achieve reliable modelling is to employ a discrete model, which explicitly takes the structural details into account by evaluating mutual interaction between all the elements. In the context of metamaterials, such an approach was first applied a few years ago in connection with research on magnetoinductive excitations in SRR arrays [27] or evaluation of the effective permeability of finite SRR samples [24]. This method have been, for example, successively applied to 'swiss-roll' resonators [28], extended to hexagonal symmetry [29] and imaging with bilayer structures [30]. Further generalisations considered retardation effects in mutual interaction [31] or arbitrarily oriented elements [32]. In the above work, however, the total number of elements to be considered was typically of the order of tens or few hundreds (about 500 at most). A typical isotropic lens [10], in contrast, contains thousands of elements and an extra care is required to make the rigorous calculation practically feasible.

The goal of this paper is to describe in detail such a modelling approach, as applied specifically to a metamaterial lens employed in MRI and to illustrate that indeed it does reveal certain features, which are missed by the corresponding continuous modelling of [26].

2 Geometry of the problem

The metamaterial lens described in [10] is composed of capacitively loaded rings (CLRs) periodically arranged in an isotropic 3D lattice with the lattice constant $a = 1.5$ cm. The lens has three planes of 18×18 CLRs interlayered
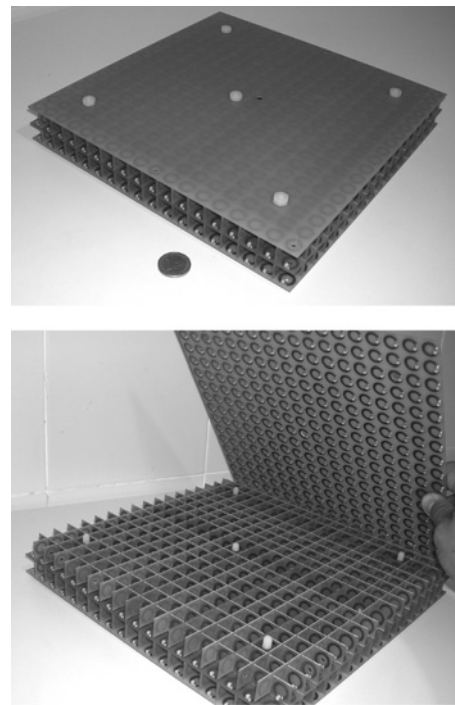

Figure 1 *Photograph of the analysed quasi-magnetostatic metamaterial lens*

with orthogonal segments providing two mutually orthogonal sets of two layers 17×18 CLRs each (see Fig. 1 for clarity), which makes it up to roughly 2200 CLRs. This lens can be optionally extended by an extra 3D-layer, resulting in having four 18×18 layers interlaced with the three orthogonal subsystems of $3 \times 17 \times 18$ CLRs, amounting to about 3130 elements. Overall dimensions of the (non-extended) lens are thus $27 \times 27 \times 3$ cm.

The CLRs themselves (Fig. 2a) are made of copper through etching metallic strips on a dielectric board. The mean radius r_0 of the CLRs is 0.49 cm ($r_0 / a = 0.33$) and the strip width w is 0.22 cm ($w / a = 0.15$). The CLRs are loaded with lumped non-magnetic 470 pF capacitors. The
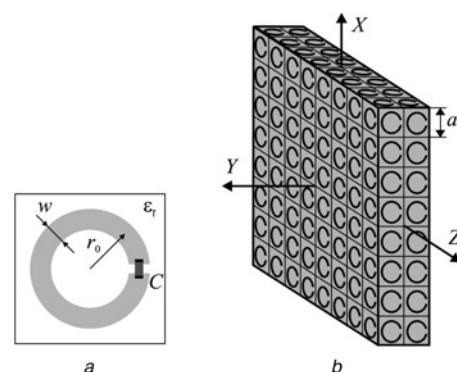

Figure 2 *Lens structure and geometry*
a Sketch of the CLR resonator
b Scheme of the lens with the corresponding coordinate system

self-inductance of the CLRs, $L = \omega_0^2/C = 13.5\text{nH}$, has been obtained from the measured value of the frequency of resonance in free space, equal to 63.28 MHz. By measurement of the quality factor of the resonator the resistance has been estimated as $R = 0.0465$ Ohm, which includes the losses in both the ring and the capacitor.

We reserve the standard coordinate system (x, y, z) for discussions of rings geometry and their mutual interactions (the next section). When referring to the overall lens geometry, we define a supplementary coordinate system (X, Y, Z) so that the lens geometrical centre is placed at the coordinate origin and the Y-axis is perpendicular to the lens as slab ('lens axis'), whereas the long edges of the lens are parallel to X and Z axes (Fig. 2b). Note that the coordinate origin is between the rings and thus the lens is completely symmetric with respect to the coordinate origin, all the axes and all the coordinate planes (in the analysis, we neglect minor asymmetry occurring in the real lens caused by specific assembly details, for example resulting from substrate thickness, as well as unavoidable production inaccuracy). For the three mutually orthogonal sets of CLRs, we will refer to as X-rings, Y-rings or Z-rings, depending on whether the rings' normals are along X, Y or Z axes. The lens therefore contains 612 of either X-rings and Z-rings, and 972 Y-rings. We also introduce a consecutive numbering through all the N CLRs with a single index n or m. The so called input and output surfaces of the lens correspond to $Y = \mp 1.5$ cm, whereas the theoretical source and image planes are at $Y \mp 3.0$ cm.

3 Discrete modelling of the lens

In line with the description of similar lattices [24, 25, 27], for the analysis of the lens response to the external field, we consider an ideal cubic array of $L-C$ circuits supporting current. With the time convention as $I \propto \exp(\text{j}\omega t)$, each of the currents is governed by equation

$$Z_0 I_n = -\text{j}\omega \Phi_n \tag{1}$$

where the self-impedance $Z_0 = (R + \text{j}\omega L + 1/(\text{j}\omega C))$ is determined by the resistance R, self-inductance L and self-capacitance C of the single CLR, whereas Φ_n represents the total magnetic flux through the considered ring which can be written as

$$\Phi_n = \Phi_n^{\text{ext}} + \sum_{m \neq n} \Phi_{nm} = \Phi_n^{\text{ext}} + \sum_{m \neq n} M_{nm} I_m \tag{2}$$

where Φ_n^{ext} is the magnetic flux from external sources and M_{nm} are the mutual inductances between the rings n and m. Combining (1) and (2), we obtain

$$\bar{Z} \cdot \mathbf{I} = -\text{j}\omega \Phi^{\text{ext}} \tag{3}$$

with $Z_{nn} = Z_0$, $Z_{nm} = \text{j}\omega M_{nm}$, which is a system of linear equations for unknown currents, provided that the external

sources are known. This is the general equation for various discrete modelling approaches. As opposed to continuous models [24, 26], which develop analytical approaches to evaluate remote mutual interactions in a (theoretically) infinite lattice, discrete modelling explicitly takes all the mutual inductances into account, so that the system (3) is solved exactly for the finite number of elements.

Note that, in practice, it is convenient first to evaluate the matrix of mutual inductances $\overline{M}$. This matrix is only determined by the geometry of the rings arrangement inside the lens and can be filled once for a given lens geometry, while the impedance matrix $\bar{Z} = \text{j}\omega\overline{M}$ can be then obtained for any particular set of frequencies as required.

Mutual inductance between the flat rings (which is the case under consideration) carrying the currents I_n and I_m along the ring contour is, most generally [33]

$$M_{nm} = \frac{\mu}{4\pi I_n I_m} \int_S \int_{S'} \frac{\mathbf{K}_n(\mathbf{r}) \cdot \mathbf{K}_m(\mathbf{r}')}{|\mathbf{r} - \mathbf{r}'|} \, \text{d}S \, \text{d}S' \tag{4}$$

where $\mathbf{K}$ represent surface current densities. We assume that these follow Maxwellian distribution across the strip

$$K_\varphi(\rho) = \frac{2I}{w\pi\sqrt{1 - \left(\dfrac{\rho - r_0}{w/2}\right)^2}} \tag{5}$$

and that the currents I_n and I_m are uniform along the ring contour, which is quite reasonable for this perfectly subwavelength ($a/\lambda = 0.0005$) system.

Clearly, such integration is not sufficiently fast for numerous calculations required. Although, in the first approximation, mutual inductance between CLRs can be estimated with the one between linear currents (double linear integration along the equivalent ring contour), for close CLRs this does not give a good precision. However, a trick is that the result of surface integration according to (4) can be approximated with a good precision through an average mutual inductance between two pairs of circular currents [34]. This way, each flat ring can be represented by a pair of coaxial circular currents of radii $r_0 \pm \gamma w/2$ and the sought value is calculated as an average between the four corresponding mutual inductances

$$M_{nm} = (L_{nm}^{++} + L_{nm}^{--} + L_{nm}^{+-} + L_{nm}^{-+})/4 \tag{6}$$

which essentially decreases calculation time. The value of particular parameter γ depends on the ring geometry, but does not depend remarkably on the relative orientation and distance between the CLRs (within the limits of lens structure). For the particular parameters considered here, $\gamma \simeq 0.7$ was numerically found to give a good match to the precise integration (4) (while $\gamma = 1$ would correspond to the edges of the strip).

Note that a 'linear' mutual inductance L_{nm} can be routinely obtained by integrating the vector potential of one ring along the other one, while the vector potential can be easily determined through elliptic integrals [33]. Given the fact that the fast pre-defined routines for elliptic functions are available in a number of computational platforms (e.g. Matlab®), the approximation (6) effectively reduces the double surface integration (4) to just four single ones.

For such a lens as described above, having 2196 rings, the matrix $\overline{M}$ contains almost 5 million values and filling those with a direct calculation would be rather time-consuming even with a simplified integration described above. However, obvious reciprocity ($M_{nm} = M_{mn}$) and symmetry properties of the lens allow for a great simplification of matrix filling. Indeed, the lens is symmetric with respect to X, Y and Z axes as well as to XY, YZ and ZX planes. This implies, in particular, that the mutual inductances between X-rings and Y-rings are all the same as between Z-rings and Y-rings. Furthermore, as all the rings are identical, inductance between them is only determined by their mutual orientation and spatial offsets Δx, Δy and Δz (see Fig. 3) and for parallel rings even Δx is equivalent to Δy. Explicitly, integration for the mutual inductances between the parallel rings is performed according to

$$L^{\mathrm{P}}(\Delta b, \Delta z) = \int_0^{2\pi} A_\varphi \frac{r_2(r_2 + \Delta b \cos \alpha)}{\Delta \rho} \, \mathrm{d}\alpha$$

$$\Delta \rho = \sqrt{r_2^2 + (\Delta b)^2 + 2r_2 \Delta b \cos \alpha} \qquad (7)$$

$$\varkappa^2 = \frac{4 r_1 \Delta \rho}{(\Delta \rho + r_1)^2 + (\Delta z)^2}$$

with $\Delta b = \sqrt{(\Delta x)^2 + (\Delta y)^2}$ and for the rings with orthogonal mutual orientation

$$L^{\mathrm{O}}(\Delta x, \Delta y, \Delta z) = \int_0^{2\pi} A_\varphi \frac{r_2 \Delta y \cos \alpha}{\Delta \rho} \, \mathrm{d}\alpha$$

$$\Delta \rho = \sqrt{(\Delta x - r_2 \sin \alpha)^2 + (\Delta y)^2} \qquad (8)$$

$$\varkappa^2 = \frac{4 r_1 \Delta \rho}{(\Delta \rho + r_1)^2 + (\Delta z - r_2 \cos \alpha)^2}$$
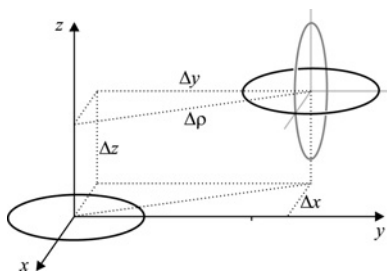

Figure 3 *Geometry of the linear currents for parallel or orthogonal ring orientations, as relevant for mutual inductance calculations*

In both the integrals, the only component of the vector potential is calculated as

$$A_\varphi = \frac{\mu_0}{4\pi} \sqrt{\frac{r_1}{\Delta \rho}} \left(\frac{(2 - \varkappa^2)\mathcal{K}(\varkappa) - 2\mathcal{E}(\varkappa)}{\varkappa} \right)$$

where the corresponding $\varkappa$ (as shown within either of equations) also serves as the argument of complete elliptic integrals of first and second kind, $\mathcal{K}$ and $\mathcal{E}$ [33]. Note that, in the above equations, we imply a general case that the radii of the two rings (r_1 and r_2) can be different.

Thus, a number of ring pairs within the lens share the same value of mutual inductance, so it is only necessary to calculate a full set of non-equivalent mutuals [27] and then assign those values depending on the mutual offsets. With the particular lens considered here, there are only 1924 independent inductances for the parallel ring orientation and 1668 for the orthogonal one, so the total number of calculations with (6) amounts to 3592, which is orders of magnitude smaller than the number of matrix elements. This way, filling the entire matrix is a matter of seconds on a conventional personal computer.

Another preliminary step is to determine the external flux $\mathbf{\Phi}^{\mathrm{ext}}$ imposed to each ring by a given source. For a homogeneous field or a plane wave excitation, calculation is straightforward with the known coordinates of each ring: $\Phi_n^{\mathrm{ext}} = \pi r_0^2 (\mathbf{B}_n \cdot \mathbf{n})$, where $\mathbf{n}$ is a ring normal while magnetic field $\mathbf{B}_n$ can be evaluated at the ring centre as the field variation across the ring is negligible.

In practice, the lens is typically used along with excitation/measuring coils employed in MRI practice. In that case, instead of calculating the field produced by a coil over each ring (which has an extra complication as this field is not even uniform across each ring), it is much easier to obtain the flux directly $\Phi_n^{\mathrm{ext}} = M_n^{\mathrm{c}} I^{\mathrm{c}}$ in terms of mutual inductance M_n^{c} between the coil and each ring, which can be calculated with the same method as the one between the rings, only that the distances and ring radii are different in (7) and (8). Then, the total current I^{c} in the coil (induced in the coil by the external voltage source as well as by the lens) can be encompassed by the entire vector of currents $\mathbf{I}$ as $I_{N+1} \equiv I^{\mathrm{c}}$. Imposing a given voltage V_{c} to the coil with the self-impedance Z_{c}, we can thus include the coil mutual impedances into system (3), modified as

$$\bar{Z} \cdot \mathbf{I} = \mathbf{V} \qquad (9)$$

$$Z_{nn} = \begin{cases} Z_0 \\ Z_{\mathrm{c}} \end{cases} \quad Z_{nm} = \begin{cases} \mathrm{j}\omega M_{nm}, & \text{for} \quad 1 \le n \le N \\ \mathrm{j}\omega M_n^{\mathrm{c}}, & \text{for} \quad n = N + 1 \end{cases}$$

with $V_n = V_{\mathrm{c}} \delta_{n,N}$. Clearly, additional coils, if necessary, can be included by extending the system in an analogous way. Matrix equations in this form are typically used in the analysis of magnetoinductive waves in finite arrays [27–31].

After the above procedures, it is finally possible to solve the systems (3) or (9) obtaining currents I_n in each ring for any given excitation. With these known, it is further possible to calculate any desired response of the lens, such as magnetic field produced by the lens (using standard Biot–Savart expressions) or impedance as measured by the MRI coil (see below).

4 Results and discussion

Armed with the above precise method, we can have a detailed look into lens features and its response to external field sources. In the previous work [26], it was concluded that the accurate model, developed for a 2D-infinite slab with the same structure and thickness as the real lens, is capable of predicting the observations made in connection to lens use in MRI practice. In a typical setup, a coil of 3 inch in diameter is placed parallel to the lens interface at the source plane, $Y = -3$ cm (that is, at a distance 1.5 cm from the lens surface − equal to one half of the lens thickness). The super-lens behaviour implies that the magnetic field produced by the coil, is then reproduced in the space behind the image plane ($Y = 3$ cm), as if the coil itself were present in place of the image.

A straightforward example to test the discrete model and to compare it with practice as well as with earlier models, is to evaluate the impedance as measured by a coil in front of the lens, depending on frequency. With the discrete model, it is easily calculated as

$$Z^{coil} = \sum_{n=1}^{N} j\omega M_n^c \frac{I_n}{I^c} \qquad (10)$$

while with the continuous model it can be obtained from numerical simulations with a homogeneous slab having an appropriate effective permeability (of [25]), as

$$Z^{coil} = -\frac{1}{I^c} \text{Re} \int_{coil} \mathbf{E}^r \cdot \mathbf{dl}^c \qquad (11)$$

where $\mathbf{E}^r$ is electric field reflected by the lens. The two modelling results are compared in Fig. 4 along with the experimental data. Although there is no exact quantitative matching to the measured data, it is clear that the frequency dependence provided by the discrete model is much closer to experiment than that of the continuous calculation. The latter only provides a qualitative picture, predicting an overall course of the impedance frequency dependence.

With both the continuous model [26] and the model described above, it is easy to obtain the axial magnetic field H_Y behind the lens for a given excitation. Comparison between the predictions of the two models is shown in Fig. 5. One can see that at distances smaller than about one lattice constant ($a = 1.5$ cm), H_Y is essentially
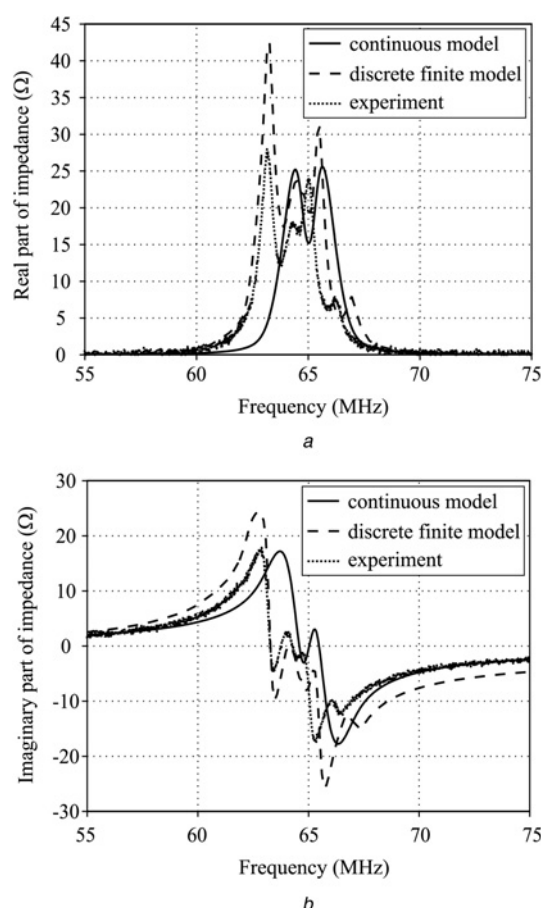

Figure 4 *Frequency dependence of the impedance measured by a 3 inch coil placed at the 'source' plane (1.5 cm from the lens surface)*
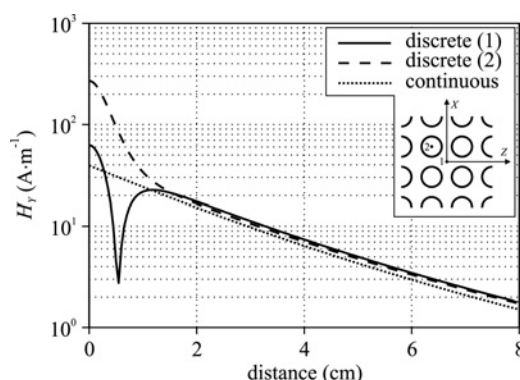
a Imaginary part
b Real part

Figure 5 *Axial component H_Y of the total magnetic field observed behind the lens surface along the lens axis (1) or along the parallel line (2) slightly displaced in X- and Z- directions so that it passes through the centre of one ring (see the inset for the labels of the axes)*

Comparison between the two models for the lens excited by 3 inch coil, centred with respect to the lens axis and placed at 1.5 cm from the lens surface

inhomogeneous as the near field of the individual rings dominates, so that the total field is quite different whether traced along the lens axis (which passes between the rings) or along a line that passes through a ring centre, while both are remarkably different from the continuous model. This is an obvious consequence of the discrete structure, which cannot be revealed by a homogenised model but is apparent in practice [30]. At distances larger than approximately one lattice constant (1.5 cm), the field observed along the two axes converge and are qualitatively similar to the continuous model with a fair numerical agreement (see Fig. 5).

Further comparison can be made by looking at the axial magnetic field patterns at various $X-Z$ planes as shown in Fig. 6. It can be clearly seen that close to the lens (5 mm) the field calculated with the discrete model is locally inhomogeneous so that even the individual rings can be distinguished in the field pattern. Clearly, the field as predicted by the continuous model is quite different

(compare (*a*) and (*d*) plots in Fig. 6). At larger distances, the field calculated through the discrete model becomes reasonably smooth and can be favourably compared to the continuous model calculation, although certain extra features presumably imposed by the square shape of the lens lattice as well as of lens itself, are visible (compare (*b*) to (*e*) and (*c*) to (*f*) plots in Fig. 6). The key discrepancy between the continuous and discrete models here is that the circular area corresponding to the minimum of axial field at the 'image' of the coil, quite apparent in (*b*) plot, is hardly traceable in the (*e*) counterpart. On the other hand, comparison between (*c*) and (*f*) patterns suggests that the agreement between the discrete and continuous models is improved at larger distances, which is reasonable to expect.

One can also check how the imaging properties of the system change when the exciting coil is moved away from the ideal source plane (Fig. 7). These results suggest, analogously, that as the excitation becomes more remote
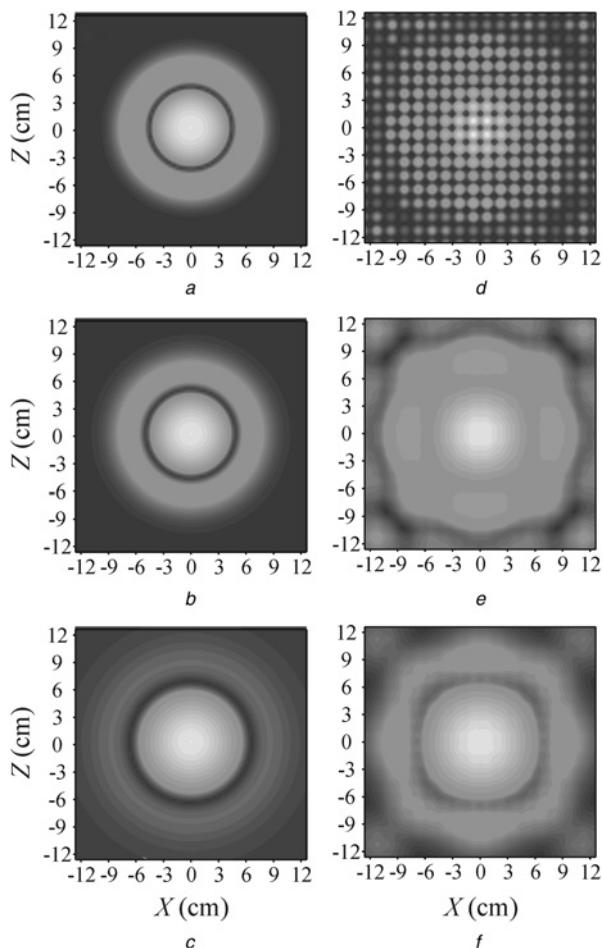

Figure 6 *Patterns of the axial magnetic field (H_Y) observed in $X-Z$ planes at various distances from the lens surface*

a and *b* 0.5 cm
c and *d* 1.5 cm
e and *f* 4.5 cm
Comparison between the continuous *a, c, e* and discrete *b, d, f* models for the lens excited by 3 inch coil, centred with respect to the lens axis and placed at 1.5 cm from the lens surface
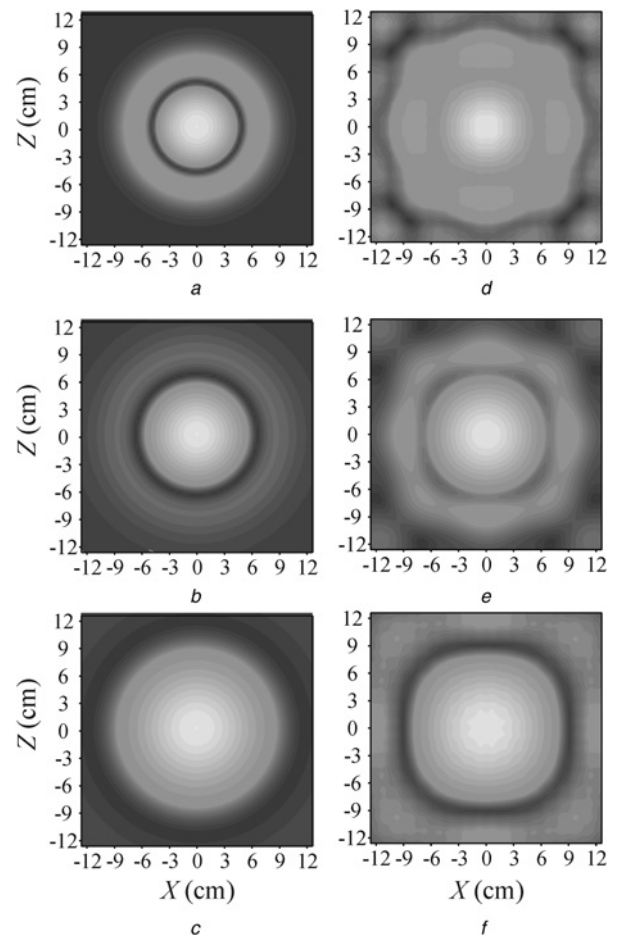
Figure 7 *Patterns of the axial magnetic field in the $X-Z$ plane fixed at 1.5 cm behind the lens, when the 3 inch coil is placed at various distances from the lens surface*

a and *b* 1.5 cm
c and *d* 4.5 cm
e and *f* 9.0 cm
Comparison between the continuous *a, c, e* and discrete *b, d, f* models

from the discrete structure, the field patterns as obtained by the two models, tend to agree better. At the same time, these field patterns support an idea that the lens produces an image of the field pattern available at the source plane: the patterns show the same trend as the field of an isolated coil observed at increasing distances (not shown). However, if the distance from the coil to the lens is comparable to the transverse size of the lens, influence of the overall rectangular shape is noticeable with the discrete model (Fig. 7f).

Evidently, a lens cannot resolve any details of the source field which are of the order of lattice constant in size. In attempt to identify the actual limitation, we test the magnetic field distributions originating from using the coils of various small radii (Fig. 8). For this series of calculations, we assume the lens with a ten times lower resistance of the CLRs, in order to reduce the impact on the resolution imposed by the losses [2]. For excitations with a coil of the ring size (r_0), the entire lens is dominated by strong excitations and the field pattern does not suggest any hints for resolving the source (Fig. 8a). Indeed, practically the same field pattern is observed with a three times larger coil, two lattice constants in diameter (Fig. 8b). With a still larger coil, encompassing four lattice constants, one may argue that the pattern starts to clarify (Fig. 8c), although still it cannot be reliably used to assess the source
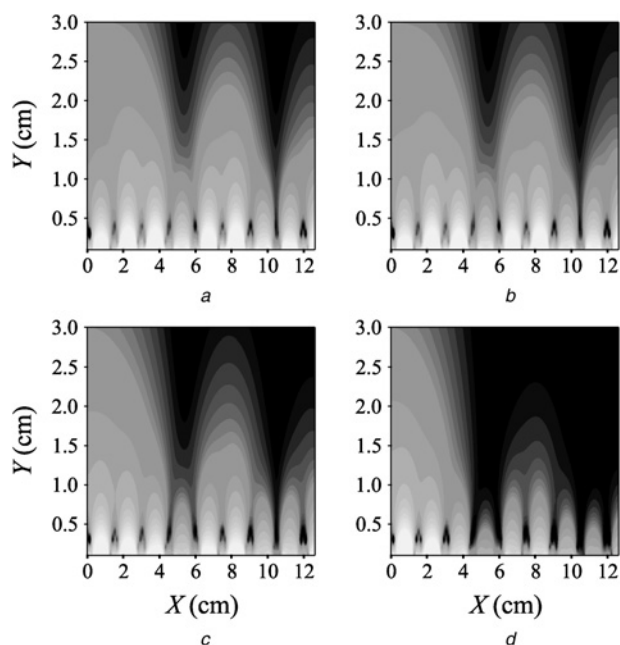
location and size. A reasonable picture is obtained for a 4.5 cm coil radius, where the field farther than the image plane looks as expected with super-lens performance (Fig. 8d). We can therefore make a preliminary conclusion that spatial resolution of the discrete lens can be assumed to be of the order of 5 lattice constants. This observation is in good agreement with the general concerns regarding the lattice effects in metamaterials [24].

With the above examples, we clearly demonstrate that the discrete modelling is suitable for a reliable description of the metamaterial lens and makes it possible to predict specific observations, which might be missed by a continuous model. At the same time, we should note that the question of the discrete lens resolution is not trivial, and further careful analysis is required to address this question in a satisfactory manner. This is the subject of our ongoing research.

5   Acknowledgments

6   References

Figure 8 *Axial component H_Y of the magnetic field observed behind the lens surface*

Horizontal axis corresponds to the lens surface (parallel to X–Z plane), whereas the vertical one is normal to the lens (Y). Only one half of the symmetrical field spatial distribution is presented. Excitation with coils of different radii (0.5, 1.5, 3 and 4.5 cm), centred with respect to the lens axis and positioned at 1.5 cm from the lens surface

[1]   SOLYMAR L., SHAMONINA E.: 'Waves in metamaterials' (Oxford University Press, 2009)

[2]   MARQUÉS R., MARTÍN F., SOROLLA M.: 'Metamaterials with negative parameters' (Wiley, 2008)

[3]   LAPINE M., TRETYAKOV S.: 'Contemporary notes on metamaterials', *IET Microw. Antennas Propag.*, 2007, **1**, pp. 3–11

[4]   SIHVOLA A.: 'Metamaterials in electromagnetics', *Metamaterials*, 2007, **1**, pp. 2–11

[5]   PENDRY J.B.: 'Negative refraction makes a perfect lens', *Phys. Rev. Lett.*, 2000, **85**, pp. 3966–3969

[6]   SHAMONINA E., KALININ V.A., RINGHOFER K.H., SOLYMAR L.: 'Imaging, compression and Poynting vector streamlines for negative permittivity materials', *Electron. Lett*, 2001, **37**, (20), pp. 1243–1244

[7]   MASLOVSKI S., TRETYAKOV S., ALITALO P.: 'Near-field enhancement and imaging in double planar polariton-resonant structures', *J. Appl. Phys.*, 2004, **96**, (3), pp. 1293–1300

[8] MESA F., FREIRE M.J., MARQUÉS R., BAENA J.D.: 'Three-dimensional superresolution in metamaterial slab lenses: experiment and theory', *Phys. Rev. B*, 2005, **72**, article id 235117

[9] FREIRE M.J., MARQUÉS R.: 'Planar magnetoinductive lens for three-dimensional subwavelength imaging', *Appl. Phys. Lett.*, 2005, **86**, article id 182505

[10] FREIRE M.J., MARQUÉS R., JELINEK L.: 'Experimental demonstration of a $\mu = -1$ metamaterial lens for magnetic resonance imaging', *Appl. Phys. Lett.*, 2008, **93**, article id 231108

[11] GRBIC A., ELEFTHERIADES G.V.: 'An isotropic three-dimensional negative-refractive-index transmission-line metamaterial', *J. Appl. Phys.*, 2005, **98**, article id 043106

[12] ALITALO P., TRETYAKOV S.: 'Subwavelength resolution with three-dimensional isotropic transmission-line lenses', *Metamaterials*, 2007, **1**, pp. 81–88

[13] SOLYMAR L., ZHUROMSKYY O., SYDORUK O., SHAMONINA E., YOUNG I.R., SYMS R.R.A.: 'Rotational resonance of magnetoinductive waves: basic concept and application to nuclear magnetic resonance', *J. Appl. Phys.*, 2006, **99**, article id 123908

[14] SYMS R.R.A., SOLYMAR L., YOUNG I.R.: 'Three-frequency parametric amplification in magneto-inductive ring resonators', *Metamaterials*, 2007, **2**, pp. 122–134

[15] SYMS R.R.A., YOUNG I.R., SOLYMAR L.: 'Flexible magnetoinductive ring resonators: design for invariant nearest neighbour coupling', *Metamaterials*, 2010, **4**, pp. 1–14

[16] WILTSHIRE M.C.K., HAJNAL J.V., PENDRY J.B., EDWARDS D.J., STEVENS C.J.: 'Metamaterial endoscope for magnetic field transfer: near field imaging with magnetic wires', *Opt. Express*, 2003, **11**, pp. 709–715

[17] IKONEN P., BELOV P.A., SIMOVSKI C.R., MASLOVSKI S.I.: 'Experimental demonstration of subwavelength field channeling at microwave frequencies using a capacitively loaded wire medium', *Phys. Rev. B*, 2006, **73**, article id 073102

[18] RADU X., GARRAY D., CRAEYE C.: 'Toward a wire medium endoscope for MRI imaging', *Metamaterials*, 2009, **3**, pp. 90–99

[19] FREIRE M.J., JELINEK L., MARQUES R., LAPINE M.: 'On the applications of $\mu = -1$ metamaterial lenses for magnetic resonance imaging', *J. Magn. Reson.*, 2010, **203**, pp. 81–90

[20] AGRANOVICH V.M., GARTSTEIN YU.N.: 'Electrodynamics of metamaterials and the Landau–Lifshitz approach to the magnetic permeability', *Metamaterials*, 2009, **3**, pp. 1–9

[21] SIMOVSKI C.: 'Analytical modelling of double-negative composites', *Metamaterials*, 2008, **2**, pp. 169–185

[22] SILVEIRINHA M.G., BAENA J.D., JELINEK L., MARQUÉS R.: 'Nonlocal homogenization of an array of cubic particles made of resonant rings', *Metamaterials*, 2009, **3**, pp. 115–128

[23] SILVEIRINHA M.G.: 'Metamaterial homogenization approach with application to the characterization of microstructured composites with negative parameters', *Phys. Rev. B*, 2007, **75**, article id 115104

[24] GORKUNOV M., LAPINE M., SHAMONINA E., RINGHOFER K.H.: 'Effective magnetic properties of a composite material with circular conductive elements', *Eur. Phys. J. B*, 2002, **28**, pp. 263–269

[25] BAENA J.D., JELINEK L., MARQUÉS R., SILVEIRINHA M.: 'Unified homogenization theory for magnetoinductive and electromagnetic waves in split-ring metamaterials', *Phys. Rev. A*, 2008, **78**, article id 013842

[26] JELINEK L., MARQUÉS R., FREIRE M.J.: 'Accurate modelling of split ring metamaterial lenses for magnetic resonance imaging applications', *J. Appl. Phys.*, 2009, **105**, article id 024907

[27] SHAMONINA E., KALININ V.A., RINGHOFER K.H., SOLYMAR L.: 'Magnetoinductive waves in one, two, and three dimensions', *J. Appl. Phys.*, 2002, **92**, pp. 6252–6261

[28] WILTSHIRE M.C.K., SHAMONINA E., YOUNG I.R., SOLYMAR L.: 'Experimental and theoretical study of magneto-inductive waves supported by one-dimensional arrays of "Swiss rolls",' *J. Appl. Phys.*, 2004, **95**, pp. 4488–4493

[29] ZHUROMSKYY O., SHAMONINA E., SOLYMAR L.: '2D metamaterials with hexagonal structure: spatial resonances and near field imaging', *Opt. Express*, 2005, **13**, pp. 9299–9309

[30] SYDORUK O., SHAMONIN M., RADKOVSKAYA A., *ET AL*.: 'Mechanism of subwavelength imaging with bilayered magnetic metamaterials: theory and experiment', *J. Appl. Phys.*, 2007, **101**, article id 073903

[31] ZHUROMSKYY O., SYDORUK O., SHAMONINA E., SOLYMAR L.: 'Slow waves on magnetic metamaterials and on chains of plasmonic nanoparticles: driven solutions in the presence of retardation', *J. Appl. Phys.*, 2009, **106**, article id 104908

[32] SYDORUK O., SHAMONINA E., SOLYMAR L.: 'Tailoring of the subwavelength focus', *MOTL*, 2007, **49**, pp. 2228–2231

[33] LANDAU L.D., LIFSCHITZ E.M.: 'Electrodynamics of continuous media' (Pergamon Press, Oxford, 1984)

[34] ROSA E.B., GROVER F.W.: 'Formulas and tables for the calculation of mutual and self induction', *Bull. Bureau Stand.*, 1916, **8**, (I), (Washington, 1948)

Appendix 16

This appendix contains a full text of Ref. [49]

Realistic metamaterial lenses: Limitations imposed by discrete structure

M. Lapine,[1] L. Jelinek,[2] M. J. Freire,[1] and R. Marqués[1]

[1]*Department of Electronics and Electromagnetism, Faculty of Physics, University of Seville, 41012 Seville, Spain*
[2]*Department of Electromagnetic Field, Czech Technical University in Prague, 16627 Prague, Czech Republic*

We study the peculiarities of a metamaterial "superlens," caused by its discrete structure and finite size. We show that precise modeling of the lens provides remarkable distinctions from continuous medium approximation. In particular, we address the problem of highest resolution that can be achieved with a realistic electrically thin metamaterial lens. We conclude that discrete structure imposes essential limitations on the resolution and that the resolution cannot be improved by decreasing dissipation in the system. Further implications related to effective medium description of discrete structures are discussed.

I. INTRODUCTION

Metamaterials attract heaps of research attention for the last 10 years.[1,2] Although there is no consensus on the very definition of metamaterials,[3,4] the number of publications rises exponentially and ever new directions are proclaimed promising. A major flow of work and speculations is related to the idea of super-resolution with the so-called "perfect lens,"[5] which is perhaps among the few key triggers[6] of the research outburst. While it was soon apparent that the perfect lens is not so perfect,[7–9] the overall idea appeared to be fruitful enough to be developed up to a level of applications. In particular, metamaterials based on split-ring resonators were put forward for various superlenses.[10,11]

Practical solutions are so far available at microwave and radio frequencies, with the key goal to aid at magnetic resonance imaging (MRI). A metamaterial superlens suggested[11] for MRI applications employs an idea of imaging with a sufficiently subwavelength slab having negative permeability or permittivity.[5] This must be distinguished from another approach, based on a multiple point-to-point channelling (canalization), as can be achieved with wires[12] or "Swiss rolls,"[13] although such method is also applicable for MRI.[13,14] With the split rings, on the other hand, other MRI enhancements are possible, being, for example, the eased detection with flexible ring resonators,[15] or parametric amplification of MRI signals.[16]

While the latter practical devices allow for a precise and exact theoretical description (in terms of accounting for their structure and all the few elements explicitly), larger metamaterials are normally analyzed with the help of effective medium modeling,[17,18] so that split-ring structures can be described with effective permeability.[19–21] Since for a thin lens (comprising just a few structural units in one direction) the effective permeability approach is not directly applicable, a specific continuous slab model was developed[22] which could be used to calculate transmission/reflection properties with the only approximation that the lens is assumed homogeneous and infinite in transverse directions. Although the latter model was quite efficient to predict the overall performance of the lens,[22,23] it was soon noticed[24] that some of the lens properties can differ remarkably whether evaluated with a continuous medium approximation, or assessed experimen-

tally. In order to achieve better accuracy in theoretical description, we should follow an explicit approach (see, e.g., Ref. 25) which takes into account interaction between all the elements in a finite structure. Preliminary comparison[24] revealed that the predictions of the discrete model are quite close to the experimental findings while deviate sometimes from the continuous model approximation.

The aim of this paper is to analyze in detail what is the consequence of the discrete structure of the lens and its finite size; how this affects the general lens properties, such as imaging frequency, transmission between the MRI coils, etc.; and how the continuous model can be modified in order to describe some of such features.

II. SETUP OF THE PROBLEM

Geometry of the problem and the corresponding discrete modeling approach were described in great detail in a previous publication.[24] Here we only repeat the most general information as long as necessary for discussing the results.

The isotropic metamaterial lens proposed in Ref. 11 is composed of capacitively loaded rings (CLRs) periodically arranged in an isotropic three-dimensional lattice with the lattice constant $a=1.5$ cm. The lens has three planes of 18 by 18 CLRs interlayered with orthogonal segments providing two (mutually orthogonal) sets of two layers 17 by 18 CLRs each, which makes it up to roughly 2200 CLRs. Overall dimensions of the lens are thus $18 \times 18 \times 2$ lattice constants, although it must be noted that "unit cells" are incomplete at the edges of the structure and that there are neither two nor three unit cells across the lens.

The CLRs have the mean radius $r_0=0.49$ cm $(2r_0/a =0.66)$ and are loaded with lumped nonmagnetic capacitors so that the frequency of resonance in free space equals to 63.28 MHz $(k_0a=0.02)$. The total resistance has been estimated as $R=0.0465$ Ohm (obtained indirectly by measurements of the quality factor of the resonator).

We define a Cartesian coordinate system (x,y,z) so that the lens geometrical center is placed at the coordinate origin; the y axis is perpendicular to the lens as slab (lens axis) while the long edges of the lens are parallel to x and z axes (Fig. 1). The lens is thus completely symmetric with respect to the coordinate origin, all the axes and all the coordinate
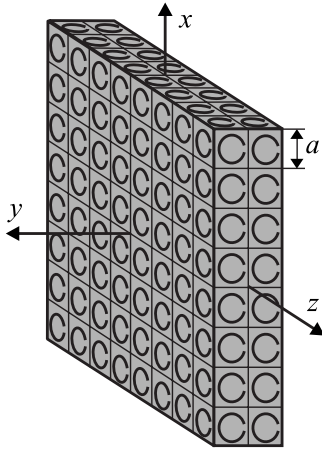
FIG. 1. Scheme of the lens with the corresponding coordinate system. Note that the actual number of elements along x and z directions is not reflected in this sketch.

planes (we neglect minor asymmetry occurring in the real lens caused by specific assembly details such as resulting from substrate thickness; these deviations are of the same order as unavoidable production inaccuracy). The so-called input and output surfaces of the lens correspond to $y = \mp 1.5$ cm while the theoretical source and image planes are xz planes at $y = \mp 3.0$ cm.

The discrete analysis of the systems of resonators is well appreciated in literature, particularly in studying magnetoinductive waves in CLR arrays.[25–28] It constitutes in solving the matrix multi-impedance equation

$$\bar{\mathbf{Z}} \cdot \mathbf{I} = -j\omega \boldsymbol{\Phi}^{\text{ext}} \tag{1}$$

with $Z_{nn}=Z_0$ and $Z_{nm}=j\omega M_{nm}$. The self-impedance $Z_0=R+j\omega L+1/(j\omega C)$ is determined by the resistance R, self-inductance L and self-capacitance C of a single CLR. Here, $\boldsymbol{\Phi}^{\text{ext}}$ represents the total *external* magnetic flux through the corresponding ring while the mutual interaction between all the rings is expressed in terms of mutual inductances M_{nm}. Solving the system (1) for currents with a given distribution of external sources of magnetic field provides the complete description of the lens, as all the interesting characteristics, such as impedance measured by the coil, spatial distribution of the magnetic field produced by the lens, can be calculated as soon as all the currents I_n are known. Further specific details of such analysis applied to a large lens are given in.[24]

III. RESULTS AND DISCUSSION

A. Imaging frequency

Within the continuous medium approach, it is well known[2] that the best imaging with a slab having negative effective permeability occurs at a frequency where $\mu=-1$. For a discrete lens of a finite size, however, the question is less trivial as it is too small to be described with effective parameters.[29] The assessment can be attempted through some indirect characteristics. Continuous modeling approach suggests[2] that at the imaging frequency impedance measured with a sufficiently large coil placed at the source plane has a
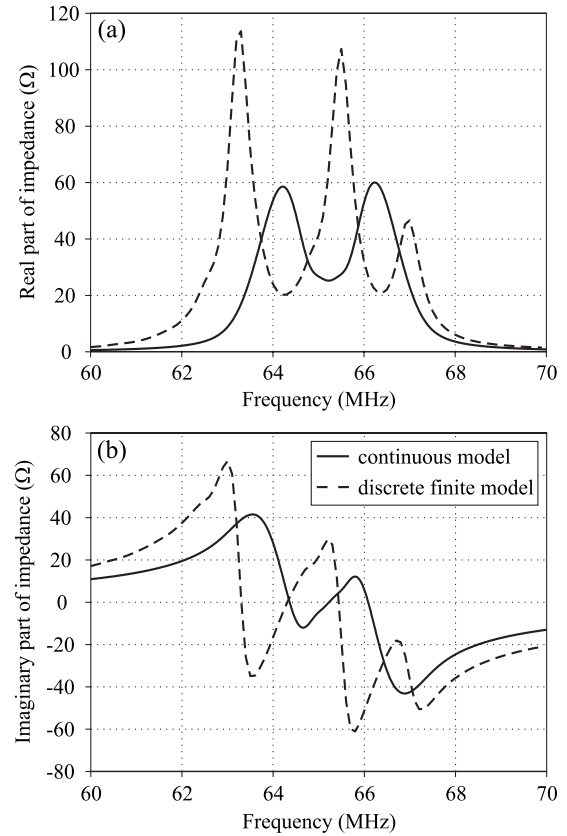

FIG. 2. (a) Real and (b) imaginary parts of impedance for a 5-inch coil placed in the source plane (15 mm from the lens surface): comparison between a slab of continuous medium (solid) and discrete model (dash).

local minimum (between the two peaks) in the real part while the imaginary part is crossing zero (Fig. 2, solid curves). However, discrete model predicts a different pattern (Fig. 2, dash curves), expressing a more complex picture of peaks.

Further complication is that with the discrete model, the impedance frequency dependence is not the same for the coils of different size and also depends on the distance between the coil and the lens. With an increase in the coil size, the frequency dependence of the impedance changes qualitatively (Fig. 3). For small coils, a peak at 63.2 MHz (close to the resonance frequency of the corresponding bulk medium) is dominant in the resistance. For moderate coil sizes ($5a$–$10a$ in diameter), second peak at 65.5 MHz emerges, although the main resonance is still present. For larger coils, this second peak starts to vanish while the third one, at 67 MHz, becomes stronger and for coils larger than $20a$ is clearly dominant.

These observations imply that the lens shows distinct properties caused not only by the discrete structure but also by its finite size. For this reason, it is only possible to use the corresponding criterion for the coils of moderate size: large enough to make an averaging over many unit cells but still sufficiently small not to be affected by the lens size limitations. From Fig. 3, we can conclude that for moderate coil sizes, (first) local minimum of the resistance occurs within 64.0–64.5 MHz, and the zero crossing of the reactance hap-
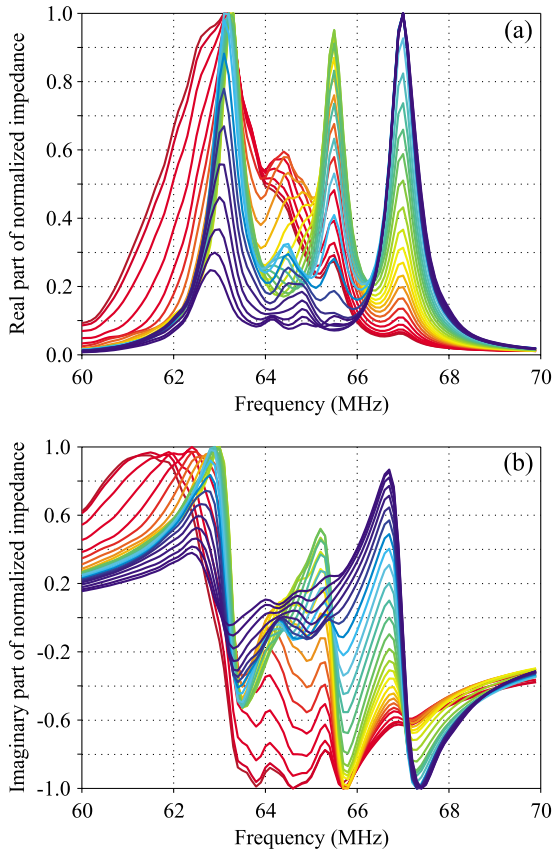
FIG. 3. (Color online) (a) Real and (b) imaginary parts of impedance for coils of different size, placed in the source plane. The color sequence from red to blue (curves upwards at 66.5 MHz) corresponds to the coils from 1 to 13 cm in radius, with a step of 0.5 cm. The data are renormalized to have a unity maximum.
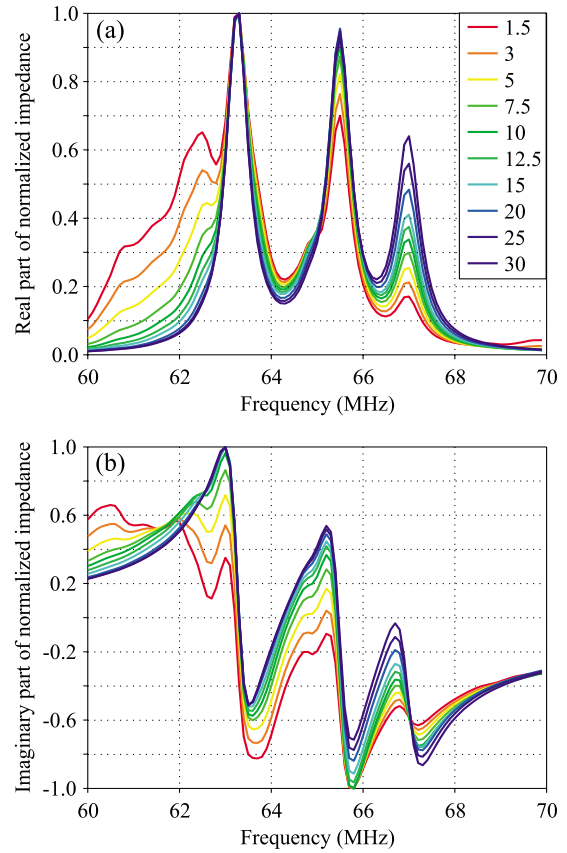

FIG. 4. (Color online) (a) Real and (b) imaginary parts of impedance for a 5-inch coil, placed at various distances from the lens surface (millimeter, shown in the inset). The data are renormalized to have a unity maximum.

pen within the same frequency interval, although we must note that the two characteristic frequencies do not exactly coincide for each particular coil radius.

Similar conclusions can be made by studying the impedance measured by a coil placed at various distances from the lens (Fig. 4). Apart from the case when the coil is too close to the lens surface (when close proximity of some lens rings to the coil apparently has a dominating effect on the pattern of frequency dependence), we can see that characteristic frequencies converge within the interval mentioned above. For this particular coil size (5 inch diameter), the frequency of 64.2–64.4 MHz can be assumed.

Another approach to evaluate the imaging frequency (or, as it is likely, frequency range) lies in the calculation of the transmission between the two identical coils, placed in the source and image planes, respectively.[9] An easy measure of this quantity can be the ratio of the current induced in the receiving coil, to that in the transmitting coil. For a continuous slab at the imaging frequency (not shown), this ratio has a local minimum (equal to unity in a lossless case); naturally, this occurs exactly at the same frequency as the minimum in the resistance measured by the coil, and zero reactance.[22] The imaginary part of the current ratio is zero, as there is no phase shift between the two currents. However, the discrete model reveals different observations. Figure 5 shows the ab-

solute value and imaginary part of this ratio for different coil sizes. Comparing the absolute values of transmission for different coils, we can admit that while the data for small and large coils vary considerably, there is certain uniformity (aggregation of curves at a local minimum around 64 MHz) for intermediate coil sizes, $6a-10a$ in diameter. This local minimum roughly corresponds to the zero crossing of the imaginary part (renormalized to a unity maximum in Fig. 5 for clarity). For the representative coil sizes mentioned above, the frequency of zero crossing varies between 63.5 and 63.7 MHz, and this frequency range can be assumed to be the result of the transmission criterion for imaging. Note that this result differs from the impedance approach.

So far, we were discussing indirect criteria to evaluate the imaging frequency. The necessity to employ such criteria, in spite of the ambiguity discussed above, is driven by the fact that direct observations of the field patterns produced by the lens from various sources, might be equally unclear. Indeed, as the resolution of the lens is still to be determined (see Sec. III B), we cannot be certain about choosing an appropriate geometry to check if an image can be observed at some frequency. For example, the field patterns observed in the imaging plane for various coils were not found to reproduce the source field in detail at any frequency between 60 and 70 MHz while a clear central spot could be observed several times across the frequency sweep, interchanged with more
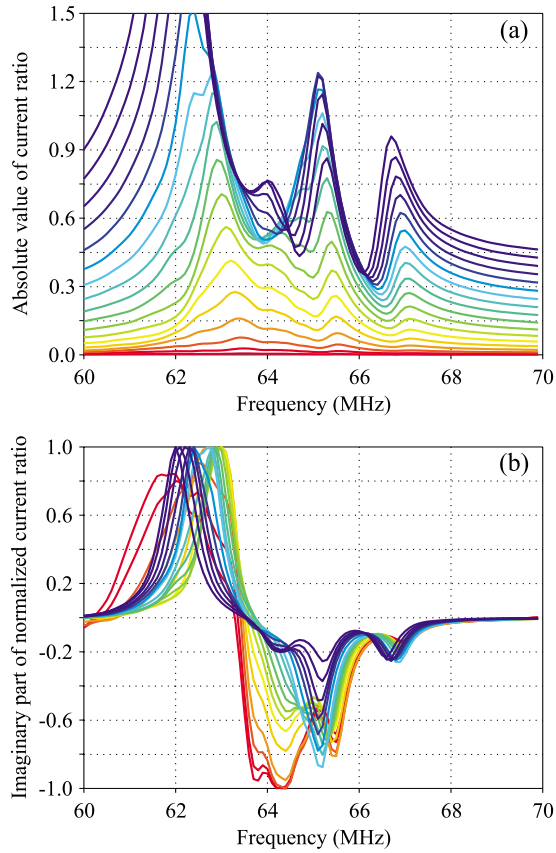
FIG. 5. (Color online) (a) Absolute value and (b) normalized imaginary part of the ratio between the current induced in a coil in the image plane, to the current in the identical coil in the source plane, for coils of different size. The color sequence from red to blue (curves upwards at 64 MHz) corresponds to the coils from 1 to 9.5 cm in radius with a step of 0.5 cm.
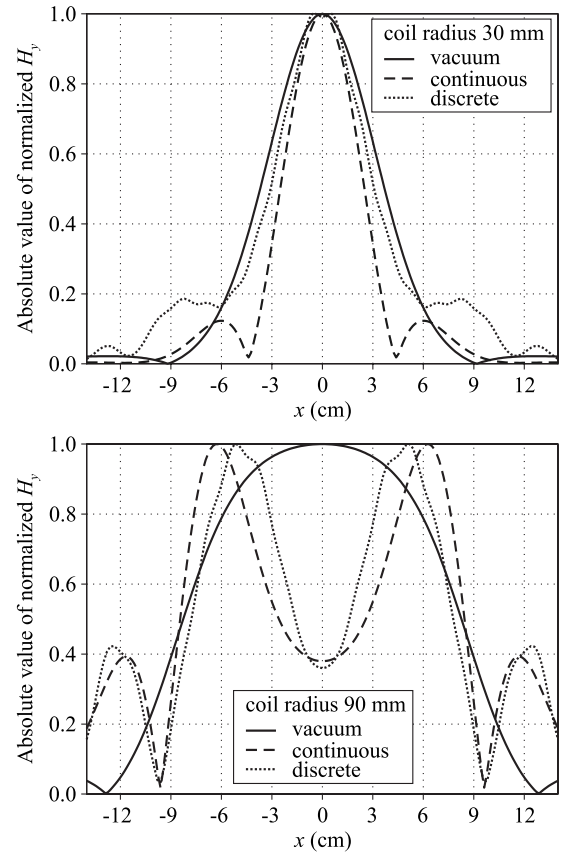

FIG. 6. Spatial profile of the axial component (H_y) of the total magnetic field observed across the image plane ($y=3$ cm, $z=0$) for a small or a large coil placed in the source plane. Comparison between the field obtained with a discrete lens (at 63.6 MHz) with a continuous slab (with $\mu=-1$) and in vacuum.

complex patterns of excitations (data not shown). For the reasons explained in Sec. III B, it appears more reasonable to try an arrangement of two sufficiently distant small sources: two coils of 5 mm radius positioned symmetrically at $7a$ distance. Detailed observation of the changes in the field pattern with frequency, illustrated by an animation[30] made with a 0.1 MHz step in the 60–70 MHz interval, demonstrates that the pattern obtained around 63.6 MHz appears most clear, although we should note that none of the patterns actually correspond to the source field of the small loops. The frequency found this way, is consistent with the criterion based on the transmission between two coils but deviates from the impedance criterion (at 64.0–64.5 MHz, further maxima emerge in the field pattern and overall image is less clear). However, we should note that the frequency difference is minor, so for experimental evaluation both the criteria appear to be fairly suitable.

One may argue that a further discrepancy lies in the fact that, contrary to the continuous model which predicts the imaging frequency to be symmetrically between the two resonances of the slab (Fig. 2, solid curves), the frequency we choose is much closer to the first resonance. This is, however, consistent with the findings of paper,[22] where it was demonstrated that the imaging frequency of the thin slab

is indeed expected to be closer to the first resonance. We therefore should not seek to find imaging phenomena between the second and third peaks of the impedance predicted by discrete model, even though some of the field patterns might look promising.

We should also comment that one further qualitative criterion for a superlens behavior could have been the observation of evanescent field enhancement. However, the field structure inside the lens is strongly nonuniform and cannot show a clear analogy to a field inside a homogeneous slab. At the same time, field analysis in the outer areas faces the same difficulty: there is no unique frequency to be selected with such criterion, as the best visual analogy (field decay from the source and a subsequent decay, from a larger value, on the other side) occurs at different frequencies depending on the coil size and distance to the lens.

All this analysis suggests that, although no direct coincidence between the continuous model and the discrete calculation can be found, the general criteria formulated with the help of continuous model are still applicable. Although we cannot select an exact frequency, ideal for imaging, we can safely speak of a relatively narrow frequency interval—63.5 to 63.7 MHz—where the phenomena, analogous to the imaging with a continuous $\mu=-1$ slab, can be observed with a discrete finite lens. Since the field patterns do not change
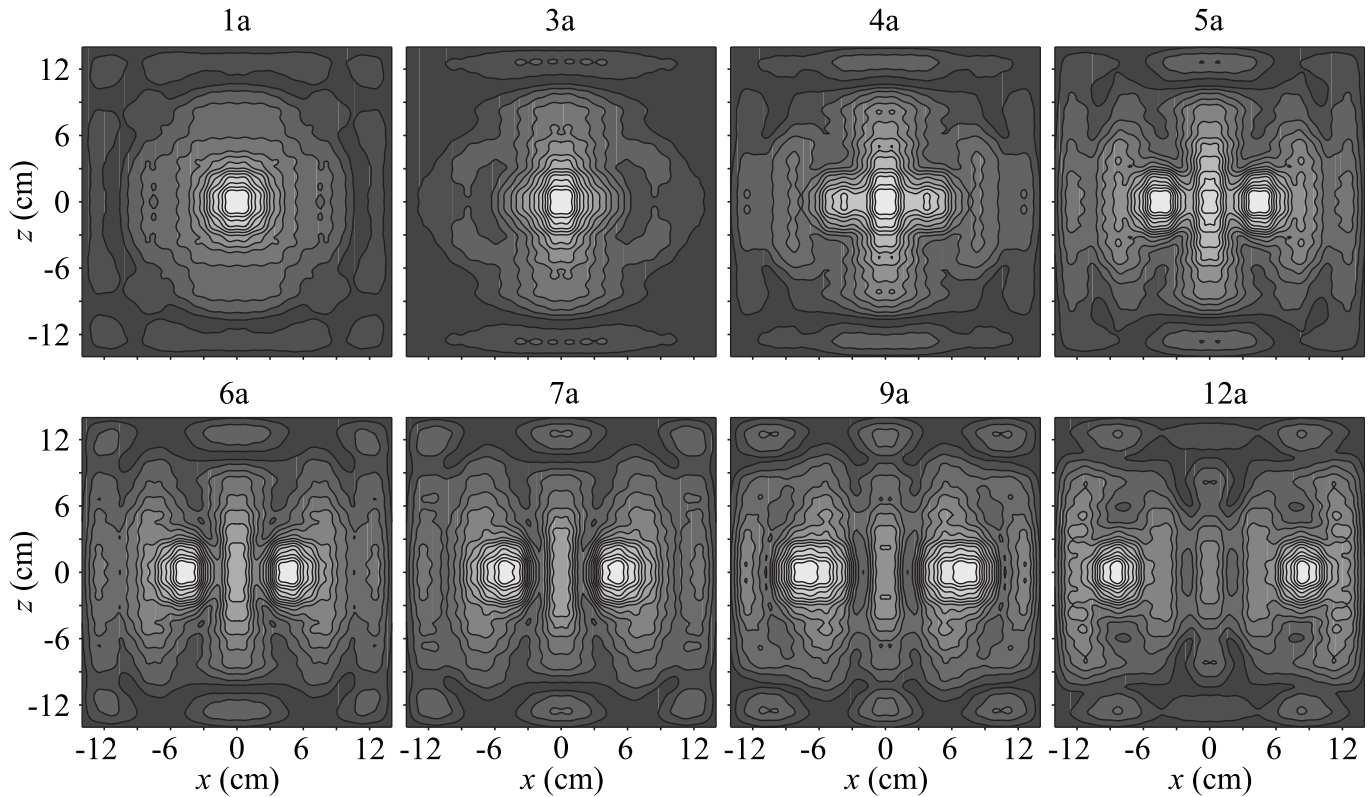
FIG. 7. Axial component (H_y) of the total magnetic field observed at 63.6 MHz in the image plane for the two small sources (coils of 5 mm radius) placed in the source plane at various distances ($1a-12a$) between each other.

remarkably within this frequency range, we have chosen 63.6 MHz in order to convey calculations necessary to evaluate the spatial resolution of the lens, analyzed in the following section.

B. Spatial resolution of the lens

Now that we are confident that the lens behavior corresponding to the imaging phenomena can be reliably studied at frequencies discussed in the previous section, we are able to proceed to the important question of the resolution that can be achieved by the lens. Within the continuous theory, resolution is limited by lens thickness and by dissipation, according to the relation[2]

$$\Delta = \frac{2\pi d}{\ln(2/\delta)}. \tag{2}$$

For the lens under consideration, having loss tangent $\delta=0.2$ and thickness $d=2a$, resolution is thus limited by $5.5a$. This value might be not a good starting point to study the resolution of a discrete structure if we expect it to be of the order of a few lattice constants. Nevertheless, it is interesting to check the behavior of the realistic lens with this respect.

As it was already noticed,[24] magnetic field distributions behind the lens excited by relatively small coils, are visually rather similar regardless of the coil size. Now, we have systematically studied the patterns in the image plane for coils of different radii, and conclude that the field profiles are practically identical for small coils up to 5 cm in radius.

These profiles are characterized by $4.3a$ full-width at half-maximum, so are almost as wide as the coil field in vacuum (in the absence of the lens) for same coils (Fig. 6). For coil radii larger than 6 cm, the profiles obtained with the lens tend to give a clearly better spot size accuracy than in vacuum. On the other hand, even for larger coils the image field remains unresolved in details, demonstrating only a central spot (of appropriate size) but not the source profile. Only with a coil as large as 9 cm radius further features in the profile are visible, which are qualitatively analogous to the source field, as also with the continuous model (Fig. 6). Going to much larger sizes is not appropriate as the size of coil becomes comparable with the lens dimensions, and edge effects are be essential, deteriorating the image (not shown). For checking bigger coils, studying a much larger lens would be necessary, which is numerically challenging but will be probably done in the future.

Clearly, the above observations cannot be considered entirely appropriate for understanding the resolution. More consistent approach to test the resolution limitations is to analyze if the lens can distinguish the two point sources with various spacing. As we know that the field patterns obtained with coils smaller than four lattice constants in diameter are practically identical, we can safely choose a coil with the same radius as the ring inside the lens, as a fair representative of a point source. Placing two such coils at various distances between each other in the source plane provides the field patterns in the image plane as shown in Fig. 7. We can see that indeed coils close enough provide either one central spot or a complex pattern which does not reflect actual loca-
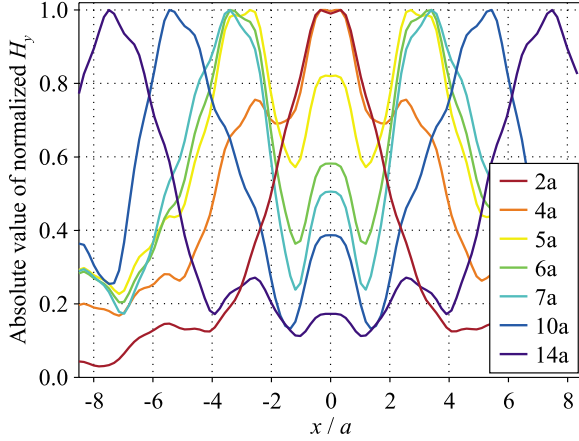
FIG. 8. (Color online) Profiles of the axial component (H_y) of the total magnetic field observed at 63.6 MHz along x axis in the image plane (at $y=3$ cm, $z=0$) for the two sources at various distances between each other. The data are renormalized to have a unity maximum.

tion of the sources unambiguously. With separation of $6a$, the two spots can be distinguished although the "spurious" maximum between them is still strong; for separations larger than $7a$, resolution is apparent, although of course not the size of the spots but only location corresponds to the source geometry. This can be also conveniently seen on a field profile across the line of the source images in the image plane (Fig. 8). Note, though, that the shape of these profiles makes a standard half-maximum criterion for peak separation barely applicable.

In spite of these complications, we can nevertheless conclude that the spatial resolution of the lens is limited by 5–7 lattice constants. This conclusion can be supported with the continuous model. Indeed, if we force certain truncation for the k vectors which can be transmitted by the lens, we can obtain the field patterns for the corresponding resolution. Figure 9 shows the difference between the virtually unrestricted case ($k \leq 300$ m^{-1}, corresponding to $1.5a$ resolution), and the truncated calculation ($k \leq 65$ m^{-1}, which corresponds to a restriction by $6.5a$). The difference is clearly visible: complete separation of the source spots occurs starting from about $4a$ in the first case but only at $6a$ in the second. This test supports indirectly the conclusion on resolution made from field pattern observations.

However, with the theoretical limitation, Eq. (2), being of the same order, one may doubt whether these results reflect the limitations specific for the discrete structure. In order to make a reliable check, it is possible to study an artificial case of lower losses. Because of the logarithmic dependence in Eq. (2), we would need to assume the resistance a few orders of magnitude lower in order to improve dramatically the prediction of continuous model. In general, the overall characteristics of the lens, such as its impedance to the coil or transmission between the coil, remain qualitatively similar, however, the analysis is more complicated as all the resonant features are sharper and extra resonances emerge. We therefore restrict this consideration by assuming a ten times smaller dissipation. The frequency interval given for the imaging phenomena by the impedance criterion, is confined to
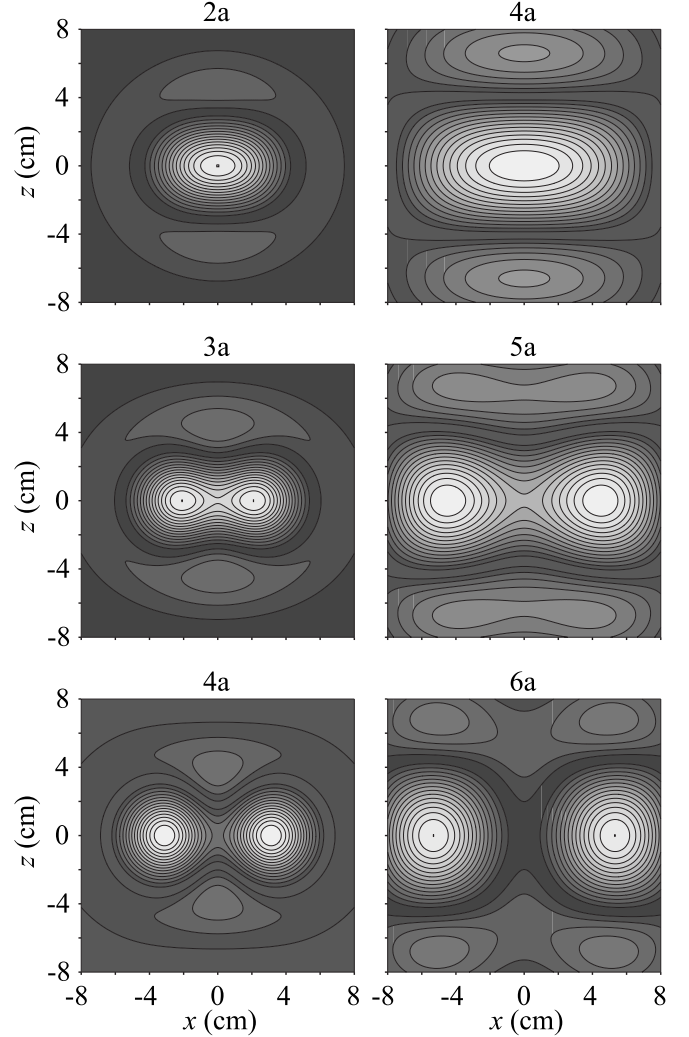

FIG. 9. Assessment of the resolution with a continuous slab model. Axial component (H_y) of the total magnetic field observed in the image plane for the two point sources at various distances between each other (as shown above each image). Spatial harmonics are cut at either 300 m^{-1} (left column) or 65 m^{-1} (right column).

64.0–64.2 MHz while the transmission approach suggests 63.4–63.5 MHz. As to the field patterns in the image plane, further complication is brought by very rapid change in the patterns with frequency and numerous multiple additional maxima observed practically in the whole frequency range. By analyzing the patterns for $6a$ separation between the two small sources, we were able to give preference to the frequency interval of 63.46 to 63.50 MHz, which is once again close to the transmission optimum. We should note, though, that such a favorable interval may appear different for different geometry, and is not very reliable. With this precaution, we performed a resolution check analogous to that of Fig. 7 at a frequency 63.48 MHz. It can be seen (Fig. 10) that although the patterns look much more "noisy" with extra excitations, the two sources can be reasonably distinguished at separations more than $5a$ while at a smaller distance the central spot dominates. As for these losses resolution predicted by Eq. (2) is less than $3a$, we feel confident that the
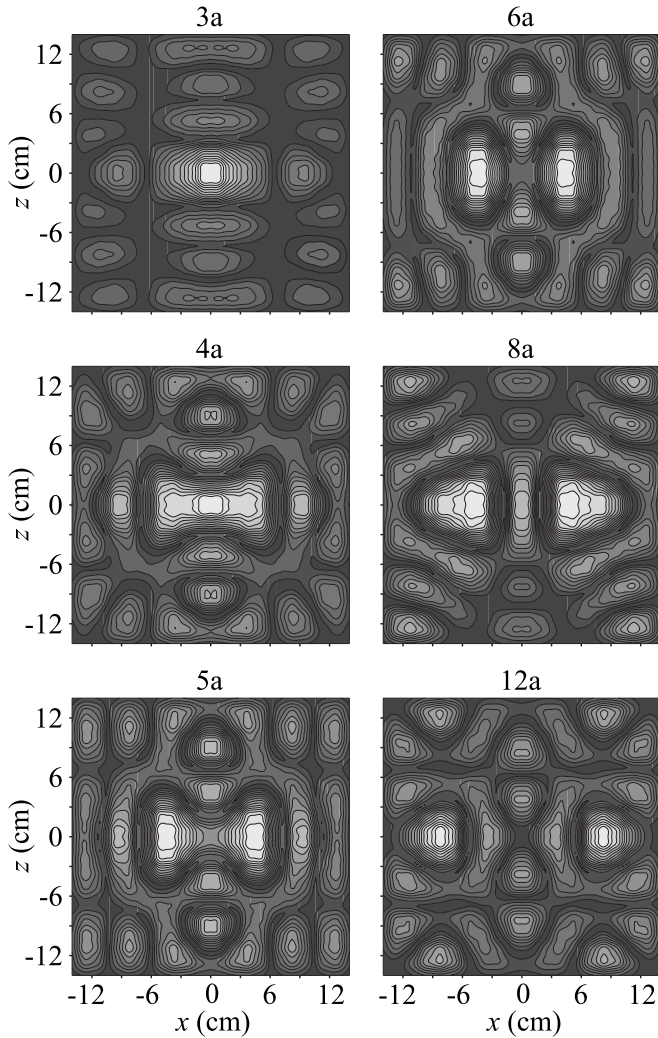
FIG. 10. Axial component (H_y) of the total magnetic field observed (at 63.6 MHz) in the image plane for the two small sources (coils of 5 mm radius) placed in the source plane at various distances between each other. Dissipation in the lens is assumed to be ten times smaller as compared to Fig. 7
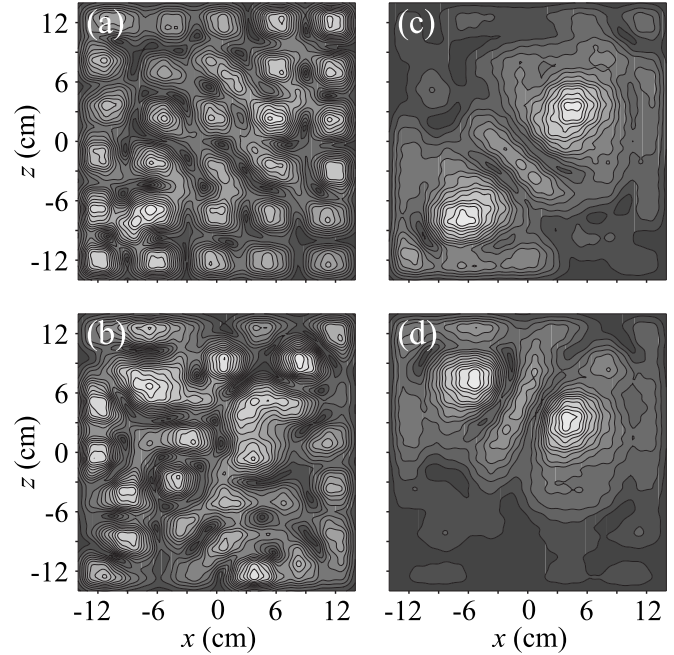

FIG. 11. Axial component (H_y) of the total magnetic field observed (at 63.6 MHz) in the image plane for the two small sources (coils of 5 mm radius) placed nonsymmetrically in the source plane: one source is at $x_1=3a$ and $z_1=2a$ from the lens center, the other one is at either [(a) and (c)] $x_1=-4a$, $z_1=-5a$ (distance approximately $10a$) or [(b) and (d)] $x_1=-4a$, $z_1=5a$ (distance approximately $7.5a$). Comparison between the low-loss case [(a) and (b)] and realistic dissipation [(c) and (d)].

observed limitation should be attributed to the discreteness effect.

On the other hand, with low losses the above patterns of magnetic field are very sensitive to subtle variations in frequency and setup geometry. The additional peaks can be comparable or even exceed the image peaks in magnitude. This is especially remarkable when the coils are placed nonsymmetrically with respect to the lens center (Fig. 11): while with the realistic losses the shifted sources can be well resolved, the patterns at low loss are not comprehensive and could not be improved even by frequency variation. This is a consequence of numerous magnetoinductive excitations (spatial resonances) across the lens structure[25,26] which are favored by low dissipation and relatively small size of the entire lens. This leads to various standing wave patterns which depend on frequency and coil parameters. In other words, a clear analogy to the phenomena, predicted for homogenized media, are not possible here because of the strong spatial dispersion.[17,20,21] For these reasons, we feel that it is

impossible to discuss consistently lens resolution at low losses, as the whole structure does not perform as intended with the original design. Note that the presence of such inhomogeneities is also noticeable for realistic losses (Fig. 7) but in that case they are largely suppressed and do not interfere so significantly with the image patterns.

Nevertheless we can conclude that the spatial resolution is not improved by decreased dissipation and that a reasonable distinction between the small sources is only possible for the same separations as with realistic losses. Therefore, resolution is indeed severely limited by discreteness of the lens and cannot be made better than five lattice constants.

Finally, we should comment that the result which we obtained with regards to resolution, is consistent with the effective medium theory. Indeed, it was shown explicitly for CLR metamaterials that the characteristic length of response formation in the bulk is of the order of few lattice constants.[19] This is also generally expected in condensed matter theory.[31,32] Consequently, it does not make sense to speak of any effective material properties on a smaller scale and any excitations delivered on the level of individual elements are spread out across the corresponding area encompassing numerous unit cells. This makes an important distinction to the channeling approach[12] to imaging: resolution on the level of lattice constant is only possible with an array of weakly interacting elements. When, however, metamaterial is build up as an internally coupled effective medium, the limitations discussed in this paper are unavoidable.

IV. CONCLUSIONS

We have shown that the behavior of a realistic metamaterial lens (which can be practically implemented with a limited number of capacitively loaded resonators), differs significantly from the predictions based on a continuous medium approximation. It turns out that no direct coincidence to the imaging properties of a $\mu = -1$ slab can be obtained with such a practical lens, although analogous phenomena, suitable for imaging applications, are available in a certain frequency range.

We have also assessed the resolution, achievable with a discrete lens and conclude that it is generally limited by 5–7 lattice constants. It is important to emphasize that this limitation is entirely structural and cannot be improved by decreasing losses.

The discussed peculiarities are enforced by discrete structure and finite size of the lens, and are thus in agreement with the restrictions for the classical effective medium theory. At the same time, rich phenomena observed for a practical lens, leave much room for further exploration and can be useful for various applications.

[1] L. Solymar and E. Shamonina, *Waves in Metamaterials* (Oxford University Press, New York, 2009).

[2] R. Marqués, F. Martín, and M. Sorolla, *Metamaterials with Negative Parameters* (Wiley, New York, 2008).

[3] M. Lapine and S. Tretyakov, IET Microwaves, Antennas Propag. **1**, 3 (2007).

[4] A. Sihvola, Metamaterials **1**, 2 (2007).

[5] J. B. Pendry, Phys. Rev. Lett. **85**, 3966 (2000).

[6] E. Shamonina and L. Solymar, Metamaterials **1**, 12 (2007).

[7] E. Shamonina, V. A. Kalinin, K. H. Ringhofer, and L. Solymar, Electron. Lett. **37**, 1243 (2001).

[8] S. Maslovski, S. Tretyakov, and P. Alitalo, J. Appl. Phys. **96**, 1293 (2004).

[9] F. Mesa, M. J. Freire, R. Marqués, and J. D. Baena, Phys. Rev. B **72**, 235117 (2005).

[10] M. J. Freire and R. Marqués, Appl. Phys. Lett. **86**, 182505 (2005).

[11] M. J. Freire, R. Marqués, and L. Jelinek, Appl. Phys. Lett. **93**, 231108 (2008).

[12] P. Ikonen, P. A. Belov, C. R. Simovski, and S. I. Maslovski, Phys. Rev. B **73**, 073102 (2006).

[13] M. C. K. Wiltshire, J. V. Hajnal, J. B. Pendry, D. J. Edwards, and C. J. Stevens, Opt. Express **11**, 709 (2003).

[14] X. Radu, D. Garray, and C. Craeye, Metamaterials **3**, 90 (2009).

[15] R. R. A. Syms, I. R. Young, and L. Solymar, Metamaterials **4**, 1 (2010).

[16] R. R. A. Syms, L. Solymar, and I. R. Young, Metamaterials **2**, 122 (2008).

[17] C. Simovski, Metamaterials **2**, 169 (2008).

[18] M. G. Silveirinha, Phys. Rev. B **75**, 115104 (2007).

[19] M. Gorkunov, M. Lapine, E. Shamonina, and K. H. Ringhofer, Eur. Phys. J. B **28**, 263 (2002).

[20] J. D. Baena, L. Jelinek, R. Marqués, and M. Silveirinha, Phys. Rev. A **78**, 013842 (2008).

[21] M. G. Silveirinha, J. D. Baena, L. Jelinek, and R. Marqués, Metamaterials **3**, 115 (2009).

[22] L. Jelinek, R. Marqués, and M. J. Freire, J. Appl. Phys. **105**, 024907 (2009).

[23] M. J. Freire, L. Jelinek, R. Marques, and M. Lapine, J. Magn. Reson. **203**, 81 (2010).

[24] M. Lapine, L. Jelinek, R. Marqués, and M. J. Freire, IET Microwaves, Antennas Propag. **4**, 1132 (2010).

[25] E. Shamonina, V. A. Kalinin, K. H. Ringhofer, and L. Solymar, J. Appl. Phys. **92**, 6252 (2002).

[26] O. Zhuromskyy, E. Shamonina, and L. Solymar, Opt. Express **13**, 9299 (2005).

[27] O. Sydoruk, M. Shamonin, A. Radkovskaya, O. Zhuromskyy, E. Shamonina, R. Trautner, C. J. Stevens, G. Faulkner, D. J. Edwards, and L. Solymar, J. Appl. Phys. **101**, 073903 (2007).

[28] O. Zhuromskyy, O. Sydoruk, E. Shamonina, and L. Solymar, J. Appl. Phys. **106**, 104908 (2009).

[29] V. M. Agranovich and Yu. N. Gartstein, Metamaterials **3**, 1 (2009).

[30] See supplementary material at http://link.aps.org/supplemental/10.1103/PhysRevB.82.165124 for frequency variation in magnetic field pattern.

[31] M. I. Ryazanov, *Condensed Matter Electrodynamics* (Nauka, Moscow, 1984).

[32] M. V. Gorkunov and M. I. Ryazanov, Sov. Phys. JETP **85**, 97 (1997).

Appendix 17

This appendix contains a full text of Ref. [50]

Isotropic frequency selective surfaces made of cubic resonators

J. D. Baena, L. Jelinek,[a] and R. Marqués
Departamento de Electrónica y Electromagnetismo, Universidad de Sevilla, Sevilla 41012, Spain

J. J. Mock, J. Gollub, and D. R. Smith
Department of Electrical and Computer Engineering, Duke University, North Carolina 27708, USA

Isotropic frequency selective surface (FSS) made of cubic arrangements of split ring resonators (SRRs) is proposed and analyzed. For this purpose, a suitable isotropic modification of the SRR was used in the design of a cubic unit element invariant under the tetrahedral point symmetry group. It was experimentally demonstrated that the transmission through such a FSS is angle and polarization independent. For comparison, another FSS, whose unit elements do not satisfy necessary symmetries, was measured, showing clearly anisotropic behavior. We feel then that symmetries play an important role. Potential device applications are envisioned for antenna technology at microwave and terahertz frequencies. © 2007 American Institute of Physics. [DOI: 10.1063/1.2806915]

Frequency selective surfaces (FSSs) are planar periodic arrays of scatterers exhibiting one or more passbands or stopbands for impinging electromagnetic waves. They are widely used in microwave technology as, for instance, in antenna radomes and reflectors.[1] For the aforementioned applications it is often desirable to have an isotropic transmittance and/or reflectivity of the FSS, which should be independent of both the angle of incidence and the polarization of the impinging wave.[1] Needless to say, this implies that secondary grating lobes should not be generated by the FSS.

Previous implementations of FSSs can generally be classified into two groups. The first group consists of electromagnetic band gap planar structures. In these structures, the distance between the elementary scatterers is of the order of the wavelength, which results in the generation of undesirable secondary grating lobes. The second group of FSSs is based on resonant scatterers individually interacting with the electromagnetic fields. In this case, the distance between scatterers can be made much smaller than the wavelength to prevent the generation of secondary grating lobes. There are many kinds of resonant scatterers useful for FSS design. Resonant electric dipoles, tripoles, and metallic crosses were used in many former FSS designs.[1] However, the behavior of such FSSs presents a strong dependence on the angle of incidence and the polarization of the impinging wave. Annular elements were theoretically studied in Ref. 2 and are widely used[3,4] for microwave reflector antennas and for applications at optical frequencies.[5] FSSs made of annular elements were shown to be less sensitive to the incidence angle and polarization than other previous designs.[2–5] More recently, fractal resonators were proposed as small size scatterers able to reduce the angular dependence of FSS transmittance and/or reflectance.[6,7] Split ring resonators[8] (SRRs) can also be used as small size scatterers for FSS design.[9,10] However, the transmittance/reflectance of SRR made FSSs strongly depends on the angle of incidence.[10]

The aim of this work is to develop an isotropic (i.e., polarization and angle independent) FSS by using SRRs as basic elements. It was shown in Ref. 10 that the SRR anisotropy is the main source of FSS anisotropy. Therefore, the first challenge is to find a suitable arrangement of SRRs showing an isotropic behavior. Once this arrangement is found, it can be expected that FSSs made of such elementary scatterers will show almost isotropic behavior. In Ref. 11, it was demonstrated that the cubic resonator (CR) shown in Fig. 1(a) exhibits an isotropic behavior due to its invariance under the tetrahedral point group of symmetry (or *T* group in Schöenflies notation). The planar resonator used in this CR was first introduced in Ref. 12 and called nonbianisotropic SRR (NB-SRR). In what follows, this cubic element will be called *T*-CR, in accordance with its symmetry properties.

A square network of 18×18 *T*-CRs, partially shown in Fig. 2, was assembled in order to form an isotropic FSS. To illustrate the importance of the aforementioned symmetry, another anisotropic FSS made of 18×18 CRs of conventional SRRs shown in Fig. 1(b) was also manufactured. Geometrical parameters of both samples were equal. The resonance frequencies of each individual NB-SRR and SRR were measured in an *X*-band waveguide, getting the experimental frequencies of resonance $f_{\text{NB-SRR}} = (10.00 \pm 0.22)$ GHz and $f_{\text{SRR}} = (9.65 \pm 0.28)$ GHz, respectively.

Figure 3 shows the experimental setup used for the analysis of the transmission through both FSSs. Two conventional *X*-band horn antennas were used as emitter and receiver. The FSS was measured for TE_y, TE_x, TM_y, and TM_x polarizations, where TE (TM) means that the electric (magnetic) field is tangent to the FSS and TF_x (TF_y) means that the field F of the incident wave is directed along the x (y) axis. Different polarizations were achieved by rotating either
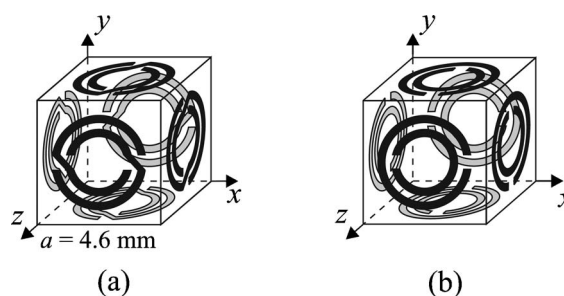

FIG. 1. Unit elements used for the design of the FSSs: (a) the isotropic *T*-CR and (b) the CR made of conventional SRRs.
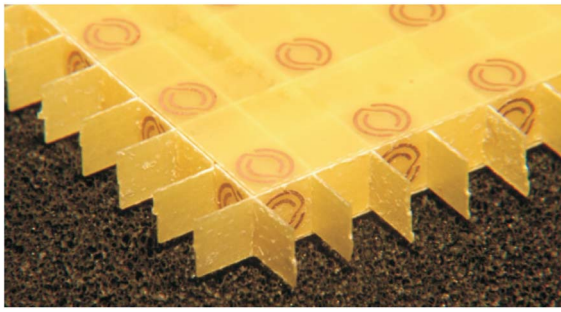
[a]Electronic mail: l_jelinek@us.es

FIG. 2. (Color online) Image of the actual experimental isotropic FSS structure made of *T*-CRs. The sample has a size of 16.6×16.6 cm^2 and contains 18×18 CRs with edge size $a = 4.6$ mm placed on a square network of periodicity $2a$. Geometrical dimensions of planar resonators are external radius $r_{ext} = 1.8$ mm, width of strips $w = 0.2$ mm, distance between strips $d = 0.4$ mm, and slit size $g = 0.4$ mm. Planar resonators were etched on a dielectric substrate FR4, with $\varepsilon_r = 4.4$, thickness $t = 0.2$ mm, and copper metallization thickness $h = 17$ μm.

the sample or the antennas. In order to avoid diffraction effects on the FSS borders, the FSS was surrounded by a microwave absorber. Finally, since a bigger incidence angle implies a smaller sample effective cross section, transmission was normalized to previous measurements of transmittance through the hole in the absorber without the sample.

Figures 4 and 5 show the transmission through the sample made of *T*-CRs for a selected set of angles (the measurement was made for angles from $-50°$ to $50°$ with $10°$ step for all polarizations). For better readability, Fig. 4 presents fewer angles showing amplitude and phase of transmission and Fig. 5 presents finer angle definition but shows only amplitudes and selected polarizations. Both figures, however, clearly reflect the angle independency of transmission for both TE and TM polarizations, except for small deviations that may be attributed to imprecision during the manufacturing process.

Transmission through the FSS made of conventional SRRs is reported in Fig. 6. It can be seen that the transmission strongly depends on the angle and the polarization of the incident wave, i.e., this FSS clearly exhibits an anisotropic behavior. Furthermore, instead of a single stopband approximately centered at the resonance frequency of a single SRR, a set of four stopbands appears. This splitting of the transmission dip cannot be attributed to fabrication imprecision (note that the distance between dips is bigger than
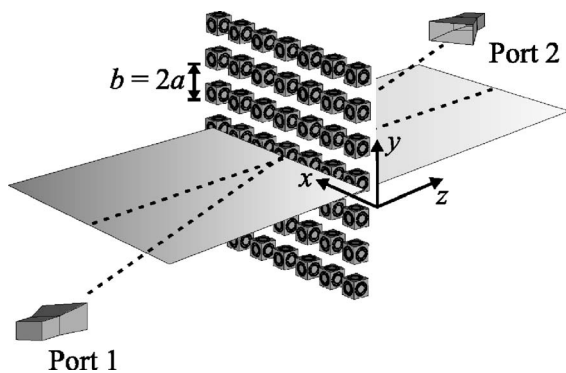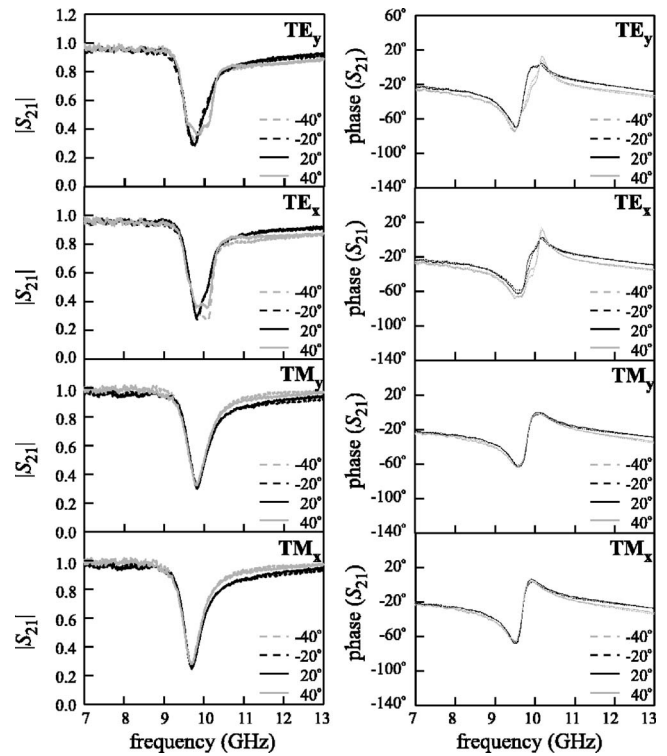

FIG. 4. Measured transmission coefficient S_{21} through the FSS made of the *T*-CR shown in Fig. 1(a) for different incidence angles and polarizations.

$\Delta f_{SRR} = 0.28$ GHz) but to internal couplings in the unit element.[13] We feel that these results show the importance of geometrical symmetries in order to obtain an isotropic behavior for the FSS.

Finally, a model of isotropic FSS describing its overall characteristics is presented. This model is based on approximation by slab of homogeneous isotropic medium of thickness $t = 2a$ equal to the FSS periodicity. Although we admit that such model cannot be rigorous, since there is no periodicity along the direction normal to the FSS, it can serve as first order approximation. The model assumes that the coupling between adjacent cubic resonators is not strong. In such case, the relative permeability of the three-dimensional lattice of cubic SRRs can be approximated as $\mu_r = 1 + \mu_0 \alpha / V$, with $V = (2a)^3$ being the volume of unit cell and $\alpha = 2\omega^2 A^2 / [(L+M)(\omega_0^2 - \omega^2 + j\omega\gamma)]$ the *T*-CR free space polarizability, where A is area of planar SRR. The self-inductance L was calculated using the inductance model from Ref. 14 and the mutual inductance M as coupling between two circular loops. The resonance frequency ω_0 was taken equal to the experimental resonance frequency of the FSS and the damping factor γ was fitted so that the trans-

FIG. 3. Sketch of the experimental setup for measuring the transmission through the FSSs. Two *X*-band horn antennas, located at $l = 61$ cm from the sample, are used as emitter and receiver. The FSS is placed in a window opened in a wood panel covered with microwave absorber. The size of this absorber panel is 122×122 cm^2.
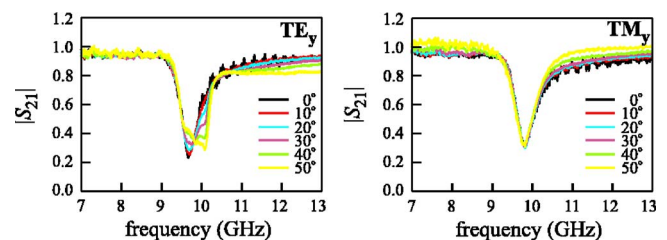

FIG. 5. (Color online) Measured amplitudes of transmission coefficient S_{21} through the FSS made of the *T*-CR shown in Fig. 1(a) for different incidence angles and TE$_y$ and TM$_y$ polarizations.
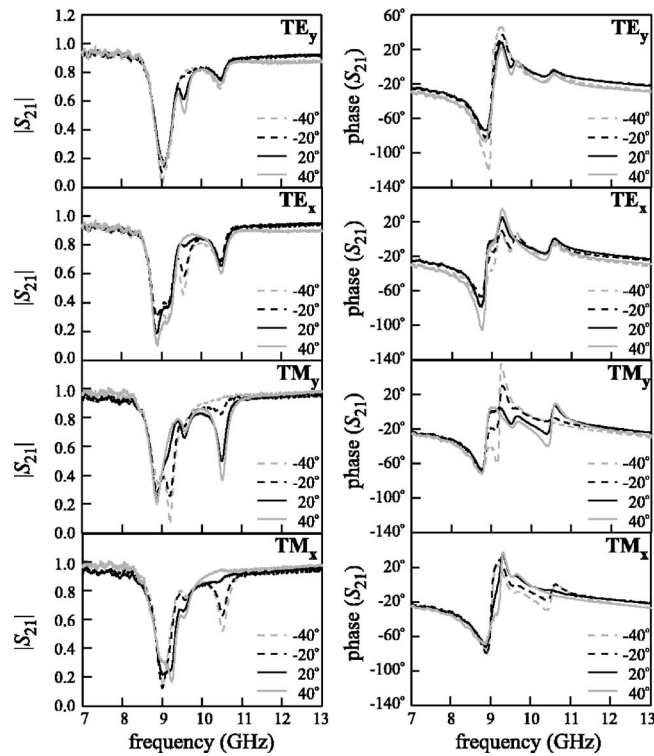
FIG. 6. Measured transmission coefficient S_{21} through the FSS made of conventional SRR CRs shown in Fig. 1(a) for different incidence angles and polarizations.

mission coefficient through the slab coincides with experimental value at normal incidence. The resulting transmissions through the slab are shown in Fig. 7 for both polarizations. It can be observed that transmissions in Fig. 7 show a similar behavior to those in Figs. 4 and 5. Figure 7, however, also shows that the slab model predicts a dependence of the minimum transmission on the angle of incidence bigger than the experimental values. Thus, the bulk isotropic material model may offer a reasonable first order approximation. However, more precise calculations are
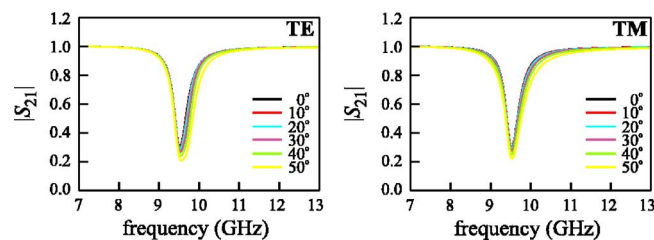

FIG. 7. (Color online) Amplitudes of transmission coefficient S_{21} through a slab model of FSS for different incidence angles and polarizations. Parameters of the model are $\omega_0 = 6.0 \times 10^{10}$ s^{-1}, $a = 4.6 \times 10^{-2}$ m, $A = 6.2 \times 10^{-6}$ m^2, $L + M = 3.0 \times 10^{-9}$ H, and $\gamma = 1.6 \times 10^9$ s^{-1}.

needed to reproduce all the observed effects in detail.

In summary, an isotropic polarization and angle independent FSS has been designed by using previously proposed isotropic SRR cubic resonators that are invariant under the tetrahedral point group of symmetry and an *ab initio* physical model has been proposed. Practical applications of the reported device may arise in the design of frequency selective antenna reflectors and antenna dichroic subreflectors.[1] Since magnetic response of SRRs has been shown from the radiofrequency to the terahertz range,[15] applications of the proposed design may cover all the aforementioned range of frequencies. In fact, the proposed isotropic FSS design is the first practical application of the isotropic cubic resonators already proposed in Ref. 11 for metamaterial design. We feel that this application will pave the way for future applications, including truly isotropic three-dimensional magnetic metamaterials with interesting applications in lenses and other bulk metamaterial devices.

[1]B. A. Munk, *Frequency Selective Surfaces: Theory and Design* (Wiley, New York, 2000).

[2]A. Roberts and R. C. McPhedran, IEEE Trans. Antennas Propag. **36**, 607 (1988).

[3]J. Huang, T. Wu, and S. Lee, IEEE Trans. Antennas Propag. **42**, 166 (1994).

[4]T. Wu and S. Lee, IEEE Trans. Antennas Propag. **42**, 1484 (1994).

[5]D. Labeke, D. Gerard, B. Guizal, F. I. Baida, and L. Li, Opt. Express **14**, 11945 (2006).

[6]L. Zhou, C. T. Chan, and P. Sheng, J. Phys. D **37**, 368 (2004).

[7]W. Wen, L. Zhou, B. Hou, C. T. Chan, and P. Sheng, Phys. Rev. B **72**, 153406 (2005).

[8]J. B. Pendry, A. J. Holden, D. J. Robbins, and W. J. Stewart, IEEE Trans. Microwave Theory Tech. **47**, 2075 (1999).

[9]F. Falcone, T. Lopetegi, M. A. G. Laso, J. D. Baena, J. Bonache, M. Beruete, R. Marqués, F. Martín, and M. Sorolla, Phys. Rev. Lett. **93**, 197401 (2004).

[10]M. Beruete, M. Sorolla, R. Marqués, J. D. Baena, and M. Freire, Electromagnetics **26**, 247 (2006).

[11]J. D. Baena, L. Jelinek, R. Marqués, and J. Zehentner, Appl. Phys. Lett. **88**, 134108 (2006).

[12]J. D. Baena, J. Bonache, F. Martín, R. Marqués, F. Falcone, T. Lopetegi, M. A. G. Laso, J. García-García, I. Gil, M. Flores, and M. Sorolla, IEEE Trans. Microwave Theory Tech. **53**, 1451 (2005).

[13]J. D. Baena, L. Jelinek, and R. Marques, "Towards a systematic design of isotropic bulk magnetic metamaterials using the cubic point groups of symmetry," Phys. Rev. B (2007) (to be published).

[14]R. Marqués, F. Mesa, J. Martel, and F. Medina, IEEE Trans. Antennas Propag. **51**, 2572 (2003).

[15]T. J. Yen, W. J. Padilla, N. Fang, D. C. Vier, D. R. Smith, J. B. Pendry, D. N. Basov, and X. Zhang, Science **303**, 1494 (2004).